Present and future hadronic physics studies with the HADES and ̄ PANDA experimental set-ups Diplôme d'HabilitationàHabilitationà Diriger des Recherches

B. Ramstein

Present and future hadronic physics studies with the HADES and P̄ANDA experimental set-ups

mémoire présenté par

Béatrice RAMSTEIN

pour obtenir le

Diplôme d'Habilitation à Diriger des Recherches

Institut de Physique Nucléaire d'Orsay, CNRS/IN2P3-Université Paris Sud 11

Contents

Introduction

1 Preamble

This document describes the context of my activities during approximately the last five years. The latter where roughly equally shared between the preparation of future experiments with the P̄ANDA detector and the antiproton beam at the future FAIR facility and the data analysis from the HADES experiment. This document however describes in more detail the activity on PANDA. The natural reason is that this was a pionneering activity for which a lot of preliminary work and bibliography had been performed before the publication of our final results and not gathered in any document. The HADES part is written with less details, since more informations can be found either in the publications or in Emilie Morinière's thesis or will be found very soon in Tingting Liu's thesis.

2 HADES and PANDA: two set-ups dedicated to QCD studies

The theory of the strong interaction is the Quantum Chromodynamics (QCD), the quantum field theory of interacting quarks and gluons. Together with the electroweak theory, QCD is part of the standard model of particle physics.

QCD is well tested at high energies, where the strong coupling constant is small and perturbation theory applies. The success is such, that there is no serious doubt that QCD is the correct theory for strong interactions. In the low-energy regime, however, the coupling constant is large and perturbative calculations are no longer possible.

One particularity of the strong interaction consists in the fact that gluons interact among themselves since they carry color charge. On the other hand, the interaction is large and attractive at large distances. This prevents from seing direct manifestations of quark and gluon degrees of freedom. Indeed, in any strongly interacting system, apart from the valence quarks, many quark-antiquark pairs and many gluons are involved. Therefore a very complex many-body problem has to be solved. As a consequence, in the non perturbative regime, it is very hard to make quantitative predictions starting from the QCD lagrangian. Two ways of solving this problem are proposed by theoreticians: effective field theories or lattice QCD calculations. On the other hand, precise data, ranging from the low regime to the region were perturbative QCD holds are needed to check the predictions.

Both HADES and PANDA experimental programs have as a central goal the study of QCD. Very schematically, HADES main objective is to explore the phase diagram of the strongly interacting matter, while PANDA highlights the study of the QCD bound states, including the search for the most exotic ones. Both aspects are connected to the problems of confinement and mass generation.

An important feature of the QCD lagrangian is the chiral symmetry. The spontaneous breaking of this symmetry plays an important role in the hadron spectrum. In hadronic matter, it is expected that a partial restoration of this symmetry occurs, which could induce modifications of vector meson properties. The HADES experiment, described in Part I was built in order to study these effects in the dense matter produced by heavy-ion collisions at 1-2 AGeV. In addition, the dilepton production in elementary reactions is sensitive to the intrinsic electromagnetic structure of the involved hadrons.

Taking advantage of the high intensity antiproton beams that will be available at the

future FAIR facility at Darmstadt, the PANDA project, described in part II, proposes many measurements addressing fundamental questions of QCD, ranging from the non-perturbative to perturbative regimes. One of them is the measurement of proton Time-Like electromagnetic form-factors for which we performed a full feasibility study described in Part II.

Part I
The HADES experiments

1 HADES, in the general context of dilepton experiments

1.1 Strongly interacting matter

The exploration of the different phases of the strongly interacting matter is at the heart of the research in nuclear physics. The most common form of this matter around us is the atomic nucleus, made of bound neutrons and protons. Further in the universe, neutron stars correspond to very high neutron densities and low temperatures. In the early universe, a few μs after the BigBang, a deconfined phase of quarks and gluons (the Quark Gluon Plasma) existed, with large temperatures and essentially zero baryonic density. A phase diagram of strongly interacting matter can be defined, using the baryonic chemical potential (μ_B) and the temperature (T) (fig. 1), where these different objects find their place.
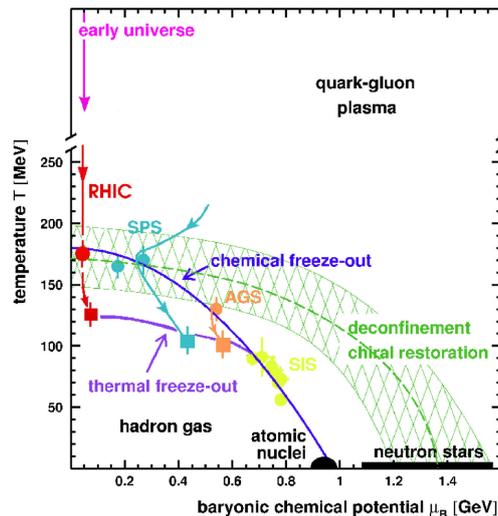
Figure 1: Schematic QCD phase diagram from [1]. The chemical potential and thermal freeze-out temperature (μ_B,T) values are deduced from analysis of observed hadron production spectra at the different facilities. The hatched region shows lattice-QCD and model estimates for the transition between hadronic matter and the Quark-Gluon Plasma.

In nuclear reactions, assuming that a thermal equilibrium is reached, the interacting system explores different zones of the phase diagram, depending on the energy and type of the initial collision. With low energy projectiles (E < 100 AMeV), the nucleus can be studied in its ground state or can be excited into a hot nucleus, still consisting of interacting nucleons. In Ultra-Relativistic Heavy-Ion Reactions as studied at RHIC or at CERN, a deconfined "state", the so-called Quark-Gluon Plasma, might be reached. Between these two extremes, at SIS energies (E $\sim$ 1-2 AGeV), a hadronic matter made of interacting mesons and baryonic resonances is created. Under these conditions, the system clearly stays in the confinement region. However, a partial restoration of chiral symmetry is expected, as will be discussed in the following, with the prediction of sizeable modifications of the properties of the hadrons.
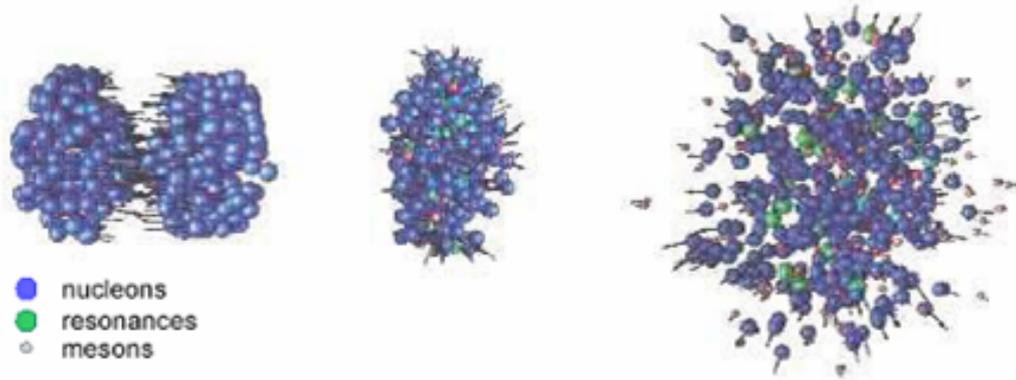
Figure 2: Sketch of a heavy-ion collision with three stages: first chance collisions, dense phase, and freeze-out.

The main goal of the HADES experiments is the search for such effects.

The end point of the thermodynamical evolution of the system is the thermal freeze-out, where all the interactions between the constituents stop, i.e. the momenta of all the particles are fixed. Beforehand, the system passes through the chemical freeze-out point, where the inelastic interactions end and therefore particle production is switched off. At SIS energies however, the chemical freeze-out coincides with the thermal freeze-out. The black squares on the picture indicate estimates for these chemical freeze-out points, deduced from particle production at the different facilities [2]. These points are aligned on a curve corresponding approximately to E/N~1 GeV, where E is the total energy in the system and N the number of particles in the system. These particles are purely nucleons at the low temperature end of the freeze-out curve, but, the more the temperature increases, the more mesons are present in the system and heavier mesons can also be produced.

One can distinguish different stages in a nucleus-nucleus collision:

- First chance collisions between a nucleon in the target and a nucleon in the projectile, where resonances or mesons can already be produced, in conditions close to a nucleon-nucleon collision in vacuum.

- The production of a presumably dense and hot equilibrated system, the "fire-ball", where mesons and baryonic resonances are continuously produced and absorbed.

- The freeze-out, where the type of the emitted particles and their kinematics is fixed.

1.2 Vector mesons

The well-known advantage of the dilepton probe is its insensitivity to strong interactions. Dileptons are therefore faithful witnesses of the different phases of the hadronic matter from which they can originate. With $J^P=1^-$, i.e. the same quantum numbers as a real photon, vector mesons have a direct decay to dilepton channel (see Table 1). Despite the small branching ratio, dilepton spectroscopy is thus the ideal tool to study in-medium vector mesons and more especially the ρ meson, which, due to its small life time, has a higher probability to decay inside the dense zone.

Schematically, the principle of dilepton experiments is to reconstruct the invariant mass of the e^+e^- pair in order to measure the mass of particles decaying into an e^+e^- pair. More

meson	mass (MeV/c^2)	Γ (MeV/c^2)	$c\tau$ (fm)	main decay	e^+e^- branching ratio
ρ	768	152	1.3	$\pi^+\pi^-$	$4.4 \ 10^{-5}$
ω	782	8.43	23.4	$\pi^+\pi^-\pi^0$	$7.2 \ 10^{-5}$
ϕ	1019	4.43	44.4	K^+K^-	$3.1 \ 10^{-4}$

Table 1: Vector meson main characteristics
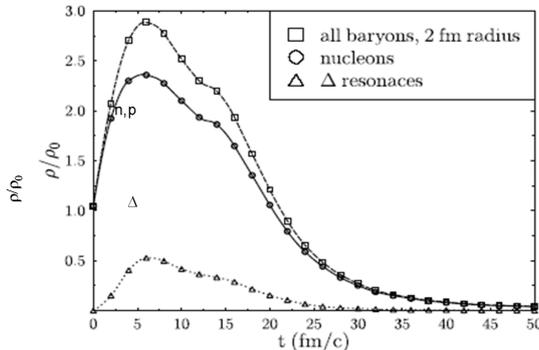
Figure 3: Evolution with time of the density of all baryons, nucleons and Δ in a Au+Au collison at 1 AGeV in UrQMD calculation [3].

realistically, a dilepton invariant mass spectrum is built, which results from the superposition of different electromagnetic processes, which overlap subtantially. In fact, the dilepton spectroscopy can be seen as the response of nuclear matter to an electromagnetic probe with $q^2 = M_{\gamma*}^2 = M_{ee}^2$. Since q^2 is positive, it is a time-like probe, complementary to electron scattering, for which q^2 is negative. The search for medium effects therefore requires the detailed decsription of all the elementary mechanisms which build this response. It belongs also to the objectives of the HADES experiment to provide a better understanding of these electromagnetic processes.

1.3 Role of baryonic resonances in dilepton production

One of the specificities of the 1-2 AGeV is the importance of baryonic resonance excitation. The dominance of $\Delta(1232)$ in inelastic nucleon-nucleon collisions is well-known. In addition, it has been outlined, that a kind of "resonance matter" was created in heavy-ion collisions at these energies, 15% to 30% of the nucleons being excited as baryonic (mainly $\Delta(1232)$) resonances (fig. 3). Due to the quite long life-time ($\sim$15 fm/c) of the dense phase in these collisions, these resonances can therefore propagate and regenerate and the modification of their spectral function inside the baryonic medium is an important issue for the dynamics of these collisions, as will be shown in sec. 1.5.3).

The $\Delta(1232)$ resonance is the most copiously produced, but as the incident energy increases, higher lying resonances play an increasing role. While all of them contribute to pion production, the N(1535) for example is important for the η production and the N(1520), $\Delta(1620)$ and others for the ρ production. Through the direct dilepton decay ($\rho/\omega \rightarrow e^+e^-$) or Dalitz decay ($\pi^0/\eta \rightarrow \gamma e^+e^-$ or $\omega \rightarrow \pi^0 e^+e^-$) modes of these mesons, the baryonic resonances therefore play a crucial role in dilepton emission. They are also expected to contribute directly to dilepton emission via their own Dalitz decay modes. For example, the $\Delta(1232)$ should present a Dalitz decay (e.g. $\Delta \rightarrow Ne^+e^-$) branching ratio of $4.2 \ 10^{-5}$, according to QED calculations. As it has never been measured up to now, the experimental study of this

10

decay mode is an experimental challenge. In addition, the Δ Dalitz decay process is in principle sensitive to the electromagnetic structure of the N-Δ transition and the kinematics is suited to test the Vector Dominance Models, as will be discussed in the next section.

1.4 Vector Dominance

The coupling of vector mesons to virtual photon appear in fact in other processes than their mere decay, due to the Vector Meson Dominance (VDM), which stipulates that the coupling of a real (or virtual) photon to any electromagnetic hadronic current is mediated by a vector meson [4], as sketched on fig. 4. Following the Vector Dominance Model, dilepton spectroscopy can therefore be considered as an in-medium vector-meson spectroscopy.

VDM is a very good prediction for the mesonic transition, and works pretty well also for baryonic transitions. In practice, this is included in the electromagnetic elastic or transition baryonic form-factors which are parametrizations of the hadron electromagnetic structure in the electromagnetic currents. Due to the creation of an e^+e^- pair, the four-momentum transfer squared $q^2 = M^2_{\gamma\star}$ in these electromagnetic decays is a positive quantity, which means that these form-factors are Time-Like. In the case of the Dalitz decays of baryonic resonances $(R \rightarrow Ne^+e^-)$, values of q^2 close to the vector meson poles can be reached, and hence a higher sensitivity to the VDM electromagnetic form-factors might be observed. These VDM form-factors take in fact into account an off-shell production of vector mesons. This is illustrated in fig.5, where the dilepton production from the Dalitz decay of many different baryonic resonances are calculated with the RQMD model (see section...) using e-VDM [1] electromagnetic form-factors for the baryonic resonances. This picture is modified in the medium due to the couplings of mesons and baryonic resonances with surrounding medium.

Figure 5: Cross-sections for pp→ppe$^+$e$^-$ at a kinetic proton energy T=1.61 GeV, with the contributions of various baryonic resonances [5].

Figure 4: Sketch of the Vector Dominance Model.

1.5 Medium modifications of vector mesons

I will describe here the theoretical background of the search for medium modifications in a very schematic way and only give an overwiew of the experimental results obtained so far.

---

[1]Extended-Vector Dominance model: a variant of VDM, where also excited vector mesons ρ and ω mesons are taken into account.

Recent reviews, like [6, 7, 8] give a much more comprehensive description of both aspects. In particular, [8] gives more details about experimental results. In [7], the emphasis is put on the hadronic models and the quark-hadron duality, while the chiral restoration transition of QCD is the main topic of [6].

1.5.1 QCD vacuum and Chiral restoration

Chiral symmetry is a fundamental symmetry of the QCD lagrangian [9]. However, this symmetry is spontaneously broken and it is therefore absent in the QCD vacuum and excited states. This is clearly visible at the level of the low mass part of the hadronic spectrum, where there is no degenaracy between chiral partners such as the pion or the sigma meson, the $\rho(770)$ and $a_1(1260)$ mesons, and the nucleon and N(1535). The violation of the symmetry can be quantified by different order parameters. Due the quark-hadron duality inherent to the strong interaction, two order parameters are introduced. The first one is the quark condensate $< 0|\bar{q}q|0 >$, which amounts to about $-(250 \text{ MeV})^3$ as found in effective Lagrangian calculations [10] or in recent lattice QCD calculations [11]. The second order parameter is the constant $f_\pi = 92.4 \pm 0.3$ MeV corresponding to the weak pion decay ($\pi^- \rightarrow \mu^- \bar{\nu}_\mu$). Both are related by the Gell-Mann-Oakes-Renner relation, which makes a useful connection between quark condensates and hadronic properties.

$$m_\pi^2 f_\pi^2 = -2m_q < 0|\bar{q}q|0 > \tag{1}$$

While the Higgs mechanism generates the current quark masses, and therefore contributes to only about 2% of the mass of a proton, the chiral symmetry breaking is responsible for the hadronic masses in a much larger extent. The underlying mechanism at the origin of this dynamical mass is the coupling of the constituent quarks with the QCD vacuum quark condensate, resulting in an effective quark mass of about 300 MeV.

While the spontaneous chiral symmetry breaking is an essential feature of the hadron spectrum in vacuum, full restoration of chiral symmetry is predicted at high temperatures and/or densities, in the Quark-Gluon-Plasma. However, the transition towards such a state is difficult to describe theoretically. Numerical computations on the lattice at finite temperatures predict that chiral symmetry restoration occurs at a temperature of 160-190 MeV [12, 13]. This transition is characterized by a rapid decrease of the quark condensate. Such an effect, observed as a function of increasing baryonic density or temperature had already been predicted long before [14]. The quark condensate is not an observable, the hope is thus to detect the consequences of its decrease on the hadron spectrum. However, although QCD sum-rules provide useful constraints, the connection to hadronic observables cannot be made in a model independent way.

There is now a long history of models, providing more or less spectacular shifts and increase of widths of hadrons.

1.5.2 Quark models

In these models, the modifications of the properties of the hadrons are related to the changes of the condensates in strongly interacting medium. Models using the Nambu-Jonia Lasinio approach predicted the spectral degeneracy of π and σ mesons, the ρ and a1 in dense matter, but no mass shift of the ρ meson. Using QCD sum rules, Hatsuda and Lee [15] predicted a linear drop of the vector meson with increasing density. Brown and Rho [16] predicted a universal scaling of the masses of light mesons and of the nucleon as a function of density and temperature, a well-known conjecture which can be justified in the context of Chiral Effective Theories [17]. In both approaches, the effect is a decrease of about 20% for the ρ

meson at normal nuclear matter density. Such decrease of hadron masses are also predicted,
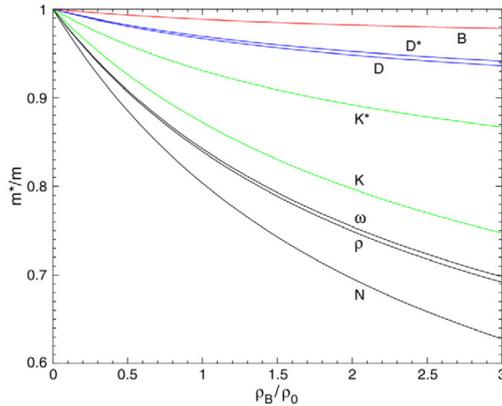
Figure 6: Changes of hadron masses predicted by the Quark Gluon Coupling [18].

for example, in Quark-Meson Coupling models [18], where quarks and gluons are confined in a bag and interact with scalar and vector potentials in the hadronic medium (fig. 6).

1.5.3 Hadronic models

Quark models can predict mass shifts, but cannot provide a full description of the hadron properties in the nuclear medium. The latter are however contained in hadronic spectral functions, which can be deduced from the propagator of the meson in the hadronic matter. It is thus necessary to use models to provide these spectral functions, based on our present understanding of meson-baryon interactions. This is the approach followed by the hadronic many-body models.

Pions and Δ-hole states

The first well-known effect is the modification of the pion propagator in nuclear matter. The coupling of the pion to the Δ-hole states (fig. 7) produces a collective mode, called "pionic branch", or "pisobar". As a consequence, pions and Δ's do not exist as such in nuclear matter, but propagate through these collective spin-isospin modes.

To show evidence for this collective effect, a probe is needed, which transfers the energy ω and momentum $\vec{q}$ in the appropriate kinematical range to excite this pionic branch. Charge exchange reactions, as studied at the Laboratoire National SATURNE (see [22, 23, 24] and references therein) proved to be well-suited for these studies. These reactions are indeed quite selective for spin-isospin interactions and enhances the spin-longitudinal excitations for which the collective effects are expected to be maximum. So, despite the peripheral character of this reaction, it is widely admitted that the experiments performed at SATURNE were able to show evidence for this collective mode. In particular, in the (^{3}He,t) reaction, a shift of the Δ resonance peak excited on nuclei, from ^{12}C to ^{208}Pb of about 70 MeV was observed, in comparison with the measurement on the proton. This effect could be explained by the calculations only when attractive Δ-hole correlations were included [20, 25] (fig. 8). This confirmed the prediction that longitudinal spin-isospin excitations propagate in the nuclear medium as depicted in fig. 7a. Exclusive channels studied in the same reaction have subtantially confirmed this picture. In particular, the coherent pion production mode (fig. 7b), thought to be most directly related to these longitudinal spin-isospin correlations, was observed [26, 27, 28].

Coupling of vector mesons to resonances
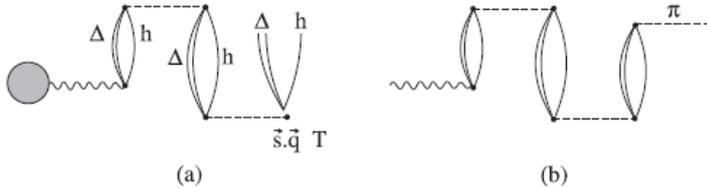
Figure 7: (a) Propagation of the longitudinal spin-isospin excitation in the nuclear medium. (b) Coherent pion production. Picture from [19]
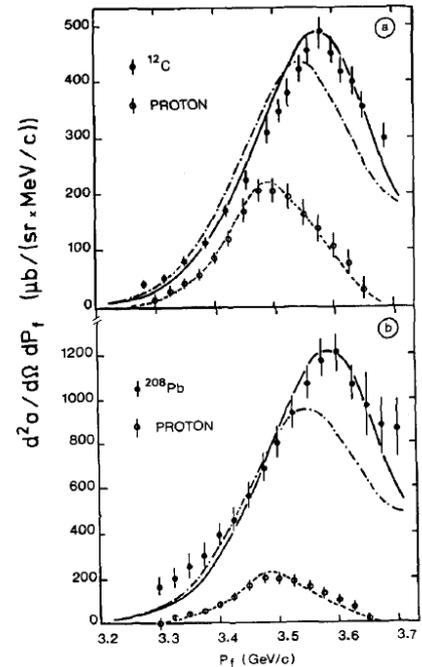
Figure 8: Comparison of theory [20] to experiment [21] for Δ excitation in ^{12}C and ^{208}Pb by the (^{3}He,t) reaction at 2 GeV and 0° triton angle. The full and dot-dashed curves correspond respectively to calculations with and without Δ-hole correlations.

The ρ propagator is affected directly by the dressing of the two decay pions in hadronic matter (fig.9a). But, it is also modified by the interactions with baryons (fig.9b). The vector meson propagates by exciting resonance-hole states, and the resonance itself is dressed through the interaction with the medium. This is very similar to the "pisobar", built on the coupling of π to Δ-hole states and this effect is therefore sometimes called "rhosobar".

The spectral function of the meson is related to the imaginary part of the propagator, and depends on the hadron energy and momentum, but also on its polarization. This is illustrated in the case of a coupled channel analysis by Post et al. [29, 30] in fig. 10. The broadening of the peak is more important in the transverse response, especially at high momenta, due to the coupling to resonances like $F_{35}(1905)$ and $P_{13}(1720)$. An additionnal structure well below the ρ peak is clearly present at low momenta, due to the coupling to the $D_{13}(1520)$ resonances. The dependence of the ρ meson peak with density is illustrated in fig. 11 in the case of Rapp and Wambach's model [31]. The peak is found to be slightly upward shifted and significantly broader when the baryonic density increases. Both models give similar results. However, the strong coupling of the ρ to $N(1520)N^{-1}$, used by both models and responsible for the low energy structure is in contrast to [32], which predicts an overall lower in-medium ρ broadening. As all these models use the experimental constraints from πN phase-shifts and inelasticities and $\pi N \to \rho N$ and $\gamma N \to \rho N$ cross-sections, it stresses the fact that these coupling constants need to be better constrained by experimental data. The measurement by HADES of ρ and ω production in pp and πp, and more especially the subthreshold production, should bring more constraints on these quantities, as will be shown in the following. A crucial parameter of these calculations is the strength of the ρ-nucleon-baryonic resonance couplings. For the

(a)　　　　　　　　(b)　　　　　　　　(c)
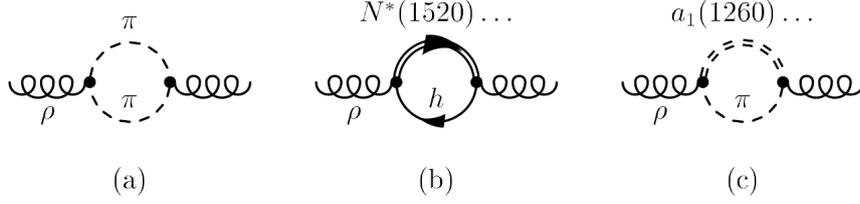
Figure 9: Dressing of the ρ in the nuclear medium via 2π propagator (a), coupling to baryonic resoances (b), coupling to mesonic resonances (c).
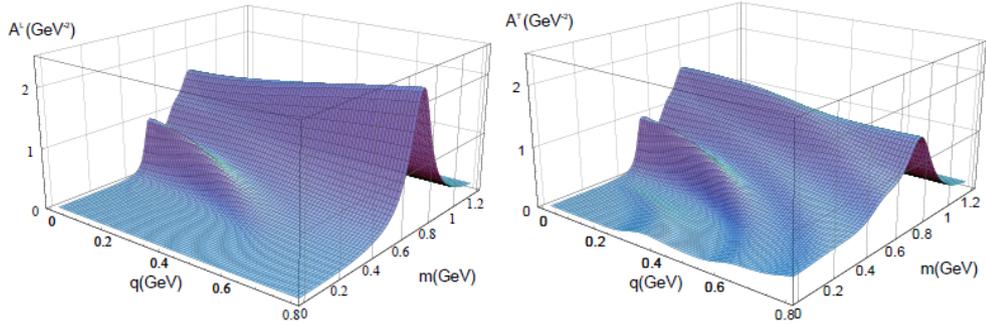
Figure 10: Imaginary part of the ρ propagator (or spectral function), for spin-longitudinal excitation (left) and transverse (right) as a function of the mass and momentum *at which*
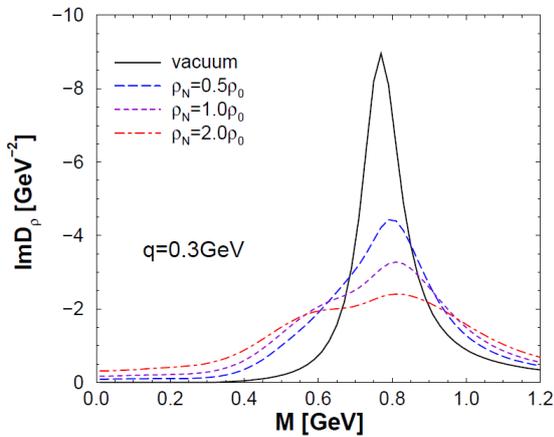
Figure 11: Imaginary part of the ρ propagator (or spectral function), as a function of the mass for different baryonic densities in the calculation of [31, 6].
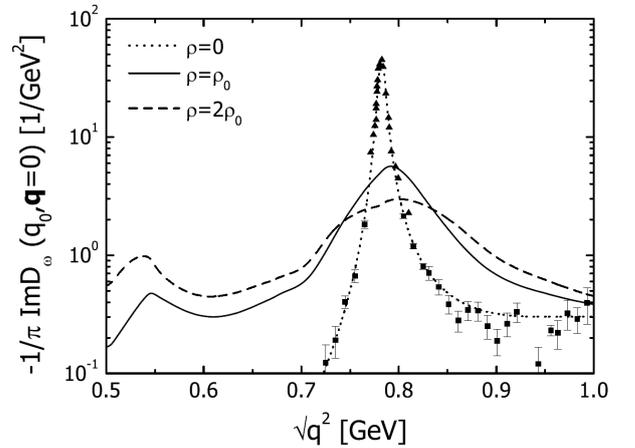
Figure 12: The ω spectral function for an ω meson at rest in vacuum (dotted line), for density $\rho = \rho_0 = 0.16$ fm^{-3} (thin solid curve) and $\rho = 2\rho_0$ (dashed curve).

ρ meson, the couplings of several resonances (i.e. the $D_{13}(1520)$), $S_{11}(1650)$, $D_{13}(1700)$ are reasonably well known [33], which reduces the uncertainty of the calculations. For the ω or ϕ, the situation is more difficult, since various resonances contribute coherently to the observed production cross-sections. It is therefore very difficult to extract experimentally the individual

couplings. One can however rely on theoretical analyses constrained by the existing $\pi N \rightarrow \omega N$ and $\gamma N \rightarrow \omega N$. In contrast to early predictions, there is now a general agreement that the ω mass is only very weakly changed in the medium. Predictions by [34], shown on fig. 12 indeed exhibit a subtantial broadening, but no shift. The bump at low momenta is due to the coupling to $S_{11}(1535)$ and $D_{13}(1520$ resonances. This structure is however much reduced in comparison to the ρ case, due to the smaller couplings.

Access to the in-medium width can however be achieved by measuring the transparency ratio:

$$T = \frac{\sigma_\omega^A}{A\sigma_\omega^N}, \tag{2}$$

where σ_ω^A and σ_ω^N are the cross-sections for production of the ω meson with elementary projectile such as γ or p respectively on a nucleus and on the nucleon. Sometimes the reference is a light nucleus instead of the proton, to reduce isospin effects. This ratio is related to the in-medium ω-nucleon cross-section, which is in turn related to the in-medium ω width.

It is a very challenging task to bridge the gap between the hadronic models and a QCD picture in terms of quarks and gluons and to relate medium modifications to Chiral Symmetry Restoration of QCD vacuum. One connection is obtained through the current-current correlation functions which can be calculated from the many-body hadronic models and at the same-time are constrained by QCD sum-rules [35]. The results are found compatible, which is a good sign of the consistency of both pictures. Further constraints arise from lattice-QCD calculations, so that much progress towards a consistent description of the transition towards Chiral Symmetry Restoration is expected in the next years.

1.6   Evidence for medium effects from previous experiments

First experiments looking for medium effects started in the late 1980's using heavy-ion reactions in the 1-2 AGeV at Berkeley with the DiLepton Spectrometer [36] and at 200 GeV at CERN with the HELIOS experiment [37]. These pioneering experiments stimulated the experimental programs developped later respectively at GSI with HADES and at CERN by the CERES and NA60 collaborations, as well as more recently at RHIC with the PHENIX experiment.

The interest of studying cold nuclear matter using elementary probes became also obvious and experiments using photons or protons were performed at JLab, ELSA, MAMI and KEK. We will first discuss the results concerning ultra-relativistic heavy-Ion reactions and cold matter and then explain the DLS puzzle, which was one of the motivation of the HADES experiment.

1.6.1   Ultra-relativistic heavy-ion reactions

The CERES (NA45) collaboration at CERN reported an excess in the e^+e^- mass spectrum in the system Pb+Au at 200 AGeV ($\sqrt{(s_{NN}} = 19 GeV$) [38] in the mass range between 300 and 700 MeV when comparing to a cocktail of hadronic decay channels. This effect was originally explained as a decrease in the mass of the ρ meson. However a second CERES measurement [39] with improved mass resolution favors a broadening of the ρ-meson in agreement with the expectations from the hadronic models rather than a simple mass shift.

A strong improvement in the sensitivity of the heavy-ion results with respect to medium effects has been achieved with the high quality NA60 results [40]. The dimuon measurement in In-In collisions at 158 AGeV indicates a doubling of the ρ-meson width, with no change in the mass. This result seems to confirm the prediction of many-body hadronic models [41]

and to rule out the prediction of a shifted mass "à la Brown and Rho". The ϕ meson, also measured in these reactions, does not present any modification [42].

The first RHIC data [43], obtained at $\sqrt{s_{NN}} = 200$ GeV show a very large excess e^+e^- signal concentrated in the mass region around 300 MeV, which can however not currently been explained by in-medium spectral functions.

1.6.2 Cold nuclear matter studies

The TAGX collaboration made an attempt to use the $\rho \to \pi^+\pi^-$ decay to study medium modifications on the ρ meson in γA reactions at the INS electron synchrotron in Tokyo, at incident energies between 600 and 1120 MeV. Although the first estimates [44] have been revised downwards, a shift of the ρ-meson mass was observed [45]. The results were however questionnable, due to the unavoidable pion rescattering effect.

The E325 collaboration detected at KEK ρ, ω, and ϕ mesons decaying into e^+e^- pairs from a reaction of 12 GeV protons incident on C and Cu targets [46, 47]. They reported a decrease of about 9% with no broadening for the ρ meson, no modification for the ω and both a 3.4 % decrease of the mass and a factor 3-4 increase of the width for the ϕ meson for slow momenta. A drawback of this experiment is the absence of measurement of like-sign pairs. The combinatorial background suppression therefore relies on the mixed-event technique, with an arbitrary normalization.

The Crystal Barrel/TAPS collaboration is studying the photoproduction of ω meson in the photon energy range 0.64-2.53 GeV, using the $\pi^0\gamma$ branching ratio of about 9 %. The $\rho \to \pi^0\gamma$ is suppressed, due to its lower branching ratio (6.10^{-4}). They first reported a decrease [48] in the mass of low-momenta ω mesons produced in Nb. When applying a new procedure for the background subtraction, the ω spectrum is now compatible with the one measured on the LH2 target [49]. The absence of in-medium shift is in agreement with predictions of BUU models.

In the G7 experiment at JLab using the CLAS detector, the ρ meson mass spectra have also been extracted for H, C and Fe-Ti targets in photon induced experiments at energies between 0.6 and 3.8 GeV. No shift is observed for the ρ meson mass and the increase of the width of about 70 MeV is consistent with collisionnal broadening. This contradicts the KEK results.

The transparency ratios (eq.(2)) have been measured for the ω meson produced in nuclei in the CLAS and CB/ELSA experiments and the in-medium widths deduced using either the Valencia or the BUU models. Widths of 130-150 MeV/c^2 are obtained, corresponding to very large ωN cross-sections (70 mb) for the CB/ELSA experiment and even larger widths ($\Gamma_\omega >$ 200 MeV) are obtained for the CLAS experiment. For the ϕ measurement at JLab, the width is 70 MeV/c^2.

These experimental observations, which are still missing a global understanding, are summarized in Table 2. The only strong evidence of medium effects is the broadening of the ρ meson observed in ultra-relativistic heavy-ion reactions and the ω collisonnal widths observed in the transparency ratios.

1.6.3 The DLS puzzle

The region of high densities and low temperatures was investigated by the DLS experiment at the BEVALAC facility at Berkeley in the years 1988-1993. The dilepton production was measured in C+C and Ca+Ca systems at incident energies of 1.04 AGeV [36], as well as in p+p and d+p reactions at energies between 1.04 GeV and 4.88 GeV [52]. A strong excess of the dilepton production over hadronic cocktails was observed, even for the small-size system

experiment	reaction	momentum acceptance	ρ	ω	ϕ
KEK-E325	pA 12 GeV	p > 0.6 GeV/c	$\frac{\Delta m}{m} \sim$ -9% $\Delta\Gamma \sim 0$	$\frac{\Delta m}{m} \sim$ -9% $\Delta\Gamma \sim 0$	$\frac{\Delta m}{m} \sim$ -3.4% $\Gamma \sim$ 15 GeV/c^2
CLAS	γA 0.6-3.8 GeV	p > 0.8 GeV/c	Δ m$\sim$ 0 $\Delta\Gamma \sim$ 70 MeV $\rho \sim \rho_0/2$	$\Delta\Gamma \sim$ 200 MeV $\star$ < p >> 1. GeV/c	$\Delta\Gamma \sim$ 70 MeV
CBELSA /TAPS	γA 0.9-2.2 GeV	p > 0 GeV/c		Δ m$\sim$ 0 $\Delta\Gamma(\rho_0) \sim$ 130 MeV $\star$ < p >$\sim$ 1.1 GeV/c	
SPring8	γA 1.5-2.4 GeV	p > 1.0 GeV/c			Δ m$\sim$ 70 MeV$\star$ < p >$\sim$ 1.8 GeV/c
CERES	Pb+Au 158 AGeV	p_t > 0 GeV/c	broadening favored over mass shift		
NA60	In+In 158 AGeV	p_t > 0 GeV/c	$\Delta m \sim$ 0 strong broadening		

Table 2: Experimental results on in-medium modifications of ρ, ω, and ϕ mesons reported by different experiments (adapted from [50]). The average densities or average momenta of the vector meson in the analysed events is sometimes indicated. The results indicated with a star correspond to transparency ratio measurements.
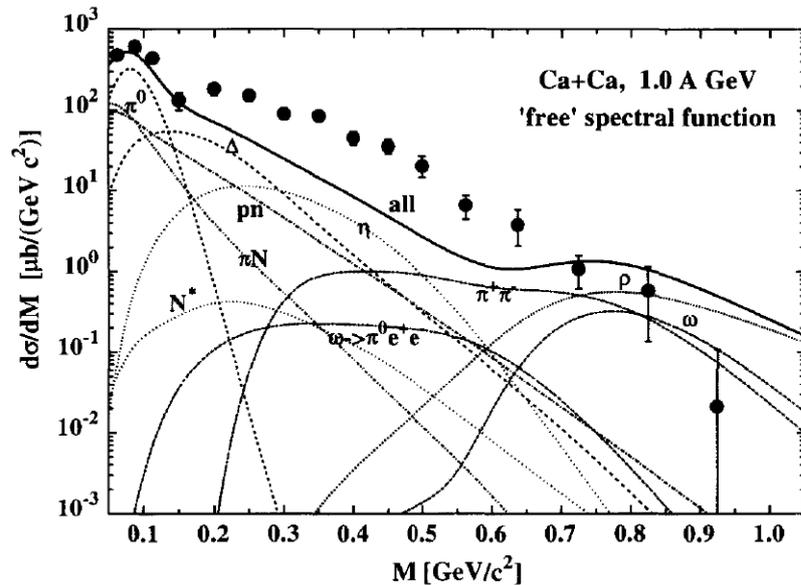
Figure 13: DLS data [36] compared to HSD calculations with free spectral functions [51].

C+C, as shown in fig 13. Even when medium effects were included, no model was able to reproduce these enhancements [53, 51]. On the other hand, the spectra measured in p+p and d+p reactions were reasonably well reproduced. This situation was known as the "DLS puzzle" and remained as such for more than ten years, until the HADES data were published, as will be explained in sec.4.2. The acceptance of the DLS set-up was reduced, due to its two-arm configuration (one for electrons, one for positrons). These data also suffered from a low mass resolution (10-20%), a small acceptance, and large systematic errors (30-40%).

1.7 The HADES "strategy"

The HADES experimental program adresses the question of in-medium modifications both in hot and dense matter, using the heavy-ion reactions and in the cold matter, through the

dilepton production induced by protons or, in the future, by pions on nuclei. One of the first goal was to revisit the dilepton production in the 1-2 AGeV with a much improved set-up with repect to the DLS.

HADES has naturally to face the problems inherent to all dilepton experiments. Three kinds of backgrounds have to be subtracted to analyse the ρ spectral function.

- First, the photons (from $\pi^0 \to \gamma\gamma$ decay or Dalitz decays of $\pi^0 (\pi^0 \to \gamma e^+ e^-$, $\eta \to \gamma e^+ e^-$,...) can convert in the detector material, producing $e^+ e^-$ pairs, which have to be rejected in the analysis, and also contribute to the combinatorial background. To reduce this contribution, which goes as Z^2, where Z is the atomic number of the element constituting the material, the HADES detector design (see sect.3.1 and [54]) is based on the "low-Z" concept. Following the same goal, the widths of the detectors are reduced as much as possible, and the solid targets are segmented.

- The second source of background is the combinatorial background. We will see in sec. 3.4 that both the mixed-event and the like-sign pair techniques are used for the subtraction and that it is reduced by a sophisticated analysis procedure.

  It has also to be noted that, in contrast to reactions at ultrarelativistic energies, the multiplicity of produced pions per participant remains of the order of 10% in the 1-2 AGeV range, which ensures much higher signal over background.

- The third background is the physical background due to the other dilepton sources. Its subtraction is to some extent model dependent. To reduce these uncertainties, a large part of the HADES experimental program is devoted to providing precise data to constrain the models. This philosophy appears very clearly in the elementary reaction study, which is performed at different energies to get sensitivity on the different dilepton sources. For the analysis of dilepton spectra in heavy-ion reactions, the distinction will be made, according to the sketch of the reaction in fig. 2 between long-lived sources which decay outside the dense zone and to short-lived sources which are sensitive to in-medium effects.

date	system	physics goal
2001-2002	C+C 2 AGeV	dilepton spectrum in small size system
2004	C+C 1 AGeV	+ check of DLS
2004	p+p 2.2 GeV	Validation of detector performance (pp elastic) π^0 and Δ Dalitz decays (helicity distribution)
2005	Ar+KCl 1.75 AGeV	medium effects
2006	p+p 1.25 GeV	Δ Dalitz decay , exclusive pp→ppe$^+$e$^-$ analysis
2007	d+p 1.25 AGeV	pn Bremsstrahlung
2007	p+p 3.5 GeV	inclusive ρ/ω production cross-sections
2008	p+Nb 3.5 GeV	vector mesons at normal density
2009-2010	HADES upgrade	
2010-2011	Ni+Ni 1.65 AGeV, Au+Au 1.25 AGeV	vector mesons at high densities
2011-2012	π^- + A, π^- + p 1.17 GeV, 1.8 GeV	vector mesons at normal densities and off-shell production

Table 3: The HADES dilepton experimental program

Table 3 shows the dilepton HADES experimental program and a shematic and restrictive description of the goal of each experiment. This table does not mention the hadronic channel

measurements, which I will deal with in the case of elementary reactions. It also omits the very important strangeness program, developped by the HADES collaboration, which will not be discussed here. My discussion of the HADES results will be in fact limited to the C+C and elementary reactions at 1.25 GeV and 2.2 GeV. The other systems will be mentionned briefly in the outlook.

2 Theoretical tools for the interpretation of HADES data

Three kinds of theoretical tools are used for the interpretation of the HADES data:

- The PLUTO event generator [55, 56] simulates dilepton production through different processes, which are added incoherently.

- Transport models describe the full dynamical evolution of the collision. They also add the different processes incoherently, but they give a much more accurate description of heavy-ion collisions, taking into account non-equilibrium particle emission and multi-step processes.

- For the nucleon-nucleon reactions (pp and pn), One Boson Exchange calculations are available, which give a quantum treatment of the pp→ppe$^+$e$^-$ and pn→pne$^+$e$^-$ reactions.

In the following, I present the ingredients of these theoretical tools, with emphasis on the new developments of the event generator PLUTO in which I took active part. This work was done in collaboration with the PLUTO responsible person, Ingo Fröhlich. The technical aspects were studied by Emilie Morinière for the Δ resonance parametrization and Dalitz decay branching ratio and by Tingting Liu for the angular distribution of the pionic and Dalitz decays aspects. We benefitted from a close collaboration with Jacques Van de Wiele, Francesco Iachello and with the theoreticians working on the interpretation of the HADES data, and more especially Elena Bratkovskaya and Boris Martemyanov.

2.1 Dilepton sources

In the 1-2 AGeV energy range, the main dilepton sources are:

- The Dalitz decays of mesons: $\pi^0 \to \gamma$ e$^+$e$^-$(branching ratio 1.2%), $\eta \to \gamma$ e$^+$e$^-$(branching ratio 7.10^{-3}), $\omega \to \pi^0$e$^+$e$^-$(branching ratio 8.10^{-4})

- The ρ and ω vector meson decay (see Table 1)

- The Dalitz decay of baryonic resonances: $\Delta \to$ N e$^+$e$^-$, N(1535) $\to$ N e$^+$e$^-$,.....The branching ratios have not been measured, but can be calculated using the constraints of the radiative decays.

- The nucleon-nucleon Bremsstrahlung: NN→NNe$^+$e$^-$.

The knowledge of the branching ratio of the meson or baryonic resonances decay is only one aspect of the problem. The dilepton yield depends also on the production cross-section of the given particle and of its mass distribution, which can also be modified in the medium. The consistent description of the dilepton production in heavy-ion collisions is therefore an intricated porblem, which still suffers from theoretical uncertainties.

2.2 Dilepton cocktails for heavy-ion reactions

Microscopic transport models are suited tools to describe heavy-ion collisions.

BUU models as well as Hadron String Dynamic (HSD) transport models are based on the Boltzmann-Uehling-Uehlenbeck (BUU) equations describing the flow of quasi-particles of different species, which includes mesons, nucleons and baryonic resonances. The Hadron String Dynamics (HSD), also based on the BUU model, includes particle production through string fragmentation at high energies.

The UltraRelativistic Quantum Molecular Dynamics (UrQMD), Isospin Quantum Molecular Dynamics (IQMD) and Relativistic Quantum Molecular Dynamics models (RQMD) are based on a semi-classical approach, where the trajectories of the particles are explicitly followed. In IQMD and RQMD, the only explicit degrees of freedom are nucleons, pions and baryonic resonances and heavier meson production occur via baryonic resonance excitation. In RQMD models, the vector meson production is not explicit and the dilepton production through vector meson decay is included via the electromagnetic form factors of the resonances parametrized in the Extended Vector Dominance Model, as was already shown in fig. 5.

To take into account medium modification predictions, in-medium spectral functions of the vector mesons can be introduced, based on the models described in sec. 1.5.

To generate dilepton cocktails for heavy-ion reactions, the PLUTO event generator uses the fire-ball model, i.e., a system in thermal equilibrium at a given temperature is considered and the energy of the particles is sampled according to the Boltzmann distributions. A radial expansion of the source can also be taken into account. The mass of the unstable particles are sampled according to Breit-Wigner distributions [55]. The π^+, π^-, π^0 and η meson production cross-sections in heavy-ion collisions are constrained by the TAPS, KAOS and FOPI measurements and the m$_T$-scaling is used for the ρ and ω mesons [51].

2.3 Meson production cross-sections

The existing ρ and ω vector meson production cross-sections and, when available the information on the production angular distributions are used by the different transport models as well as by the PLUTO event generator. The problem is, however, that these cross-sections were measured for the exclusive pp→ppρ or pp→ppω reactions, with the exception of one measurement of the inclusive ρ meson production cross-section at $\sqrt{s} \sim 5$ GeV. Well above threshold, the exclusive cross-section corresponds only to a small fraction of the inclusive production cross-section. The second limitation is related to the fact that these data, measured using the pionic decays of the mesons correspond to on-shell production, i.e., production above the two or three-pion threshold. Dilepton production, on the other hand, is sensitive to off-shell production, which occurs via intermediate baryonic resonances. As a consequence, the vector meson production depends on the production cross-section of the various baryonic resonances and on the coupling of these resonances to the vector mesons. Both ingredients have significant uncertainties, due to the lack of experimental constraints.

The pp reaction measured with HADES at 3.5 GeV (see Table 3), and currently being analysed [57] will provide a measurement of the inclusive pp cross-section. In addition, these data offer the possibility of both a leptonic analysis: (via pp→ppω/ρ →ppe^+e^-) and a hadronic analysis (via pp→ppω → pp$\pi^+\pi^-\pi^0$and pp→ppρ → pp$\pi^+\pi^-$) of the exclusive production, which will bring precious information on on-shell and off-shell productions. The fore-seen measurements in π-nucleon reactions (see sec. 6) will also be crucial to constrain the couplings to vector mesons, with the advantage of lower uncertainties on the production cross-sections of the resonances.

2.4 The resonance model

An extensive use of the resonance model [58] is made to derive the baryonic resonance production cross-sections in pp and pn reactions. It starts from the observation that, in the 1-3 AGeV, the pion production is mainly driven by the excitation of intermediate resonances. The contribution of $\Delta(1232)$, which is dominant for pion production at the lowest energies is taken from the One Pion Exchange model of Dmitriev et al.[59], which describes quite well the measured cross-sections, invariant mass distributions, and angular distributions of the pp→pnπ^+ reaction at incident momenta around 1.5 GeV/c, as will be shown in the next section. The available cross-section values for one or two pion production in pp and pn reactions were used to fit the contributions of the different resonances, which are linked by isospin factors in the different isospin channels.

The cross-sections for the production of the ρ and ω mesons are then derived from the contributions of the different resonances. However, the branching ratios of the resonances to ρN or ωN suffer from larger uncertainty, as discussed in [60] for the case of the N(1535) resonance.

This resonance is also assumed to be the only one coupling to the η, with a branching ratio of 45%. The η exclusive production cross-section is then fixed by the the pp→pN(1535) cross-section. Keeping the resonance model cross-section, we modified the fully resonant hypothesis to take into account in our event generator the proportion (N(1535):58%,non-resonant:42%), as measured by the DISTO experiment [61]. This non-resonant contribution was generated using phase-space ditributions.

2.5 Δ Resonance contribution

2.5.1 Production cross-section

Figure 14: Direct (left) and exchange (right) graphs for the Δ production in pp reactions in the 1π exchange model.

The Δ production cross-section can be factorized as:

$$\frac{d^2\sigma}{dmdt} = \frac{d\sigma}{dt}\rho(m),$$

where t is the four-momentum transfer squared between the beam and scattered nucleons and $\rho(m)$ is the relativistic Breit-Wigner distribution [59] of the Δ mass:

$$\rho(m) = \frac{2}{\pi}m^2\frac{\Gamma(m)}{\left(m^2 - m_\Delta^2\right)^2 + m^2(\Gamma(m))^2} \tag{3}$$

where

$$\Gamma(m) = \Gamma_\Delta\frac{m_\Delta}{m}\left(\frac{k}{k_\Delta}\right)^3\left(\frac{k_\Delta^2 + \delta^2}{k^2 + \delta^2}\right)^2 \tag{4}$$
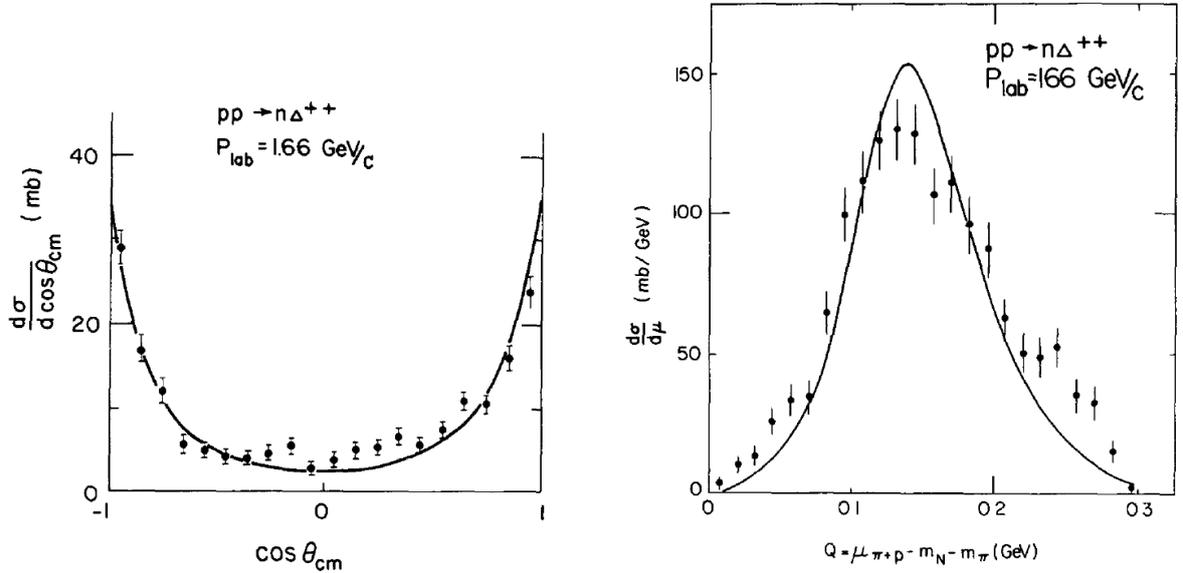
Figure 15: Angular (left) and invariant mass distributions (right) calculated in the OPE model of [59] compared to data measured in the pp→nΔ⁺⁺ reaction at 970 MeV [64].

with m_Δ=1232 MeV/c² and $\Gamma_\Delta = 120$ MeV/c². k and $k_\Delta = 229$ MeV/c correspond to the three-momenta of the pion in the reference frame of a Δ resonance with mass m and m_Δ, respectively. The factor $\left(\frac{k}{k_\Delta}\right)^3$ is related to the fact that the Δ resonance is a π-N wave of angular momentum l=1. The effect is a very large increase of the width as a function of the Δ mass, while the cut-off factor $\left(\frac{k_\Delta^2+\delta^2}{k^2+\delta^2}\right)^2$ takes into account the off-shellness of the Δ resonance at the decay vertex and reduces this effect. The explicit form is taken from Moniz with $\delta = 300$ MeV/c, adjusted to reproduce the π-N phase shifts [62]. A slightly different off-shell factor is taken in [59], with however no influence on the mass and angle distributions, as was shown in [63].

The transition amplitude is calculated in most models in the hypothesis of 1π exchange. For a fixed mass m of the resonance, the differential cross-section is:

$$\frac{d\sigma}{dt} = \frac{1}{64\pi I^2}\left|M_{NN\to N\Delta}\right|^2 \tag{5}$$

I is a constant depending on the beam energy and $|M_{NN\to N\Delta}|^2$ is the squared amplitude of the $NN \to N\Delta$ transition, with a sum on the spins of the final state particles and an average over the spins of the initial state. All the details can be found in [59]. The amplitude $M_{NN\to N\Delta}$ is the sum of the amplitudes of the direct and exchange graphs (cf. fig. 14). For each graph, the amplitude presents a very steep decreasing slope as a function of t (for the direct graph) or u (exchange graph), which further suppresses the high Δ masses. The final result is a slightly asymmetric mass distribution, as shown in the right part of fig. 15. The angular distribution is shown in the left part of fig. 15 together with data from [64]. The strongly forward/backward peaking is characteristic of the peripheral character of the 1π exchange. The interference between the direct and exchange graphs has a strong destructive effect around $\cos\theta_{CM} = 0$, as studied in detail in Tingting Liu's PhD.

2.5.2 Δ pionic decay angular distribution

In principle, the angular distributions of all the exit particles can be calculated within the one pion exchange model. Nevertheless, Dmitriev's amplitudes were provided only for the
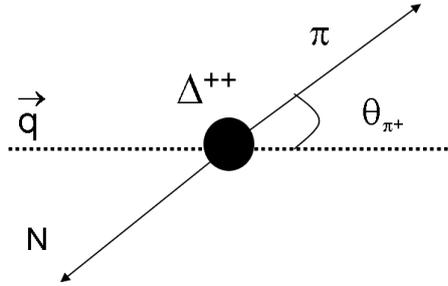
Figure 16: Sketch of the decay angular distribution with the definition of decay angle.

Δ production (NN→NΔ). In transport models, the Δ pionic decay is taken isotropic. Experimentally, as will be discussed, there is evidence for an anisotropic decay. We therefore modified the PLUTO event generator, to take this into account.

Spin-density matrix

The Δ decay angular distribution depends on the population of different spin states excited in the NN→NΔ process. The latter can be parametrized in terms of a (4x4) spin density matrix ρ_{ij} [65]. By choosing the axes in an appropriate way, the pion angular distribution can be expressed quite simply in function of ρ_{ij}. Thus, the pion angles are calculated in the Δ reference system, and the axis for the polar angles is the direction of the Δ in the reference system of the excited nucleon at rest[2] (see fig. 16). This definition takes care of the direct graph, where the Δ is excited on the target, as well as of the exchange graph, where it is excited on the projectile nucleon. In the latter case, the Δ is first boosted to the beam particle rest frame.

Experimentally, however, the direction of the Δ resonance can not be defined unambiguously, due to the contribution of both direct and exchange graphs (fig. 14). In the case of pp→pΔ^+ →pπ^0p, the two exit protons cannot be distinguished, which adds an additionnal ambiguity. The case of pp→π^+pn is more favourable in this respect. In addition, in this isospin channel, the non-resonant contribution is lower. The contribution of pp→pΔ^+ → p π^+n is 9 times lower than pp→nΔ^{++} →npπ^+, so that the Δ^{++} can be reconstructed using the π^+p pair.

In [66] and [67], the spin density matrix coefficients were extracted from an analysis of the pion angular distributions in pp→pπ^+n reactions performed at Argonne, with incident proton momenta ranging from 1.18 to 12 GeV/c. The polar axis was defined as the direction of the π^+p system, in the reference system of the beam proton at rest, since the detection selected forward emitted protons, which favoured the exchange graph, in the definition of fig. 14. According to Tingting Liu's analysis of the One Pion Exchange Amplitudes, for $|\cos\theta_\Delta| > 0.8$, the contribution of either the direct or exchange graph is more than 90%. We therefore used the coefficients extracted in this region, since they should really reflect the decay angular distribution of the Δ resonance. Their dependency with the Δ (or more precisely π^+p system) angle is anyway quite smooth, as can be seen in fig. 17. The anisotropy of the polar angular distribution[3] is defined by the parameter ρ_{33} as:

$$\frac{d\sigma}{d\cos\theta} \sim (\frac{1}{2} - \rho_{33})(1 + 3\cos^2\theta) + 3\sin^2\theta\rho_{33}. \tag{6}$$

---

[2]or equivalently the direction of the excited nucleon in the Δ rest frame.

[3]we neglect the azimuthal dependence since we are always looking at observables integrated over the full azimuthal range

Figure 17: ρ_{33} parameter extracted from the pion angular distributions in the pp→pnπ^+reaction [66]

In the pure one pion exchange, ρ_{33}=0, and one retrieves the $1 + 3\cos^2\theta$ angular distribution, which is characteristic of the P$_{33}$ πN scattering.

According to [66], the experimental value is ρ_{33}= 0.16 ± 0.03, corresponding to an anisotropic angular distribution, $\frac{d\sigma}{d\cos\theta} \sim 1+$ B $\cos^2\theta$, with B= 0.66+0.29-0.25. In [68], in the same reaction at an incident energy of 2 GeV, a coefficient $\rho_{33} = 0.14 \pm 0.03$, was found, in agreement with Wicklund's result. In addition, Shimizu et al [69] also mentions $\rho_{33} \sim 0.2$. So, the anisotropy of the Δ decay is clearly established, but less pronounced than expected from the pure one pion exchange model.

Spin structure of the NN→NΔ transition

The 1π exchange model corresponds to a pure longitudinal spin excitation ($\vec{S}.\vec{q}$). It reproduces the yields and production angular distributions rather well, but, failed with the spin obervables, measured in ($\vec{p}$,n) [70], which showed approximately equal longitudinal and transverse contributions. Interactions including transverse contributions were also used. For example, Oset et al. [71] used a $\pi+\rho$ interaction, Osterfeld et al. took an isotropic spin transition [23]. Such types of interactions were for example used to calculate the Δ excitation in the (^{3}He,t) reaction, which, except for the projectile-ejectile form-factor, is equivalent to a (p,n) reaction. In the exclusive $^1H(^3He,t)\pi^+$p reaction studied with the detector DIOGENE, pion angular distribution anisotropies of the same order than Wicklund's were measured [72]. Different types of interactions were tested, with no real success. Tensor terms were invoked to reconcile both the spin observables and the Δ decay angular distributions [73]. Additionnal complexity came from Final State Interaction which was likely to modify the pion angular distributions and distorsion effects on the projectile or scattered nucleon might smear

the polarization observables. So, a full description of the spin observables and pion angular distributions was not fully achieved. It seems to be generally admitted that the one pion exchange model is sufficient to describe the Δ production angular distribution and the decay is then taken isotropic in th models.

Δ decay angular distribution in PLUTO

Aiming at the most realistic description of the pion production, the anisotropy of the Δ decay is taken into account in PLUTO in the following way [55]: for each mass and angle in the Δ production process, the direction of the Δ is sampled according to the direct and exchange graph weights, neglecting the interference. The pion angle is then sampled according to the distribution: $1 + 0.66 \cos^2 \theta$. The distributions of $e^+ e^-$ pairs from the π^0 Dalitz decay is not affected very much by the anisotropy of the distribution. The effect is higher for the hadronic exclusive channels, where one hadron from the $\Delta \to N\pi$ decay is detected.

2.5.3 Δ Dalitz decay
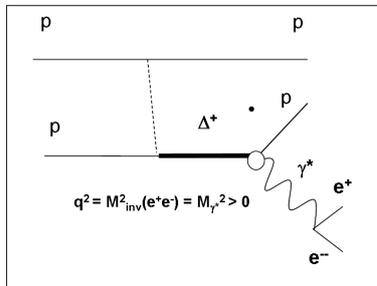
Figure 18: Dalitz decay diagram

As stressed in [74], inconsistent formula for the differential decay width of this process can be found in the litterature. As this process is a very important source of dileptons, in the dilepton mass range, between the π^0 and vector mesons, it was important to investigate how this affects the theoretical predictions. We also aimed at choosing a consistent description for our PLUTO event generator. So, Jacques Van de Wiele tackled himself the QED calculation. I carefully checked his derivation and studied the aspects related to the N-Δ transition form-factors and compared the different parametrizations found in the litterature. During Emilie Moriniere's PHD, we also had the chance to collaborate with Francesco Iachello, and, to our request, he adapted the existing N-Δ transition form factor parametrization for the Δ Dalitz decay case.

Derivation of the differential decay width of the Δ Dalitz decay

The differential decay width is:

$$\frac{d^5\Gamma}{dq^2 d\Omega_q d\Omega_e} = \frac{1}{2M_\Delta} \frac{1}{4} \sum_{m_N^s, m_\Delta^s, m_{e^+}^s, m_{e^-}^s} |\mathcal{M}|^2 \Phi(\Delta \to Ne^+e^-), \tag{7}$$

where $\Phi(\Delta \to Ne^+e^-)$ is the phase space for the Δ Dalitz decay process, and $\mathcal{M}$ is the transition amplitude for the different spin projections $m_N^s, m_\Delta^s, m_{e^+}^s, m_{e^-}^s$ of respectively proton, Δ, electron and positron, which is expressed as a product of the leptonic ($J^{L\mu}$) and hadronic

(J_μ^H) currents:

$$\mathcal{M} = c_{isospin} J_\mu^H(m_N^s, \vec{p}_N, m_\Delta^s, \vec{p}_\Delta) J^{L\mu}(m_{e^-}^s, \vec{p}_{e^-}, m_{e^+}^s, \vec{p}_{e^+}) \frac{1}{q^2} \qquad (8)$$

Without entering all the details of these currents, it is useful to note that the electromagnetic hadronic current J_μ^H consists in three independent amplitudes, due to the spin 3/2 of the Δ. It can be expressed as a function of the magnetic dipole, electric quadrupole and Coulomb quadrupole covariants: J_μ^M, J_μ^E, J_μ^C and the corresponding form-factors $G_M(q^2)$, $G_E(q^2)$, $G_C(q^2)$, which take into account the intrinsic hadronic structure of the nucleon and Δ.

$$J_\mu^H = G_M(q^2)J_\mu^M + G_E(q^2)J_\mu^E + G_C(q^2)J_\mu^C \qquad (9)$$

as for example used by [74] or equivalently as a function of a so-called "standard normal parity set:", with corresponding form-factors.

$$J_\mu^H = g_1(q^2)J_\mu^1 + g_2(q^2)J_\mu^2 + g_3(q^2)J_\mu^3 \qquad (10)$$

The latter expression is used by [75]. We chose the Electric, Coulomb and Magnetic covariants and could derive the following expression for the differential Dalitz decay branching ratio:

$$\Gamma_{m_\Delta}^{\Delta \to \Delta\gamma^*}(m_{ee}) = (|G_M^2(m_{ee})| + 3|G_E^2(m_{ee})| + \frac{m_{ee}^2}{2m_\Delta^2}|G_C^2(m_{ee})|)$$

$$\times \frac{\alpha}{16} \frac{(m_\Delta + m_N)^2}{m_\Delta^3 m_N^2} \sqrt{y_+ y_-^3}, \qquad (11)$$

$$y_\pm = (m_\Delta \pm m_N)^2 - m_{ee}^2 \qquad (12)$$

This expression is the same as in [74]. Note that eq.(11) implies a normalisation of the form factors as in [76] (Jones and Scadron convention), since the isospin factors appear as a numerical factor in eq.(8), while sometimes the latter are absorbed in the form-factor value, as in [77]. We could also check the validity of the expressions derived in [75], with the other sets of covariants.

Electromagnetic N-Δ form-factors
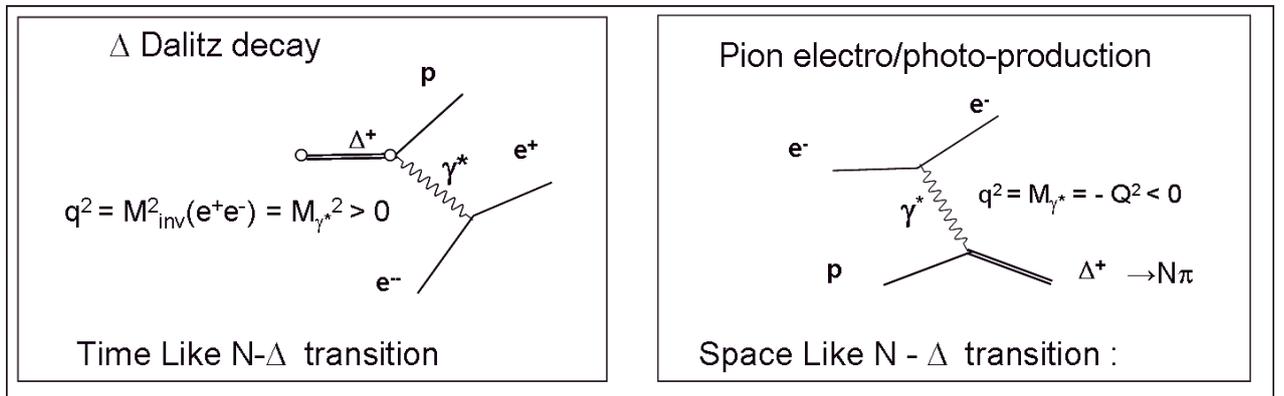
Figure 19: Sketch of the Time-like N-Δ transition, which is probed in the Δ Dalitz decay and the space-like N-Δ transition, which is probed in pion electro- or photoproduction experiments.

Following the graphs displayed in fig. 19, the Δ Dalitz decay process implies an electromagnetic vertex $\gamma^\star N\Delta$, which differs from the vertex of the pion electroproduction only by the kinematics. More specifically, in the Δ Dalitz decay process, the electromagnetic vertex is time-like, since the four-momentum transfer squared q^2, which is equal to the squared dilepton mass, is a positive quantity. For negative four-momentum transfer squared (space-like region), the three N-Δ transition form factors (G_M, G_E and G_C as magnetic, electric, and Coulomb form factors respectively) have been measured at MAMI, MIT/Bates and Jlab in electroproduction experiments in a quite wide range of Q^2, where $Q^2 = -q^2$ and in photo-production experiments at $Q^2 = 0$. The study of the electromagnetic N-Δ transition form-factors is indeed of high interest to study the strong interaction in the non-perturbative regime. It is a very important complement to the study of elastic nucleon form-factors, which will be discussed in detail in part II. The electric and Coulomb form-factors, which are quadrupole excitations are related to the non-spherical shape of the Δ resonance.

Fig. 20 exhibits a recent status of the world measurements of these form-factors [78]. The plot in the right part of the picture shows the magnetic form-factor divided by 3 $G_D(Q^2)$ ($G_D(Q^2) = 1/(1+Q^2/0.71)^2$ is the dipole form-factor). On the right part, the ratios R_{EM} and R_{SM} of respectively the electric and charge amplitudes to the magnetic amplitudes are displayed, which shows that for low Q^2, the electric and Coulomb form-factors, although not zero, are much smaller than the magnetic one.
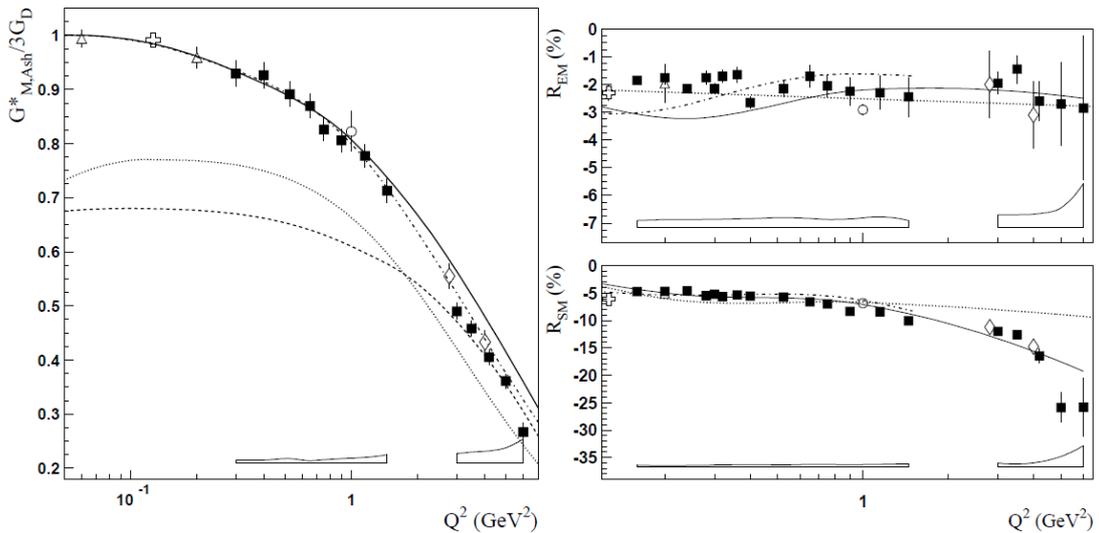
Figure 20: Left pannel: the form-factor G_M for the N-$\Delta(1232)$ transition normalized by the dipole form-factor ($G_D(Q^2) = 1/(1+Q^2/0.71)^2$). Right pannel: the ratios R_{EM} and R_{SM} of respectively the electric and charge amplitudes to the magnetic amplitudes. The data points are from MAMI, MIT/Bates and Jlab [78]. The curves represent different models.

The time-like region is unexplored. The dependence of the form-factors for positive q^2 can only be given by models, constrained by the fact that the form factors have to be analytical functions of q^2 in the complex plane and should reproduce the available space-like data. Due to the small q^2 values probed by the dilepton production in the Δ Dalitz decay and the very steep decrease of the differential branching ratio with $q^2 = M_{ee}^2$, the major requirement is that the values of the form factors at $q^2 = 0$ should be in agreement with the pion photoproduction experiments (photon point $G_M(0) = 3.02 \pm 0.02$, $G_E(0) \sim 0.07$, $G_C(0) \sim 0.2$ [79]) and correlatively to the radiative decay width ($\Gamma(\Delta \to \gamma N) = 0.66$ MeV $\pm$ 0.06 MeV). Despite the limitation to low q^2, the kinematical region probed by the Δ Dalitz decay ($q^2 < 0.3$ (GeV/c)^2 for an

incident energy of 1.25 GeV) is of high interest to check the Vector Dominance Model. In such a model, the electromagnetic baryon form factors present broad structures, which extend well below the vector meson pole masses and might be probed by the Δ Dalitz decay process. This was illustrated for a pp reaction at an energy of 1.61 GeV in fig. 5 and we will study later the influence of Iachello's two component quark model on the dilepton yield. We will for the moment stick to constant form-factors and discuss the problem of different parametrisations of the Δ Dalitz decay width in the litterature.

Comparison of Δ Dalitz decay yields in the litterature

We tested different analytic formula for $\Gamma_{M_\Delta}^{\Delta \to N\gamma^*}(M_{ee})$ used in recent transport model calculations for the analysis of the HADES C+C data or for the DLS p+p data:

- The "Ernst" formula can be found in [53] and is used in the most recent HSD papers [80]. It was also used in our PLUTO event generator before 2008.

- The "Wolf" formula comes from [81] can be found in the recent IQMD papers. It was also used in the HSD papers until 2007 [82].

- The "Krivoruchenko" formula was given in [74] and is used in RQMD calculations [60].

- The "Zetenyi" formula, explicitly given in [83] is employed in a resonance model calculation used for comparison to the DLS p+p data [75] .

They differ in fact both by the analytical formula and by the form-factors used, and, as already mentionned, we could reproduce the "Krivoruchenko" and "Zetenyi"'s expressions, but not the other ones. The general expression for the Δ Dalitz decay differential cross-section can be factorized as

$$\frac{d\Gamma_{M_\Delta}^{\Delta \to Ne^+e^-}}{dM_{ee}} = \frac{2\alpha}{3\pi M_{ee}} \Gamma_{M_\Delta}^{\Delta \to N\gamma^*}(M_{ee}), \tag{13}$$

which makes an explicit link with the radiative width $\Gamma_{M_\Delta}^{\Delta \to N\gamma}$. We therefore used first the radiative decay to compare the formula. The Krivoruchenko's parametrization is used with form-factors from the e-VDM models, which have the good "photon-point" value, $G_M(0)=3$. Zeteny's et al. use the alternative amplitude sets, with a constant g_1, which at $q^2=0$, is equivalent to a magnetic form factor close to 3. So, both formula are in perfect agreement with the radiative decay width. On the other hand, "Wolf" and "Ernst" coupling constants, with the most recent values used in the transport codes, are equivalent to $G_M=3.3$. They give radiative decays which are too high by respectively 10% and 25%. The higher value of the magnetic form-factor compensates in some extent the different normalisation of the analytical expressions.

However, the Dalitz decay dilepton yields present larger differences. As shown in fig. 21, and more quantitatively in fig. 22, the dilepton yields are the same within 30% at the Δ pole and for small q^2, which is related to the normalisation to the radiative decay width. The difference between the yields from the "Zetenyi" and "Krivoruchenko" formula is very small at any Δ mass or dilepton mass, which shows the very small influence of the two choices of form-factors (constant G_M or constant g_1). On the other hand, the deviations of the "Wolf" and "Ernst" formula increase with Δ mass and dilepton mass. Taking as an example a mass of 1.450 GeV/c^2, close to the threshold for a pp reaction at 1.25 GeV, variations of the differential Dalitz decay width of 50 to 75% are observed with the Ernst formula with respect
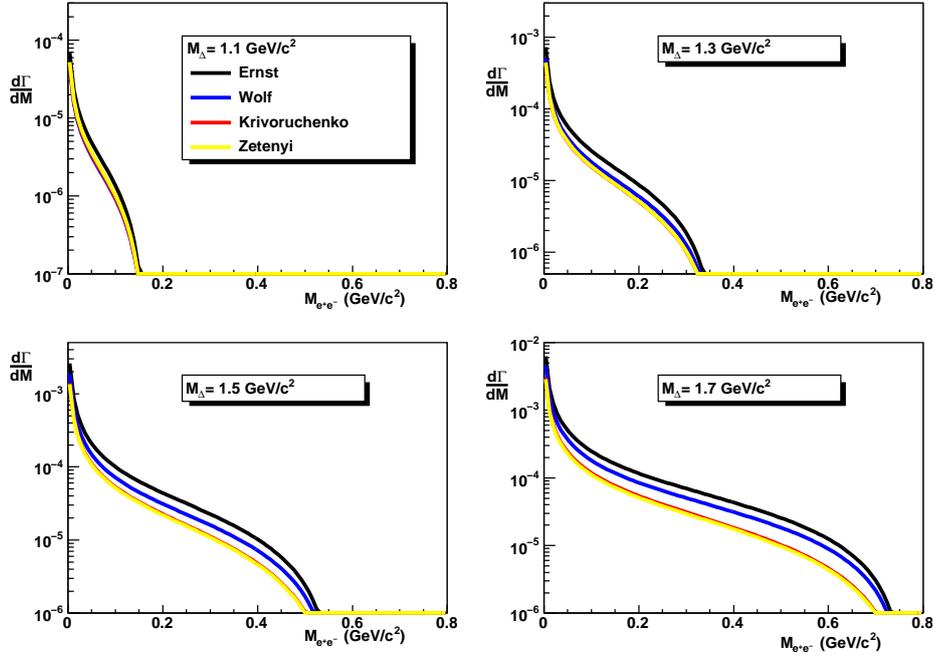
Figure 21: Comparison between dilepton yields from Dalitz decays of Δ isobars with different masses according to different formula found in the litterature.

to the "Krivoruchenko" yields. In collaboration with Elena Bratkovskaya, older formula were also tested, which provided also significant differences [84, 85].

Following these studies, which were discussed with the transport model theoretician groups, it seemed clear that the non-consistent formula should not be used. The PLUTO event generator was modified to take into account the "Krivoruchenko" formula. It has however to
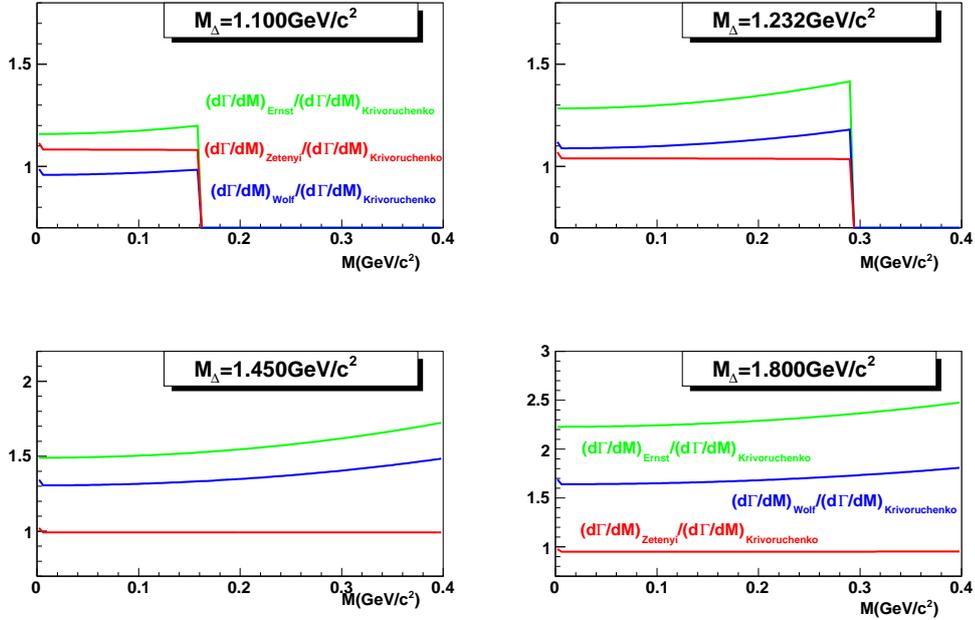
Figure 22: Ratios of Dalitz decay dilepton yields from Ernst (green), Wolf (blue), Zetenyi (red) to Krivorucneko as a function of e^+e^- invariant mass for different Δ masses.

be stressed that the Δ Dalitz decay yield also depends on the Δ mass distribution and, in heavy-ion reactions, on the multi-step Δ propagation, so that the dilepton yields in the different models might differ for other reasons than just this problem of differential width analytic formula.

Iachello N-Δ transition form-factor

Iachello's model provides a unitary description of all baryonic form-factors [86, 87]. The ingredients of the calculation are the wave functions of the initial and final states and the form of the interaction. The algebraic approach [88] is used to describe the baryonic structure and the interaction consists of a direct coupling of the photon to the quarks and a coupling mediated by vector mesons, hence the name "two-component model". The calculation is fully analytical. We used the simplest version of the calculation, where spin-flavor symetry is assumed. The parametrization appears as the product of an intrinsic form-factor and a vector meson propagation term. All form-factors are given in terms of three or four parameters, which can be associated to a typical size of the wave functions and the strengths of respectively the direct and ρ couplings, as well as of the ω coupling in the case of isoscalar transition. The four parameters of the elastic form-factors are constrained on the existing Space-Like data (see PartII sec. 3.3.2). For the N-Δ transition, one parameter is fixed from the elastic form-factor parametrization and the two others are fitted to the N-Δ transition magnetic form-factor measurements (fig. 23).

The analytical continuation of the N-Δ transition form-factor is not straightforward. Approximations are introduced to the kinematical part to avoid the appearance of poles at positive q^2. In addition, the form-factor in the Time-Like region has to be complex, above the two-pion threshold. An imaginary part is therefore introduced, both in the ρ meson propagator and in the intrinsic form-factor. The former derives from $\rho \to \pi\pi$ decay and for the latter, a prescription is used, which reproduces the Time-Like elastic proton form-factor (see PartII sec. 3.4.2) [89].

The intrinsic form-factor is described as :

$$g(q^2) = \frac{1}{(1 - a^2 e^{i\theta} q^2)^2} \tag{14}$$

and the overall expression for the time-like $N - \Delta$ transition form factor is:

$$G_M(q^2) = \mu_p \left(\frac{4}{3\sqrt{2}}\right) \sqrt{\frac{2m_N m_\Delta}{m_\Delta^2 + m_N^2}} g(q^2) \times (\beta' + \beta F_\rho(q^2)),$$

where μ_p=2.793 is the proton magnetic moment, β and β' are the constants for the direct and ρ meson coupling to the quarks. The ρ meson term is given by

$$F_\rho(q^2) = \frac{m_\rho^2 + 8\Gamma_\rho m_\pi/\pi}{m_\rho^2 - q^2 + 4m_\pi(1 - x)\Gamma_\rho(\alpha(x) - i\gamma(x))}, \tag{15}$$

where we have introduced $x = q^2/4m_\pi^2$ and

$$\left. \begin{array}{c} \alpha(x) = \dfrac{2}{\pi}\sqrt{\dfrac{x-1}{x}} \ln\left(\sqrt{x-1} + \sqrt{x}\right) \\[20pt] \gamma(x) = \sqrt{\dfrac{x-1}{x}} \end{array} \right\} \quad \text{if } x > 1 \tag{16}$$

$$\alpha\left(x\right) = \sqrt{\frac{1-x}{x}} \left[1 - \frac{2}{\pi} \cot^{-1} \sqrt{\frac{x}{1-x}}\right] \Biggr\} \text{ if } x < 1 \qquad (17)$$

$$\gamma\left(x\right) = 0$$

eson propagator vanishes for $q^2 < 4m_\pi^2$. The
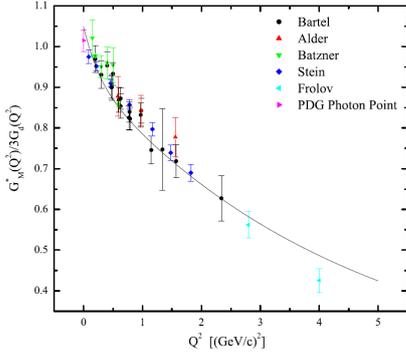
Figure 23: Two-component quark model fits for the magnetic N-$\Delta(1232)$ transition form factor normalized to $3 \times G_D(Q^2)$ ($G_D(Q^2)=1/(1+Q^2/0.71)^2$ is the dipole form-factor)
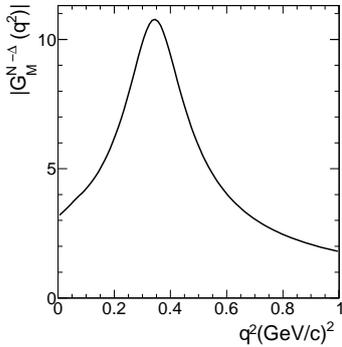
Figure 24: Magnetic N-Δ transition form-factor from the two component quark model [86, 87].
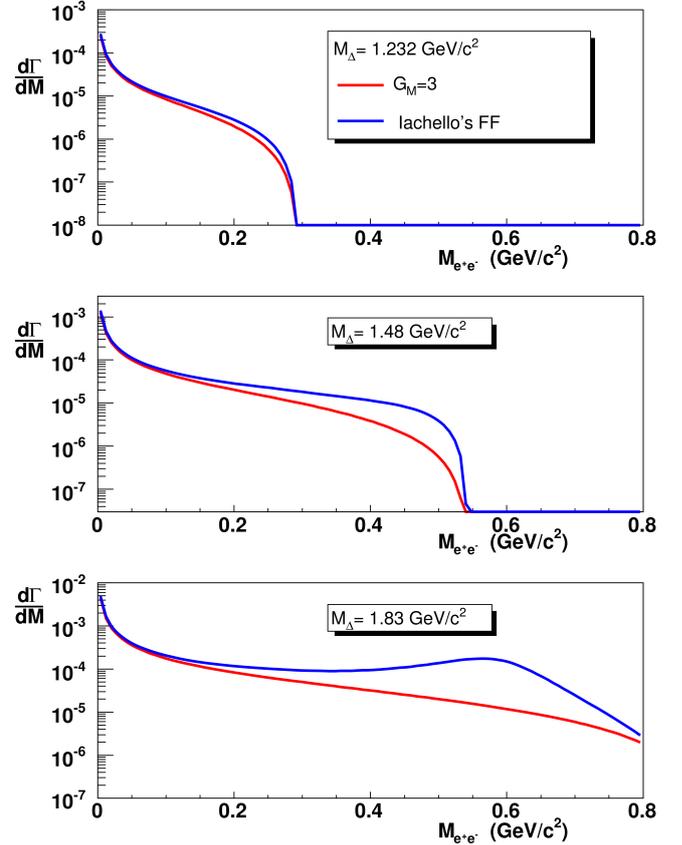
Figure 25: Comparison of Dalitz decay dilepton yield for a Δ resonance at different masses in a calculation with a constant magnetic form factor (G_M=3) (red) and with the Iachello form-factor (blue).

value of the parameters a=0.29 GeV^{-2}, θ=53°, β=1.2147 and β'=0.004 results from fits to the available experimental information as discussed above. The resulting distribution of form-factor values (fig.24) shows a broad peak centered around $q^2 = m_{ee}^2 \sim 0.6m_\rho^2$. Due to the small value of the β' parameter, the contribution of the coupling to the quark core in this model is negligible up to $q^2 = 5$ $(GeV/c)^2$, the dominant feature of the model in the kinematic range probed by the Dalitz decay process is therefore the vector dominance. Fig. 25 shows the effect of this form factor model on the Δ dalitz decay dilepton yield. The results clearly exhibit a rising decay width for larger Δ masses. In a proton-proton collision at 1.25 GeV incident energy, the mass of the produced baryonic resonance is limited to 1.48 GeV/c^2, the

Figure 26: Sketch describing the helicity angle in the Δ Dalitz decay

latter effect will nevertheless affect the shape of the di-electron mass spectrum. This form-factor model illustrates how the off-shell ρ meson production is related to the electromagnetic structure of the baryonic resonances.

$\gamma^\star$ angular distribution:

Similarly to the pionic decay angular distribution, the $\gamma^\star$ angular distribution in the $\Delta \to \gamma^\star N$ decay is sensitive to the polarization of the Δ resonance and hence to the Δ production mechanism. In the pure one pion exchange, the Δ Dalitz decay is the inverse process of pion electroproduction. Considering the dominant magnetic interaction for which the photons are transverse, the same angular distribution as in the pion photo-production reaction is expected, i.e. $5 - 3\cos^2\theta$. To implement this distribution in PLUTO, the same recipe based on the direct and exchange graph amplitudes, as for the pionic decay, was used to choose the excited nucleon as the projectile or the target.

Helicity distributions

We also derived from the QED calculation of the N-Δ electromagnetic transition the angular distribution of electrons or positrons in the $\gamma^\star$ rest frame, using a purely magnetic transition to simplify the problem. In this case, the differential Dalitz decay factorizes as:

$$\frac{d^2\Gamma}{dq^2 d\cos\alpha_e} = \frac{d\Gamma}{dq^2}(1 + cos^2\alpha_e) \tag{18}$$

We retrieved in this way the result of [90]. This result can be explained as follows: for magnetic or electric transitions, transverse photons are selected, and the helicity conservation at the $\gamma^\star e^+ e^-$ vertex yields the $1 + \cos^2\alpha_e$ distribution [91]. The angular distribution is therefore the same as in the Dalitz decay of pseudoscalar mesons (like π^0 or η). In the latter case, the selection of transverse photons occurs due to the spin 0 of the mesons, while in the case of the Δ Dalitz decay, it is due to the interaction.

The distribution given in eq.(18) was implemented in the PLUTO event generator and a lot of investigations were made to study the sensitivity of the experimental distributions.

2.6   Other resonances

The parameters for the Δ resonance excitation are constrained quite precisely by the phenomenology of πN and γN reactions. While the Δ appears as a prominent peak in pion production experiments either induced by pions or by photons, there are more than 20 resonances with masses between 1.4 and 2 GeV, which make their study much more delicate. The precision on the widths, branching ratios, but also on the production mechanisms in NN collisions is therefore much lower.

For the N(1440) resonance, a forward/backward production angular distribution in the center of mass was implemented in our PLUTO event generator, following the OBE model of [92], instead of the original isotropic distribution. For the other resonances, the isotropic distribution was kept, by lack of other prescription.

The decay angular distributions are also taken isotropic, which is anyway valid for I=1/2 resonances. The most important problem for the dilepton production is the production cross-section of these resonances and their couplings to the vector mesons. In the Vector Dominance Model, the latter are related to the electromagnetic form-factors of the corresponding baryonic transitions. An extensive experimental program is developped at electron facilities to access these form-factors by measuring the helicity amplitudes of $ep \rightarrow ep\pi$ transitions at the pole mass of the resonances. A lot of data start to exist for the nucleon-P_{11} transition or for the N(1520) and the measurements will be extended at higher Q^2 with the CLAS12 project. Powerful analysis tools to handle these data are also developped: the Excited Baryon Analysis Center (EBAC) created at JLab, is taking into account in a very systematic way the world measurements of pion, double pion and η production in reactions induced by photons, electrons and pions in coupled channel calculations. This intensive work will undoubtedly help to enhance the knowledge of all these baryons [93].

2.7   NN Bremsstrahlung
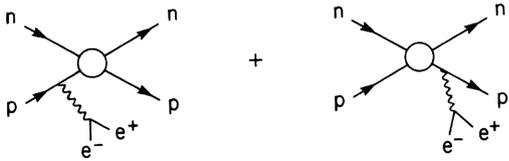
Figure 27: Sketch for the Soft Photon Approximation
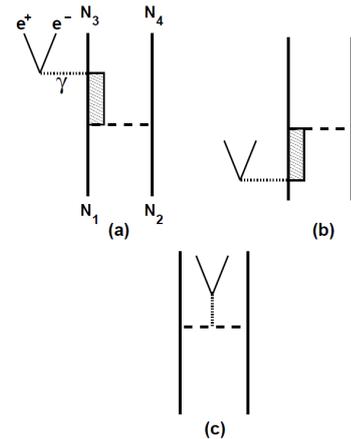
Figure 28: Diagrams for the reaction NN→NNe$^+$e$^-$. (a): post-emission, (b) pre-emission, (c) in-flight emission (for pn reaction). The box represents an off-shell nucleon or Δ.

The nucleon-nucleon Bremstrahlung is the emission of a virtual photon in the strong interaction field created by the interaction of two nucleons. The description of this process has to combine the NN$\gamma^\star$ electromagnetic vertex and the nucleon-nucleon interaction. The Soft Photon Approximation (SPA) [94] offers a possible way to take both aspects into account, with a factorization of the photon emission probability and of the strong interaction process, as sketched in fig. 27. The limitation is that the NN$\gamma^\star$ vertex is taken on-shell, which is in principle appropriate only in the limit of low energy photons. In addition, the emission from internal line is not taken into account. SPA results were however found to be in reasonable agreement with more complete calculations [95], at least for the pn case, where the bremsstrahlung process is the most important. As a consequence, SPA is still widely used in

transport model calculations, the Dalitz decay dilepton yield being calculated independantly and added incoherently. We will see that in the most recent HSD calculations, the SPA estimates have been renormalized by a factor 4 to take into account the higher yields provided by the calculations of Kaptari and Kämpfer [96].

2.8 OBE models

The Δ Dalitz decay and NN bremsstrahlung correspond to the same exit channel of the pp or pn reactions, i.e. ppe$^+$e$^-$and pne$^+$e$^-$ respectively. As a consequence, the two processes interfere. A reliable description of these processes can only be accessed in full quantum mechanical and gauge invariant calculations. Two One Boson Exchange (OBE) calculations, which fulfill these requirements were performed recently, respectively by Kaptari and ämpfer [96]) and by Shyam and Mosel [97]. In such calculations, the N and Δ graphs are included and the amplitudes added coherently (see fig. 28). The first surprise came when the yields of the nucleon graphs were compared and were found to be higher in the calculation by [96] than in the calculation by Shyam and Mosel [97] by a factor 4 for the pn reactions, and by a factor about 2 for pp reactions, as shown in fig. 29. The calculation is closer to the SPA predictions. Then, the Δ contributions were also compared and similar differences were found. An experimental check of these predictions is therefore needed to clarify the situation.
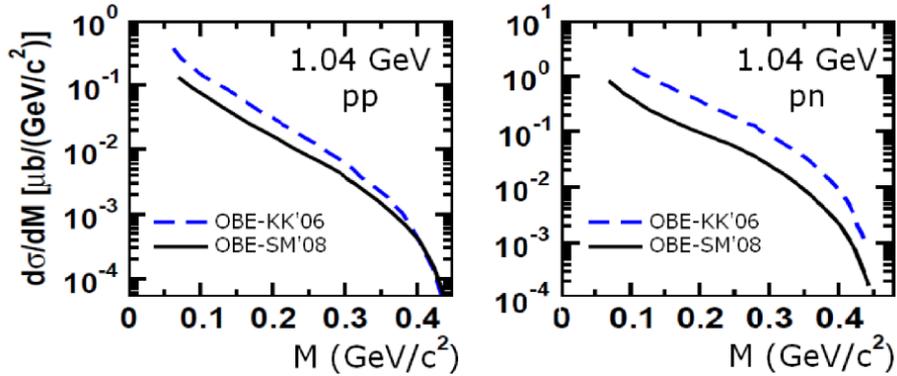
Figure 29: Comparison of cross-sections NN$\rightarrow$ NNe$^+$e$^-$ reactions in the OBE models [98] for the nucleon graphs. Solid lines: Shyam and Mosel calculation (SM'08) [97], dashed lines: Kaptari and Kämpfer calculation (KK'06) [96].

Both models use the same coupling constants and form-factors. The only apparent difference is the πNN coupling, which is taken as PseudoVector in the case of the Kaptari and Kämpfer calculation and as PseudoScalar in the case of Shyam and Mosel. Gauge invariance has to be taken into account carefully in such calculations. Each Δ graph fulfills gauge invariance by itself. This is not the case for the nucleon graphs, for which gauge invariance is fulfilled when taking into account different graphs. In the case of pn reaction, the in-flight emission graph is needed. However, when the pseudo-vector coupling is used, contact terms, as shown on fig.30 have also to be added. This could be a reason for the difference between the yields obtained in both calculations for the nucleon graphs. However, this can not explain the discrepancy between both calculations for the pp case, where the in flight graph does not contribute.

Despite these differences, qualitative features are common to both models and can be exploited experimentally. As seen on fig.31 for an incident energy of 1.25 GeV, the Δ graphs are widely dominant in the case of the pp reaction, except above 400 MeV/c^2, while, for the pn reaction, the nucleon graphs are much more important.
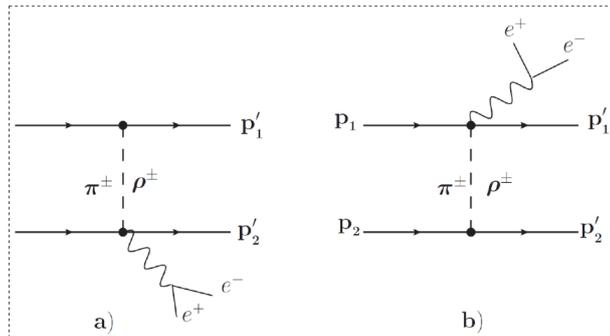
Figure 30: Contact terms for the emission of dileptons in pn reactions [96].
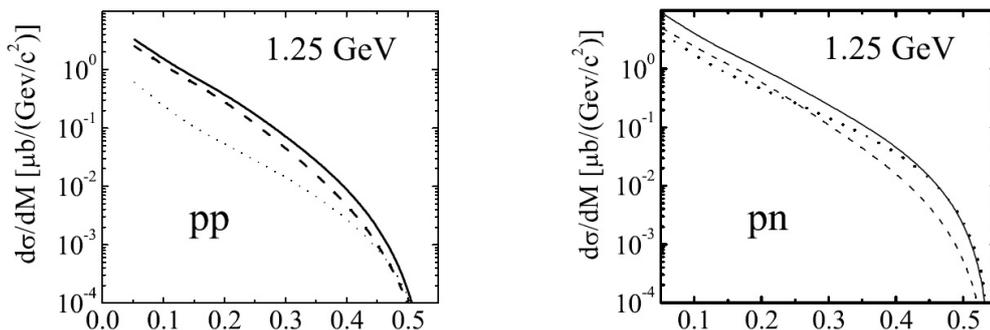
Figure 31: Predictions for the dielectron mass distributions in the pp (left part) and np (right part) reactions at 1.25 GeV/nucleon [96]. Solid lines: full calculations; dashed lines: Δ graphs only; dotted lines: nucleon graphs only.

For Δ graphs, it has been shown in [97] that the pre-emission is very small for invariant masses M_{ee} lower than 350 MeV/c^2. This justifies in some way the Dalitz decay model, as described in sec. 2.5.3, which takes into account only the post-emission graph with an intermediate Δ (graph (a) on fig. 28). Interference effects have also been studied in [95] and are shown to be important only at the very end of the pp spectrum [95] (see fig. 32). However, these effects seem to be more important according to the most recent K&K calculations [99].

The calculations also involve the N-Δ transition form factors and nucleon elastic form-factors. The latter are half off-shell elastic form-factors, (one on-shell,one off-shell nucleon), and in addition, the q^2 is well below the p$\bar{p}$ threshold. The form-factors are therefore in the unphysical region not accessible to p$\bar{p} \rightarrow$ e$^+$e$^-$ or e$^+$e$^- \rightarrow$p$\bar{p}$ experiments. In other words, no experimental information on these form-factors exist, but, as for the N-Δ transition, one can rely on models. For example, the influence of elastic nucleon form factors taken in Vector Dominance Models (VDM) has been studied in [96], but in the current version of the calculations, constant form-factors are used, which are in reasonable agreement with the measured values at q^2=0.

As a conclusion, it seems necessary to check experimentally the contradictory predictions of OBE calculations. One can learn from these predictions that, by measuring dilepton spectra in pp and np reactions, a selective sensitivity to the Δ and nucleon graphs can be obtained. Moreover, the pre-emission in Δ graphs and the interference between Δ and nucleon graphs are important mainly at the largest invariant masses, which justifies, at least to obtain the good orders of magnitude of the yields, the use of the Δ Dalitz decay calculation.
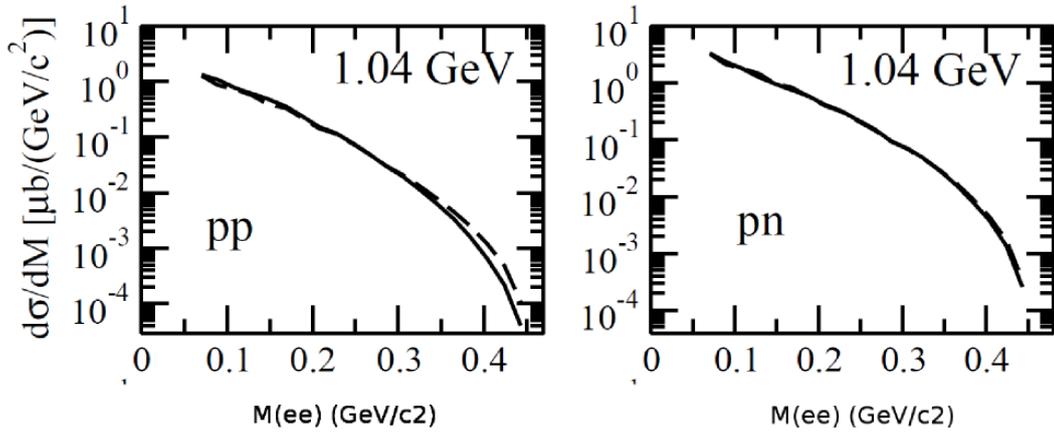
Figure 32: Full calculation (solid line) for pp→ppe⁺e⁻ compared to the incoherent sum of resonant and non resonant contributions.

2.9 Description of elementary reactions at 1.25 GeV and 2.2 GeV with PLUTO

The cross-sections of the main hadronic channels contributing at 1.25 GeV and 2.2 GeV deduced from the resonance model are indicated in Table 4. The reactions are then generated as described in sec.2.5. The contribution of non-resonant production has been also studied, assuming a phase-space distribution, as well as the effect of adding higher lying resonances, as N(1520) and $\Delta(1600)$, in the case of 2.2 GeV, to test the sensitivity of the data. In the case of the η production, the cross-section comes from the resonant model, but the proportion of non-resonant to resonant contribution is taken from DISTO analysis [61].

reaction	exit channel	1.25 GeV	2.2 GeV
pp	pp → pp elastic	23.5 mb	17.8 mb
pp → Δ^{++} n	pnπ^+	16.9 mb	10.8 mb
pp → Δ^+ p	pnπ^+ (1/3)	1.9 mb	1.2 mb
	ppπ^0(2/3)	3.8 mb	2.4 mb
pp → N ⋆(1440) p	pnπ^+(0.65 × 2/3)	0.2 mb	1.6 mb
	ppπ^0(0.65 × 1/3)	0.1 mb	0.8 mb
pp → N⋆(1535)p → ppη (58%)	ppη → pp$\pi^+\pi^-\pi^0$ (22.7%)	0.	0.017 mb
non-resonant pp→ppη (42%)		0.	0.012 mb

Table 4: Cross-sections for the different exit channels of the pp reactions according to [58].

	σ(mb)		σ (mb)
pp→ppπ^0X	4.45	pn→ pnπ^0X	8.56
pp→p Δ^+	5.7	pn→n Δ^+	5.7
		pn→p Δ^0	5.7

Table 5: Cross-sections for π^0, Δ^+ and Δ^0 production in p+p and p+n reactions at 1.25 GeV.

Two different approaches were followed to generate dilepton production at 1.25 GeV in pp and pn reactions:

The first one is based on the resonance model and the dominance of the Δ resonance. The dilepton yields are generated with two contributions, the π^0 and Δ Dalitz decays using the

37

cross-sections from the resonance model listed in Table 5. Two options for the N-Δ transition form factors are used: either a constant magnetic form factor (G_M=3, in agreement with the photon-point measurements), or the two-component quark-model from Iachello et al., as described in sec.2.5.3.

The limitations of this generator have to be clearly stressed: the latter is indeed based on two steps consisting respectively of the production and decay of the resonance. The Δ resonance production is treated in an exact way taking into account the interference between the direct and exchange graphs. However, the decay is described independently, with some prescription to reproduce the experimental angular distributions (see sec.2.5.2). In the case of the pp→pnπ^+, the contribution of the Δ^+ is added incoherently. In the case of the pp→ppπ^0, the indiscernability of the protons in the exit channel is neglected.

The influence of these limitations for the analysis of the inclusive dilepton channels is expected to be small, the most important ingredient being the π^0 and Δ production cross-sections. The acceptance of dilepton pairs in the inclusive dilepton channels is not very sensitive to the details of the distributions. The approximations of the model have a larger influence for the exclusive channels. In this case, one hadron is indeed detected in the final state, and the sensitivity to the distributions and correlations between particles is higher.

The second approach avoids these limitations and aims at a direct comparison with the OBE predictions, the differential cross sections (dσ/dM) produced by the models [96, 97] have been parameterized, an isotropic virtual photon emission was further assumed and corrections due to Final State Interaction of the two outgoing nucleons were included.

The quasi-free n+p reaction is simulated using the participant-spectator model. The deuton energy is shared between an on-shell proton with no momentum change during the interaction. The available energy in the reference system of the participant off-shell neutron and the target proton is then calculated using a neutron momentum distribution in the deuteron from the Paris potential. The energy dependence of the cross-sections is then taken into account. In particular, the η production is taken into account, when the energy of the pn system exceeds the threshold, with cross sections taken from existing data [100].

2.10   Comparison to the data

To compare the theoretical predictions to the experimental spectra measured by HADES, two problems have to be faced: the combined efficiency of the detectors, reconstruction and anlysis cuts and the geometrical acceptance. The spectra are usually corrected for efficiency, but in most cases, the spectra measured by HADES cannot be extrapolated in a model-independent way. As a result, the calculations have to be filtered to be compared to the experimental spectra. The events generated in a calculation can be processed using full GEANT simulations, to take into account all the details of the acceptance and instrumental effects. However, a simple filtering, based on acceptance matrices and a smearing to simulate the momentum resolutions is often used.

3   The HADES experimental set-up and its performances

3.1   Overview

The HADES (High Acceptance Dielectron Spectrometer) detector (fig. 33) consists in 6 identical sectors covering the full azimuthal range and polar angles between 18° and 85°, hence providing a lepton pair acceptance of the order of 0.35. A detailed description can be found in [54], thus only the main features are given here and more details about the tracking system

are given in sec.3.3. A hadron-blind Ring Imaging CHerenkov detector (RICH), based on a C_4F_{10} gas radiator and CsI photocathodes placed around the target region is used for electron identification, together with Time Of Flight (TOF/TOFINO) and an electromagnetic
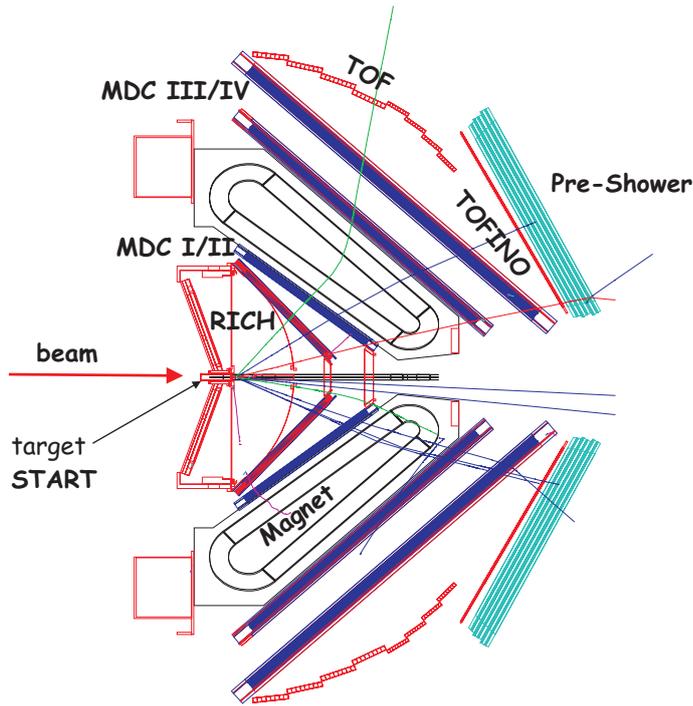
Figure 33: HADES set-up

Figure 34: Picture of the Liquid-hydrogen target vessel. The entrance window is glued on a stainless-steel tube.

pre-shower detector (Pre-Shower). Particle identification is also provided using the correlation between time-of-flight and momentum for charged pions and protons and using in addition the time-over-threshold of the signals measured in the MDC's for charged kaons. Time of flight measurements in a Forward Wall scintillator hodoscope (FW) located 7 m downstream the target was used in d+p reactions. It allowed indeed for the detection of forward emitted particles with the characteristics of spectator protons in order to select quasi-free n+p reactions. The first level trigger selects events within a defined charged particle multiplicity range, while the second level trigger corresponds to electron candidates defined by RICH and Pre-Shower/TOF information. In the case of the d+p experiment, the first level trigger also requires a coincidence with at least one particle in the FW. Segmented solid targets with thicknesses corresponding to interaction probabilities of less than 5% were used, as well as a 5 cm long liquid-hydrogen target (1% interaction probability). The beam intensities were typically 10^6 for heavy ions and 10^7 particles/s for deuterium and proton beams.

3.2 Liquid hydrogen target

The Liquid-hydrogen target (fig. 34) has been developped at IPN Orsay. The target consists of a cell (50 mm long, 25 mm in diameter) filled with liquid hydrogen at atmospheric pressure and a temperature of 20K. The liquid is contained in a vessel built out of Mylar foils of 100 μm thickness, glued together. The thermal insulation is achieved using a carbon fiber housing, 4 cm in diameter and 0.5 mm thick, placed around the vessel and covered by 10 layers of superinsulation material (6 μm thick aluminized Mylar). The forward endcap is made of a 100 μm thick Mylar foil.

3.3 HADES tracking system
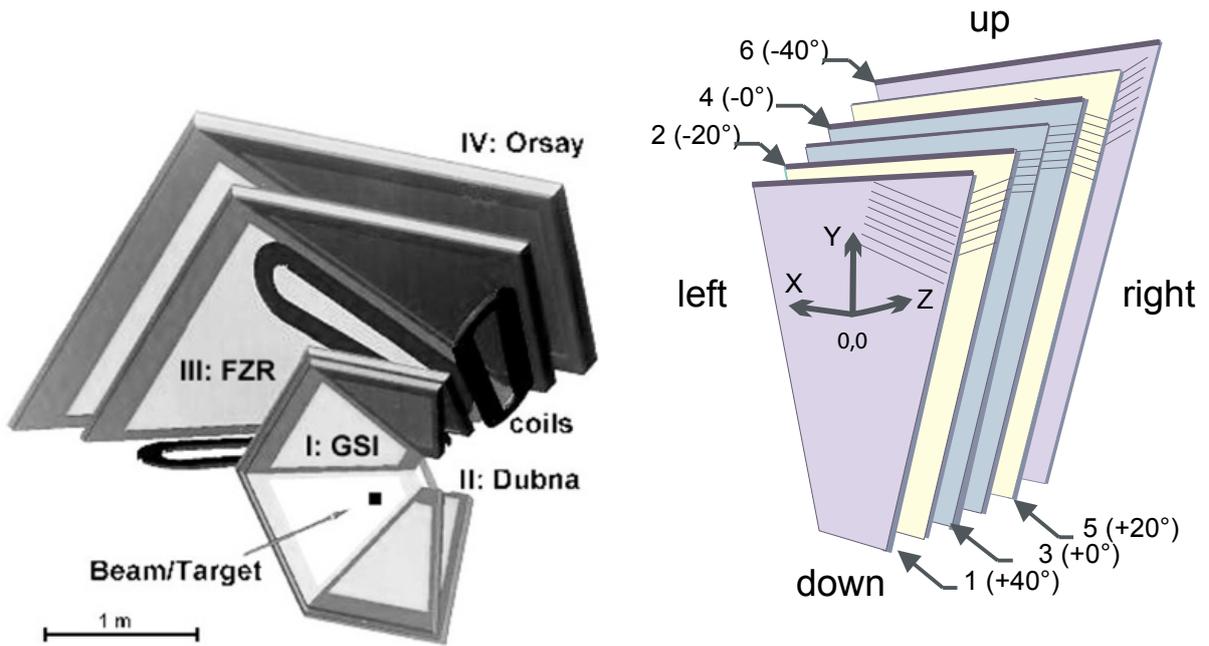
Figure 35: left: schematic layout of the HADES tracking system, with the coils of the magnet and the four planes of Mini Drfit Chambers. Right: schematic view of the six anode wire frames inside a HADES MDC, with the respective wire angles.

3.3.1 Technical aspects

The tracking system (fig.35) is the essential piece to obtain the requested mass resolution ($\Delta M/M \sim 2.7$ %, as checked in the recent measurements at the ω peak). It consists of 24 trapezoidal planar Mini Drift Chambers arranged in six identical sectors. In each sector, two modules (MDCI-II) are placed in front of and two (MDCIII-IV) behind the toroidal magnetic field of the supra conducting magnet. The geometry of the chambers is designed to cover the region between the six coils, forming four tracking planes of increasing sizes, 0.35 m^2 (plane I) up to 3.2 m^2 (plane IV). All four chambers contain about 1100 drift cells each, with increasing size from 5x5 mm^2 (plane I) to 14x10 mm^2 (plane IV).

The IPN Orsay was responsible for the construction of the fourth plane. The six modules were constructed one after the other during the period 2001-2006. The difficulty of this construction was related to the unusual big size of the chamber (see fig. 36). In addition to the inconvenience to handle large frames, the length of the wires requires special care. Loss of tension have indeed larger influence, since the dip goes like L^3, and the high electrostatic forces can induce wire mechanical instabilities. The winding was realized using the machine at CEA. First, a full-size prototype made of only one anode and two cathode planes was built, to check the mechanical, electrostatic concepts. This allowed to adjust some parameters of the design, for example the diameter of gold-plated tungsten sense wires which was increased from 20 μm to 30 μm, to reduce the breaking probability of the wires. The wires were first glued, then soldered. Special care was taken during the construction to avoid creeping of the wires, which could induce looser tension. A carbon bar was also added to maintain the tension at the value of 110 N after mounting of all the frames.

Figure 36: One MDC-IV in construction at IPN Orsay

The tests performed in Orsay comprised stability checks up to 2.6 kV in air and at the nominal voltage of 2.4 kV with the gas mixture (helium:60, isobutane:40). Currents of the order of 100 nA at the maximum high-voltage were measured for all layers. No problems related to the gas tightness were observed, which proves the efficiency of polishing the o-ring grooves in the Epoxy frames.

Taking advantage of repair action on one chamber, systematic studies of tension stability have been performed. Loss of tension are below 10% in 5 years. A detailed investigation of the positions at both ends of each wire was made for one chamber and the distribution was found gaussian-like with a σ of about 50 μm.

3.3.2   Momentum reconstruction and resolution

The track reconstruction procedure and the different methods used for momentum reconstruction are carefully described in [54]. The efficiency of the procedure has been investigated in proton-proton elastic scattering at a 1.25 GeV kinetic energy. The measurement of (θ, ϕ) angles in TOF and Pre-shower detectors was indeed sufficient to select a clean sample of elastic scattering events. In this way, the reconstruction efficiency of the inner and outer tracking systems could be measured (respectively 92% and 87 %).

The detection of both protons from p+p elastic scattering allows for extensive momentum resolution studies. An average resolution of 4% was obtained, while the GEANT simulation, based on the time resolution from GARFIELD simulations predicts a resolution between 1.9 and 1.2 %. We performed such investigations at 2.2 and 1.5 GeV, the final result obtained at 3.5 GeV [54] is shown in fig. 37. To reproduce the experimental values, the position resolution has to be artificially increased by a factor 4.

A consistent part of Emilie Morinière's PHD thesis [63] was devoted to detailed investigations of possible uncontrolled systematic errors in the momentum reconstruction to explain the experimental observation.

The multiple scattering has a strong effect on the momentum resolution, especially for electrons. This can be seen on fig. 38, where the resolution is shown both for a simulation with only multiple scattering effects (Runge-Kutta ideal) and for a simulation also including the position resolution increased by a factor 4. For a given momentum, the multiple scattering increases with polar angle, since the path in the air also increases. The contribution of the position resolution also increases due to the decrease of the field integral with increasing angle, which explains the worse resolution in the simulation at 53°. This increase is much
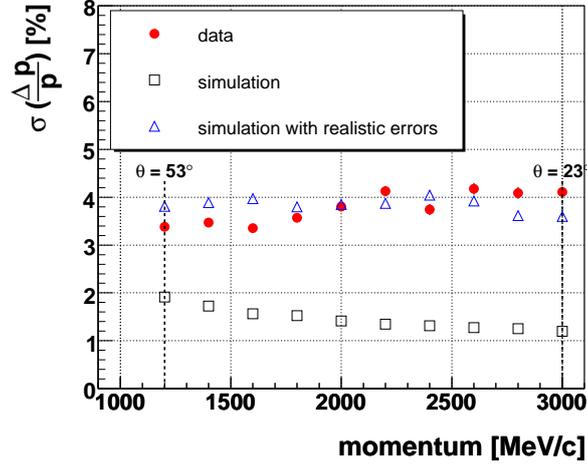
Figure 37: Comparison of momentum resolution measured in the pp elastic scattering as a function of the proton momentum at 3.5 GeV (red points) to the resolution deduced from GEANT simulation with time resolution as expected from GARFIELD simulations (black open squares) and increased by a factor 4 (blue open triangles).

reduced between 53° and 75°, due to the positive effect of the larger track incidence angle on the chambers. Using the drift time information in the two 0-degree layers and selecting
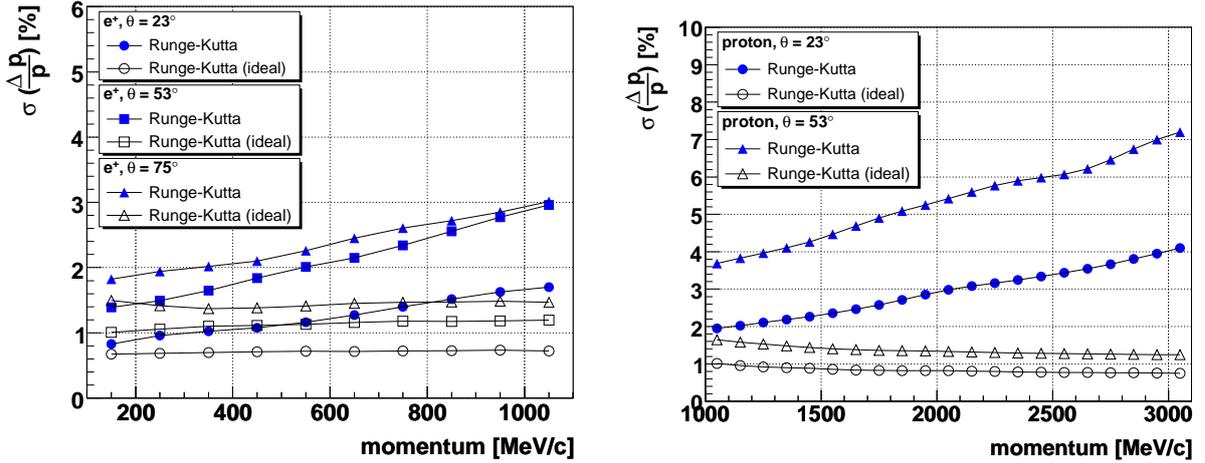
Figure 38: Simulated momentum resolution for e$^+$ (left) and protons (right) at different polar angles: The full symbols correspond to Geant simulations with Garfield resolutions multiplied by a factor 4, and the open symbols to simulations with only the contribution of multiple scattering and energy loss. In both cases, the Runge-Kutta method is used for the momentum reconstruction.

events with incidence close to normal, a time resolution of 3.6 ns is measured for the MDCIV chambers, excluding events at a distance smaller than 1.5 mm from the field wires, for which the errors are much larger. This is in fair agreement with the mean error expected from GARFIELD calculations [101]. The parametrization of the time-distance correlation in the cell used for the track fitting could also be checked, with however limited sensitivity in the last 2 mm of the cell (the maximum drift distance is 7 mm).

The drift time calibration procedure has been investigated. The first method, which was based on the rising slope of the drift time spectrum, induced a systematic effect, which has been corrected in the actual method. The influence of the start time fluctuation for the drift

time measurement was also studied, especially for the p+p reaction, since no start detector was present, but only small effects have been found.

The magnetic field map is calculated using 3D calculations from the coils geometry and the intensity in the magnet. The precision of the calculation is controlled by measurements, and the stability of the current is below 10^{-4}, so that no contribution to the resolution is expected from this side.

A major problem which has driven a lot of activity in the HADES collaboration is the detector alignment. The alignment procedure consists in several steps: first, a photometric measurement gives the position of MDCI and MDCII with respect to the magnet. A cosmic event sample is used to align adjacent sectors with respect to each other. Finally, data are taken without magnetic field to align the four chambers of one sector. Six parameters are adjusted in this way, three coordinates to define the position of the center of the chamber and three angles defining the orientation of the chamber in space. This neglects the possible misalignment of different wire layers inside one chamber. Emile Morinière and Thierry Hennino proposed a new method for this "intrinsic" alignment. The relative shifts of one wire layer with respect to the others could be determined by the residues of the positions on this layer. The most efficient result was obtained when this very wire layer is excluded from the fit. The efficiency of the method was checked and it was later applied by O. Pechenova (Giessen and GSI), in a modified version, but the improvement of the resolution was not larger than 20%. The efficiency of the tracking was also slightly increased, but it is clear that the alignment of wire layers did not solve the problem. We also investigated the effect of wire to wire alignment. A dispersion of the wire position distribution, with a rms of 50 μm, was observed in the measurements on the Orsay chambers, as described above. Assuming a similar dispersion on all chambers, the effect on the momentum resolution is too small to explain the experimental value.

As a conclusion, the origin of the bad resolution could not be explicitly identified, but the only possible effects are misalignments or increased error in the time-distance correlation far from the anode.

It has to be noted that this problem of momentum resolution has a bad effect first of all for fast protons, and the effect on leptons is much lower, due to their lower momenta and to the strong multiple scattering contribution. The measured invariant mass resolution is indeed Δ M/M $\sim$ 2.7 % at the ω peak, to be compared to the design value (2%).

3.4 Data analysis

The data analysis method and all the related checks have been described in detail in different PHD thesis. I refer for example to T. Galatyuk's manuscript [98] for the most recent update concerning elementary reactions at 1.25 GeV. The methods and analysis cuts slightly differ for each data set. I will just summarize here the common important features.

Dilepton pairs are selected using different criteria to check the track and ring qualities, as well as the identification of the electron and positron. The conversion pairs, which are due to the interaction of photons with the target or detector material, have small invariant masses and small opening angles. They originate mostly from the conversion of the photons of the π^0 two-photon decay or from the π^0 Dalitz decay, or with a lower probability from the η Dalitz decay. A rejection of events with opening angles lower than 9^0 is applied basically on each data set, which, according to the simulations, removes 99% of the conversion pairs and affects the other dilepton sources only for the lowest invariant masses. The corresponding tracks are removed from the event, which also reduces the combinatorial background.

The correlated combinatorial background is due to the combination of one positron and

one electron from the same meson decay (fig. 39 top). The corresponding dilepton invariant mass distribution is peaked at around the half of the π^0 mass. The uncorrelated combinatorial
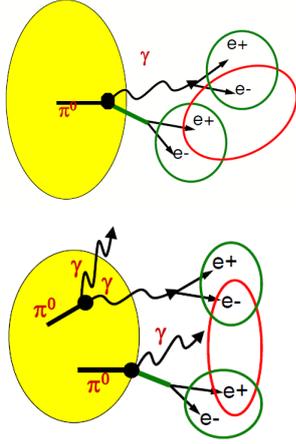
Figure 39: Examples of correlated (top) an correlated (bottom) combinatorial backgrounds.
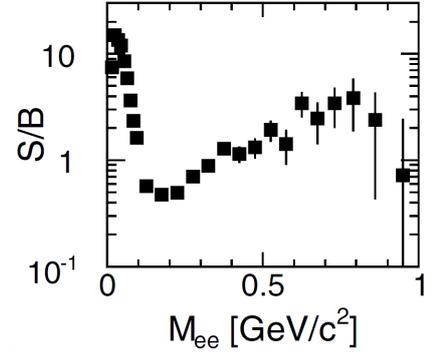
Figure 40: Signal/background ratio for the C+C reaction at 2 AGeV

background is created by random combinations between leptons originating from two independent sources (fig. 39 bottom), with a smooth corresponding invariant mass distribution.

For a large fraction of these converted photons, only one lepton is detected, the one with the lowest energy having a smaller probability to reach the outer tracking system. A very sophisticated algorithm was therefore developed to recognize these events from the hits in the inner tracking system [98]. This results in a further reduction of the combinatorial background.

To subtract the remaining combinatorial background, HADES exploits both the mixed-event and like-sign pair techniques. The former consists in sampling randomly electrons and positrons from different events to form pairs. This method is very efficient for heavy-ion collisions and provides high statistics. However, to provide the normalization of the combinatorial background yield, the like-sign pair technique is used. This method is based on the fact that the combined e^+e^- pairs have the same probability as like-sign (e^+e^+ or e^-e^-) pairs. As a consequence, the background is evaluated by calculating the arithmetic or geometric mean of like-sign pairs. This method is anyway necessary for elementary reactions, where correlation cannot be neglected.

The resulting Signal/Background ratio is shown in fig. 40 for the C+C system at 2 AGeV. This ratio is even larger for C+C at 1 AGeV and p+p and p+n reactions. It can be noted, that this ratio is very low, in comparison to ultrarelativistic heavy-ion reactions (e.g. S/B$\sim$1/7 in average over the di-muon spectrum in Na60 [40]), which is expected, due to the much lower number of emitted pions at SIS energies. It is also more favorable than in the γC or γFe-Ti reactions measured at JLab [102], where S/B$\sim$1 at M_{ee}=0.4 GeV/c^2.

Efficiency corrections are calculated with GEANT simulations taking into account the missing electronic channels for the given experiment, and are applied to the data. Acceptance matrices, also deduced from these simulations, are used to filter the theoretical predictions (see sec. 2.10). The HADES acceptance is much larger than the acceptance of the former DLS detector. The proportion of HADES data inside the DLS acceptance is indeed about 1%, and the non-overlapping region corresponds to less than 20% for the η decay for example. In particular, the HADES acceptance at the small invariant masses, i.e. in the π^0 Dalitz region, is much higher (as will be seen in sec. 4.2), which is very useful for a reduction of systematic errors and for normalization checks in the case of elementary reactions.

The spectra measured in heavy-ion reactions are normalized to the π^0 multiplicity, which is derived from the measurement with HADES of π^+ and π^- production in the same reaction. In the case of the elementary reactions, the spectra are normalized using the elastic (or quasi-elastic) pp scattering measured simultaneously by HADES.

4   Results obtained in C+C reactions

The first results from the HADES collaboration, obtained for the ^{12}C+^{12}C reaction at 1 and 2 AGeV [103, 104], marked an important turning point. I will first show the comparison with a "free" dilepton cocktail, to understand the main dilepton sources, then discuss the comparison with the DLS data and then the comparison with various transport models.

4.1   Comparison with a PLUTO cocktail
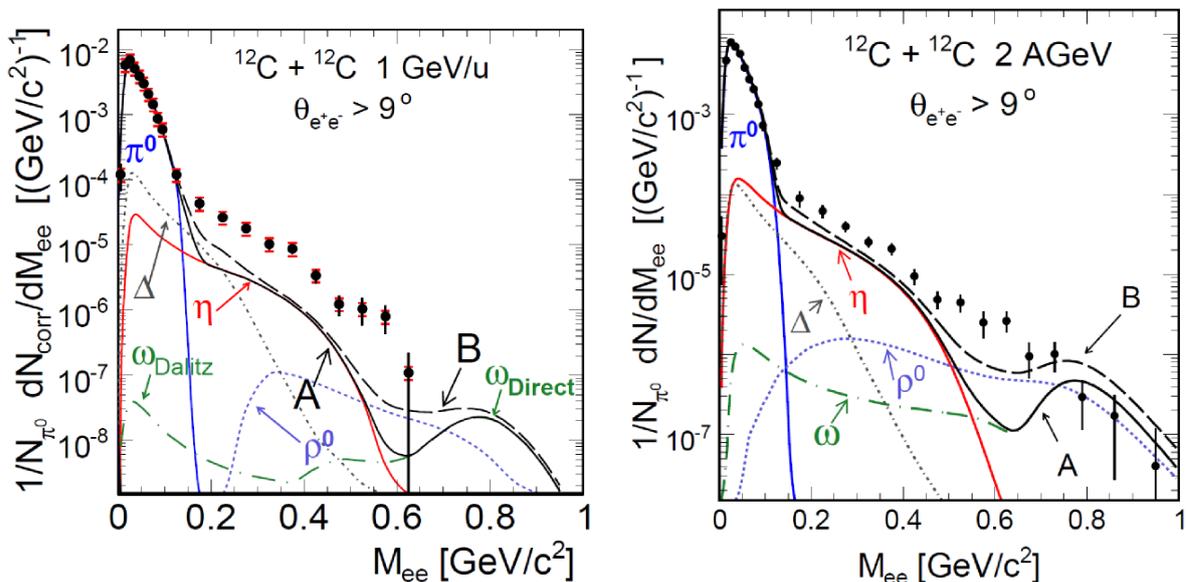
Figure 41: Dilepton spectra measured with HADES in the C+C reactions at 1 AGeV (left) and 2AGeV (right). The cocktail A corresponds to long-lived dilepton sources (π^0 and η Dalitz decay, ω direct and Dalitz decay). In the cocktail B, the Δ Dalitz decay and the ρ meson decays are also added.

The dilepton spectra, measured at 1 and 2 AGeV in the C+C system, are shown in fig. 41. They are compared with a dilepton cocktail built with the PLUTO event generator, using a fire-ball model, as described in sec. 2.2. Following the philosophy discussed in sec. 1.7 (see fig. 2), the experimental spectra are first compared to a dilepton cocktail of long-lived sources (cocktail A on fig. 41), which are expected to decay after the freeze-out, and hence to be unaffected by medium effects. It contains the π^0 and η Dalitz decays and the ω direct and Dalitz decays. The η contribution is well constrained by the TAPS data and the characteristics of the fire-ball are deduced from the analysis of the pion spectra (see [103] for the details) and the ω cross-section, which is unknown is deduced from m_T scaling, but its contribution is small below M_{ee}=600 MeV/c^2. So this cocktail A gives a well-defined reference of long-lived source contribution.

The contributions of short-lived sources are much more difficult to simulate in the frame-work of our event generator. In the cocktail B, the ρ dilepton decay is added with the m_T

scaling prescription, assuming a vacuum mass distribution. This contribution is important for M_{ee} larger than 450 MeV/c^2. As for the Δ contribution, it is added with a cross-section scaled to the pion cross-sections, like in elementary reactions ($\sigma_\Delta = 3/2\sigma_{\pi^0}$). This assumption is based on the fact that the pion production in this energy range is mostly due to the Δ resonance, which is justified. But, it also neglects pion absorption and Δ propagation ($\Delta N \to$ NN). In this calculation, the further interaction of the Δ resonance with surrounding nucleons is neglected, which is not realistic. It is therefore clear that transport model calculations are needed to describe the short-lived sources realistically.

In the region of M_{ee} lower than 0.55 GeV/c^2, the cocktail A is mainly due to the η contribution and the excess of the data with respect to this reference, quantifies the contribution of the short-lived sources. This excess has been extensively studied as a function of energy and system size, using the more recent Ar+KCl measurement [105]. The excess seems to have roughly the same trends as the pion contribution, hence the conclusion that it is related to baryonic resonance contribution.

4.2 The end of the "DLS puzzle"

A dilepton excess over the η contribution had already been measured in the ^{12}C+^{12}C reaction at 1 GeV by the DLS experiment [36] and remained unexplained (see sec. 1.6.3). The new
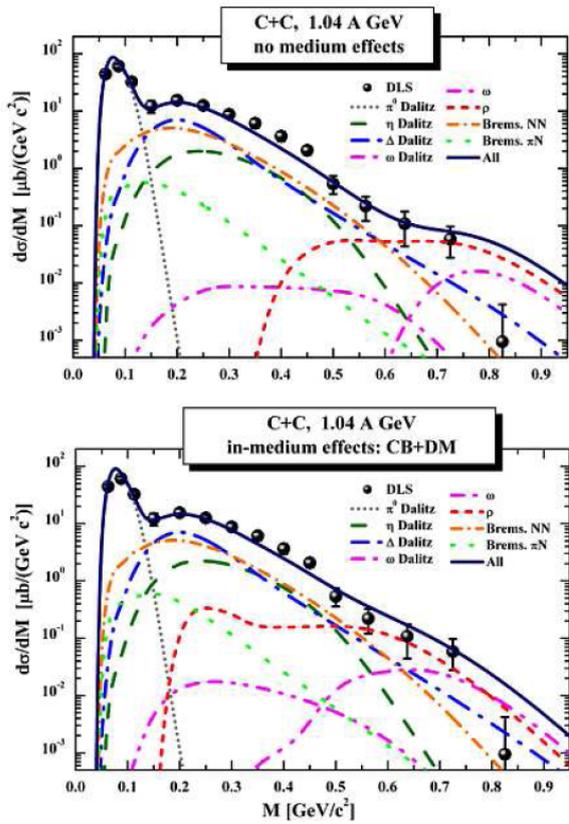
Figure 42: HSD calculations [80] compared to DLS experimental spectra measured in C+C system at 1 AGeV. Top: vacuum calculation. Bottom: in-medium calculation.
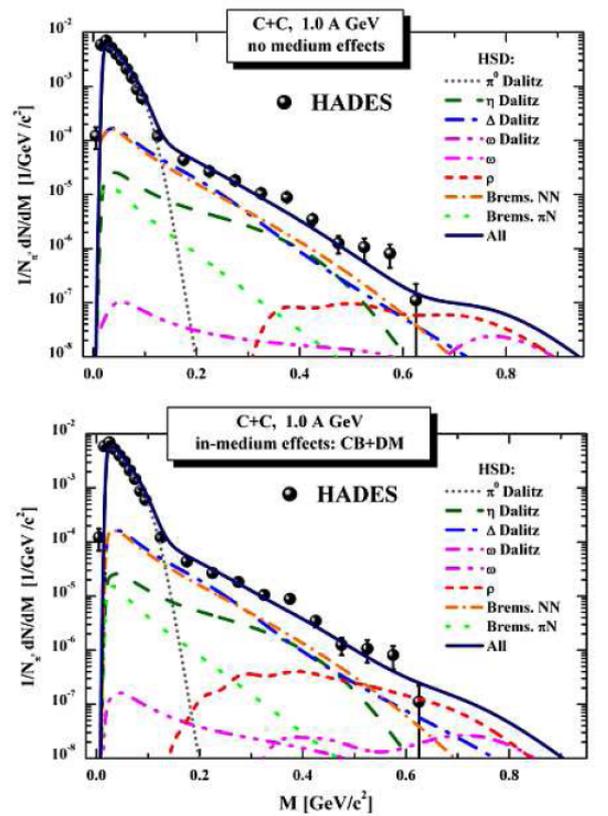
Figure 43: HSD calculations [80] compared to HADES experimental spectra measured in C+C system at 1 AGeV. Top: vacuum calculation. Bottom: in-medium calculation.

HADES data, measured for the same system, allowed to solve this "DLS puzzle". Taking into account the much smaller DLS acceptance, a direct comparison of the two data sets

was performed, showing very good agreement. This result, published in [104], has been largely advertised and all the technical details about this comparison can be found in [106]. This confirmation of the DLS results triggered new transport model calculations, resulting in an impressive improvement with respect to the "DLS" puzzle situation. This can be appreciated by comparing fig.42, where the new HSD transport calculations are shown, both for vacuum and in-medium spectral functions to the old calculations shown in fig. 13. The predictions of the same model are compared to the HADES spectra in fig. 43, to demonstrate the consistent description of both data sets. As expected, medium effects have a quite reduced influence for this system. The origin of the better agreement of the new calculations in the intermediate mass region ($140 < M_{ee} < 500$ MeV/c^2) and the changes of the various ingredients of the models are not fully easy to trace back. They consist probably mainly in adjustments of the cross-sections or couplings of vector mesons to resonances. In the case of the HSD transport model, the most important change is the use of the recent bremsstrahlung calculation from [96], which, as explained in sec. 2.8, predicts a yield about a factor 4 higher than the SPA calculation, which was used before. According to the authors of [80], this provided the solution to the "DLS puzzle". However, this is not fully convincing, since this bremsstrahlung prediction is contradicted by the other approaches [95] (see sec. 2.8). In addition, other transport model calculations reproduce quite well the excess with different relative contributions of bremsstrahlung and Δ Dalitz decay processes.

This is illustrated in fig. 44, where the experimental spectra obtained in the C+C system at 2 AGeV are compared to a serie of transport model predictions. For example, the RQMD and UrQMD calculations do not include any bremsstrahlung contribution and use e-VDM form-factors which induce a large yield below the vector meson mass, related to off-shell ρ meson production. In the UrQMD calculation, the Δ contribution is significantly higher, and the η contribution lower. The yield in the region of vector mesons is usually too large, which is also confirmed by the analysis of the other systems (p+p at 3.5 GeV, p+Nb at 3.5 GeV, Ar+KCl at 1.5 AGeV).

Although this abundance of theoretical calculations for the HADES data is very flattering for the collaboration, the scattering of the pn bremsstrahlung or Dalitz decay yields is not fully satisfactory. Following our dicussion in sec. 2.5.3, the freedom about the Δ Dalitz decay contribution in elementary reactions is only at the level of electromagnetic form-factors, which have an influence only at the largest invariant masses. Although in heavy ion reactions the interaction of the Δ resonance with surrounding nucleons may induce differences in the dilepton yields, it seems important to test the Dalitz decay contribution with elementary spectra. The contradictory results concerning the pn bremsstrahlung contribution have also to be checked experimentally. This gives the motivation for the study of the pp and pn reactions of the C+C spectra.

5   Results obtained in pp and quasi-free pn reactions

The pp reaction was studied at three different energies:

- E = 1.25 GeV, i.e. below the η production threshold, to study selectively the Δ Dalitz decay. The quasi-free n+p reaction was also studied at the same energy to investigate the pn bremsstrahlung process. The results for the pp reaction consist in inclusive dilepton spectra, exclusive pp$\rightarrow$ppe$^+$e$^-$ analysis and hadronic exclusive channels. For the np experiment, I will only discuss the inclusive dilepton spectra.

- E = 2.2 GeV, to study in an exclusive way the π^0 and η production using both the Dalitz decay (pp$\rightarrow$ppγe$^+$e$^-$) and the hadronic reconstruction (pp$\rightarrow$ppπ^0, pp$\rightarrow$pp$\pi^+\pi^-\pi^0$) in
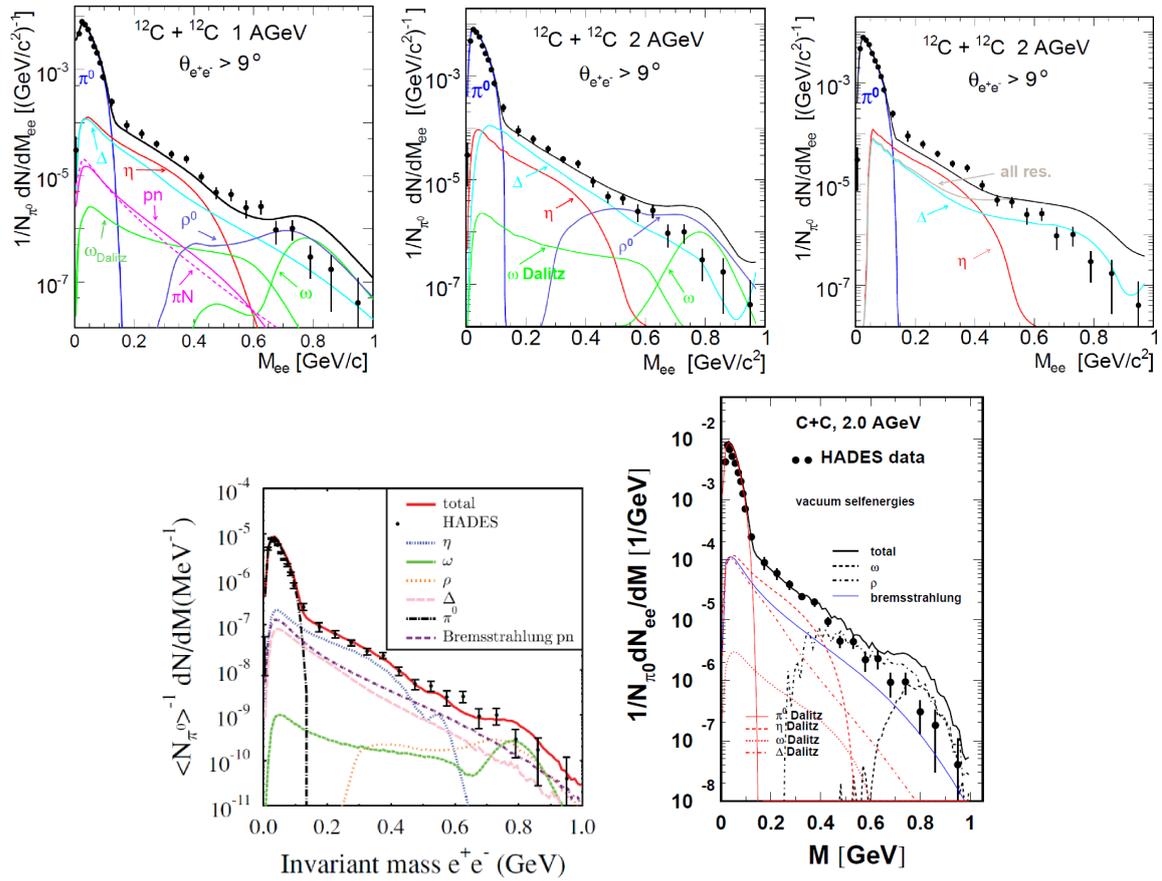
Figure 44: Transport model calculations compared to HADES dilepton spectra measured for the C+C reaction at 2AGeV. First row: HSD (left), UrQMD (center) and RQMD (right). Second row: IQMD [107] (left) and BUU [108] (right). All the calculations use vacuum spectral functions.

exclusive analysis.

- E=3.5 GeV, where the focus is on the vector meson production. The preliminary analysis can be found in [57] and I will not present these results here.

Most of my contribution to these analysis was performed in the framework of the collaboration between IN2P3 and the Jagellionian university of Cracow, in close collaboration with Piotr Salabura and his team, and more particularly Witold Przygoda, Marcin Wisniowski and Anna Kozuch. My contribution to the analysis of the dilepton spectra for the pp and pn reactions was at the level of the analysis tool for the simulations, as described in sec. 2 and of the data interpretation. Concerning the Δ Dalitz decay, the role of the Orsay team (Emilie Morinière PhD and Tingting Liu's PhD) was first to produce simulations which were used for the experimental proposal. They serve now as a guide for the analysis performed in Cracow and as a way to estimate systematic errors. The analysis of the exclusive pp→pnπ$^+$ reaction at 1.25 GeV is the subject of Tingting's Liu PHD's thesis. I also took a quite active part in the analysis of the other hadronic exclusive channels, which I am now gathering in a draft for publication, in close collaboration with PIotr Salabura and the different actors in the analysis work.
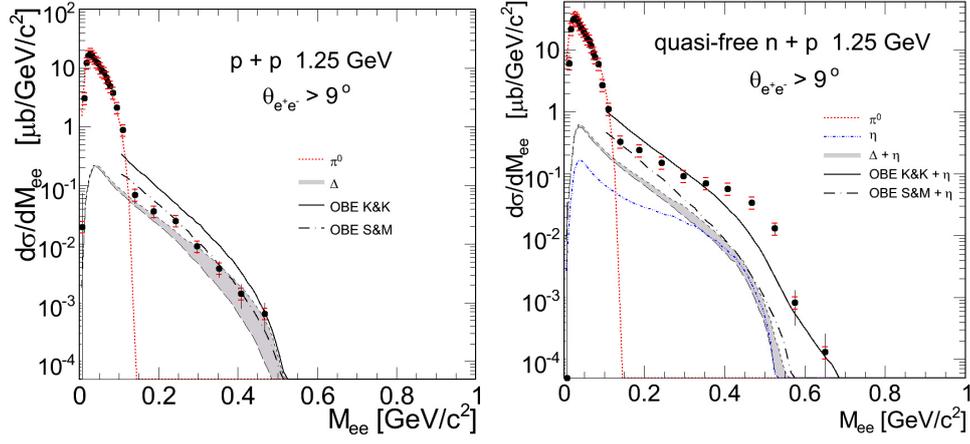
Figure 45: Dielectron mass distribution measured in the pp (left part) and quasi-free np (right part) reactions at a beam energy of 1.25 GeV/nucleon. The dotted (red on-line) and dashed lines show the contributions of π^0 and Δ Dalitz decay, respectively, in simulations using the resonance model. The enhancement due to the N-Δ transition form factor is shown as the grey area. The dashed and full lines are the results of simulations using the OBE models [97] and [96], respectively
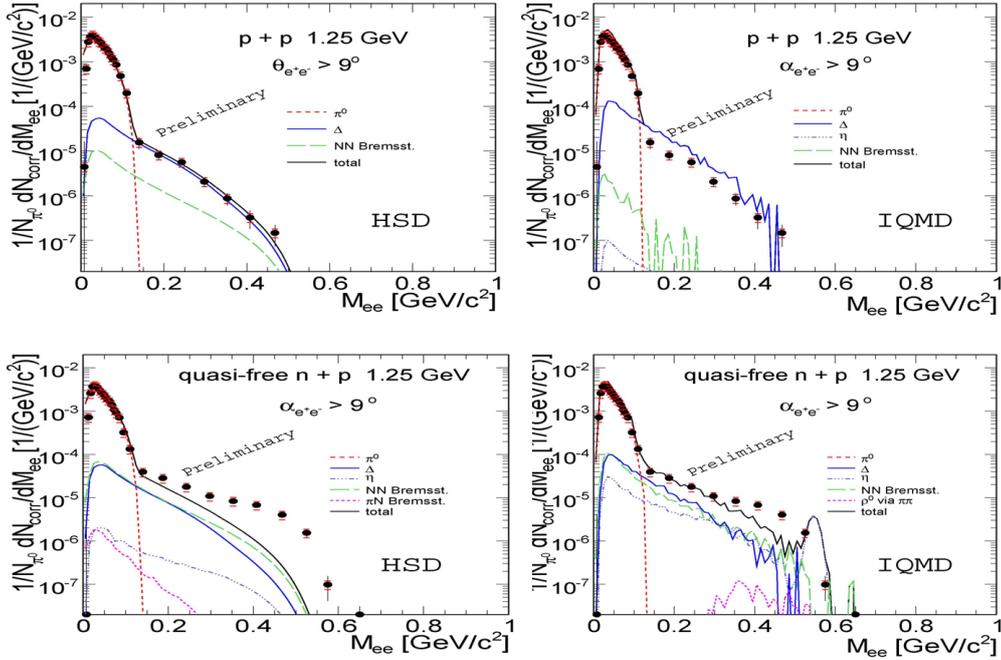
Figure 46: Dilepton spectra measured in pp and pn experiments compared to HSD (left column) and IQMD (right column).

5.1 Inclusive dilepton channels

Figure 45 shows the dilepton mass spectra measured in the pp and quasi-free np reactions [109] compared to the simulations as described in sect. 2. For both reactions, there is a good agreement between the dilepton yield measured at low invariant masses and the simulation of the π^0 Dalitz decay, which confirms the normalization and analysis procedures. In the case of the pp reaction, the region of invariant masses larger than 140 MeV/c^2 is also well described by the simulation of the Δ Dalitz decay. An even better agreement is obtained when the

two-component quark model is used instead of the constant magnetic form factor(G_M=3), which illustrates the sensitivity of these data to the electromagnetic structure of the N-Δ transition. However, the description of Δ Dalitz decay in this resonance model is too crude to extract direct information on the time-like N-Δ transition form factor. A more accurate description is expected from the OBE models, since they take into account all graphs involving intermediate Δ or nucleons. The predictions of [97] (shown as dashed line) are indeed in pretty good agreement with the data, considering the systematic error bars. The form factors used are equivalent at low invariant masses to a constant G_M=3.2, instead of G_M=3 which has a 15% effect on the yields. The remaining difference with respect to the Dalitz decay model should be therefore related to the pp bremsstrahlung contribution and to the pre-emission graphs. The other OBE model [96] (full line) is not compatible with the data.

The shape of the spectrum changes dramatically when going from p+p to n+p interactions. In the mass region between 0.15 and 0.35 GeV/c^2, the yield is about a factor 9 higher in the case of the n+p reaction, while only a factor 2 is expected for the Δ Dalitz decay contribution. The resonance model simulation widely underestimates the measured dilepton yield. The η Dalitz decay contribution is rather small and the inclusion of the N-Δ transition form factor model does not help either. Nevertheless, this simulation is missing the nucleon-nucleon bremsstrahlung contribution which is expected to be in the case of the pn system much larger than in the case of pp. The comparison to the OBE exchange models is thus more relevant, but no satisfactory agreement is achieved, even with the model of [97], despite its good behaviour in the case of the pp data. To select more strictly quasi-free reactions, a smaller angular selection on the spectator proton angle ($0.3° < \theta < 2°$) has been applied, with no change in the shape of the invariant mass distribution. No clarification was provided either by the transverse momentum and rapidity spectra, which present very similar shapes as compared to the p+p reaction.

These results are also in agreement with the DLS spectra measured in pp and pd reactions [52], with lower statistics and precision. In the case of the pd reaction, only indirect confirmation could be obtained through the comparison of the same models, while in the case of the pp reaction at 1.04 GeV and 1.27 GeV, the direct comparison was possible [98], showing a very good agreement. The interpretation of the pn dilepton spectra is still the subject of theoretical investigations, related for example, to possible ρ or ω meson off-shell production by higher-lying resonances.

The role of these elementary data is also to test the ingredients of the transport models. Two examples of such comparisons are shown in fig. 46. The HSD model reproduces very well the pp dilepton spectra, while IQMD has a too high Δ Dalitz decay contribution. No model at the moment is able to reproduce the quasi-free pn dilepton spectra.

These dilepton spectra measured in pp and quasi-free np experiments are used to build a reference spectrum defined by $0.5/\sigma_{\pi^0}^{NN}(d\sigma_{ee}^{pp}/dM_{ee} + d\sigma_{ee}^{pn}/M_{ee})$, where $\sigma_{\pi^0}^{NN}$ is the mean inclusive π^0 cross-section in a nucleon-nucleon collision. The η contribution, deduced from the PLUTO simulation is subtracted from the the C+C dilepton spectra, which are then compared to this reference spectrum (fig. 47). The conclusion is that, except for the largest invariant mass region, due to the different available energies, the spectra are in fair agreement, considering the systematic errors. The C+C system seems therefore to behave mainly as a superposition of pp and pn collisions. This also hints to the fact that the excess dilepton yield measured in C+C systems above the η contribution is due to some additional dilepton source already present in the np system. This is, however, in contradiction with the transport model calculations, which are able to reproduce the C+C spectra (see fig. 44), but not the p+n distributions.
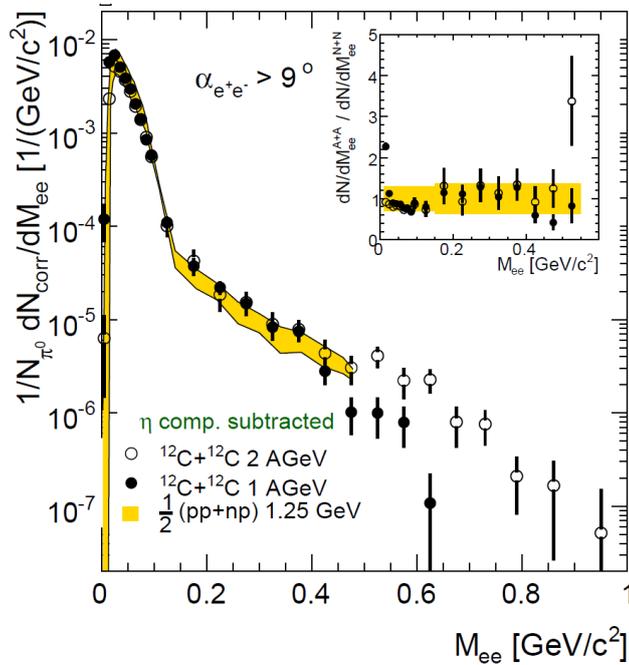
Figure 47: The dilepton invariant mass spectra obtained for the C+C systems at incident energy of 1 and 2 AGeV are shown after subtraction of the η contribution. The yellow band indicates corresponds to the average of the spectra measured in pp and quasi-free pn reactions. For each system, the spectrum is normalized to the respective π^0 multiplicites [109]

5.2 Exclusive meson production via hadronic channels

Hadronic exclusive channels ($pp \to pn\pi^+$, $pp \to pp\pi^0$ and $pp \to pp\eta$) have been isolated, by exploiting the capability of HADES to measure charged hadrons and are intensively studied within the resonance model.

5.2.1 Signal extraction

Both positive and neutral pion production channels are selected by using the mass of the missing neutral particle. In the case of $pp \to pp\pi^0$, the elastic events are first removed, using mainly the angular correlation of the 2 protons. I will not give the details of the selection procedure, which can be found in M. Wisniowski's PhD thesis for the 2.2 GeV case and Tingting Liu's and Anna Kozuch's PhD at 1.25 GeV, together with discussions of the systematic errors on this selection. Only one example of missing mass peak for the $pp \to pn\pi^+$ reaction, centered at the neutron mass, is shown in fig. 48.

The case of the $pp \to pp\eta$ was studied in A. Rustamov's and S. Spataro's PhDs [110, 111], but was revisited recently to estimate the cross-section. The $\eta \to \pi^+\pi^-\pi^0$ decay is used and the signal is selected from $pp\pi^+\pi^-X$ events. First, the background from the $pp \to pp\pi^+\pi^-$ is suppressed by applying a $\pm 3.5\,\sigma$ wide cut on the $pp\pi^+\pi^-$ missing mass around the π^0 mass. The pp missing mass after this cut is shown on fig. 49. The region of the η peak is then excluded and a polynomial fit is performed. The latter is used as a parametrization of the $\pi^+\pi^-\pi^0$ background and the η signal is defined as the yield above this background. In such studies, a great care has to be taken to evaluate the systematic errors related to the signal extraction. This is achieved by studying the sensitivity of the extracted yield to variations of the fit functions and ranges.
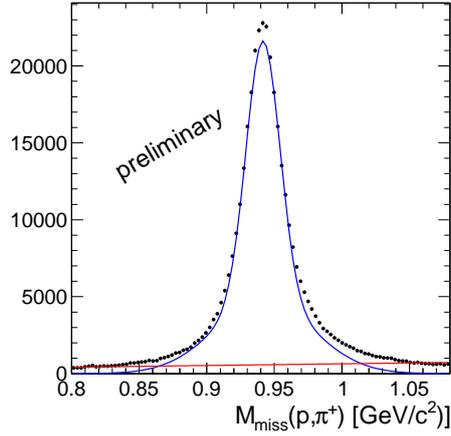
Figure 48: (p,π^+) missing mass distribution in the reaction $pp \to p\pi^+X$ at 1.25 GeV. The signal is extracted as a gaussian fit peaked at the neutron mass (blue curve) over a linear background (red line).
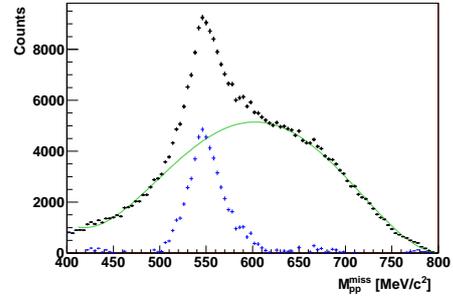
Figure 49: Analysis of $pp\pi^+\pi^-$ events in the pp reaction at 2.2 GeV. The missing mass for the reaction $pp\to ppX$ is shown, after selection on the $pp\to pp\pi^+\pi^-X$ reaction missing mass around the the π^0 mass. The green curve shows the fit of the non resonant 3 pion background. The blue points show the η signal defined as the remaining yield after subtraction of this background.
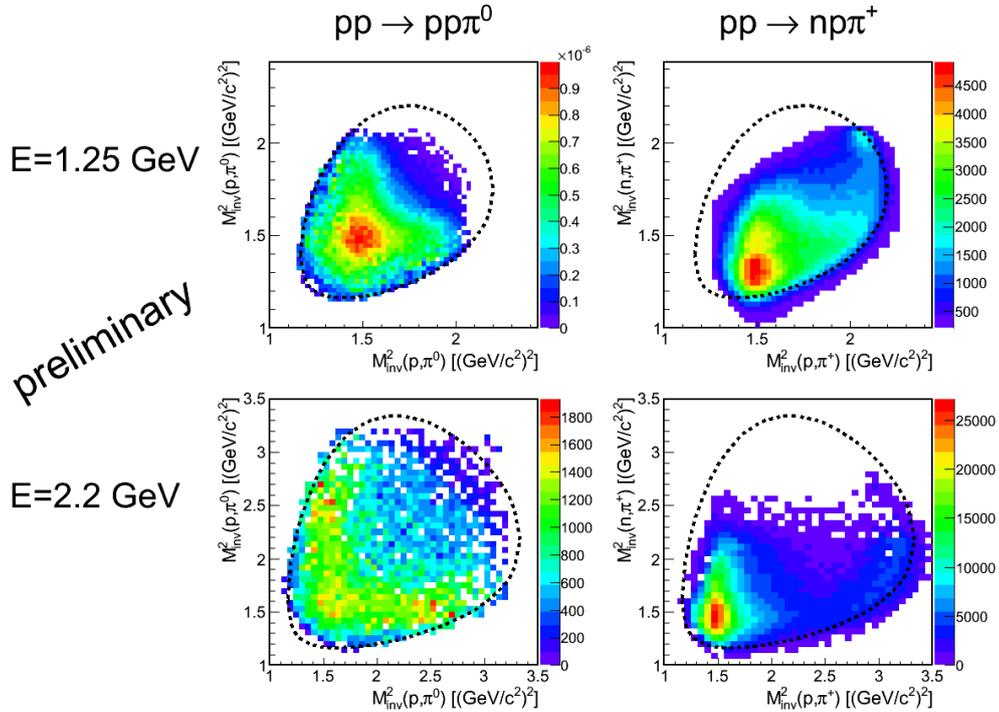
Figure 50: Dalitz plots of the $pp \to pp\pi^0$ and $pp \to pn\pi^+$ reaction: $n\pi^+$ invariant mass and $p\pi^0$ invariant mass squared distributions at 1.25 and 2.2 GeV. The kinematic limit for the $pp\to NN\pi$ reaction is shown as a dashed line.

5.2.2 Results

The Dalitz plots allow to investigate the resonant behaviour of the pion production. For the $pp\pi^0$ channel, an accumulation of yield for $M^2_{inv}(p,\pi^0)=1.5$ $(GeV/c^2)^2$, corresponding to the excitation of the Δ^+ resonance can be clearly seen at both energies.

For the $pp\to pn\pi^+$ reaction, the Δ^{++} signal stands out markedly at $M^2_{inv}(p,\pi^+)=1.5$ $(GeV/c^2)^2$, while the Δ^+ signal located at $M^2_{inv}(n,\pi^+)=1.5$ $(GeV/c^2)^2$ is less pronounced.

At 1.25 GeV, the spot appearing for $M_{inv}^2(p,\pi^+)$ and $M_{inv}^2(n,\pi^+)$ around 2 $(\text{GeV}/c^2)^2$ is due to the pn Final State Interaction (FSI). These events indeed correspond to small relative momentum between the proton and the neutron and this enhancement is confirmed qualitatively by a simulation where the pn FSI was implemented using the Jost function [112]. This effect is absent in the $pn\pi^+$ channel at 2.2 GeV, due to the forward peaking of these events at angles below the acceptance limit and in the $pp\pi^0$ data due to the trigger configuration, which for this experiment required two charged particles in opposite sectors of the HADES detector.

Fig.51 exhibits the projection on the $p\pi^0$ (left) and $n\pi^+$ (right) invariant masses and a comparison to simulation. The error bars include statistical and systematic errors due to event selection (5%) and correction of trigger condition which has been applied for some of the bins. The uncertainty on the normalization to pp elastic scattering is also considered as a source of systematic error (6%) but not included in the error bars here. In overall, both the yields and the shapes of the invariant masses are consistent with the cocktail from the resonance model. In this picture, The Δ^+ and Δ^{++} production cross-sections are correlated by the isospin factors ($\sigma(pp\to n \Delta^{++})= 3 \sigma(pp\to p \Delta^+)$). The dominant contribution comes from the Δ resonance excitation, but N(1440) and N(1520) also play a significant role at 2.2 GeV. At 1.25 GeV, the relation $\sigma(pp\to pn\pi^+) = 5 \sigma(pp\to pp\pi^0)$ is fulfilled, as expected from the dominance of the Δ resonance and the isospin factors in the different Δ decay channels.

The neutron angular distribution in the center of mass system (fig .54) is sensitive to the angular distribution of Δ resonance production since the dominant process is pp $\to$ nΔ^{++} (see fig.5.2.2). The asymmetry of the neutron angular distribution around $\cos\theta$=0 is due to the acceptance hole for positive charged particles emitted below 18° in the laboratory, which effect is well reproduced by the simulation. To minimize the model dependence, a two dimensional acceptance correction has been performed. For each $(\cos\theta_n, M_{inv}(p, \pi^+))$ bin, the correction factors are calculated as the ratio of events from simulation in full phase space and
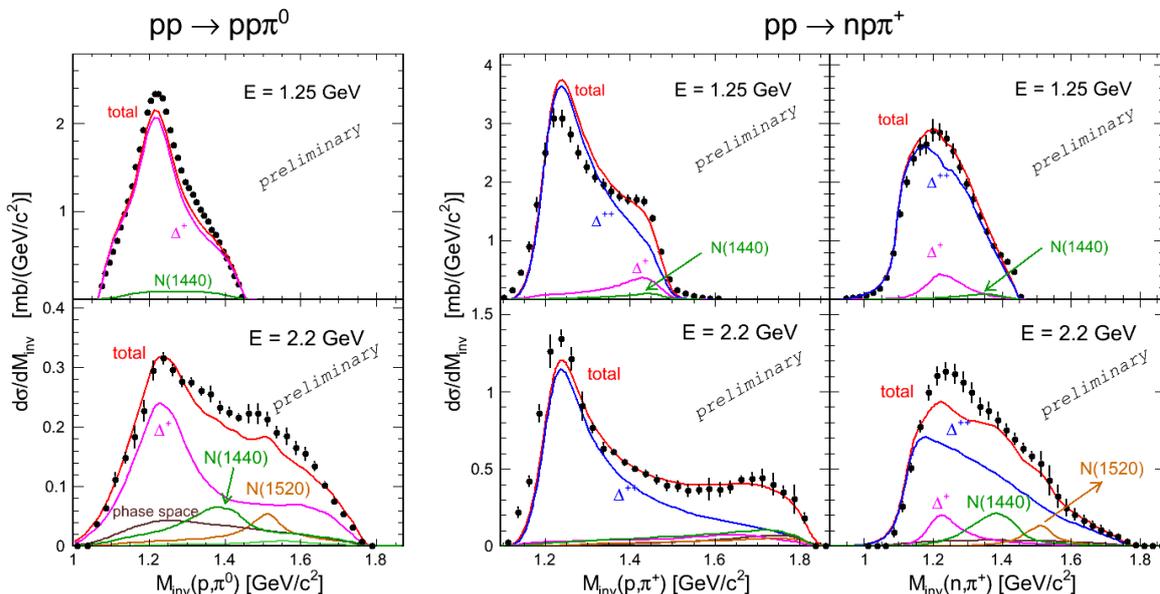
Figure 51: π N invariant masses measured in pp$\to$ ppπ^0 and pp$\to$ pnπ^+ reactions at 1.25 and 2.2 GeV. HADES data (full dots) are compared on an absolute scale to the predictions from the resonance model, with contributions of the following resonances Δ^+(1232) (pink), Δ^{++}(1232) (blue), N(1440) (green), N(1520) (light brown) and Δ(1600) (light green) and an additional small phase space contribution (dark brown).
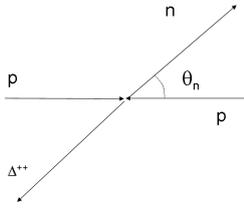
Figure 52: Sketch of the production angular distribution in the pp→ Δ++ reaction.
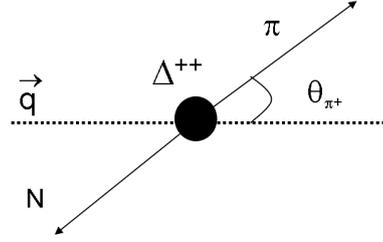
Figure 53: Sketch of the angular distribution of the Δ→ πN decay .
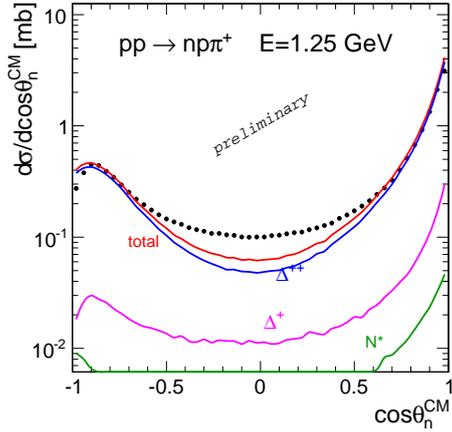
Figure 54: Center of mass angular distribution of neutron for the pp→pnπ+ reaction at 1.25 GeV. Data (black points) are compared to Pluto simulation (red solid line) including Δ++ (blue), Δ+ (pink) and N⋆ (green). The red dashed line includes an additional non-resonant contribution (orange dashed line).
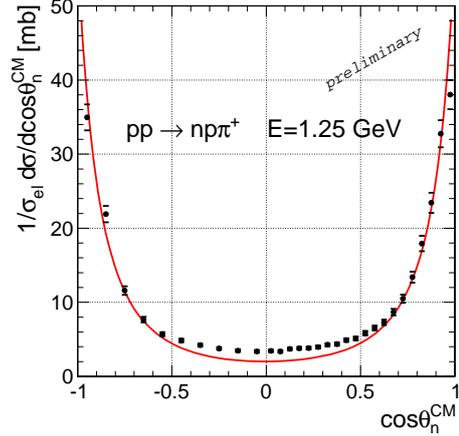
Figure 55: Acceptance corrected neutron angular distribution in the center of mass for the pp reaction at 1.25 GeV. Data (black points) are compared to PLUTO simulations (red line).

in geometrical HADES acceptance, then they are applied to correct the data. The width of the bins is adjusted to optimize the precision of the correction. The almost perfect symmetry of the acceptance corrected angular distribution with respect to $\cos\theta=0$ demonstrates the consistency and the precision of the acceptance correction.

The data clearly exhibit the forward/backward peaking of the Δ resonance production, which is characteristic of the peripheral character of these reactions. The one pion exchange model, provides a good description of this distribution, despite the excess observed around $\cos\theta_n = 0$. This is the region where the t and u four-momentum transfer squared are the highest and ρ exchange can contribute. On the other hand, the interference between the Δ^{++} and Δ^+, which is not included in our simulation can also stand out in this region, where the relative contribution of Δ^+ is higher. The analysis of the invariant masses as a function of neutron angle supports this hypothesis.

The agreement between the simulation and the data around $\cos\theta_n= 0$ can be enhanced, but not fully recovered if a small contribution of phase-space production is added. An upper limit of 0.5 mb (i.e. about 2.5% of the total pp→pnπ+ cross-section) can be determined, using as a constraint the shape of the invariant mass and the yield at forward/backward angles.

The decay angular distribution of the Δ resonance (see fig. 53) has been studied in this channel as well by looking at the angular distribution of π^+ in the (p,π^+) center of mass system.
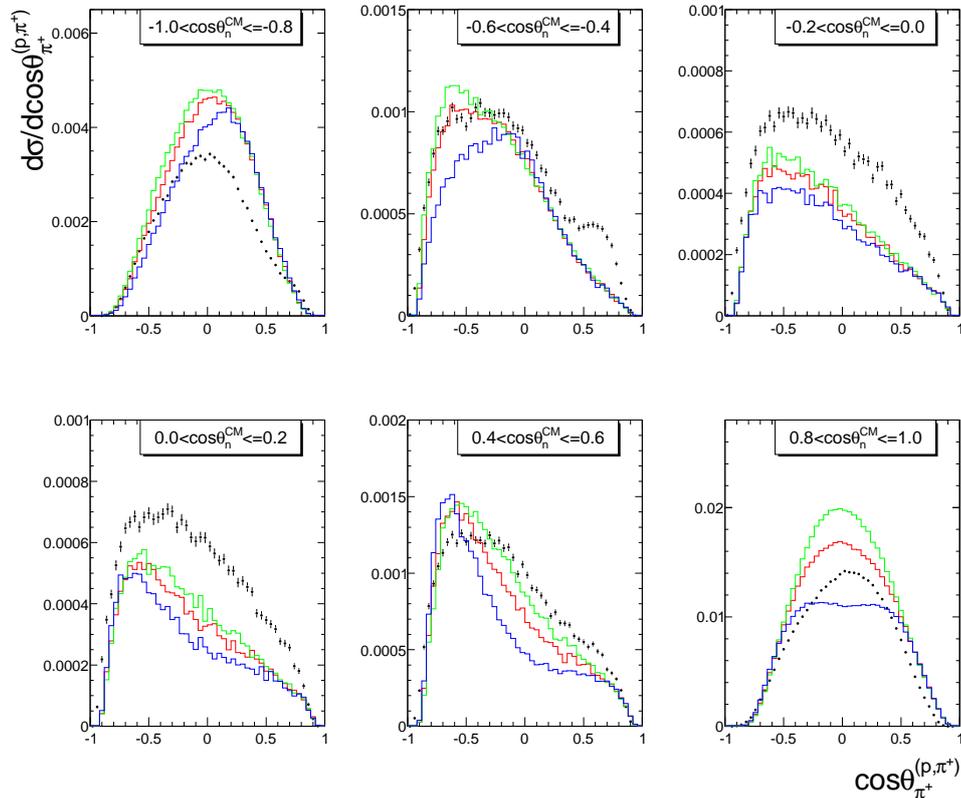
Figure 56: π^+ angular distribution in the (π^+,p) system for different neutron angle bins. the curves correspond to PLUTO simulations with different anisotropy parameters B of the decay angular distribution $1+B\cos^2\theta$ (green:B=0, red:B=0.65 and blue:B=3)

Following our discussions in sec. 2.5.2, the reference axis was taken as the Δ momentum in the laboratory frame. This choice is relevant when the direct graph, corresponding to the Δ excited on the target nucleon (see fig. 14), dominates, which is the case for the most forward neutron angles, where most of our statistics can be found. The evolution of this distribution is shown for different neutron angle bins in fig. 56 in comparison with simulations with different assumptions on the Δ decay angular distributions (isotropic, $1+3\cos^2\theta$ and $1+0.65\cos^2\theta$). The simulation clearly shows that the π^+ angular distribution in the (p,π^+) reference frame is sensitive to the Δ decay angular distribution only at the most forward angles, where the direct graph dominates. The comparison with the different shapes of decay angular distributions is however not conclusive. The influence of ϕ dependent terms in the Δ decay angular distribution, which have been neglected up to now, is currently under study. The best description of the shape is obtained for the asymetry parameter B=0.65, in agreement with the previous data [66, 68, 69]. The final analysis will be presented in the publication and in Tingting Liu's PhD thesis.

Another interesting aspect is the anisotropy of the π^0 production in the center of mass of the pp reaction, which is studied by Ania Kozuch in Cracow. Its measurement in NN collision serves as a reference for heavy-ion collisions, where the measured anisotropy is interpreted as a remnant of the very forward/backward peaking of the NN$\rightarrow$ NΔ process in the center of mass. An analysis of charged pion angular distributions measured in C+C reactions at 1 and 2 AGeV [113] was performed by the HADES collaboration and the anisotropies, of the order of 1-1.5, were found in agreement with UrQMD calculations. Together with Tingting Liu, we checked that, in pp collisions, the Δ decay angular distribution has also a significant influence on the π^0 anisotropy. This analysis will be presented in the publication in preparation.
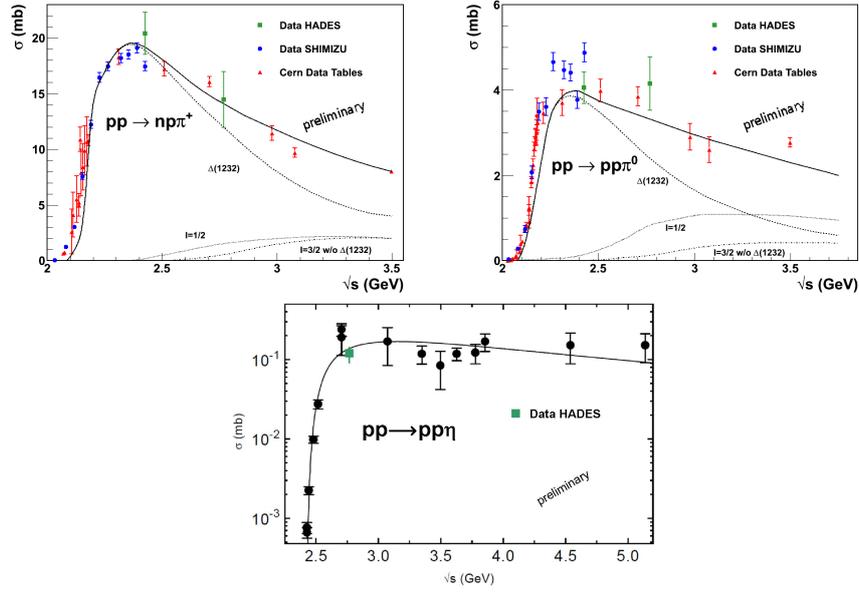
Figure 57: The cross-sections for the pp→pnπ⁺ (top left), pp→ppπ⁰ (top right), and pp→ppη reactions (bottom) measured with HADES (green squares) are compared to existing measurements (blue and red symbols). The lines show the resonance model fit with the different contributions ($\Delta(1232)$, I=1/2 and other I=3/2).

For the pp→ppη, the simulation, as explained in sec. 2 uses angular and invariant mass distributions measured in the DISTO experiment [61]. Due to the reduced resolution and acceptance of the HADES experiment in this channel, the sensitivity of the data to these distributions is unfortunately small.

The cross-sections of the different channels are obtained either by extrapolating the yield to the 4π acceptance using the simulation, or, when possible, by integrating the acceptance corrected distributions (like in fig. 55). The results are shown in fig. 57 together with existing data and with the resonance model fits. The calculation of systematic errors, which are probably too large at the moment, need to be finalized, but the global agreement with the resonance model and with the previous data is very good. Pion production cross-sections have been measured in the same energy range than the HADES experiment at KEK [69], Birmingham [64], Brookhaven [114, 115]. Detailed recent analysis of the pion and proton distributions in pp→nπ reactions are also available from COSY-TOF, [116, 117] or from PNPI at Gatchina [118], at energies below 1 GeV. For the η production, the cross-section is in fair agreement with the very bad precision measurement by Pickup et al. at [119] using a bubble chamber at BNL in 1962.

5.3 Exclusive dilepton channels

5.3.1 π^0 and η Dalitz decay exclusive reconstruction

The exclusive production of unstable particles, which present a known leptonic or Dalitz decay branching ratio, can be studied both in pp→ ppe⁺e⁻X channels, and in purely hadronic channels, which is suited for a cross-check of the analysis efficiencies. This possibility has been exploited in the case of pp→ppπ⁰ reaction and pp→ ppη reactions at 2.2 GeV. The π^0 and η Dalitz decay signals are extracted from the pp missing mass distributions, measured for ppe⁺e⁻X reactions (see fig. 58). The yields are in good agreement with the resonance model, with cross-sections given in Table 4 and also with the cross-sections deduced from the
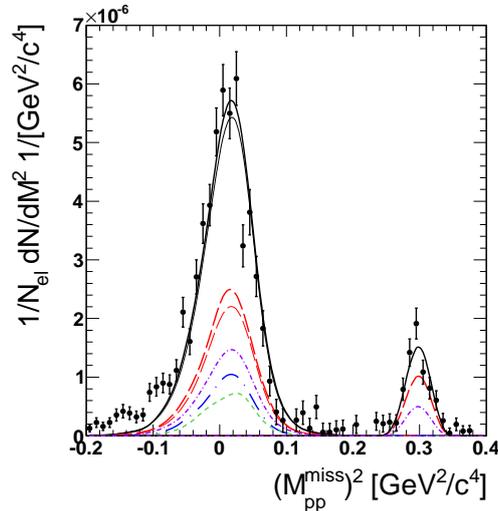
Figure 58: Missing mass spectrum of two protons for the ppe$^+$e$^-$ events after subtraction of a multipion background. The lines show the predictions from the PLUTO event generator using the resonance model [58]. The solid black lines are the sum of all contributions. For the π^0, the short-dashed line (green) is the N*(1520), the long dot-dashed (blue) line is the the N*(1440), the short-dot-dashed (violet) is the non-resonant production and the long dashed red line is the Δ(1232) contribution. For the Δ(1232), the thin line correpsonds to a decay angular ditribution in 1+3cos$^2\theta$ and the thick line to the standard PLUTO option (see sec.2.5.2). For the η, the short dot-dashed (violet) line is the non-resonant production and the long dashed (red) line correponds to the N*(1535).

hadronic channel analysis, as described in sec. 5.2.

This exclusive analysis of the π^0 and η Dalitz decays was also used to study the helicity angle distributions. In the same way as for the Δ Dalitz decay case (fig. 26), the helicity angle α is defined as the angle between the momentum vectors of the lepton in the virtual photon ($\gamma^\star$) frame and of the $\gamma^\star$ in the decay meson rest frame, after a first boost to the meson rest frame. After acceptance corrections, these angular distributions are in agreement with a 1+ cos$^2\alpha$ distribution (fig.59) for both π^0 and η. This is a very nice experimental check of the trend which is expected from QED, since, in the decay of these pseudoscalar mesons, only transverse photons can be produced. This check is useful to trust the reconstruction of the helicity angle in the case of pp→ppe$^+$e$^-$ at 1.25 GeV, as we will see in the next paragraph.

5.3.2 Δ Dalitz decay reconstruction

Emilie Morinière had investigated in simulations the feasibility of the exclusive measurement of the Δ Dalitz decay using ppe$^+$e$^-$ events to elaborate the experimental proposal for the p+p experiment at 1.25 GeV in 2004. This work has been then continued to be used as a guide for the analysis. The simulation was based on the resonance model [58], with the cross-sections given in the table 5. The kinematics had been studied in detail to understand the acceptance and efficiency effects. The overall acceptance is 1% for π^0 Dalitz decay and 2% for Δ Dalitz decay. The missed events correspond mainly to low energy electrons, to forward protons, since the Forward Wall informations were not recorded for the pp experiment, as well as to slow backward protons due to the momentum cut. The e$^+$e$^-$ opening angle cut has an influence only for the lowest invariant masses.

The main problem to identify the Δ Dalitz decay is the rejection of the π^0 ($\pi^0 \rightarrow \gamma$e$^+$e$^-$) Dalitz decay which has a cross-section about a factor 200 higher. The simulated invariant
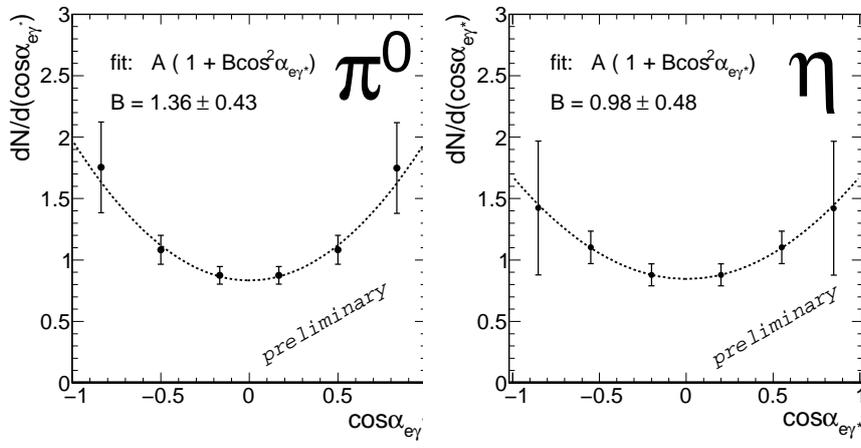
Figure 59: Helicity angular distributions for π^0 (left panel) and η (right panel) Dalitz decays reconstructed from pp→pp(π^0/η) →ppe$^+$e$^-\gamma$ exclusive channels at 2.2 GeV after acceptance and efficiency corrections.
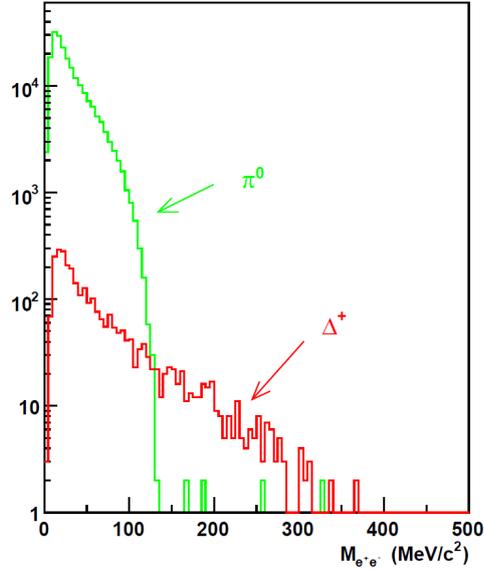
Figure 60: Simulation nresults for π^0 Dalitz and Δ Dalitz decays in the pp reaction at 1.25 GeV. The invariant mass spectra within the HADES acceptance and after a cut on the dilepton opening angle ($\theta_{ee} > 4^{\{circ}$ are shown for about one week of beam time.

mass spectra for both π^0 and Δ Dalitz decay are shown in fig. 60. The possibility to reject this background by applying a suited cut on the pe$^+$e$^-$ missing mass has been carefully investigated. A method was proposed, consisting of adjusting the width of the cut as a function of the proton momentum, in order to optimize the signal/background ratio. According to the prediction, the background level could be reduced to 20% while reducing the signal by 40%. A subtraction would then have been possible, considering that the π^0 Dalitz decay was known to a good precision. The systematic errors linked to this background suppression had been also carefully evaluated. Due to the worse than expected resolution, and more precisely to the tails of the non-gaussian distribution of the momentum resolution, the proposed method could not be applied. As a consequence, the Δ Dalitz decay signal is extracted only for e$^+$e$^-$ invariant masses M_{ee} larger than 140 MeV/c^2, where the π^0 Dalitz does not contribute.

This analysis is currently developped by our colleagues in Cracow, using the Post DST Analysis Tool (PAT). One major task is the choice of the analysis cuts to optimize the signal/combinatorial background ratio, which after this optimization, ranges from 5 to 10 for $M_{ee} > 0.14$ GeV/c^2. In parallel, Tingting Liu studies the sensitivity of the measured distribu-

tions to the Δ Dalitz decay process and the model dependence of the acceptance corrections. The pe^+e^- missing mass distribution is displayed in fig. 61. The nucleon peak is clearly seen
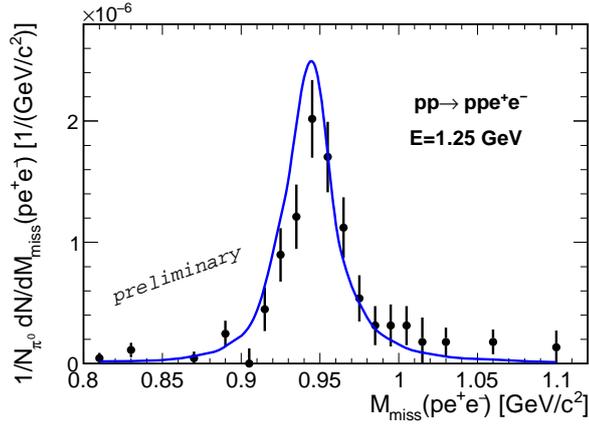
Figure 61: pe^+e^- missing mass for pp→pe^+e^-X reaction at 1.25 GeV, after a cut on e^+e^- invariant mass: $M_{ee} > 0.14$ MeV/c^2. The blue line is the simulation for the Dalitz decay channel.

with the expected width from the resolution including only the Δ Dalitz decay process, which confirms that the combinatorial background is efficiently subtracted. The contribution at higher missing masses, which would correspond to an additionnal pion emitted is small. The number of reconstructed signal pairs is about 200.
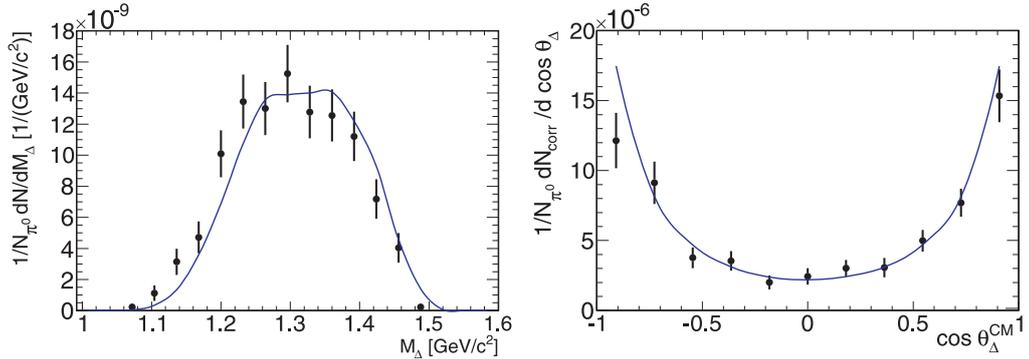
Figure 62: pe^+e^- Invariant mass (left) and acceptance and efficiency corrected angular distribution in the CM frame (right), compared to the simulation (blue line).

It is important to prove that the data reveal the Δ resonance properties despite the unavoidable smearing due to the fact that both the scattered proton and the one coming from the Δ decay have to be added in the distributions. The invariant mass and center of mass angle distributions of the reconstructed pe^+e^- systems are shown in fig. 62 and are in good agreement with the simulation, which confirms that these events originate from Δ Dalitz decay.

These distributions can be compared to the ones measured with the hadronic channels (see sect. 5.2). In the case of the pe^+e^- events analysis, the cut on M_{ee} favours higher Δ masses, which explains why the pe^+e^- invariant mass distribution is shifted to higher values with respect to the invariant mass distribution measured from pπ^0 events (fig. 51). The center of mass proton angular distribution of the pp→ppπ^0 events was not analysed, but a connection can be made with the neutron center of mass distributions (fig. 55) in the pp→pnπ^+ reaction,

which reflects directly the Δ^{++} production angular distribution, if the smaller Δ^{+} contribution is neglected.

The measured yields are in good agreement with the resonance model cross-sections for Δ production and consistent with the inclusive yields (see fig. 45 left part). Considering statistic and systematic errors on the measured yields, which are respectively 9% and less than 20%, and neglecting the pp bremsstrahlung, the branching ratio is in agreement with the value 4.2 10^{-5} predicted by the QED calculations. The integrated yield for $M_{ee} > 0.14$ GeV/c^2 is not sensitive to the N-Δ transition form factor model, so the main model-dependent uncertainty comes from the description of the angular distributions, which is well constrained by the analysis of the hadronic channels as shown in sec. 5.2.
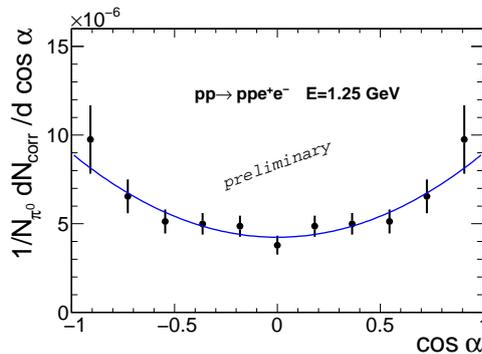
Figure 63: Helicity angle distribtution after acceptance and efficiency correction, as defined in sec. 2.5.3. The blue line shows a fit by a$(1+ b \cos^2 \alpha)$ (b=1.11 $\pm$ 0.32).

Another quantity which is expected to be sensitive to the Δ Dalitz decay process is the helicity angle (see sec. 2.5.3). The measured helicity angle distribution, corrected for acceptance and extrapolated to the whole invariant mass range, using the simulation, is presented in fig. 63. The distribution is in agreement with the $1+\cos^2 \alpha$ distribution expected from the QED, when neglecting the Coulomb transition amplitude, as discussed in sec. 2.5.3. As the Δ resonance cannot be unambiguously reconstructed, since the two protons cannot be distinguished in the final state, a smearing of the distribution was first expected. However, for the small M_{ee} invariant masses, which dominate the total e$^+$e$^-$ pairs, this angular distribution does not depend very much on the reference frame for the $\gamma^\star$ momentum, as a result of relativistic effects. This is an important result, since it allows to investigate the helicity angle distribution also in inclusive e$^+$e$^-$ production, where the $\gamma^\star$ can only be calculated in the lab or total CM frame. The distorsion of the distribution increases at large invariant masses, but the anisotropy remains of the order of 0.7 for invariant masses larger than 0.2 GeV/c^2. These investigations willl be presented in detail in Tingting Liu's thesis.

5.4   Conclusion and outlook concerning pp and pn reactions

The HADES measurements in pp and dp reactions at 1.25 GeV allow crucial tests of the models. The pp spectra test the description of the Δ Dalitz decay process, which is more or less accurate, depending on the model. The quasi-free pn spectra are puzzling and the available descriptions underestimate significantly the high invariant mass yield.

In the pp reaction, three types of channels, namely the inclusive dilepton production, the pion and eta exclusive production and the exclusive pp$\rightarrow$ppe$^+$e$^-$ reaction are analysed with success with the same model. The good agreement of the yields and distributions for these three analysis is therefore a good check of the consistency of the three analysis and of the ingredients of the resonant model.

The exclusive hadronic channels, measured in pp reactions at 1.25 GeV and 2.2 GeV, carry information on the Δ production mechanism at 1.25 GeV and the contribution of other resonances at 2.2 GeV. An analysis of hadronic exclusive channels (one pion and two-pion channels) is on-going for the quasi-free pn reactions. The check of the contribution of other resonances than $\Delta(1232)$ is of special interest to understand the dilepton production in this system. This bulk of data should be of interest for theoreticians to test in detail pion and η production models.

The Dalitz decay process has been for the first time identified and the branching ratio is in agreement with the QED expectations ($4.2\ 10^{-5}$). This also confirms that the pp bremsstrahlung is small, although an upper limit on this contribution has not yet been estimated. Similar investigations are made in the case of the pn reaction, where the different distributions are very helpful to disentangle the pn bremsstrahlung and Δ Dalitz decay contributions and to constrain the models. This on-going analysis will also help to understand the origin of the dilepton excess in the quasi-free pn reaction.

Further interesting information on the pn reactions could be obtained by measuring the pd reactions at higher energies. It would be particularly interesting to measure the dilepton spectra in this reaction below and above the vector meson production threshold. This would give more information about the contributions of the different resonances to dilepton production. In the present dp experiment, the information of the Forward Wall was used to trigger the data acquisition, in order to enhance events from the quasi-free np reaction. This condition could be removed, in oder to measure all the charged particles emitted in the dp reaction. It would then allow for a measuremnt at the same time of pp and pn interactions from the dp reaction.

6 Perspectives of pion beam experiments

6.1 Physics case
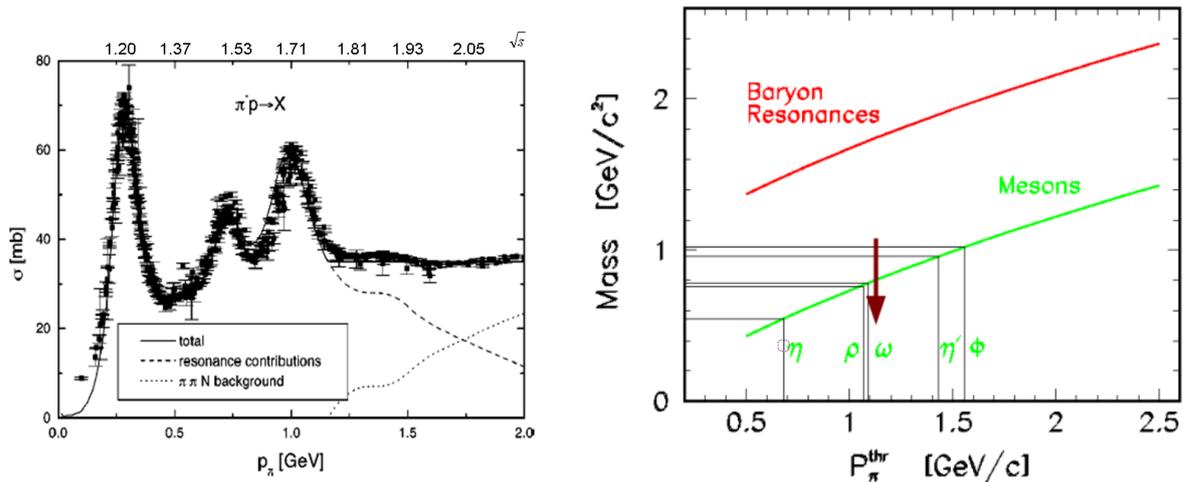
Figure 64: Left: π^-p cross-sections as a function of π^- momentum. Right: the horizontal axis is the momentum of a π beam for threshold production of mesons or baryonic resonance with mass indicated in the vertical axis. The arrow indicates one possible pion momentum value to study in-medium ρ-ω production.

Pion nucleon interactions have been used in the past to produce and identify baryonic resonances (fig. 64). On the other hand, pion induced reactions on nuclei have brought a lot

of informations about the role of these resonances and of multi-step mechanisms in particle production. Pion beams have been intensively used with energies in the vicinity of the $\Delta(1232)$ resonance at LAMPF and PSI and at higher energies at KEK to study scattering, charge exchange or absorption reactions with nuclei. At GSI, a pion beam with momenta between 0.6 and 1.5 GeV/c can be used, which is suited to explore the "second and third resonance region". This beam is used by the FOPI experiment to measure the production of K_S^0 in π^- induced reactions on several nuclei [120]. The HADES collaboration plans to study dilepton and strangeness production in pion induced experiments.

6.2 Medium effects

The dilepton spectroscopy in π induced reactions on nuclei is proposed in order to study medium effects on ρ and ω mesons in cold matter. Such experiments will therefore complement the on-going studies of ρ/ω production at normal nuclear density in the p+Nb system.

To identify clearly medium modifications, it is important to gather both various experimental informations and to test the models in different conditions. In a classical picture, reactions induced by pions or by protons consist in a cascade of subsequent baryon-baryon, baryon-meson or meson-meson reactions. The primary interaction plays however an important role and different relative yields of the baryonic resonances might be expected, as a consequence of the different reaction mechanisms. Due to the crucial role of these resonances, it is therefore important to study the simpler case of pion induced reactions. The role of nucleon-nucleon and pion-nucleon Bremsstrahlung is also obviously different in the two types of reactions.

One advantage of the pion probe is that the dynamics of the reaction is much simpler. The interaction lagrangians are indeed well defined, while in the case of incident protons, the production mechanism is not so well known, and can imply the exchange of different mesons.. But, the specificity of the pion induced experiments relies also in the fact that the medium modification effects could be measured also for the ω meson. For a given available energy in the center of mass, the vector meson is indeed produced with much less momentum than in a nucleon induced reaction. The ω meson has then a higher probability to decay inside the nuclear medium, and hence to show modified properties, as was first advertized in [122]. The sensitivity to dropping mass and broadening has also been investigated in Intranuclear Cascade Calculations [123, 124], as well as in BUU transport model calculations [121], as shown in fig.65 where the sensitivity to different types of medium effects is shown. All these calculations produced increased effects on the ω mesons, if a higher limit was put on the e^+e^- pair momentum. These calculations motivated the proposal of measuring dilepton production with pion beams.

New HSD calculations, not yet published, have been produced recently for the π^-+Au system. A strong sub-threshold ρ meson production by the N(1520) resonance can be observed up to an energy of 0.7 GeV. To study medium effects, energies of the order of 1.4 GeV are more suited, in order to produce ω and ρ with large yields. The medium effects induce a damping of the omega peak and an increase of the yield in the region below the peak. These effects are already significant in the spectra calculated for π^-+C and much enhanced for the π^-+Au system. In these calculations, an important πN Bremsstrahlung contribution is expected, the nucleon-nucleon Bremsstrahlung being very much suppressed.

6.3 Pion-nucleon reactions

The interest of a measurement of the $\pi N \to N\ e^+e^-$ reaction has been mentionned in different papers, where various aspects were stressed, corresponding to the different graphs contributing
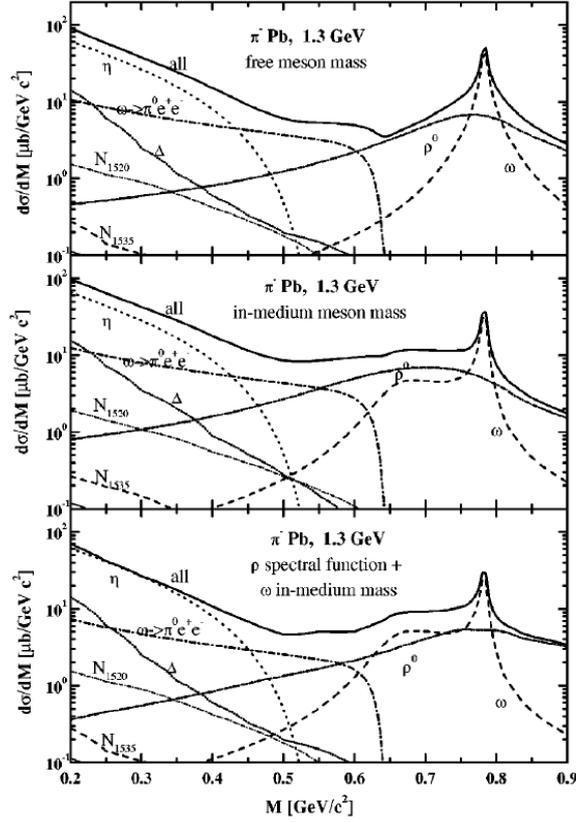
Figure 65: Dilepton invariant mass for π^-Pb at an incident energy of 1.3 GeV for BUU calculations with free meson masses (upper part), with the collisionnal broadening effect and a "dropping mass" of ρ and ω mesons. (middle part) and with a in-medium ρ spectral function and a dropped ω meson (bottom). The lines indicate the different dilepton sources [121].

to the reaction (fig. 66 and fig. 67).

In 1962, the π N $\rightarrow$ N e$^+$e$^-$ reaction is discussed in [126], in connection with the determination of the charged π meson electromagnetic form-factor in the time-like region, which plays a role at the $\pi\pi\gamma^*$ vertex in the pion exchange graphs (fig. 67 b).

In 1965, M.P. Rekalo [127] was interested by the nucleon pole diagram shown in fig. 67, which should be important at large center-of-mass angles of the nucleon. If events from this graph could be selected, the sensitivity to the time-like electromagnetic nucleon form-factor at the NNγ^* vertex could be studied. In addition, the kinematical region of these form-factors corresponds to the so-called unphysical region, i.e. below the $\bar{p}$ threshold, above which the study with $\bar{p}$p$\rightarrow$e$^+$e$^-$ or e$^+$e$^- \rightarrow$ $\bar{p}$p reactions can be done (see sect.5.2 in Part II). It is also proposed to use the $\bar{p}$p$\rightarrow$ e$^+$e$^-\pi^0$, which is the crossed-channel reaction of $\pi N \rightarrow$ N e$^+$e$^-$ to
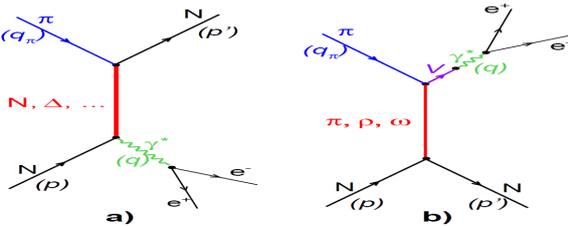
Figure 66: t-channel graphs for π-N reactions
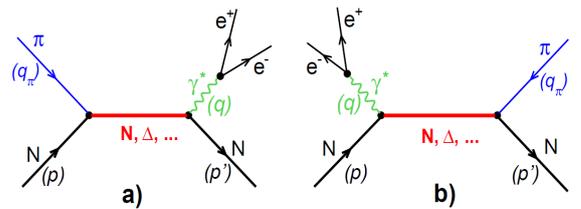
Figure 67: s-channel graphs for π-N reactions

63
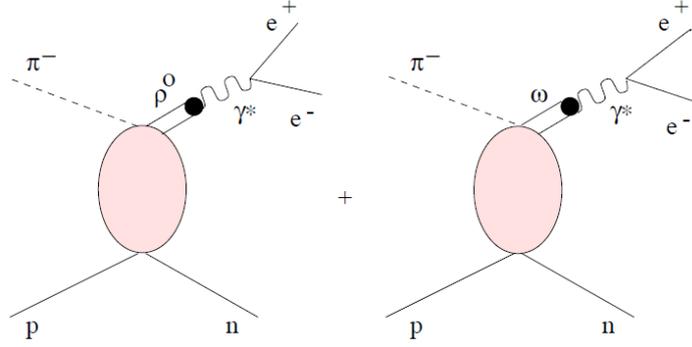
Figure 68: Sketch for the $\pi N \rightarrow \rho(\omega)N$ amplitude.
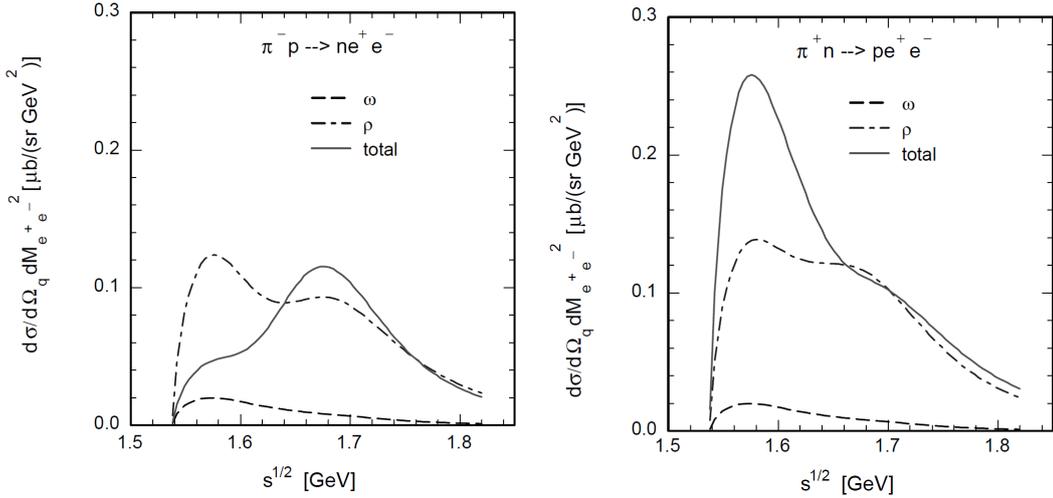
Figure 69: Differential cross-sections for the $\pi^- p \rightarrow e^+ e^- n$ reaction (left) and $\pi^+ p \rightarrow e^+ e^- p$ (right) at a fixed $e^+ e^-$ invariant mass $M_{ee} = 0.6$ GeV/c^2 [125]

access these time-like nucleon form-factors in the unphysical region.

Recent studies put emphasis on the $e^+ e^-$ production via vector meson decay. In [125], the s and u-channels graphs are calculated for the different known resonances up to $\Delta(1700)$, with coupling constants deduced from a quark-model [128] or from the measured $N\rho$ decay widths [129]. On the other hand, [130] provides a unified description of meson-nucleon and photon-nucleon interaction, restricted to s-channel amplitudes where the coupling constants are deduced from a large set of data. As shown in fig. 69 and fig. 70, both calculations demonstrate the crucial role played by the interferences in the ρ and ω channels in the $e^+ e^-$ production. The latter are destructive in the case of $\pi^- p \rightarrow n e^+ e^-$ and constructive in the case of $\pi^+ n \rightarrow p e^+ e^-$. The sensitivity to the vector-meson coupling constants of the resonances also appears clearly. In [125], the $S_{11}(1535)$ is dominant at low energies for both ω and ρ production and the $S_{11}(1650)$ at larger energies. In [130], due to much smaller coupling constants for these resonances, the cross-sections are smaller, especially for the ρ and the interference pattern is different. The effect of the destructive ρ-ω interference is very spectacular in [130]. As seen on fig. 70, the cross-section in the $\pi^- p \rightarrow n e^+ e^-$ is very small at $\sqrt{s} = 1.5$ GeV, i.e. about 220 MeV below the ω threshold. An experimental check of these predictions would be very interesting. As the couplings of the resonances to the vector mesons are related to the electromagnetic structure of the resonances, these measurements present a fundamental interest.

An "inverse pion electroproduction calculation" is also proposed by G. Lykasov [131].
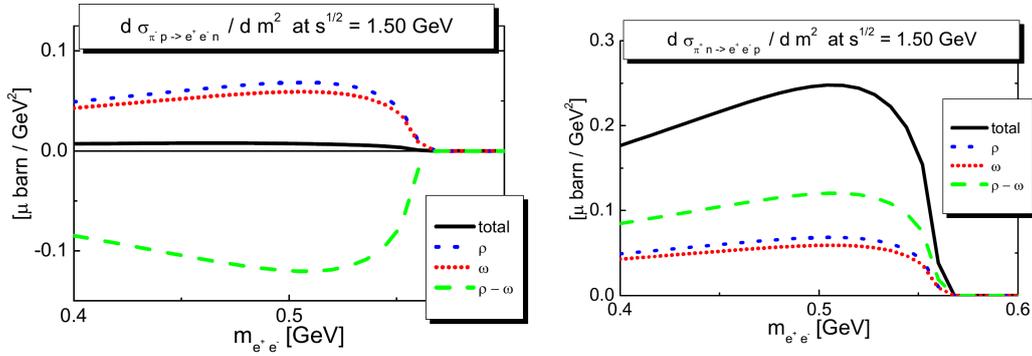
Figure 70: Differential cross-section for the $\pi^-p\to e^+e^-n$ reaction (left) and $\pi^+n\to e^+e^-p$ (right) at $\sqrt{s}$=1.5 GeV as a function of the e^+e^- pair invariant mass. The ρ^0 and the ω contributions are shown by short-dashed and dotted lines repsecively. The long-dashed line shows the $\rho^0 - \omega$ interference. The solid line is the sum of the three contributions.

Along the same line, the calculations of Ong et al. [132] for pion electroproduction could also be adapted for dilepton production in pion induced reactions. The interest to study subthreshold ρ/ω production in πd and πA reactions is also mentionned to study Short Range Correlations [131].

The estimates from the experimental proposal in 2001 have been revisited, taking into account realistic projections concerning beam intensities, with no big changes with respect to previous estimates. Assuming a cross-section for the reaction $\pi^-p\to \omega$n of 2.5 mb, according to HSD transport model and taking an intensity of $5\ 10^5$ π/s, which corresponds to the half of the Space Charge Limit and taking conservative numbers for duty factors (0.7) and acquisition dead time (0.5), about 50 ω's/day will be measured. In the π^-+p reaction, the exclusive channels π^-+p $\to$ ne$^+$e$^-$ can be measured, using a missing mass cut. In this way, the π^-+p $\to$ ppη $\to$ pp γ e$^+$e$^-$ can be suppressed, and a clean study of the ω and ρ production can be realized. This is illustrated in fig.71.

6.4   Strangeness program

Strangeness production measurements with pion beam induced reactions are also possible. The $\Lambda(1405)$ can be produced in π+p reactions possible at an incident momentum around 1.7 GeV/c. This object is very attractive, due to the open questions about its structure. In medium modifications and K$^-$ absorption can also be studied in π^-+p and π^-+A reactions at 1.7 GeV/c. The proposed program also includes the study of the K^0_S production, as already done by the FOPI collaboration [120], in π^-+p, π^-+C and π^-+Pb at lower energies.

6.5   Technical challenges

From the technical point of view, some developments are still needed to check the feasibility of these experiments.

As a secondary beam, the pion beam is limited in intensity and is spread in momentum and position. These three features imply technical problems, which have to be solved to prove the feasibility of the experiment [133].

- intensities: This is a crucial issue, due to the low dilepton rate. In the actual conditions, the highest pion beam intensities (10^7 pions/cycle $\sim 10^6$ pions/s) can be achieved with ^{12}C or ^{12}N primary beams. In previous tests, intensities of $6.5\ 10^{10}$ N$_2$ ions/cycle
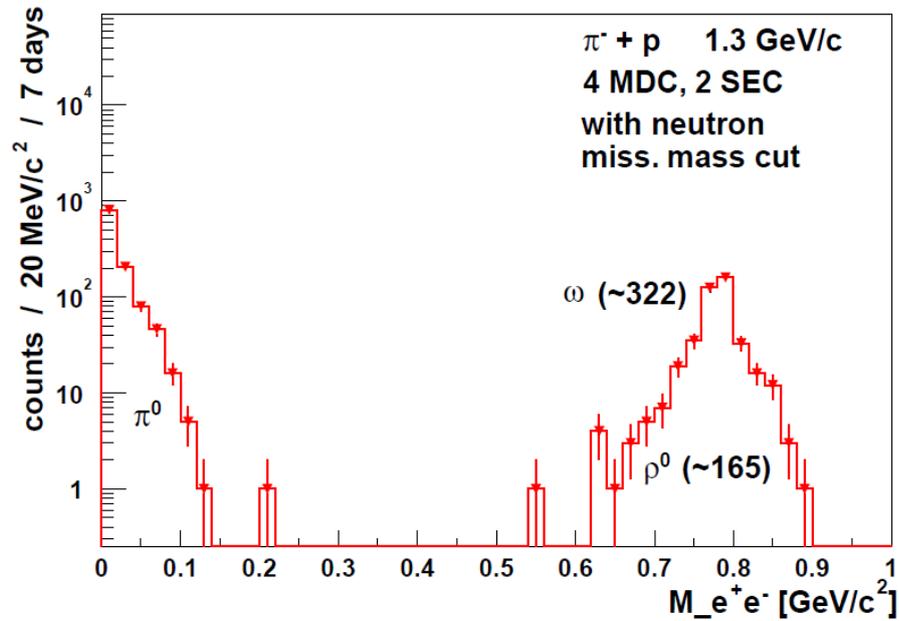
Figure 71: Expected dielectron invariant mass distribution for the π^-p reaction at a beam momentum of 1.3 GeV/c and one week of beam at an intensity of 10^6/s on target. The yield is calculated for a set-up with only two sectors equipped with 4 MDC planes, which was the situation in 2006. A missing mass cut around the neutron mass has been applied on the dilepton channel.
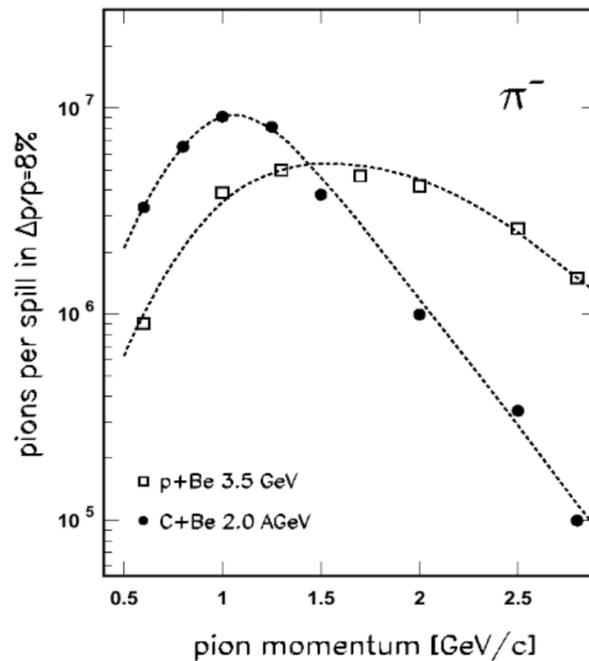
Figure 72: Pion beam intensities available at GSI for production by the reaction p+Be at 3.5 GeV and C+Be at 2 GeV.

could be reached, corresponding to about half the space-charge limit. It has now to be proven that the space-charge limit can been reached. π^+ are not used due to the proton contamination.

The pion beams are obtained by impinging ^{12}C or ^{14}N beam on a 10 cm long berryllium
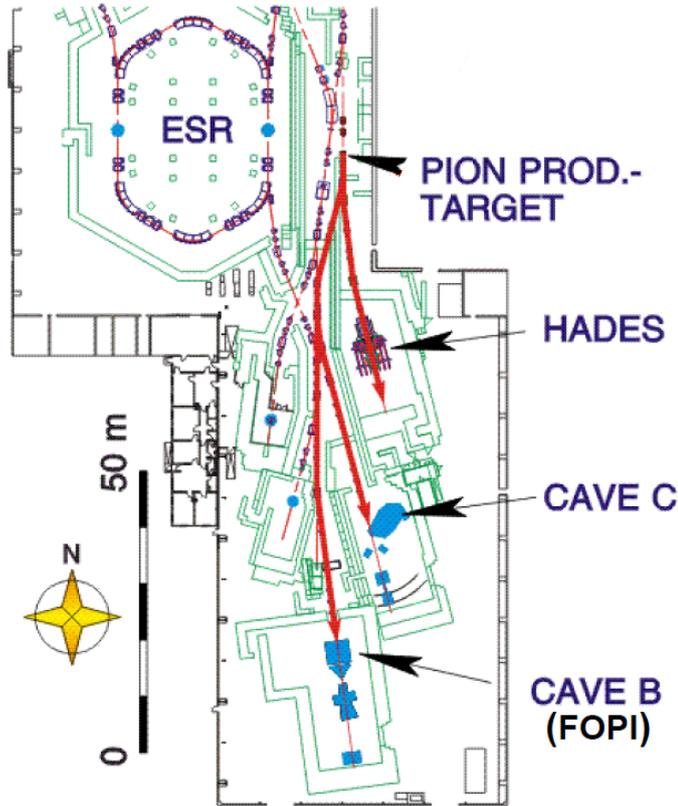
Figure 73: View of one part of the GSI facility, with the π production target and the HADES and FOPI experimental areas
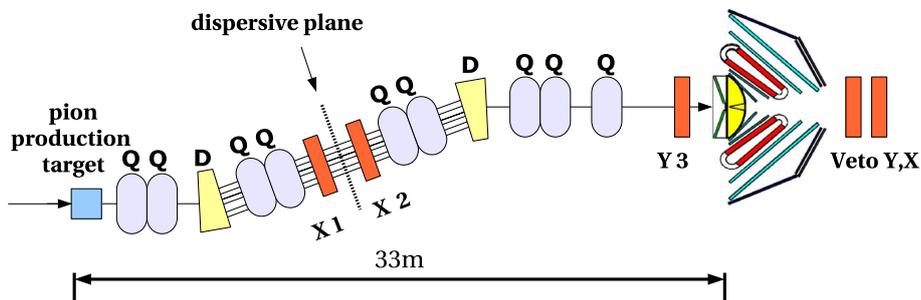
Figure 74: Shematic drawing of the pion beam line from the production target to the HADES detector, with detectors (indicated in orange), as used in the tests in October 2007.

target located in the beam line, 33 m in front of the HADES detector. The second bottleneck is the duty cycle of the accelerator. Taking advantage of the fast-ramping magnets (4T/s) now available at GSI, it could be increased by a factor 1.5-2.

Finally, the extraction efficiency has to be checked.

The possibility of having stable beams with these three factors at their maximum value will be soon checked in a test run end of june 2010.

- Momentum spread and spatial width: Considering the acceptance of the beam line, the pion beam has a dispersion of ±4%. In-beam position sensitive detectors located on each side of a dispersive plane are therefore needed to measure the pion momentum with a resolution of about 0.1%. The concept of this momentum measurement was checked

in early tests [133].

A detector in front of the target is also necessary to reject background reactions, due to the beam halo. This detector should be thin, in order not to introduce too much multiple scattering, nor interactions. It should also be position sensitive and deliver fast signals, which could be included as an anti-halo in the LVL1 trigger to activate the acquisition only on interactions of beam particles with the target.

With these three detectors, the tracking of the beam particles will be possible and will allow an off-line rejection of the interactions with the material around the target.

This is illustrated in fig. 74, where the set-up used for the pion beam test in November 2007 is displayed. For these tests, the detectors at the dispersive plane consisted of Si-strips with a thickness of 5 mm (X_1,X_2) and fibers (Y_3) were used in front of the target [54]. These tests allowed for a check of improvements of the beam profile, and more precisely of the tail reduction, after the adjunction of a third quadrupole at the end of the beam line. The beam profile at the target measured in the Y direction is gaussian, with a width of 6 mm, in agreement with beam optics simulation.

This large width is worrying for $\pi^- p$ experiments, since the diameter of the entrance window of the LH2 target (see sec.3.2) is presently 15 mm. A modification of its geometry might be envisaged.

However, the detectors used at the dispersive plane were much too thick and induced a huge background in the detectors around the target. In the mean time, much improvement was achieved concerning the availability of thin and fast detectors of large area.

For the detector at the target, diamonds are foreseen. The challenge is to have large enough detectors (of the order of 10 mm x 10 mm). Diamond would also be ideal for the detectors at the intermediate plane. This solution would however need a long and expensive R&D. At the moment, it is envisaged to use 300 μm thick silicon microstrip detectors covering an area of 10 cm by 10 cm with 128 channels in both x and y directions. For the read-out electronics, 2 systems are developed in parallel by GSI and München teams: a "conservative" discrete electronics based on HADES TRB read-out and a more challenging n-xter device.

6.6 Conclusion on the project of π beam experiments

Although experiments with pion beams were part of the HADES original experimental program, the HADES collaboration has first performed "easier" experiments, with heavy ion, proton or deuterium beams. The feasibility of pion beam experiments, which depends on the available intensities and on the quality of in-beam has indeed still to be demonstrated. The interest for dilepton production as well as strangeness studies, both in experiments on the nucleon and on nuclei is very clear. These experiments could be foreseen strating from 2012.

Part II

The PANDA project

1 The FAIR and PANDA projects

1.1 The new FAIR facility

1.1.1 FAIR physics program
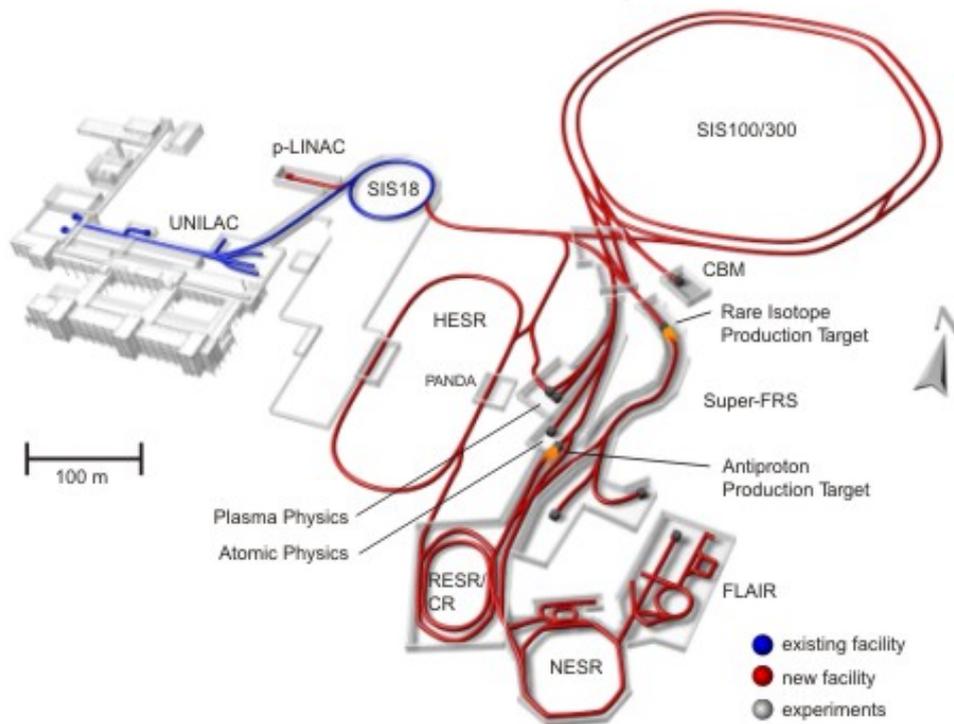
Figure 75: General lay-out of the future FAIR facility

The goal of this new facility is to provide Europe with a state of the art accelerator system for research in nuclear physics and connected fields [134, 135]. FAIR is designed to deliver primary beams of all ion species from Hydrogen to Uranium with energies up to a few tens of GeV/nucleon and, in the same range of energies, secondary beams including both rare-isotope nuclei and antiprotons with unprecedented quality and intensity.

The scientific goals of FAIR cover the following fields: QCD studies with cooled beams of antiprotons, nuclear matter at high baryon density, nuclear structure and nuclear astrophysics with nuclei far off stability, high density plasma physics, atomic and material science, radio-biological and other application-oriented studies.

The project builds on the present accelerator system and scientific community at GSI, but due to the much higher intensities and energies of the heavy ion beams, the scientific scope will be considerably broader. In addition, the antiproton beams attract many hadronic physicists working previously at other antiproton facilities like FERMILAB or at e^+e^- colliders like SLAC.

1.1.2 Short technical description

The general layout of the FAIR facility is displayed in fig.75. Using the different synchrotrons and storage rings, it will be possible to run up to four research programs in parallel with the highest intensities.

In the initial scheme, the central part of the FAIR facility will consist in the double superconducting synchrotron SIS100/SIS300 with a circumference of about 1100 m and rigidities of 100 and 300 T.m, respectively, which will be built on top of each other in a subterranean tunnel. Due to financial limitations, the new scheme of the FAIR facility, only comprises the SIS100 synchrotron. The SIS300 will be envisaged in a further step, and will require additionnal funding. The injection of heavy ion beams in the synchrotrons will be ensured by the UNILAC and SIS18 synchrotron, which, together with the ESR (Experimental Storage Ring) are the basic elements of the present GSI facility. A new proton linac injecting into SIS18 will be added to produce intense proton beams.

The SIS100 is designed to fullfill the requirement for very intense primary pulsed heavy ion and proton beams. The high bending power of the magnets makes it possible to use ions with low charge state, thus reducing the space charge effects. At the same time, repetition rates of 1Hz will be achieved and ramp rates up to 4T/s of the bending magnets will be used to maximize the number of particles in the bunch. In this way, 1 GeV/nucleon U^{28+} beams can be accelerated with intensities of $5\ 10^{11}$ ions per pulse and 29 GeV protons with intensities reaching $4\ 10^{13}$ per pulse.

The SIS300 synchrotron allows for further acceleration of heavy ions to provide beams of maximum energies around 45 GeV/nucleon for Ne^{10+} and close to 35 GeV/nucleon for U^{92+} with intensities up to 10^9 ions/s. Such beams will be used, in particular, for dense nuclear matter studies by the CBM experiment.

The heavy ion beams coming out of the SIS100 can be directed on the rare isotope or antiproton production targets. After selection of the isotopes in the fragment separator (Super-FRS), the secondary rare isotope beams can be directly used or conducted to the storage and cooling rings (CR, RESR, NESR), where various nuclear physics and astrophysics experiments can be performed.

Antiproton beams are collected, accumulated and cooled in the CR/RESR storage ring combination. Antiprotons with energies up to 3 GeV are then conducted to the NESR for further cooling and decelerating in view of low energy antiproton experiments. Higher energy antiprotons enter the High-Energy Storage Ring (HESR) which will provide cooled antiproton beams with energies between 0.8 GeV and 14 GeV, as will be discussed in the section1.1.4.

1.1.3 International context

The proposed concept for the new GSI facility involving a very broad range of research programs and a correspondingly versatile and highly sophisticated accelerator and storage ring system is really unique. Although there exists no project that has full overlap or competes directly with FAIR, it is interesting to have a look at the international context in the different research fields:

Concerning dense plasma research, a high energy (Kilojoule) and high power (Petawatt) laser system (PHELIX) will be installed at FAIR. Combined with the intense ion bunches with Terawatt power, it will allow unique studies in dense plasma physics. The TWAC (TeraWatt power Accelerator) project underway at ITEP, Moscow will provide heavy ion beams with similar caracteristics as FAIR, however limited to ions lighter than Cobalt and with no combination with lasers.

In the field of nuclear structure with radioactive ion beams, an ISOL-type facility is dis-

cussed by the european ISOLDE collaboration. This technique is advantageous for the production of isotopes in the vicinity of the stable isotopes and is therefore complementary to the in-flight technique chosen for the FAIR facility, which generates higher intensities for nuclei far-off stability. Meanwhile, the quality and diversity of available radioactive beams will be improved thanks to different smaller scale projects in Europe, among which SPIRAL-2 at GANIL is the most ambitious. The effort for developing radioactive beam facilities is worldwide. In Japan, the Radio Isotope Beam Factory (RIBF) at RIKEN, based on in-flight fragmentation, but with limited intensities is starting to deliver beams, and in USA a Rare Isotope Accelerator (RIA) also based on in-flight fragmentation has been proposed.

The studies of high-density nuclear matter will be complementary to the investigations at very high temperatures of the transition of nucleonic matter to quark-gluon plasma, which is explored presently at RHIC and starts at LHC with the ALICE detector.

Concerning hadronic physics, the highest energies are actually covered by HERMES and COMPASS facilities, suited to study the proton spin structure and perturbative QCD processes. Different projects of electron-ion colliders are currently discussed in Europe (ENC using FAIR, LHeC using LHC) or in the United States (eRHIC using RHIC and ELIC using JLab 12 GeV) in order to access different kinematical ranges and get a very precise "'tomography"' of the nucleon at different scales. The physics program of the multi-purpose 50 GeV proton beam facility J-PARC, which is starting to deliver beams at Tokai in Japan is focused at the moment on strangeness nuclear physics and hadronic physics with neutrino beams. However, it can also bring information in other hadronic physics field, like exotic hadron searches, structure functions or hard exclusive processes.

In the last years, several e^+e^- colliders have been intensively used for baryon spectroscopy and rare decay studies. Among them, CESR at Cornell ($\sqrt{s}$ = 3.5-12 GeV) was first used for b and then for c-quark physics, the B-factories PEPII at Stanford and KEKB in Japan were operated at a center of mass energy of $\sqrt{s}$=10.58 GeV, suited for $\Upsilon(4S) \to B\bar{B}$ studies. CESR and PEPII are now shutdown, but KEKB is very active and has just increased its luminosity by a factor 2, reaching the world record of 2 10^{34}cm^{-2}s^{-1}. The Super-KEKB project with final luminosity of 8 10^{35}cm^{-2}s^{-1} will make a new breakthrough allowing high precision matter-antimatter studies. The studies for a SuperB-factory at Rome with even higher luminosity (10^{36}cm^{-2}s^{-1}) have also started. The B-factories are operated at energies higher than FAIR, where the maximum will be $\sqrt{s}$=5.46 GeV. However, using the Initial State Radiation process, the effective center of mass energy of the e$^+$e$^-$ pair can be reduced, to study for example the nucleon time-like electromagnetic form factors, as will be discussed in Sec. 5.4.

Using lower beam energies, the BEPCII, a very recent upgrade of the existing BEPC facility at Bejing, covers the region $\sqrt{s}$= 2 - 4.4 GeV with focus on the study of the charmed resonances. DAPHNE at Frascati ($\sqrt{s}$=1.02 GeV) is designed for Φ meson studies. With the DANAE project, the energy could be flexible with $\sqrt{s}$ up to 2.4 GeV and the luminosity could be increased, reaching 10^{33}cm^{-2}s^{-1} at $\sqrt{s}$=1 GeV and 10^{32}cm^{-2}s^{-1} at $\sqrt{s}$=4.8 GeV. This project is however not supported at the moment. At Novosibirsk, the facility VEP-2000 started producing data, with a luminosity of 10^{32}cm^{-2}s^{-1} and a maximum center of mass energy of $\sqrt{s}$= 2 GeV. The physics program at VEP-2000 is focused on hadron production cross section, light vector meson spectroscopy, and time like nucleon form factors near threshold. In the kinematical region below or close to $N\bar{N}$ threshold, which is unaccessible to FAIR, the new machines BEPCII, VEP2000 or possibly DANAE, can provide complementary measurements. This is particularly true for the time-like nucleon electromagnetic form factor measurements, as will be discussed in more details in Sec. 5.4. However, the FAIR energy domain extends up to much higher values, ranging from $\sqrt{s}$= 2.24 GeV to $\sqrt{s}$= 5.46 GeV,

which is really unique and opens an extremely large variety of measurements.

Concerning fixed target experiments at lower energies, both lepton or photon facilities, like MAMI, ELSA, JLab, Bates and hadron machines like CELSIUS and COSY are presently used. This complementarity will still be exploited in the farther future and the electron beam at JLab12GeV and the antiproton beam at FAIR will both play a major and complementary role in the study of the nature of confinement, for example through the search for exotic mesons and the study of the nucleon structure.

1.1.4 Antiproton beams in the High Energy Storage Ring

The antiproton production rate is $2 \ 10^7$/s. After stochastic cooling in the CR ring and collection in the RESR ring, the 3.8 GeV/c antiprotons are injected by bunches of 10^{11} in the HESR. After pre-cooling, they are accelerated or decelerated to the desired momentum. At the highest momenta, the main origin of luminosity loss during the cycle are the hadronic interactions in the target, which only slightly depend on the beam momentum, while at lower momenta, the Coulomb interaction contribution is also important. The combination of both effects yield beam lifetimes of the order of 30 mn at 1.5 GeV/c and 2h at 15 GeV/c.

Taking into account these losses, a luminosity of $1.6 \ 10^{32}$cm^{-2}s^{-1} averaged over one cycle in the storage ring can be obtained at 15 GeV/c, and $0.7 \ 10^{32}$cm^{-2}s^{-1} at 1.5 GeV/c, with a target thickness of $4 \ 10^{15}$ atoms/cm^2, which is the goal to reach with the pellet target.

Electron cooling is provided for antiprotons up to 8 GeV and stochastic cooling between 3 GeV and 14 GeV. Two different operation modes are foreseen for the HESR: the high intensity mode, which will provide a luminosity of $1.6 \ 10^{32}$cm^{-2}s^{-1} with a beam momentum resolution $\delta p/p$ of 10^{-4}, and the high resolution mode, limited to a maximum energy of 8 GeV, using electron cooling and a luminosity of 10^{31}cm^{-2}s^{-1}, to reach momentum precisions down to 10^{-5}.

The experimental equipment includes an internal target and the large PANDA in-ring detector which will be described in the next subsection, while an option for the use of polarized antiproton beams is also studied.

1.2 The P̄ANDA physics program

The international P̄ANDA collaboration counts more than 400 physicists from 55 institutions in 17 countries. The most numerous are the german, italian and russian physicists. The french group counts, in 2009, 8 permanent physicists, one PhD student and one post-doc.

The intense antiproton HESR beams are a very powerful tool for the study of hadronic physics. The range of energies allows for the production of strange and charmed mesons and baryons and the production of gluonic excitations, as illustrated in fig. 76. A major part of the physics program therefore consists in collecting high precision data about hadronic states to understand the manifestations of QCD in the non perturbative regime, in line with the questions addressed in the introduction. In particular, one fundamental question is to understand the origin of confinement of quarks and gluons in hadrons. We give below some examples of the main topics of the very broad physics program:

- QCD states spectroscopy:

  The goal is to perform high precision charmonium ($c\bar{c}$), D meson and baryon spectroscopy. Below the $D\bar{D}$ threshold, at 3.73 GeV, most of the predicted states have been observed in experiments at e$^+$e$^-$ colliders (Cornell, SLAC, BES, KEK,...) or in p̄p reactions at Fermilab. However, while the precision on the measurement of the triplet
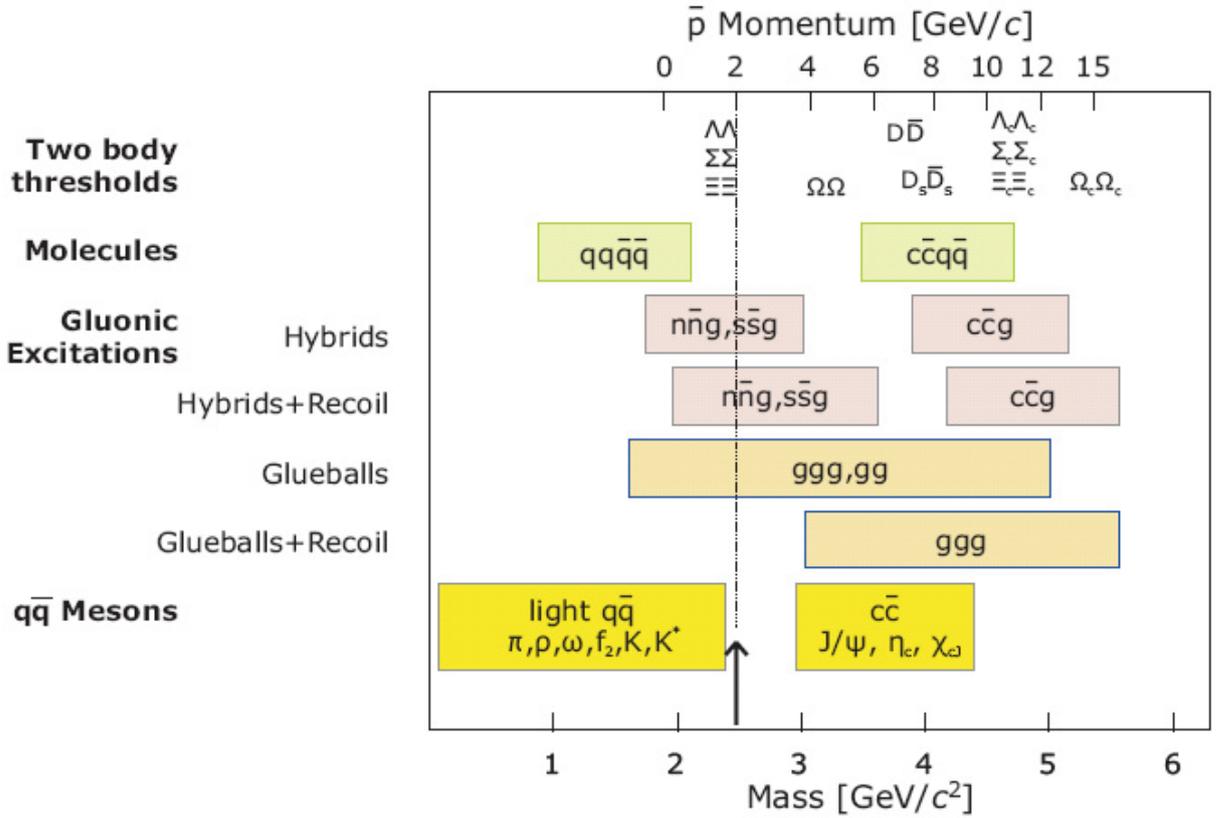
Figure 76: Schematic list of hadrons accessible at the HESR with antiproton beams. The upper (resp. lower) scale indicates the antiproton beam momentum and the lower scale the mass of the hadrons. The arrow shows the maximum energy available at the former LEAR antiproton ring at CERN

.

states (J/ψ, χ_{c0}, χ_{c1}, χ_{c2}) is very good, this is not the case for the singlet states (η_c, h_c) for which better measurements of the masses, widths and branching ratios are needed.

The region above the $D\bar{D}$ threshold has been less explored and some predicted states have to be observed and precisely measured. As already said, a significant advantage of the $\bar{p}p$ reaction with respect to e^+e^- reactions is that states of quantum number other than 1^{--} can be directly produced.

In addition, $\overline{P}ANDA$ will look for exotic states, such as gluonic hadrons (hybrid and glueballs), multiquark and molecular states. Such measurements are important to test the predictions concerning the particle spectra of models, such as non-relativistic potential models, effective field theories and Lattice QCD. The $c\bar{c}$ sector is more suitable for this study than the light quark sector studied so far, since the $c\bar{c}$ states are narrow and relatively far from each other, hence reducing possible overlaps. The overlap is fully avoided for states which have J^{PC} quantum numbers forbidden for ordinary $q\bar{q}$ states. Such states are called exotic states and can be produced in $\bar{p}p$ collisions in association with another meson (production reaction), while "ordinary" states can be produced alone (formation reactions). Hence, the $\overline{P}ANDA$ program for exotic search foresees to start with production measurements at the highest antiproton momentum (15 GeV/c), with the aim of studying all possible production channels of exotic and ordinary channels. The second step would consist of formation measurements by scanning the antiproton energy in small steps in the regions where promising candidates

have been observed. Taking benefit of the high resolution mode and of the high cross-sections an unambiguous determination of quantum numbers can be obtained, as well as a precise determination of masses and widths of the states under study.

- Non perturbative QCD dynamics:

  Hyperon pair production reaction $\bar{p}p \to \bar{Y}Y$, which can be studied for hyperons with different flavours, are suitable to study the mechanism of quark-antiquark pair creation and their rearrangement into hadrons.

- Study of hadrons in nuclear matter

  Partial chiral symmetry restoration in hadronic matter is expected to modify the properties of mesons in nuclear matter. So far, such effects have been explored for mesons in the light quark sector. Using collisions of the 15 GeV/c $\bar{p}$ beam on nuclear targets, it will be also possible to explore the effects on the charmed mesons, for which the modifications are expected to be due primarily to the gluon condensate.

- Hypernuclear physics:

  Efficient production of hypernuclei with more than one strange hadron will be possible and will open new perspectives for nuclear structure spectroscopy and for studying the interactions between hyperons and nucleons.

- Electromagnetic processes

  $\bar{\text{P}}$ANDA will be able to investigate the structure of the nucleon using electromagnetic processes, such as Deeply Virtual Compton Scattering (DVCS), and the process $\bar{\text{p}}\text{p} \to \text{e}^+\text{e}^-$ which will allow the determination of the electromagnetic time-like form factors of the proton in an extended q^2 region. These topics will be discussed in more details in sec. 3 and sec. 5.

- Electroweak physics

  The goal here is to take advantage of the high number of produced D-mesons to investigate their rare weak decays in order to test the Standard Model predictions and alternative models.

1.3 The $\bar{\text{P}}$ANDA detector

Such a wide physics program can only be accessed by a general purpose detector. One important goal is to achieve almost full hermiticity. The detector has to be able to measure momenta with good resolution and identify charged particles down to momenta of 100-200 MeV/c and photons from 10 MeV in almost full solid angle. A vertex detector is required since many channels include narrow D mesons(for example D$^+$(1869) with c$\tau \sim$312 μm). The possibility to use different targets and the capacity to stand the very high rates produced by 10^7 $\bar{\text{p}}$p collisions per second are additionnal requirements. A key component is the Electromagnetic Calorimeter to identify electrons and photons, with the unique demand for a very broad dynamics, from 10 MeV to 10 GeV. As shown on fig. 77, the general layout of the $\bar{\text{P}}$ANDA detector is based on two magnetic spectrometers. The target spectrometer, with superconducting solenoid as analyzing magnet, surrounds the interaction region, in an onion shell-like arrangement of detectors. The forward spectrometer consists of a large gap dipole in combination with tracking detectors and calorimeters suited for the most energetic forward emitted particles. Only a short description of the different detectors is given here and we
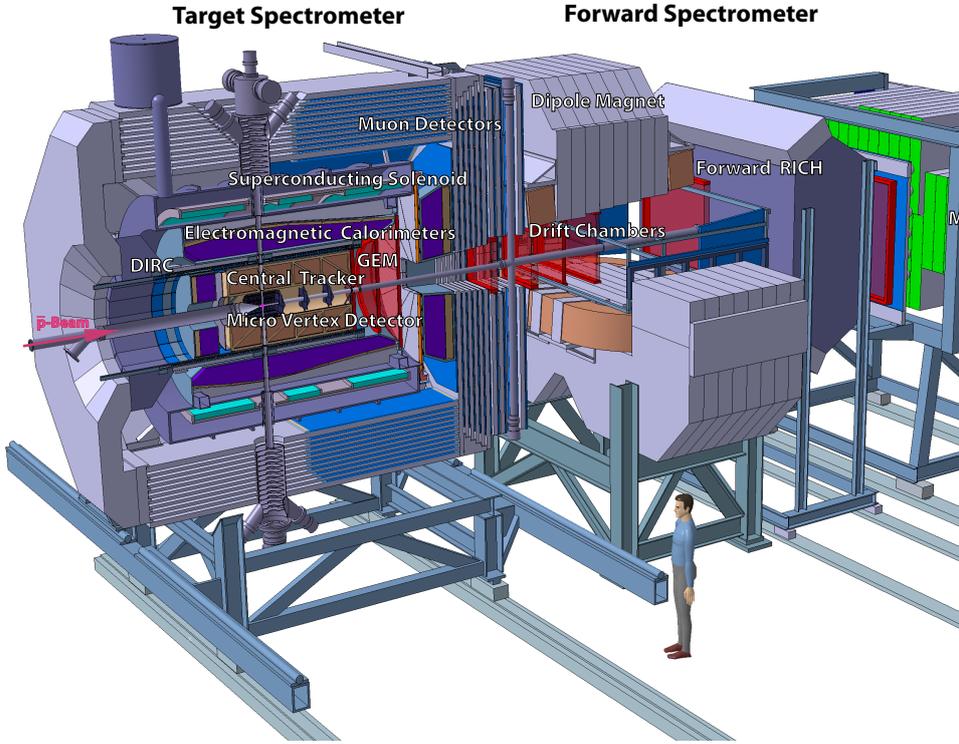
Figure 77: Side view of the PANDA detector

refer to [136] for more details, as well as to the technical design reports[137] which have been written for the different detectors.

1.3.1 The Target Spectrometer

The target spectrometer has the shape of a barrel surrounding the target. Its design is compact, in order to reduce the costs, and apart from the pipes necessary for the injection of the target material which are perpendicular to the beam line, it presents an almost perfect cylindrical symmetry.

- Target: In order to reach the design luminosity of $2 \cdot 10^{32} \text{cm}^{-2}\text{s}^{-1}$ at 15 GeV/c, a target thickness of about $4 \cdot 10^{15}$ hydrogen atoms per cm^2 is necessary. Two different techniques are developed for this internal target: the cluster-jet target and the pellet target. In the cluster jet target, clusters of hydrogen molecules are produced in the expansion of pressurized cold hydrogen gas into vacuum forming a very diluted, homogeneous target. The advantage of this technique is the stability in time of the density profile. The luminosity foreseen with this technique is at the moment 10^{15} hydrogen atoms per cm^2, i.e. below the requirements.

  The pellet target is a stream of frozen hydrogen micro-spheres traversing the beam transversally with a velocity of about 60 m/s. This technique provides the desired average luminosity, its drawback is however the variable interspacing ($\sigma \sim$ 0.5-5 mm), leading to counting rate fluctuations, which the current R&D aims at reducing.

  Both techniques allow the use of heavier gases, like deuterium, nitrogen or argon.

- Magnet: The superconducting solenoid has an inner radius of 90 cm and a length of 2.8 m. It will be operated at a maximum field of 2 T. The homogeneity of the field is expected to be better than 2 % and the transverse component very small ($\int B_r/B_z \, \text{d}z$ < 2 mm, for a 2 m long trajectory).

- The Micro Vertex Detector: The main goal of this detector is the detection of secondary
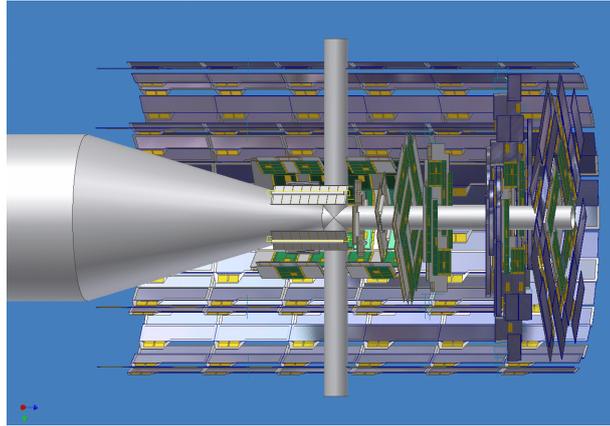
Figure 78: Side view of the Micro Vertex Detector

vertex from D and hyperon decays, but, combined with the central and forward trackers, it will also enhance the momentum resolution. It is based (fig. 78) on radiation hard silicon pixel detectors and silicon strip detectors. The barrel part consists of four layers, with an inner radius of 2.5 cm and an outer radius of 13 cm, while eight detector wheels arranged perpendicular to the beam achieve the best acceptance for forward emitted particles.

- The Central Tracker: The requirements are to stand the high-flux, to provide a momentum resolution at the % level at 1 GeV/c and to identify secondary vertices for decays which can occur outside the MVD (e.g. K_S^0 or Λ). Energy loss measurements will also improve the particle identification, which is needed, especially in the case of electron/pion discrimination. The central tracker will consist in a barrel part, for which two options are still open, the Straw Tube Tracker (STT) and the Time Projection Chamber (TPC), and a forward part consisting of three sets of GEM trackers.

    - The Straw Tube Tracker (STT) option:
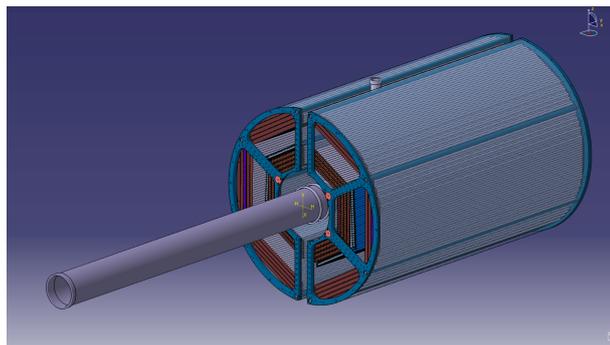
Figure 79: The Straw Tube Tracker.

This detector consists of aluminized mylar tubes ("straws"), which are self-supporting by the operation at 1 bar overpressure of Argon/CO_2. The straws have a diameter of 10 mm, the mylar foil is 30 μm thick and the wires are made of 20 μm thick gold-plated tungsten. The wires are arranged in 24 planar layers, which are mounted in

76

a hexagonal shape around the MVD, as shown in fig. 79. The eight most central layers are tilted in order to measure the z coordinate with a resolution of about 3 mm. The resolution in x and y is expected to be 150μm. Additionnal straws are added to fill the gap to the surrounding detectors in such a way that in total the STT consists of 4200 straws covering radial distances from 15 to 42 cm from the beam axis and with an overall length of 150 cm. Time and amplitude signals will be measured for each straw.

– The Time Projection Chamber (TPC) option:
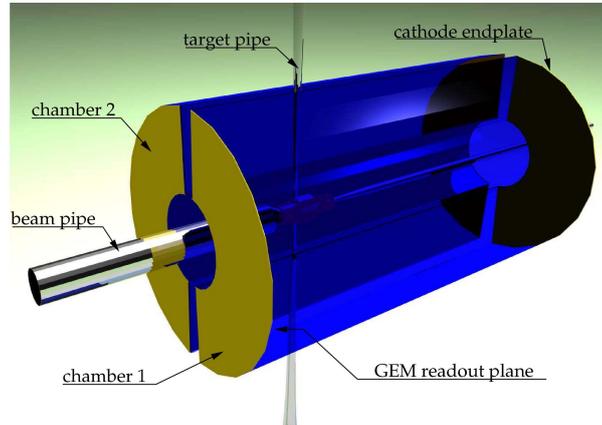
Figure 80: The Time Projection Chamber.

The TPC is a challenging option providing better position resolution and identification capabilities through energy loss measurements. A schematic view of the TPC is shown on fig. 1.3.1. It consists of two large gas-filled half-cylinders around the target and beam pipe and surrounding the MVD. Due to the effect of the electric field along the cylinder axis, the electron drift towards the anode at the upstream end face and create an avalanche detected by a pad read-out plane. This yields information on two coordinates, the information on the third one comes from the measurement of the drift time of each primary electron cluster. GEM foils will be used for the amplification stage, since they are well suited for the suppression of backward flow of the ions produced by the avalanche, which is a major problem to handle, in order to avoid too large distortions of the electric field and of the electron drift.

– Gaseous Electron Multiplier Detectors: To complement the tracking for particles emitted at angles below 22°, where the expected counting rates are very high (up to 310^4cm^{-2}s^{-1}), gaseous micropattern detectors based on GEM foils as amplification stage have been chosen.

- Barrel DIRC: At polar angles between 22 and 140°, particle identification will be performed by the detection of internally reflected Cherenkov light produced in a 1.7 cm thick quartz slab. This DIRC device (fig. 1.3.1) is similar to the one previously used at BABAR, except for the imaging that will be achieved by lenses focusing onto microchannel plate photomultiplier tubes (MCP PMTs) instead of imaging through a large volume of water onto 11000 photomultipliers tube. The choice for $\bar{P}$ANDA is driven by the sake for compactness, the possibility to measure two spatial coordinates and the good time resolution.
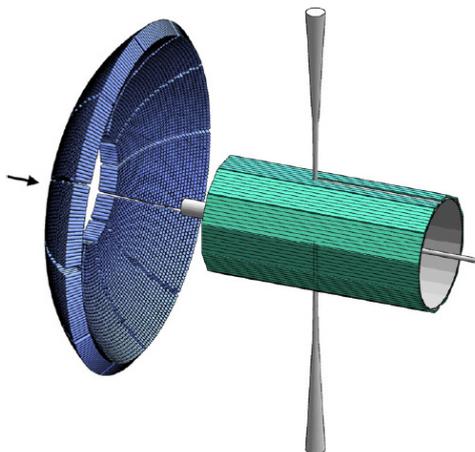
Figure 81: The DIRC detector.

- Forward endcap DIRC: A similar concept will be employed in the forward direction. The forward DIRC will consist in 2 cm thick disks of radius 110 cm, with mirrored rims allowing reflection on MCP PMTS.

- Barrel time of flight: Devices consisting of scintillator bars or of pads of multi-gap resistive plate chambers to be placed around the barrel part of the central tracker are studied. The constraint is to have good time resolution (50-100 ps) for hadron identification and small thickness in order not to degrade the resolution of the Electromagnetic Calorimeter. It has to be noted, that, due to the absence of start detector to avoid too large a material budget, only relative time of flight between the same particles of one event can be used.

- Electromagnetic Calorimeters : The expected high counting rates and the compact
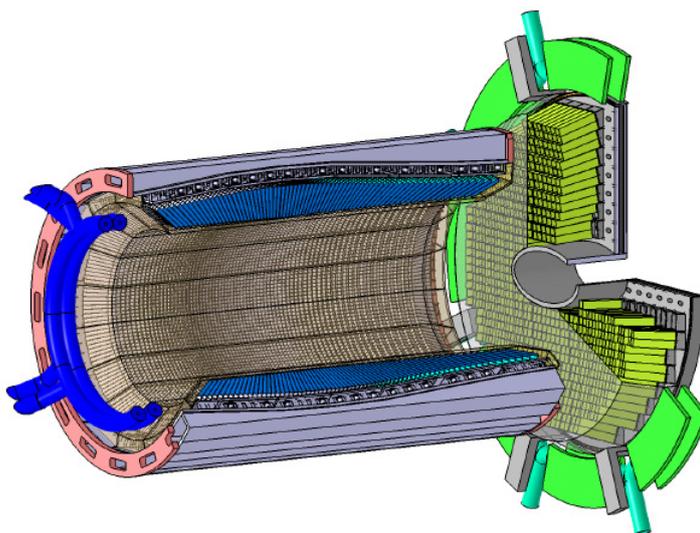
Figure 82: The Electromagnetic Calorimeter

design of the target spectrometer triggered the choice of the crystal material, namely lead tungstate (PbWO4), with a short decay time of 6 ns, a radiation length of 0.9 cm and a Molière radius of 2 cm. The detection of low energy photons down to a few

78

MeV is a challenge, that can be solved by taking special care of the crystal perfection and appropriate doping. In addition, the operation of the crystals at -25°C enhances the light yield by a factor 4 compared to room temperature. The crystals will be 20cm long, i.e. approximately 22 X_0, in order to achieve an energy resolution below 2% at 1 GeV. They will have a front size of 2.1x2.1 cm^2. This implies 11360 crystals for the barrel part of the calorimeter, at an inner radius of 57 cm, 3600 crystals for the forward end-cap and 592 for the backward end-cap, as shown in fig. 82. The read-out of each crystal will be accomplished by two rectangular section avalanche photo diodes in the case of the barrel and by vacuum photo-triodes for the forward and backward endcaps.

- Muon detectors: The principle is a segmentation of the yoke, which acts as an absorber, with interleaved tracking detectors, to measure energy loss processes and kinks from pion decays. In the barrel region, the yoke is segmented in a first layer of 6 cm iron followed by 12 layers of 3 cm thickness, with 3 cm wide gaps for the detectors. For the forward part, there will be within the door of the return yoke of the solenoid, five 6 cm thick iron layers and six detection layers. Moreover, a removable muon filter with additionnal five layers of 6 cm iron will be added between the solenoid and the dipole. As for the COMPASS experiment, rectangular aluminium drift tubes will be used, with additional capacitively coupled strips read out on both ends to obtain the longitudinal coordinate.

In addition, an hypernuclear detector, which comprises a specific active target system and a Ge-array as γ-detector can be added by removing the backward endcap of the calorimeter.

1.3.2 The Forward Spectrometer

The deflection of particle trajectories in the field of the dipole magnet will be measured with a set of wire chambers (either small cell size drift chambers or straw tubes), two placed in front, two within and two behind the dipole magnet.

- Magnet: The 1 m gap and 2 m aperture of the magnet, together with its position along the beam axis allow to cover an acceptance of ±10° in horizontal plane and ±5° in vertical plane. The maximum bending power of the magnet is 2 Tm, providing a deflection angle of 2.2 °, at the maximum momentum of 15 GeV/c. The detection of very low momentum particles, which will curl up inside the magnetic field, will also be possible, thanks to the two detectors inside the yoke opening.

  The beam deflection will be compensated by two correcting dipole magnets, placed around the $\bar{P}$ANDA detection system.

- Forward Trackers: Each chamber will have 1 cm wide drift cells and will contain three pairs of detection planes, one pair with vertical wires and two pairs with wires inclined by +10° and -10°, to reconstruct tracks in each chamber separately, and to handle multi-track events. The most central wires will be separately mounted on insulated rings surrounding the central holes, which are necessary due to the beam pipe. The expected momentum resolution is δp/p∼0.2% for 3 GeV/c protons and is limited by multiple scattering on the chamber wires and gas.

- RICH detector: The favoured design is a dual radiator RICH detector similar to the one used at HERMES and from which some elements will be reused. The two radiators are made of silica aerogel and C_4F_{10} gas, providing π/K/p separation in a broad momentum range of 2-15 GeV/c and electron/muon and pion identification at the lowest energies. The carcteristics of the different $\bar{P}$ANDA Cerenkov detectors are displayed in table6.

detector	material	refraction index	γ_{th}	minimum momentum (GeV/c)				
				e	μ	π	K	p
DIRC	fused silica	1.47	1.36	$5 \ 10^{-4}$	0.098	0.13	0.46	0.87
RICH	silica aerogel	1.0304	4.1	0.002	0.42	0.56	2.0	3.8
	C_4F_{10}	1.00137	19	0.01	2.0	2.67	9.4	17.9

Table 6: Caracteristics of the Cerenkov detectors for $\bar{P}$ANDA:material, refraction index, minimum Lorentz factor for light emission and corresponding momenta for the different particles.

- Time of Flight: A wall of slabs made of plastic scintillator placed about 7m from the target and read out on both ends by fast photo tubes will serve as time of flight stop counter. In addition, similar detectors will be placed inside the dipole magnet opening, to detect low momentum particles which do not exit the magnet. The relative time of flight between two charged tracks reaching any of the time-of-flight detectors (including the barrel TOF) will be measured. With the expected time resolution of σ=50 ps, π/K and K/p separation on a 3σ level will be possible up to momenta of 2.8 GeV/c and 4.7 GeV/c respectively.

- Forward Electromagnetic Calorimeter: A Shashlik type calorimeter, based on lead scintillators, with high resolution and efficiency will be employed for the detection of photons and electrons.

- Forward muon detector: This device is similar to the muon system of the target spectrometer, but laid out for higher momenta. It allows discrimination of pions from muons, detection of pion decays, and with moderate resolution, also the energy determination of neutrons and anti-neutrons.

1.3.3 Luminosity Detector

Elastic scattering at very low transfers is dominated by the easily calculable coulomb scattering. The principle of the luminosity detector is therefore to detect antiprotons in the range 3-8 mrad with respect to the beam axis, using a specific detector made of a sequence of four planes of double silicon strip detectors located as far downstream and as close to the target as possible. The reconstruction of the angle at the luminosity detector is mandatory, since the interaction point, in the case of the pellet target is not well defined. An absolute precision of about 3% is expected with the planned device.

1.3.4 Data acquisition

The PANDA approach differs substantially from existing systems often based on a hierarchy of different trigger conditions. Here, every sub-detector is an independant self-triggering device which selects data related to a particle hit for further processing. The trigger selection finally occurs in computing nodes which access the buffers via a high-bandwidth network. This concept provides a high degree of flexibility in the choice of trigger algorithms. However, it requires "intelligent" front-end electronics, allowing for efficient preprocessing , including noise suppression and hit clustering, as well as powerful computing units (FPGA, DSP,....), with large numbers of programmable gates to associate the different data fragments and achieve the event selection.

2 Technical contribution of IPN Orsay

The IPN detector R&D group is in charge of the mechanical and thermal studies for the barrel part of the P̄ANDA electromagnetic calorimeter, as well as its mechanical integration into the detector. The first important milestone in these R&D studies was the test of the PROTO60, which is a representative part of the barrel electromagnetic calorimeter, consisting of 60 tapered crystals, with close to final geometry. Before describing the proposed design and the tests of the prototype, we will discuss the choice of PbWO4 crystals and of avalanche Photodiodes.

2.1 Technological choices for the PANDA EMC

2.1.1 Crystals

PWO properties	
Density (ρ)	8.28 gcm^{-3}
Radiation length (X$_0$)	0.89 cm
Molière radius	2.0 cm
Energy loss (dE/dx) at MIP	10.2 MeV.cm^{-1}
Decay time	6 ns
Light yield (LY)	240 γ/MeV
dlnLY/dT	$\sim$ -2%($^\circ C)^{-1}$)

Table 7: Caracteristics of the PWO material.

The choice of PbWO4 (commonly called PWO) is first driven by its small radiation length, suited for a compact detector. The second advantage is the short decay time (6ns) for the main decay mode (dominant at 97%), which is needed, especially at the most forward angles, where high counting rates are expected. PWO crystals have however important drawbacks which will have consequences on the technological choices. First, the light yield at room temperature is very small (150 times less than NaI scintillators). It however increases rapidly with decreasing temperature, therefore the crystals will be operated at a low stabilized temperature of -25°, which will allow for an increase of the gain by a factor 3.

P̄ANDA will use 2nd generation PWO (PWOII), doped with a few ppm of Lanthanum and Ytrium, which increases the light yield by 80% with respect to the PW0 crystals used by CMS. However, the variation with temperature is then 50% higher, which makes more severe demand on the stabilization.

Another drawback of the PWO crystals is the sensitivity to radiation which is still the subject of studies inside the P̄ANDA collaboration.

2.1.2 Avalanche Photodiodes

Avalanche Photodiodes are well suited to provide a good quality electric signal for low light yield and their photosensitivity and quantum efficiencies are good at the wave length of PWO emission light (420 nm). They can also be used inside a magnetic field and have low energy consumption and are relatively compact. However, the gains are small (typically of the order of 100), with same temperature dependence (dlnG/dT $\sim$ -2 %($^\circ$C)$^{-1}$) as the light yield in the crystals, and further amplification of the signal is therefore needed.

2.2 Mechanical Studies

Considering the weight of the barrel calorimeter, about 12 t, it is easy to understand that the mechanical support of this device is a challenging task. It is made even more difficult due to the requirements of minimizing the interstices and material width while optimizing the mechanical precision. The proposed design consists in 16 "slices" of 720 crystals each, each being attached to the magnet (fig. 82 and fig. 83).
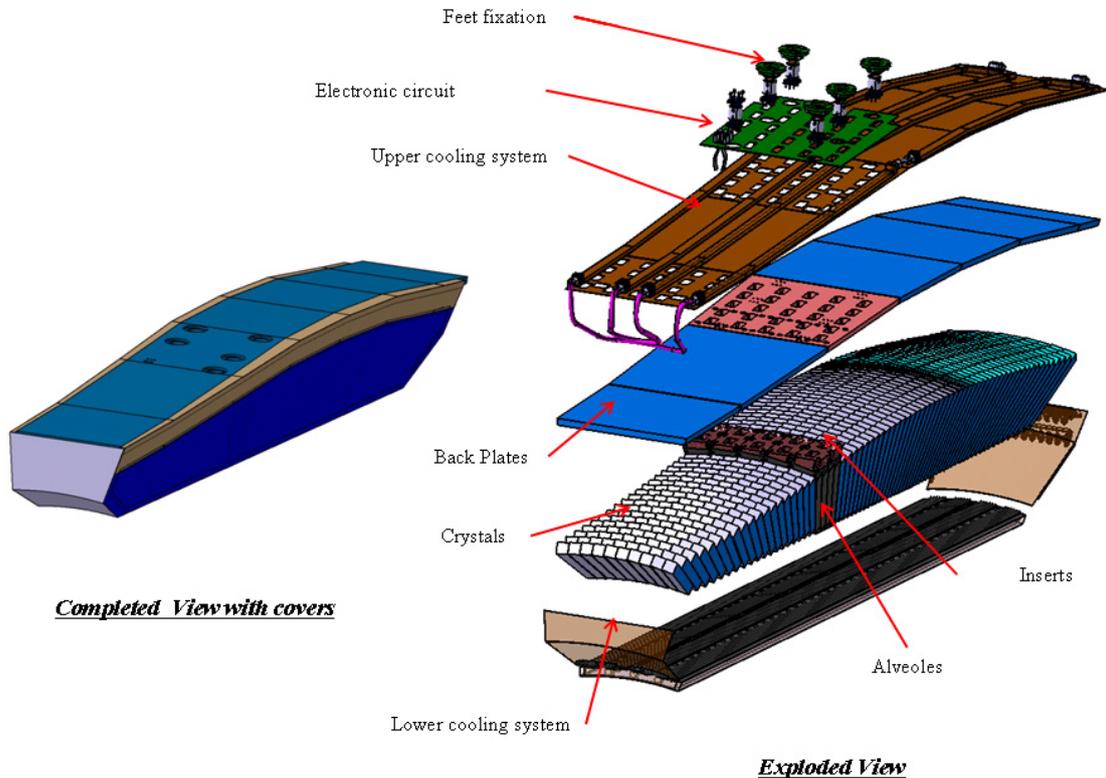
Figure 83: Exploded view of one "'slice"' (1/16 th) of the barrel electromagnetic calorimeter
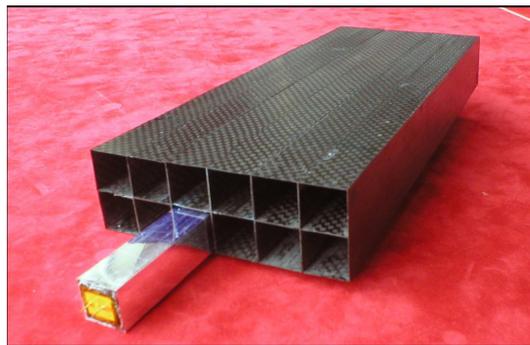
Figure 84: Carbon alveoles and one PWO crystal

In the chosen geometry, the crystals are not pointing towards the target position. A tilt of 4° is indeed added at the level of each slice, in the transverse plane and at the level of each crystal in the radial plane, in order to avoid the possibility of photons travelling through the interstices between the crystals. To reduce as much as possible these dead zones, 11 types of crystals have been designed, with rear face edge varying from 24.35 mm to 29.04 mm. The crystal length is 200 mm=22 X_0 , to stop most of the photons produced in the electromagnetic

showers produced by photons and electrons up to 15 GeV. The crystals have a trapezoidal shape, with front face section 21.9x21.3 mm^2, i.e. in the order of the Molière radius, to keep the most important part of the shower inside one single crystal.

The crystals, wrapped with VM2000 reflector, are inserted by groups of four in 200 μm thick carbon alveoles (fig. 84) tightened to Al inserts located at the back side of the crystals with a total distance of 680 μm between two adjacent crystals. The inserts are then fixed on the backplates of each slice (fig. 83), which are themselves screwed on the magnet.

The mechanical stability of the system of alveoles and inserts has been first tested with brass crystals, with same shape and approximately same weight as the PbWO4 crystals. A deformation of around 100 μm has been measured for 10 kg load, which fulfills the requirements. The concept has then been used for the construction of the 60 crystal prototype, as will be discussed in sec.2.4.1.

2.3 Thermal studies
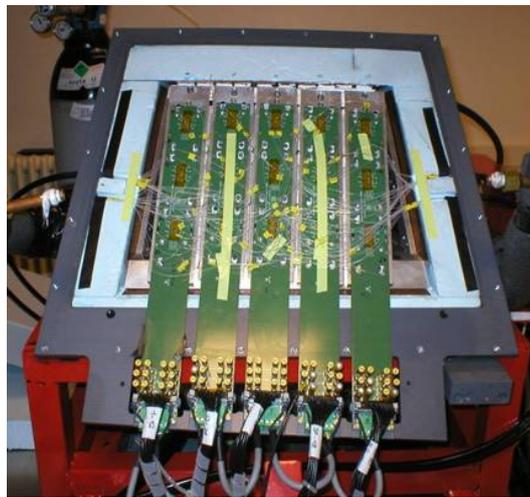
Figure 85: View of the back of the PROTO60 and read-out electronics
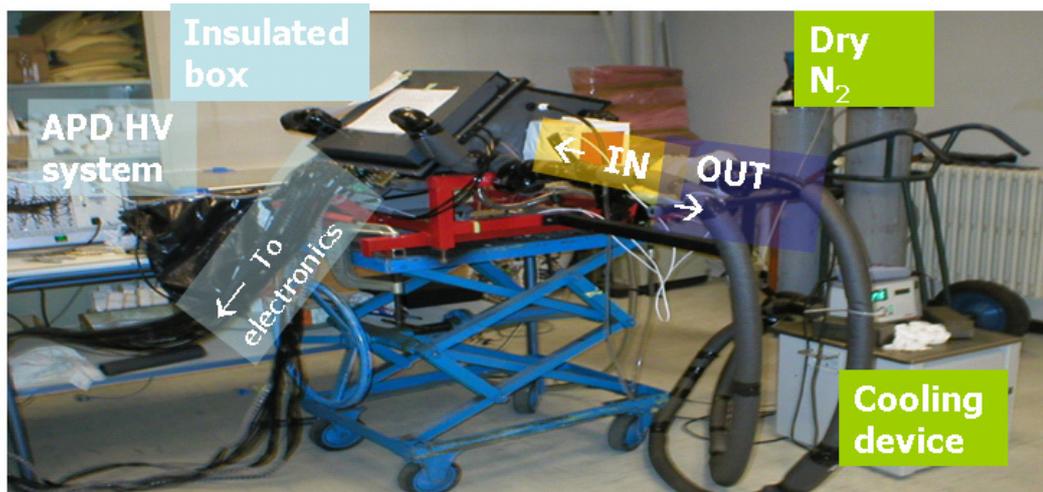
Figure 86: Set-up for the test of the PROTO60 prototype with cosmics at IPNO

The thermal aspects are also very challenging, since the crystals have to be operated at -25^{0}C, with a stability of $\pm 0.1^0 C$, to obtain a high and stable gain. This is quite important,

since the number of misidentified charged pions depends to a large extent on the precision of the energy reconstruction in the electromagnetic, as we will see in sect.4.8.

Each slice, corresponding to 1/16 th of the calorimeter will be a closed volume cooled to -25° and filled with dry N_2 (fig. 83). The presence of water has indeed to be excluded to avoid the formation of ice. Insulating is achieved by foam for the back side of the crystals (upper side of the slice) and by a thin shield made of carbon fiber and vacuum super-isolating foil to reduce the material budget in front of the crystals. The liquid coolant presently used for the tests is a water-methanol mixture. For the use at a larger scale in the future, it will be replaced by a polymer to fulfill security criteria. The heat conduction to the crystals will be ensured by copper tubes and plates surrounding the slice.

A rather powerful cooling machine will be required, since the effective cooling capacity to operate the whole system at -25°C is estimated to $\sim$ 3.3 kW. The expected time to reach the final temperature is several tens of hours, due to the low thermal conductivity of the PWO material.

The stability of the temperature will be controlled by sensors glued on the crystals. A major issue is the heat flux produced by the electronics, especially the APD's which are directly glued on the crystals and receive heat from the preamplifiers.

The thermal concept has been tested with the 60 crystal prototype (see next section) for which an insulated plastic box has been built. The tests demonstrate a stability of $\pm0.01°$ for the inlet coolant and ±0.05 °C for the crystals, with no sensitivity to room temperature variations ($\Delta T = \pm10°C$ between day and night).

However, the design of the electronics was changed in the meantime and the preamplifiers in the new design are only about 4 cm away from the APD's. According to the models, the corresponding APD temperature increase will be of the order of 0.7^0C. On-line calibrations to correct the change of the APD gain will then be necessary and the non-uniformity of the crystal temperature will also have to be taken into account.

2.4 Tests of the prototype

2.4.1 Tests with laser and cosmics

The PROTO60, a prototype of 60 crystals (6 rows of 10 crystals) has been built at IPN Orsay as a representative part of the barrel calorimeter and was tested using a dedicated electronic and acquisition system. Fig. 85 shows the rear face of the 60 crystal block before mounting the cover plate. One can notice the optical fibers which inject light pulses from a LED-pulser individually into each crystal and the printed boards connected to the preamplifiers, which are themselves connected to the rear face of the Avalanche Photodiodes. The PROTO60 has been tested with laser light and cosmic rays at IPN at -25^0C using the set-up shown on Fig. 86. With the light generator, the response and stability of the whole electronic chain can be checked. The high voltages for the operation at -25°C have first to be determined, starting from the values given by the constructor for the operation with a specific gain at 20°C. This is achieved by adjusting the high voltage to get the same response to the light generator than with the nominal voltage at 20°. This tension is about 350 V for a gain 50 at -25^0C. However, the light signal cannot be used for the individual calibration, since the quantity of light injected in each crystal cannot be made exactly equal.

The trigger for the acquisition of cosmic events was obtained by a coincidence between a crystal in the upper row and a crystal in the lower row (fig. 87). The energy deposit in one crystal is shown for events traversing a whole column of crystals on top right part of fig. 88. Bottom left of fig. 88 shows the pedestal correponding to the noise measured, when the column of crystals is not traversed. The cosmic and pedestal peaks are fitted with a
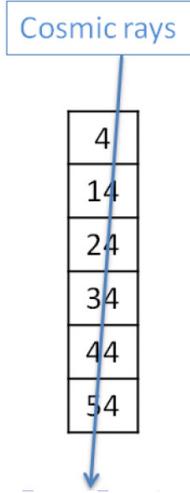
Figure 87: Sketch of the selection of cosmic events traversing one column of crystals.
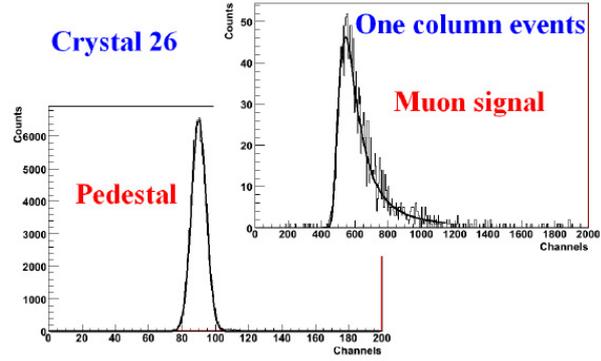
Figure 88: Energy deposit in one crystal for cosmic events. Top right (respectively bottom left): events traversing (respectively not traversing) the column of crystals are selected.

Landau and a gaussian distribution respectively to determine their mean positions. A linear calibration of the measured response is then provided using an estimated energy deposit in the crystal of 24.8 MeV, deduced from the most probable energy loss for cosmic event in PbWO$_4$ of 10.2 MeV for the average thickness of 2.43 cm. However, as it was also found by the CMS collaboration, the precision of this calibration is expected to be not better than a few % due to the combination of several effects, such as, the variation of crystal section, the energy and angular distribution of cosmics. Simple simulations [138] have shown that the main effect is due to the angular distribution, although it is very much reduced by the specific "vertical" trigger. Such simulations could be continued to get a more precise calibration. The detector is now used in a different configuration, with the axis of the crystal along the vertical direction. The goal is to increase the path length of the muons in each crystal in order to get a better precision on the calibration by cosmic events.

2.4.2 Tests with a photon beam at MAMI

The PROTO60 has been tested at the MAMI-C facility in Mainz using tagged photon beams with 15 energies between 189 MeV and 1441 MeV. Fig. 89 displays the energy deposit spectra obtained in the central crystal. While in the top corner spectrum, no selection is applied, the bottom corner spectrum is the superposition of the response for each incident photon energy.

Calibrated energy spectra are then produced, using the calibration provided by cosmic events (see sec.2.4.1). More than 80% of the incident photon energy is deposited in average in the central crystal and the sum of the energies in the 60 crystals amounts to 96% in average of the incident photon energy. This total energy distribution is then fitted by a Gabler function, defined as following:

$$G(E) = \exp\left[-2.7726\left(\frac{E-E_0}{\lambda_2}\right)^2\right] \tag{19}$$

$$if\,E > E_0,\ f(E) = NG \tag{20}$$

$$if\,E < E_0,\ f(E) = N\left(G + (1-G)\exp\left[\frac{E-E_0}{\lambda_1}\right]\right), \tag{21}$$

with adjustable parameters N,E_0,λ_1,λ_2. The reconstructed energy E_0 is compared to the
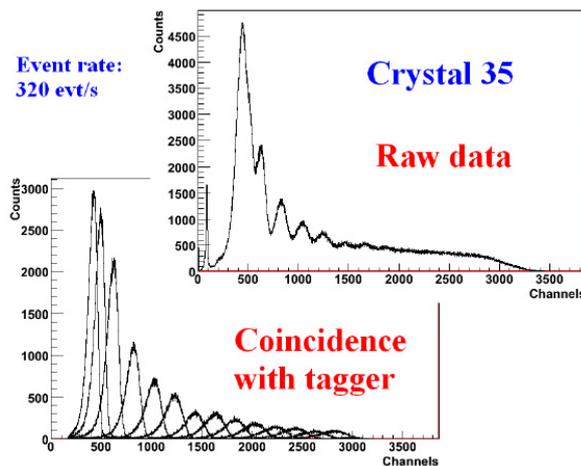
Figure 89: Energy distribution measured in one crystal without any selection on photon energy (top right), superposition of the distributions corresponding to each photon energy (bottom left)
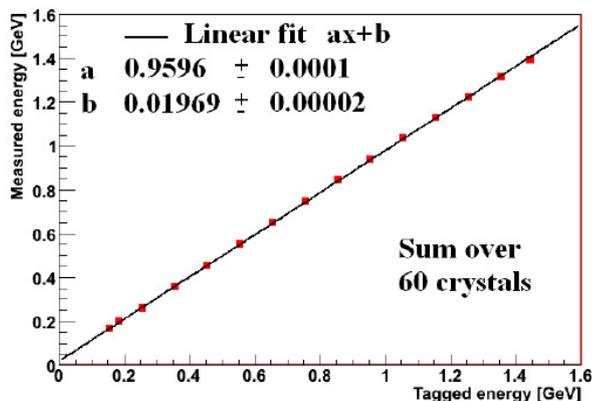
Figure 90: Measured energy in the PROTO60 after calibration wit cosmics as a function of the tagged photon energy.

photon energy on fig. 90, which allows to check the calibration as well as the linearity of the response over the whole range of energies provided by the tagged photon beams. This shows that, with the calibration performed with the cosmic rays, the photon energy can be reconstructed with a precision of few %.

The resolution σ_E is defined using the variance of the Gabler function and the following dependence is obtained as a function of the energy: $\sigma_E/E = 1.98\%/\sqrt{(E)} \oplus 1.31\%$ (fig. 91). The resolution is therefore 2.4 % at 1 GeV. Considering the rough calibration, it can be considered as consistent with the expected value of 2% at 1 GeV [136].

The effect on the resolution of changing the energy threshold in each crystal has also been studied. As expected, the sensitivity is maximum at low energy, since with a too low threshold, a significant noise contribution might be added to the signal, and with a too high threshold, the signal itself might be affected. The best resolution is found at low energies for a threshold value of 0.75 MeV, although the sensitivity is very small (as an example, at 160 MeV, the resolution is changed from 5.3% to 5.7% when putting the threshold to zero).

These results have been obtained for the most favorable case of an impact of the photon beam in the center of the central crystal of the prototype. When moving the beam to the edge of the crystal, an increase of the resolution of 0.6 % (in absolute value) was obtained,
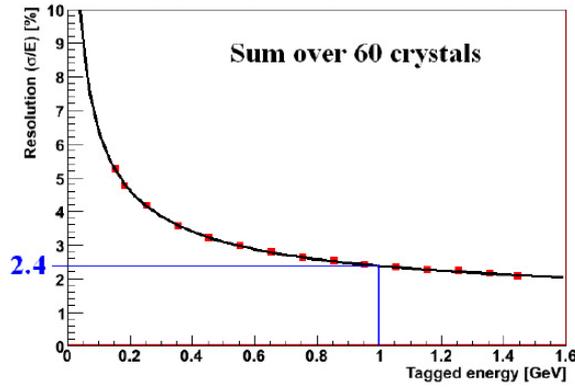
Figure 91: Resolution of the photon energy reconstruction in the PROTO60.

which has to be further investigated in order to understand the effect of dead zones on the signal reconstruction.

To reach the needed calibration precision (of a few per mille) over a very broad range of energies for the future experiments, the use of physical events will be necessary. The calibration of energy deposit by electrons at a given momentum will be checked using the momentum reconstruction in the tracking device. Some physics channels can also be exploited. This is the case when the exit channel is fully constraint by kinematics. The decay of π^0 in two γ's is an obvious source of photons in a wide energy range and in the binary process $\bar{p}p \to \pi^0\pi^0$, the strong kinematical constraints on the π^0 energies can be exploited for the calibration. The leptonic decay $J/\psi \to e^+e^-$ (BR=6 %) can also be used to check the energy reconstruction of electrons.

2.5 The 480 crystals prototype
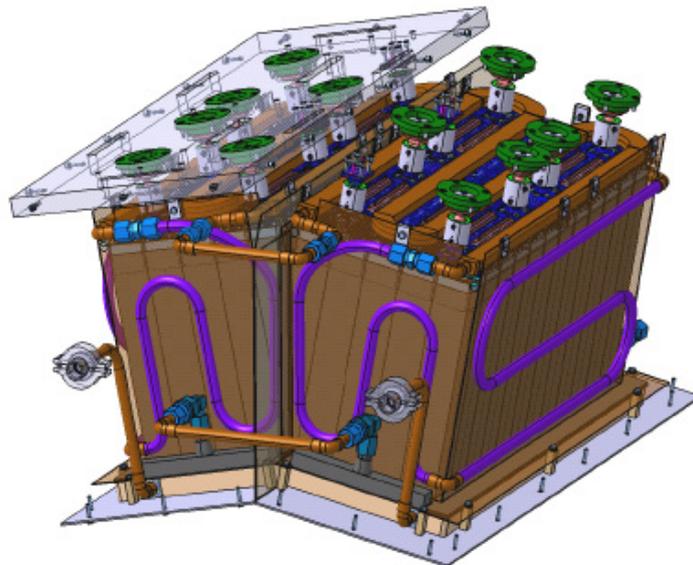
Figure 92: The 480 crystals prototype

The next step is now the test of a 480 crystals prototype made of two adjacent blocks of

240 crystals (fig. 92). This will allow to test on a larger scale the thermic concepts already validated with the PROTO60 and, in addition, to study the problem of heat transport between two adjacent slices.

Then, the construction of a slice of 720 crystals (fig. 83) will allow final tests on a larger scale.

The ultimate goal is the participation to the construction of the $\bar{\text{P}}$ANDA detector, which could consist of the mechanical and thermal design of the barrel electromagnetic calorimeter, as well as its integration in the $\bar{\text{P}}$ANDA detector.

3 Nucleon electromagnetic form factors

This section presents the experimental and theoretical context of the proposed measurement of proton form factors. It results from bibliography work, from informations obtained at the EINN09 and HADRON2009 conferences and from helpful discussions with Egle Tomasi, Jacques Van de Wiele, Saro Ong from IPN Orsay and Simone Pacetti from Frascati.

3.1 Probing the electromagnetic stucture of the nucleon

The simplest way to study the electromagnetic structure of the nucleon is to measure its response to the electromagnetic field created by an electron field. Among all the possible exit channels, which are intensively studied (inclusive deep inelastic scattering, deep virtual Compton scattering, meson production,....) elastic reactions play a major role. They allow indeed to access in a very direct way the electromagnetic form factors which contain important informations on the intrinsic structure of the nucleon. By varying the energy, a very broad range of momentum transfers can be investigated, providing a picture of the nucleon at different scales and allowing for study of QCD properties from the perturbative regime to the region of strong coupling.

3.2 Elastic electromagnetic response:
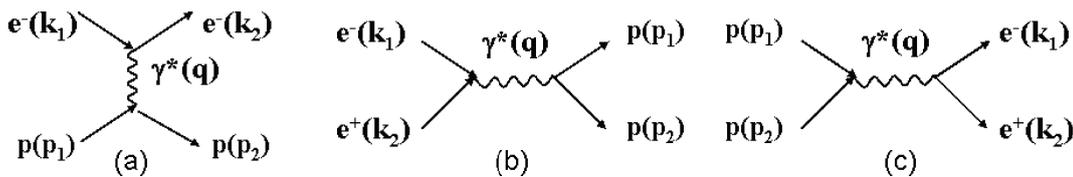
Figure 93: Attention a corriger le pbar. Different graphs for the study of electromagnetic nucleon form factors: (a) elastic e-p scattering (Space-Like), (b) $e^+e^- \rightarrow \bar{p}p$ reaction (Time-Like), (c) $\bar{p}p \rightarrow e^+e^-$ reaction (Time-Like)

The elastic response of a nucleon to the electromagnetic field can be studied in three different types of experiments: ep scattering (fig.3.2 a), electron-positron annihilation in $p\bar{p}$ (fig.3.2 b) or proton-antiproton annihilation in e^+e^-(fig.3.2 c). Depending on the quality of the available beams, these different tools have been more or less intensively and succesfully exploited along the years. Due to crossing symmetry, the three processes have the same transition matrix elements and in the one photon approximation, the calculations include the same three basic elements: the photon propagator and the $e^+e^-\gamma$ and γNN vertexes. Only the initial and final states and the kinematics make a difference in the calculation of the amplitudes. In each process, the elastic response is studied at a given four-momentum transfer

squared q², which is equal to the squared invariant mass of the virtual photon $q^2=M^2_{\gamma^\star}$, which mediates the electromagnetic interaction.

3.2.1 Space-Like and Time-Like kinematics:

In electron-proton scattering, the kinematics is such that q^2 is negative, which can be clearly seen by writing the expression for q^2 in lab frame:

$$q^2 = (p_1 - p_2)^2 = -2m_p T_2 < 0, \tag{22}$$

where p_1 and p_2 are the four-momenta of the incident and final protons respectively, T_2 is the kinetic energy of the recoil proton in the lab frame and m_p is the proton mass. In the Space-Like region, one therefore uses generally: $Q^2=-q^2$

Equivalently, using the relation between the energy E' of the scattered electron at a laboratory angle θ and the incident electron energy E, and neglecting the electron mass,

$$Q^2 = 4EE'sin^2(\theta/2) = \frac{4E^2 m_p sin^2(\theta/2)}{m_p + 2E\sin^2(\theta/2)}. \tag{23}$$

To obtain different points at the same Q^2, it is therefore needed to change both the beam energy and scattering angle (see bottom part of fig. 94). At a given incident energy, different Q^2 can be obtained by varying the electron angle.
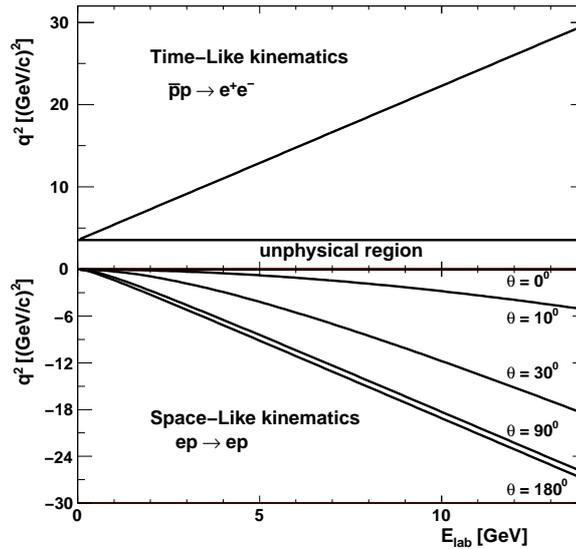
Figure 94: q^2 values accessible in $\bar{p}p \to e^+e^-$ (top) and e-p scattering (bottom) as a function of the projectile kinetic energy. The angle of the scattered electron is indicated in the case of e-p scattering.

In annihilation experiments, like $\bar{p}p$ or e^+e^-, q^2 is fixed at a given center of mass energy $\sqrt{s}$ by the relation :

$$q^2 = s > 4m_p^2, \tag{24}$$

In the case of the $\bar{p}p$ reaction, q^2 is deduced from the kinetic energy T of the incident antiproton by the simple relation

$$q^2 = 2m_p(T + 2m_p), \tag{25}$$

which is represented graphically in the upper part of fig. 94. The region, where $0 < q^2 < 4m_p^2$, cannot be accessed in any of these experiments and is called the unphysical region. We will see in the following that some reactions are sensitive to the form-factor values in this region, as for example $\bar{p}p \rightarrow e^+ e^- \pi^0$.

3.2.2 Dirac and Pauli form factors

The electron transition current j^μ results from the Dirac equation for a point-like particle in an electromagnetic field:

$$j^\mu = -q_e \bar{u}(k_2)\gamma_\mu u(k_1) \tag{26}$$

The case of the proton is different due to its intrinsic structure. Taking into account the constraints that the current has to be a four-vector fullfilling parity invariance, and should be conserved ($q_\mu J^\mu = 0$), only two independent terms remain: γ^μ and $\sigma^{\mu\nu} q_\nu$, weighted by scalar functions of Q^2 to take into account the intrinsic structure of the nucleon. So, the most general expression of the proton transition current is:

$$J_\mu = e\bar{u}(p_2)\left[\gamma_\mu F_1(Q^2) + i\frac{\sigma_{\mu\nu}q^\nu}{2m_p}F_2(Q^2)\right]u(p_1) \tag{27}$$

It consists in two terms with corresponding form factors $F_1(Q^2)$ and $F_2(Q^2)$. The former (Dirac term) does not change the spin, while the latter (Pauli term) is a spin-flip term.

In the case of $\bar{p}p \rightarrow e^+ e^-$ annihilation, the expression of the current is very similar:

$$J_\mu = -e\bar{v}(p')\left[\gamma_\mu F_1(q^2) - i\frac{\sigma_{\mu\nu}q^\nu}{2m_p}F_2(q^2)\right]u(p) \tag{28}$$

but the form factors $F_1(q^2)$ and $F_2(q^2)$, in contrast to the Space-Like region, have a non-zero imaginary part, related to the pair creation channels.

The limits at $q^2 = 0$ of the Dirac and Pauli form factors, are related to the static properties, i.e. charge and magnetic moment of the nucleons:

$$F_1^p(0) = 1, \quad F_2^p(0) = \frac{\mu^p}{\mu_N} - 1, \quad F_1^n(0) = 0, \quad F_2^n(0) = \frac{\mu^n}{\mu_N}, \tag{29}$$

where μ^p and μ^n are respectively the proton and neutron magnetic moments and $\mu_N = e\hbar/2m_p$ is the nuclear magneton. The values of $F_2^{p,n}(0)$ are therefore equal to the corresponding so-called anomalous magnetic moments, which measure the deviation of the nucleon magnetic moments from the values deduced for a point-like particle with same mass and charge. This illustrates the fact that the Pauli term is a magnetic term arising from the intrinsic electro-magnetic structure of the nucleon as can be seen from a comparison of eq.(26) and eq.(27).

The experimental values of nucleon magnetic moments

$$\mu^p = 2.792847351(28)\mu_N \text{ and } \mu^n = -1.9130427(5)\mu_N \tag{30}$$

show clearly a deviation from point-like particle behaviour. On the other hand, they are reasonably close to the values deduced from the quark constituent model:

$$s\mu^p = \frac{1}{3}(4\mu_u - \mu_d) \sim 2.82 \ s\mu_N \text{ and } \mu^n = \frac{1}{3}(4\mu_d - \mu_u) \sim -1.88\mu_N \tag{31}$$

The understanding of the nucleon structure requires the knowledge of these form-factors for both positive and negative q^2 and for values ranging from the low-q^2 regime of QCD up to the high energy perturbative regime. A part of this information is however located in the region of positive values below the $N\bar{N}$ threshold, where direct measurements of the form-factors are not possible.

90

3.2.3 Sachs form-factors

The Sachs form factors are defined as

$$G_E(q^2) = F_1(q^2) + \frac{q^2}{4m_p^2} F_2(q^2) \tag{32}$$

$$G_M(q^2) = F_1(q^2) + F_2(q^2) \tag{33}$$

with

$$G_E^p(0) = 1, \qquad G_M^p(0) = \mu^p/\mu_N, \qquad G_E^n(0) = 0, \qquad G_M^n(0) = \mu^n/\mu_N \tag{34}$$

and, by definition, $G_E(4m_p^2) = G_M(4m_p^2)$. The main interest of the Sachs form-factors is that a more simple expression of the cross-sections can be obtained, as will be seen in sect. 3.3.1.

Using the Breit frame (in which the incident and final protons have the same energy), the Space-Like form factors $G_E(q^2)$ and $G_M(q^2)$ are equal to the Fourier transforms of the spatial charge and magnetization distributions in the nucleon [139]. This remains true in non-relativistic approximation, i.e. for low q^2. However, the physical interpretation of this property is not straightforward, since the Breit frame is just a mathematical object used to make the calculations simpler.

On the other hand, as pointed out quite early by Zichichi [140], the Time-Like form factors reflect the frequency spectrum of the electromagnetic response of the nucleon, and can show poles at q^2 corresponding to the excitation of vector mesons mediating the coupling (in Vector Dominance Models) to the photon or to possible $\bar{p}p$ states.

3.2.4 Asymptotic behaviour

In the regime of very large Q^2, the form factor behaviour should follow the perturbative QCD predictions. In this case, quark counting rules [141] yield

$$F_1(Q^2) \sim \frac{\alpha_s^2(Q^2)}{Q^4}, \quad F_2(Q^2) \sim \frac{\alpha_s^2(Q^2)}{Q^6} \tag{35}$$

where $\alpha_s(Q^2)$ is the strong coupling constant. The underlying picture of the nucleon probed at very large q^2 is a three massless quark object with momenta collinear to the nucleon momentum. To keep the nucleon together in its ground state, the momentum transfer must be divided among the three quarks, which requires a two hard gluon exchange, each of them carrying a fraction of the momentum transfers. The product of the propagators yields the $1/Q^4$ behaviour. The additional $1/Q^2$ factor in F_2 arises due to the spin-flip. In this case, we can deduce from (eq.(32) and (33)) the following relation, which should be fulfilled for both Space-Like and Time-Like regions:

$$G_E^{\mathrm{SL}}(Q^2) \sim G_M^{\mathrm{SL}}(Q^2) \sim \frac{\alpha_s^2(Q^2)}{Q^4} \sim \frac{1}{Q^4 \ln^2(Q^2/\Lambda^2)}, \tag{36}$$

$$G_E^{\mathrm{TL}}(q^2) \sim G_M^{\mathrm{TL}}(q^2) \sim \frac{\alpha_s^2(q^2)}{q^4} \sim \frac{1}{q^4 \ln^2(q^2/\Lambda^2)}, . \tag{37}$$

Besides, the Phragmén-Lindelhöf theorem [142] gives a rigorous prescription for the asymptotic behavior of analytical functions

$$\lim_{q^2 \to +\infty} F(q^2) = \lim_{q^2 \to -\infty} F(q^2) \tag{38}$$

This means that, asymptotically, in the Time-Like region, the imaginary part of the form factors vanishes, and the real part is equal to the Space-Like form-factor.

3.3 Space-Like region

3.3.1 Sensitive observables

The Rosenbluth method used to determine G_E and G_M consists in measuring the elastic scattering cross-section at the same fixed $Q^2 = -q^2$, obtained by combining different beam energies and angles following eq. (39). The expression of the cross-section in the laboratory as a function of the angle θ of the scattered electron is indeed:

$$\frac{d\sigma}{dcos\theta} = \frac{\tau}{\epsilon\,(1+\tau)}(G_M^2 + \frac{\epsilon}{\tau}G_E^2)\left(\frac{d\sigma}{dcos\theta}\right)_{Mott} \tag{39}$$

$$\text{where} \quad \tau = Q^2/4m_p^2\,, \tag{40}$$

$$\epsilon = \left[1 + 2(1+\tau)\tan^2\theta/2\right]^{-1} \tag{41}$$

$$\text{and} \quad \left(\frac{d\sigma}{dcos\theta}\right)_{Mott} = \left(e^2/2E\right)^2\frac{\cos^2\theta/2}{\sin^4\theta/2} \tag{42}$$

is the Mott cross-section corresponding to the elastic scattering of an electron by a point-like proton. The electric and magnetic form-factors are then deduced from a linear fit of the reduced cross-section, the latter being defined as follows:

$$\left(\frac{d\sigma}{dcos\theta}\right)_{reduced} = \frac{\epsilon\,(1+\tau)}{\tau}\left(\frac{d\sigma}{dcos\theta}\right)/\left(\frac{d\sigma}{dcos\theta}\right)_{Mott} = G_M^2 + \frac{\epsilon}{\tau}G_E^2 \tag{43}$$

An alternative method consists in using longitudinally polarized electrons and measuring P_l and P_t, the two polarizations of the exit proton in the scattering plane in directions respectively parallel and transverse to the exit proton momentum. The ratio G_E/G_M can in this case be obtained through the relation:

$$\frac{G_E}{G_M} = -\frac{P_t}{P_l}\frac{E+E'}{2m_p}\tan\frac{\theta}{2} \tag{44}$$

where E and E' are the incident and final electron energies, and θ the final electron angle. This method has been first suggested by Akhiezer and Rekalo [143, 144] in 1968.

3.3.2 Experimental results for the proton

One of the first significant programmes in high-energy physics has been the systematic study of the electromagnetic structure of nucleons in electron scattering experiments. These pioneering works have been carried out at Cornell by Hofstadter et al. [145] and at Stanford by Wilson et al. [146] and have been followed by a lot of other works at different electron accelerators. Until the 1990's, all the measurements of electromagnetic form factors in the Space-Like region were obtained using the Rosenbluth technique, as described in sect. 3.3.1 (see the references in [147]). Many data points for the electric and magnetic proton form-factors have been measured up to $q^2 = 7$ $(GeV/c)^2$. For larger q^2, the extraction of G_E from the slope of the ϵ dependence of the reduced cross-section following eq.(43) yields large uncertainties, but G_M could be extracted from the cross-sections up to 31 $(GeV/c)^2$ assuming the relation $\mu_p G_E = G_M$. Up to about 8 $(GeV/c)^2$, the magnetic form factors (left part of fig. 95) stays close to the dipole behaviour:

$$G_M(Q^2) \sim \mu_p G_D(Q^2) \tag{45}$$

$$\text{with} \quad G_D(Q^2) = 1/(1 + Q^2/m_d^2)^2 \tag{46}$$

$$\text{and} \quad m_d^2 = 0.71(GeV/c^2)^2. \tag{47}$$

Figure 95: Available data for the proton electromagnetic form-factors [147]. Left: proton magnetic form-factor G_{Mp} divided by the dipole magnetic form factor μG_{Mp} (see eq.(47)). Right: Full squares and full dots show values for the $\mu G_{Ep}/G_{Mp}$ ratio obtained from Jlab polarization data and the thick curve is a linear fit to these data. The other data points were obtained with the Rosenbluth separation technique, including the most recent JLab Rosenbluth results (full triangles). The dashed curve is a fit of the Rosenbluth data [148].

Such a dipole distribution corresponds for low q^2 to the Fourier transform of an exponential magnetization distribution $\rho(r) \sim exp(-r/r_0)$ with $r_0 = 0.24$ fm. It has also the correct asymptotic behaviour in $1/Q^4$ (see sect.3.2.4), which is reached within 10% at $Q^2 = 15$ (GeV/c)^2.

For Q^2 larger than 8 (GeV/c)^2, the magnetic form factor starts to deviate from the dipole, which goes in the direction of a $1/Q^4$ behaviour reached at Q^2 lower than in the case of the dipole form factor. The deviations remained however lower than 30%, in the range of explored Q^2.

In addition, the electric form factor values obtained up to 6 (GeV/c)^2 using the Rosenbluth technique (right part of fig. 95) were, despite the bad quality of the data at the largest q^2, in good agreement with the corresponding dipole behaviour,

$$G_E(Q^2) \sim G_D(Q^2). \tag{48}$$

In summary, these data showed:

$$G_M(Q^2) \quad \sim \quad \mu_p G_E(Q^2) \sim \mu_p G_D(Q^2) \qquad \text{hence} \qquad G_M(Q^2)/G_E(Q^2) = \mu_p \tag{49}$$

So, the bulk of these results was in pretty good agreement with perturbative QCD expectations. However, above $Q^2=1$ (GeV/c)^2, the values extracted for the electric form-factor by the different experiments presented a large dispersion and large error bars.

More recently, the polarization transfer technique, as described in sec. 3.3.1 has been used at JLab [149, 150, 151] to measure the ratio G_E/G_M. The results obtained with these

alternative technique showed much lower values for the G_E/G_M ratio (right part of fig. 95). In contrast to the first set of data, this new behaviour of the ratio was in clear contradiction with the long-standing perturbative QCD prediction of Brodsky and Farrar [141] (eq.(37)), since G_E was shown to decrease faster with Q^2 than G_M.

However, a scaling was found, starting at $Q^2 \sim 1.5 \, (GeV/c)^2$, for the quantity

$$Q^2 F_2 / (F_1 \ln^2(Q^2/\Lambda^2)), \tag{50}$$

with Λ=0.3 (GeV/c)^2, in agreement with higher order perturbative QCD predictions [152]. On the other hand, these new form-factor measurements were in good agreement with the VDM model by Iachello [153] and are now explained by a number of other models. The preliminary results at Q^2= 5.2, 6.8 and 8.54 (GeV/c)^2 from the recent experiment GE$_p$III show a continuation of this decrease, with a somewhat reduced slope, however [154, 155]

The polarization technique has been also used at lower Q^2. A deviation from 1 by a few % of the ratio $\mu_p G_E/G_M$ is observed for q^2 between 0.3 and 0.7 (GeV/c)^2 at BLAST [156] and in the quite precise, but still preliminary results from JLab/Hall A [157]. At Mainz, the region of very low Q^2 is also the subject of investigations in order to reduce uncertainties in the determination of the charge and magnetization radii of the proton, which are defined as

$$< r_E^2 > = -6\bar{h} \left(\frac{dG_E}{dQ^2} \right)_{Q^2=0} \; ; \; < r_M^2 > = -6\bar{h} \left(\frac{dG_M/\mu_p}{dQ^2} \right)_{Q^2=0} \tag{51}$$

$$\tag{52}$$

In summary, there is an intense activity aiming at measuring or re-measuring with higher precision the nucleon electromagnetic form factors in the Space-Like region in the widest possible kinematical range.

3.3.3 Radiative corrections

It was clear from the very beginning that the polarization technique, using ratios of counting rates, was less sensitive to systematic errors than the Rosenbluth technique, which relies on the angular dependence of the cross-section, and can therefore be affected by any angular dependent effect. The observed discrepancy between both results was however much beyond the announced systematic errors. In this context, the effect of radiative corrections has been revisited. The radiative corrections are typically of the order of 10-30%, but they have a rather strong ϵ dependence, which makes a precise calculation mandatory in order to extract the form factors with the Rosenbluth method. This correction is usually treated in the formalism of Mo and Tsai [158], or by the more accurate calculation by Maximon and Tjon [159]. The overall effect is a large increase of the slope of the ϵ dependence of the cross-section. Even more spectacularly, at Q^2 of the order of 5 (GeV/c)^2, the slope observed before the radiative correction is negative. The main contribution comes from the radiation from electrons due to their lower mass, the effect being somewhat reduced by the radiation from the proton. Refined calculations of these radiative corrections [147] were performed and moved the Rosenbluth method results slightly closer to the polarization ones (see the dashed line on fig. 95), but still with a significant disgreement.

While first order radiative corrections are not sufficient to explain the discrepancy between the two sets of data, a calculation including higher order effects using the structure function method [160] could bring them in reasonable agreement.

3.3.4 Experimental and theoretical investigations of 2γ exchange

An important activity is also dedicated to more refined treatments of the 2γ exchange amplitude, which could also be a source of discrepancy between the results obtained in Rosenbluth and polarization methods [161]. In the usual radiative corrections, 2γ exchanges are taken into account using the approximation that the dominant fraction of four-momentum transfer squared is taken by one of them (one hard and one soft photon). Different calculations have been developped to go beyond this approximation [162, 163, 164, 165]. The trend is to lower the slope of the ϵ dependence of the cross-section at a given q^2. The most spectacular effect appears in the re-analysis [166] of the form factors using a hadronic model [164] for the calculation of the 2γ exchange amplitude, which is able to fully reconcile the Rosenbluth and polarization data.

Using C-invariance and crosssing symmetry, model independent properties of 2γ exchange amplitude in elastic electron-hadron scattering were derived [167, 168]. One important result is the fact that non linear terms in the ϵ dependence of the cross-section are induced by the 2γ exchange amplitude. Although the present data do not show any deviation from linearity, within the precision of the error bars, the conclusions concerning the presence of 2γ exchange are contradictory, since the non-linearities predicted by most models are too small to be measured considering the present limited precision of the data [169, 165, 170, 171]. The experiment E05-017 [172] at JLab should soon provide more accurate measurements of the ϵ dependence of the cross-section from $Q^2 = 0.5$ to 3 $(GeV/c)^2$.

In the experiment GEp-2γ in HallC at JLab [173], the ratio G_E/G_M is measured, using the polarization method, at $Q^2 = 2.5$ $(GeV/c)^2$ as a function of ϵ, with the same goal of pinging down the two-hard photon amplitude. At present, no significant deviation from linearity has been observed [155] either.

To be complete, some attempts have been made to identify 2γ effects in e+d [167] and e+^{4}He [174] scattering, but no evidence was found.

Another effect which is investigated experimentally is a difference in the cross-sections for e$^+$p and e$^-$p elastic scattering, which would be induced by the 2γ amplitude due to an interference term with opposite sign. The existing data are however not conclusive, due to the large error bars [175]. New precise results should soon appear for Q^2 up to 3 $(GeV/c)^2$ with an expected accuracy of 1% [176, 177] from an experiment with CLAS at JLab. At VEPP-IIII in Novosibirsk, a planned experiment at the storage ring aims at measuring with high precision ($\pm$ 0.3 %) the ratio of e$^+$p to e$^-$p cross-sections at $Q^2 = 1.6$ GeV/c^2 and $\epsilon = 0.4$ [178]. As for the recently approved experiment OLYMPUS at Desy, it is suited for Q^2 up to 2.2 $(GeV/c)^2$.

3.3.5 Experimental results for the neutron

Most of the data for the neutron magnetic form factors are based on cross-section measurements with deuterium targets at SLAC, ELSA and MAMI or at JLab with CLAS. More recently, polarization observables were measured using polarized electron scattering on polarized ^{3}He target at MIT-Bates and JLab at $Q^2 < 0.6$ $(GeV/c)^2$. The values measured up to $Q^2 \sim 5$ $(GeV/c)^2$ (left part of fig. 96) stay quite close to the dipole function, as confirmed by the recent and very precise data from CLAS [179] not reported on the picture, while the three points from SLAC [180] at the largest Q^2 are significantly lower.

As for the electric neutron form factors, starting from 1994, all the data points exploit measurement of polarization observables with D_2 or ^3He targets, which are proportional to $G_E^n G_M^n$, instead of $G_E^{n\,2}$, which is very small. Despite some inconsistency between the different sets of data, the electric neutron form factor can be described by a fit with a maximum of
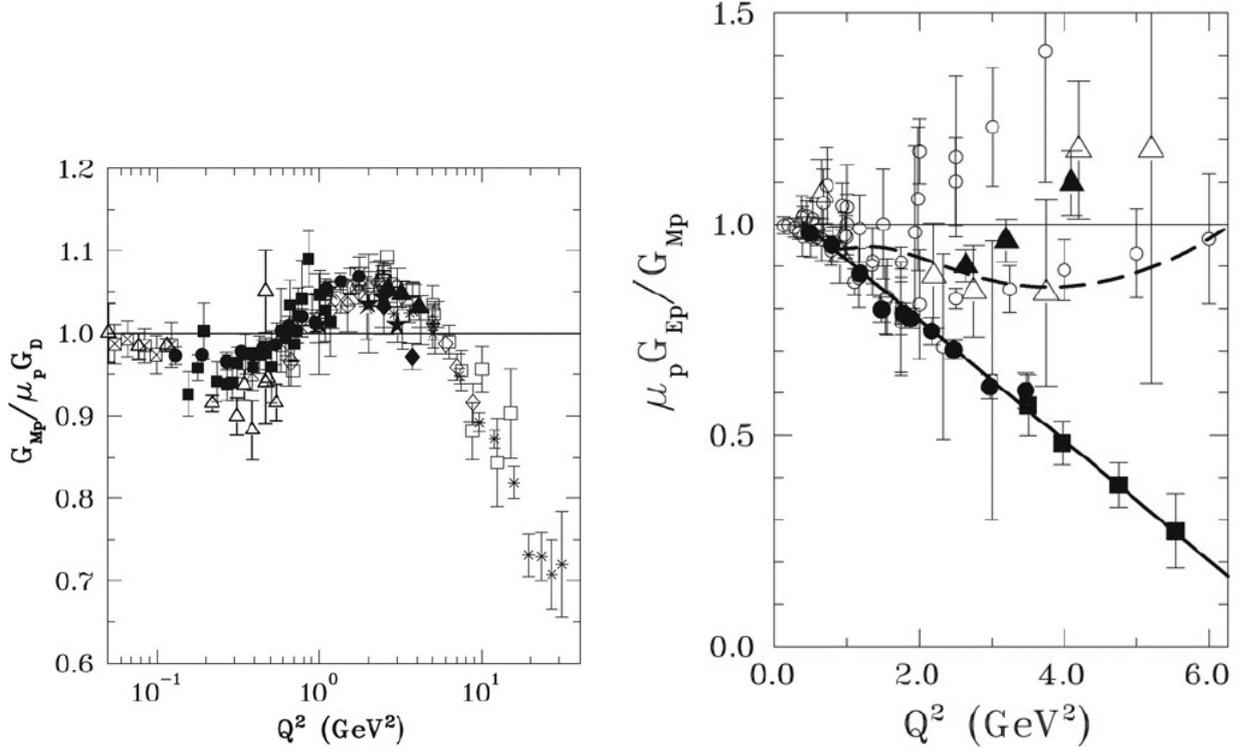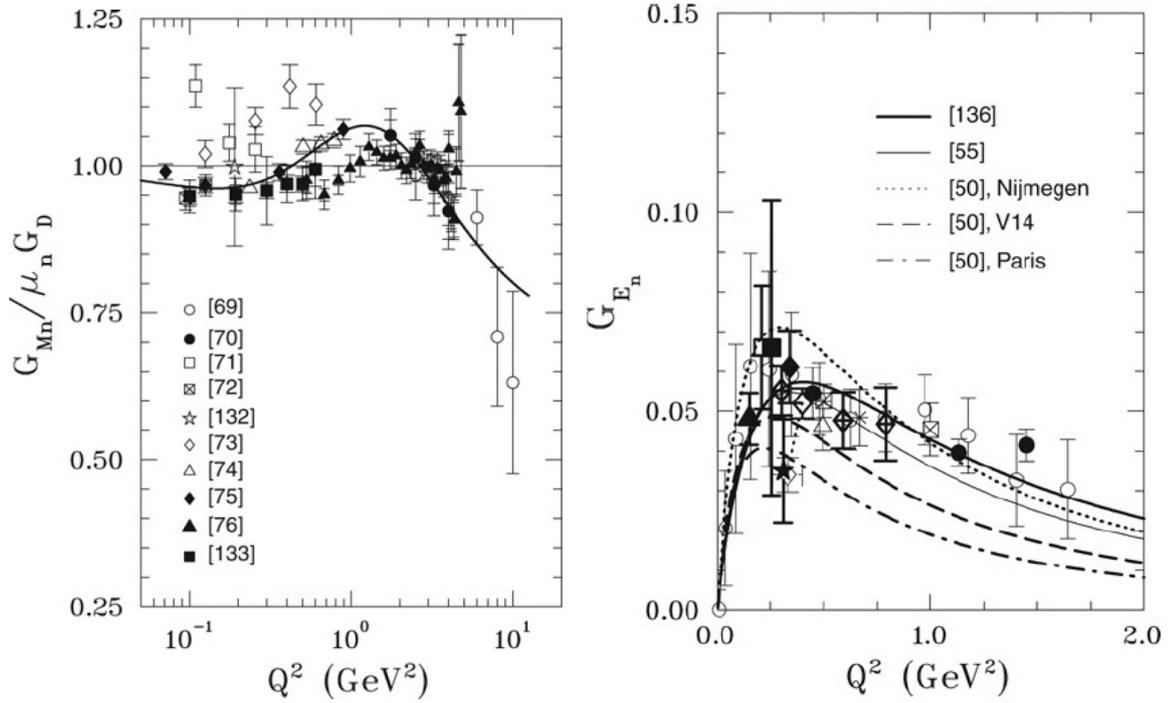
Figure 96: Available data for the neutron electromagnetic form-factors. Left: Neutron magnetic form factor G_M^n divided by the dipole magnetic form factor μG_D (see eq.(47)). Right: Neutron electric form factor G_E^n compared with different fits.

0.05 to 0.06 reached at $Q^2 \sim 0.02$ $(GeV/c)^2$ followed by a slow decrease (right part of fig. 96). In addition to the data shown in [147], recent precise measurements were obtained by BLAST at Q^2 between 0.15 $(GeV/c)^2$ and 0.4 $(GeV/c)^2$[181] and new points from MAMI at lower Q^2 should also be soon available. The precision of the neutron form factor data remains however lower than for the proton, due mainly to the absence of neutron target and to the necessity to use models to extract the neutron form factors from the observables measured in ed or e^3He interactions.

3.3.6 Conclusion on Space-Like results

As a conclusion, it is clear now that the extraction of proton form-factors using the Rosenbluth technique needs corrections, since this method is very sensitive to radiative corrections and to the possible contribution of 2γ exchange amplitude. Such effects influence marginally the results deduced from the polarization technique. Considering the present intense activity developed to clarify these corrections, the understanding of both effects should improve in the next years, which will be also very useful for our studies, as will be shown in the next sections.

3.4 Time-Like region

3.4.1 Sensitive observables

The expression of the center of mass differential cross-section for the $\bar{p}p \rightarrow e^+e^-$ reaction can be derived, in the same way as for the $e^-p \rightarrow e^-p$, using the QED lagrangian for one photon

exchange. It can be written as:

$$\frac{d\sigma}{dcos\theta} = \frac{\pi(\alpha\hbar c)^2}{8m_p^2\sqrt{\tau(\tau-1)}}(|G_M|^2\,(1+\cos^2\theta)+\frac{|G_E|^2}{\tau}\sin^2\theta) \tag{53}$$

or

$$\frac{d\sigma}{dcos\theta} = \frac{3\sigma_{tot}}{8\tau+4R^2}((\tau+R^2)+(\tau-R^2)\cos^2\theta), \tag{54}$$

where

$$R = \frac{|G_E|}{|G_M|} \tag{55}$$

and

$$\tau = \frac{q^2}{4m_p^2}. \tag{56}$$

The following equivalent expression can also be written:

$$\frac{d\sigma}{dcos\theta} = \frac{2\sigma_{tot}}{3+A}(1+A\cos^2\theta), \tag{57}$$

where

$$A = \frac{\tau-R^2}{\tau+R^2}. \tag{58}$$

So, the experimental method to extract the electromagnetic form-factors in the Time-Like region consists in a fit of the angular distribution, following eq.(53) or eq.(54).

At threshold, $\tau=1$ and the angular distribution is isotropic. Due to the $1/\tau$ factor, the sensitivity of the shape of the angular distribution to the modulus of both form factors decreases with increasing q^2. Following the prediction of constant $|G_E|/|G_M|$ ratio for very large q^2 (see sect.3.2.4), which derives from helicity conservation, a $1+cos^2\theta$ distribution will be asymptotically reached. This is typical for any helicity conserving electromagnetic process.

The total cross-section is only sensitive to a linear combination of the squared moduli:

$$\sigma_{tot} = \frac{\pi(\alpha\hbar c)^2}{6m_p^2}\frac{2\tau\,|G_M|^2+|G_E|^2}{\tau\sqrt{\tau(\tau-1)}} \tag{59}$$

The assumption $|G_E|=|G_M|$ has often been used to extract in the Time-Like region the magnetic form factor from the measured total cross-sections. This is true at the threshold ($q^2=4m_p^2$), but has not to be valid for other values of q^2. As a consequence, the extracted quantity is in this case the modulus of an effective form factor G_{eff} given by

$$|G_{eff}|^2 = \frac{2\tau\,|G_M|^2+|G_E|^2}{2\tau+1} \tag{60}$$

with following relation to the cross-section :

$$\sigma_{tot} = \frac{\pi(\alpha\hbar c)^2}{6m_p^2}\frac{(2\tau+1)\,|G_{eff}|^2}{\tau\sqrt{\tau(\tau-1)}}. \tag{61}$$

In order to give an idea of the difference between this effective form factor and the magnetic form-factor, we show in table 8 the ratios G_{eff}/G_M for three different values of the ratio $|G_E|/|G_M|$ and a list of q^2. At threshold ($\tau=1$), only the case $|G_E|/|G_M|=1$ is relevant, by definitions of the form factors. Above the threshold, any value of R is possible and the chosen values are arbitrary.

τ	q^2	G_{eff}/G_M		
	(GeV/c)^2	R=0	R=1	R=3
1	3.52	-	1	-
1.25	4.4	0.71	1	3.29
1.5	5.28	0.75	1	3
2	7.04	0.8	1	2.6
3	10.56	0.86	1	2.14
4	14.08	0.89	1	1.89
5	17.60	0.91	1	1.73
7	24.64	0.93	1	1.53
8	28.16	0.94	1	1.47

Table 8: For different values of τ and corresponding q^2, the ratios of effective form-factor to magnetic form factor are given for three values of the ratio R=|G$_E$|/ |G$_M$|.

In practice, the cross-section is measured in a restricted angular range $x_{min} < cos\theta < x_{max}$, and one has therefore first to integrate eq.(54) for R=1 from x_{min} to x_{max} to get the relation between the measured cross-section and the total cross-section.

The relation (53) is averaged over initial spins. For given beam and target polarization states, the angular distribution consists of four terms : [182]:

$$
\begin{aligned}
4\frac{d^2\sigma}{d\Omega_{e^-}} = {} & |G_M|^2\Big[\mathcal{M}^{(0)}(q^2,\theta)\left(1+\overline{\mathrm{p}}_z\mathrm{p}_z\right) + \mathcal{M}^{(2)}(q^2,\theta)\left[\left(\overline{\mathrm{p}}_x\mathrm{p}_x - \overline{\mathrm{p}}_y\mathrm{p}_y\right)\cos 2\phi + \left(\overline{\mathrm{p}}_x\mathrm{p}_y + \overline{\mathrm{p}}_y\mathrm{p}_x\right)\sin 2\phi\right]\Big] \\
& + |G_E|^2\Big[\mathcal{E}^{(0)}(q^2,\theta)\left(1+\overline{\mathrm{p}}_x\mathrm{p}_x + \overline{\mathrm{p}}_y\mathrm{p}_y - \overline{\mathrm{p}}_z\mathrm{p}_z\right)\Big] \\
& + \Re e(G_E G_M^*)\Big[\mathcal{F}^{(1)}(q^2,\theta)\left[\left(\overline{\mathrm{p}}_x\mathrm{p}_z + \overline{\mathrm{p}}_z\mathrm{p}_x\right)\cos\phi + \left(\overline{\mathrm{p}}_y\mathrm{p}_z + \overline{\mathrm{p}}_z\mathrm{p}_y\right)\sin\phi\right]\Big] \\
& + \Im m(G_E G_M^*)\Big[\mathcal{F}^{(1)}(q^2,\theta)\left(\left(\overline{\mathrm{p}}_x + \mathrm{p}_x\right)\sin\phi - \left(\overline{\mathrm{p}}_y + \mathrm{p}_y\right)\cos\phi\right)\Big]
\end{aligned}
\tag{62}
$$

where $\overline{\mathrm{p}}_i$ and p_i are respectively the beam and target polarization components. The amplitudes $\mathcal{M}^{(0)}(q^2,\theta)$ and $\mathcal{M}^{(2)}(q^2,\theta)$ refere respectively to the ϕ independent and 2ϕ dependent terms in factor of $|G_M|^2$. $\mathcal{E}^{(0)}(q^2,\theta)$ is the isotropic term in factor of $|G_E|^2$, and $\mathcal{F}^{(1)}(q^2,\theta)$ the ϕ dependent term in factor of $\Re e(G_E G_M^*)$ and $\Im m(G_E G_M^*)$. After averaging over the azimuthal angle, the polar angle distribution is

$$
\begin{aligned}
\frac{2}{\pi}\frac{d\sigma}{d\cos\theta_{e^-}} = {} & |G_M|^2\Big[\mathcal{M}^{(0)}(q^2,\theta)\left(1+\overline{\mathrm{p}}_z\mathrm{p}_z\right)\Big] \\
& + |G_E|^2\Big[\mathcal{E}^{(0)}(q^2,\theta)\left(1+\overline{\mathrm{p}}_x\mathrm{p}_x + \overline{\mathrm{p}}_y\mathrm{p}_y - \overline{\mathrm{p}}_z\mathrm{p}_z\right)\Big]
\end{aligned}
\tag{63}
$$

The interference terms indeed cancel and the coefficients of the $|G_E|^2$ and $|G_M|^2$ terms depend on the polarization only if the beam and target are both polarized in the same direction. In this case, a different sensitivity to $|G_E|^2$ and $|G_M|^2$ is induced. The most favourable, although irrealistic case would be 100% polarized beam and target in the opposite longitudinal directions ($\mathrm{p}_z = -\overline{\mathrm{p}}_z = \pm 1$), since the polar angle distribution would then be proportional to $|G_E|^2$.

It can be seen from eq.(62) that, if $|G_E|$ and $|G_M|$ are known, $\Re e(G_E G_M^*)$ can be accessed if the beam and the target are polarized in perpendicular directions.
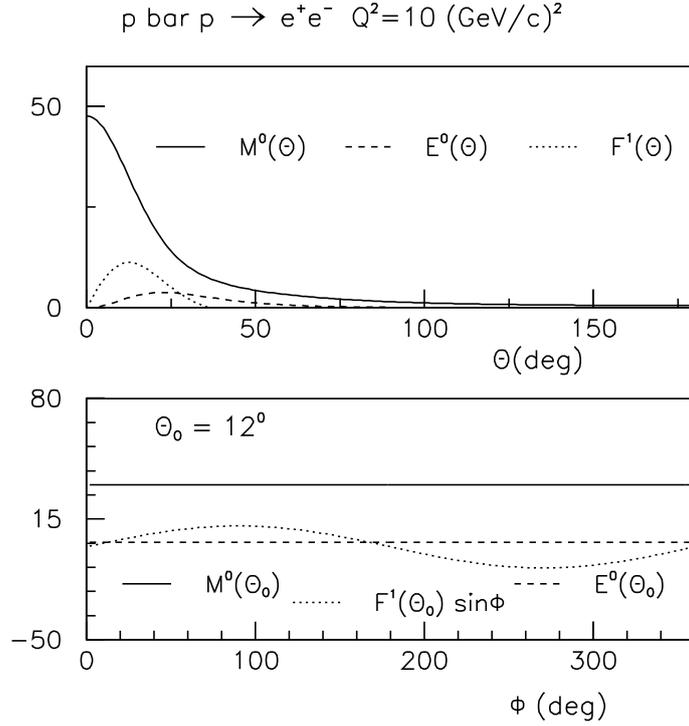
Figure 97: Contribution of $|G_M|^2$, $|G_E|^2$ and interference terms to the differential cross-sections of the reaction $\bar{p}p \rightarrow e^+e^-$ at $q^2 = 10$ $(GeV/c)^2$ for a 100% transversely polarized beam or target. The polar angle distribution is shown in the top part and the azimuthal angle distribution for $\theta = 12°$ in the bottom part.

However, due to the solenoid longitudinal field inside the $\bar{P}ANDA$ detector, only transverse beam polarization are envisaged in $\bar{P}ANDA$ although it still constitutes a difficult technical challenge. If these beams will be available, the sensitivity to $\Im m(G_E G_M^*)$ will be measured as an oscillation of the azimuthal angular distribution, which writes in this case as:

$$4\frac{d^2\sigma}{d\Omega_{e^-}} = |G_M|^2 \mathcal{M}^{(0)} + |G_E|^2 \mathcal{E}^{(0)}(q^2, \theta) + \Im m(G_E G_M^*)\mathcal{F}^{(1)}(q^2, \theta)\left(\bar{p}_x \sin\phi - \bar{p}_y \cos\phi\right) \quad (64)$$

To enhance the effect, the region in θ where the function $\mathcal{F}^{(1)}(q^2, \theta)$ is maximum can be selected. This is illustrated in fig. 97. In the upper part, the different contributions to the laboratory polar angle distributions are shown for $q^2 = 10$ $(GeV/c)^2$. In the lower part, the azimuthal distribution is displayed for the polar angle $\theta = 12°$, for which the interference term is maximum. The amplitude of the oscillation is proportional to $\Im m(G_E G_M^*)$. In this way, the absolute value of the relative phase between G_E and G_M can be deduced, since $|G_E|$ and $|G_M|$ will be known from the non-polarized angular distribution.

Note that in the whole sect.3.4.1, the reaction $\bar{p}p \rightarrow e^+e^-$ has been considered. In the case of the $e^+e^- \rightarrow \bar{p}p$ reaction, the expressions of the cross-sections differ only by a kinematical factor.

3.4.2 Experimental results for the proton

The first conclusive measurement of Time-Like proton form factors, based on 25 events, was carried out at ADONE in Frascati at 4.3 $(GeV/c)^2$ in the reaction $e^+e^- \rightarrow \bar{p}p$ and published in 1973 [183]. The idea to use $\bar{p}p$ annihilation experiments can already be found in 1962 [140],

but the first results, obtained in $\bar{\text{p}}$p annihilation at threshold at CERN [184] were published in 1976.

At the Orsay DCI storage rings, the region of q^2 up to 5.8 (GeV/c)^2 was explored in e^+e^- collisions and $|G_{eff}|$ was extracted using eq.(53). [185, 186, 187]. An attempt was already made to extract $|G_E|/|G_M|$ by analysing the proton and antiproton angular distributions [186], but the precision was very poor. The first high statistics measurement was carried out at LEAR by the PS170 experiment [188], with the observation of a steep rise of $|G_M|$ when q^2 decreases close to threshold. In these experiments, a ratio $|G_E|/|G_M|$ compatible with 1, with error bars of the order of ± 0.3 could be extracted from the lepton angular distributions [189]. ADONE also produced five points between 3.6 and 6 (GeV/c)^2 [190] and the angular distributions were found compatible with $|G_E|=|G_M|$, but once again the sensitivity was very poor.

The region of q^2 higher than 6 (GeV/c)^2 was first explored by the E760 experiment [191] and later by the E835 experiment [192, 193] at Fermilab which both assumed $|G_E|=|G_M|$. More recently, CLEO at CESR brought a quite precise measurement at $q^2=13.5$ (GeV/c)^2 [194]. None of the latter experiments could extract the $|G_E|/|G_M|$ ratio.
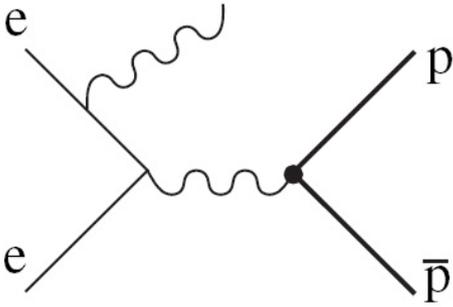
Figure 98: The diagram for the $e^+e^-\rightarrow\bar{\text{p}}p\gamma$ process (Initial State Radiation).
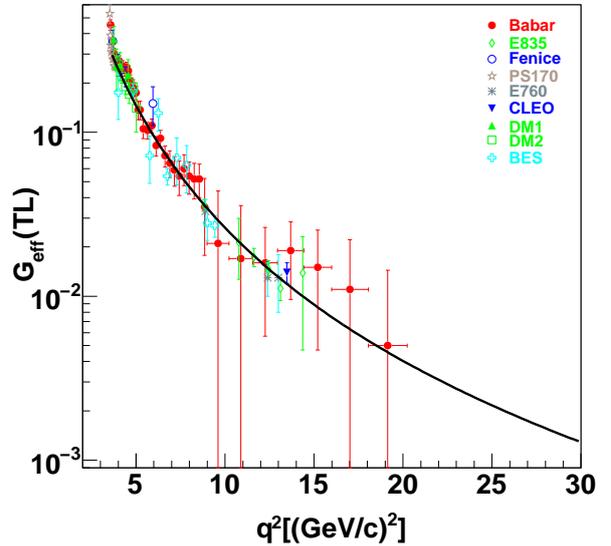
Figure 99: Effective proton form-factors measured in the Time-Like region. The figure is adapted from [195] and the fit corresponds to eq.(73).

The amount of data coming from e^+e^- colliders was, until a few years ago, limited, since these facilities were often working at a fixed energy suited to study one particular resonance. Taking advantage of the high luminosities, the Initial State Radiation technique has been used recently by the BABAR and BES collaborations working respectively at PEP-II (SLAC) and BEPC (Beijng). Instead of the direct $e^+e^-\rightarrow \bar{\text{p}}$p reaction, the reaction $e^+e^-\rightarrow \bar{\text{p}}p\gamma$ is used. In such reactions, the photons are dominantly radiated by the electrons in the initial state (fig. 98), which lowers the q^2 value at the $\gamma^\star\bar{\text{p}}$p vertex, the radiation from protons in the final state being treated as a correction. The principle of the measurement is to reconstruct the high energy photon, to identify the $e^+e^- \rightarrow \bar{\text{p}}$p reaction and to analyse the proton angular distribution to extract $|G_E|$ and $|G_M|$. In such experiments, a broad range of q^2 is explored at the same time, with limits depending on the center of mass energy $\sqrt{s}$ provided by the beams ($\sqrt{s} \sim 10$ GeV/c for BABAR and $\sqrt{s}$ between 2 and 5 GeV/c for BES).
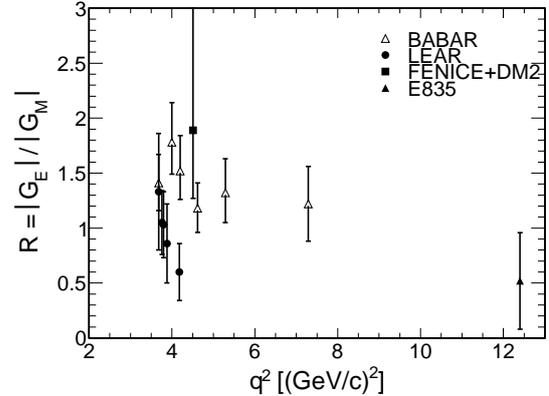
Figure 101: Available data for the ratio $|G_E|/|G_M|$ for the proton in the Time-Like region. open triangles: BABAR (SLAC), full circles LEAR (CERN), full squares FENICE (Frascati) +DM2(Orsay), full triangles E835(Fermilab)

Figure 100: Measurements of proton form factors: electric form factor in Space-Like region (G_E(SL)) obtained by polarization method (green stars) and by Rosenbluth method (red triangles); magnetic form factor in Space-Like region (G_M(SL)) (blue dots for $|q^2| < 9$ (GeV/c)^2), effective form factor in Space-Like region (G_{eff}(SL), blue dots for $|q^2| > 9$ (GeV/c)^2) and effective form factor in Time-Like region (G_{eff}(TL)) (symbols with different colors in the upper part of the plot).

The BABAR data analysis added a lot of new points to the systematics for q^2 ranging from threshold (i.e. 3.52 (GeV/c)^2), up to 19 (GeV/c)^2 [195], while the BES results cover the region between 4 and 9 (GeV/c)^2 [196]. In the case of the BABAR experiment, the proton angular distributions were analyzed to extract the $|G_E|/|G_M|$ ratio.

The world data on form factors obtained in the Time-Like region are displayed in fig. 99. As explained above, they correspond to the effective form factor modulus, or equivalently to magnetic or electric form-factor modulus in the assumption $|G_E|=|G_M|$, see eq.(60).

Most of the points above q^2=8 (GeV/c)^2 have very large error bars. They follow the trend:

$$|G_{eff}| \sim \alpha_s^2(q^2)/q^2 \sim \frac{1}{q^2 \ln^2(q^2/\Lambda^2)}, \tag{65}$$

as predicted by pQCD. However, the values in the Time-Like region are higher by a factor 2 than the values in the Space-Like region, which indicates that the asymptotic regime is not achieved. This is illustrated on fig. 100 , where G_E and G_M obtained in SL region are compared to the effective form factor G_{eff} obtained in TL region.

The knowledge of the ratio of electric to magnetic form factor is still rather poor in the Time-Like region, as can be seen from fig. 101. Only two experimental collaborations directly published values for this ratio, namely the PS170 experiment at LEAR for q^2 up to 4.2 (GeV/c)^2 and the BABAR collaboration for q^2 between 3.5 (GeV/c)^2 and 9 (GeV/c)^2. The two additional points have been produced by a combined analysis [197] of the angular

distributions measured in the experiments FENICE and DM2 around 4.5 $(GeV/c)^2$ and from two different data takings of the E835 experiment at 12.4 $(GeV/c)^2$.

The precision is clearly not sufficient and more precise data extending to higher q^2 are obviously needed. Moreover, the data from the LEAR and BABAR experiments disagree in the overlapping q^2 range, which needs to be clarified.

3.4.3 Experimental results for the neutron
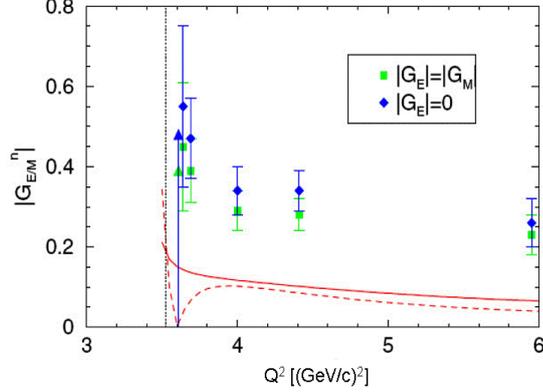
Figure 102: Neutron magnetic form-factor derived from the FENICE experiment[198] using the hypothesis $|G_E|=|G_M|$ (squares) and $|G_E|=0$ (diamonds). The dotted vertical line shows the n-n̄ threshold. The curves are Chiral Perturbative Theory calculations [199] for $|G_M|$ (solid line) and $|G_E|$ (dashed line).

The neutron Time-Like form factors have been measured at Frascati at 6 different q^2 [198]. The $|G_M|$ values have been extracted in two different hypothesis: $|G_E|=|G_M|$ and $|G_E|=0$ (fig. 102). As the knowledge of the neutron Time-Like form factors is based on this single experiment, a confirmation of these data would be very welcome. In addition, the rather high magnitude of the neutron FF (about twice as large as the proton) is surprising.

3.4.4 2γ exchange in Time-Like region

The extraction of form-factors in the Time-Like region may be also affected by the 2γ exchange mechanism. We have seen that , in the Space-Like region, the 2γ exchange amplitude adds non linear terms in the ϵ dependence of the elastic e+p cross-section (see 3.3.3). The counterpart effect of such non-linearities in the Time-Like region is the presence of odd-$\cos\theta$ terms in the p̄p↔ e⁺e⁻ center of mass angular distributions [167], which, in the 1γ approximation contains only constant and $\cos^2\theta$ terms (see eq.(54)). This model independent statement will be tested quite easily in our experiment. It has indeed been shown in our studies, that our proposed measurement of the p̄p→e⁺e⁻ angular distributions with P̄ANDA will be sensitive to a 5% contribution of odd-$\cos\theta$ terms [200]. However, exactly as in the Space-Like experiments for the size of the non-linearities, the importance of the odd $\cos\theta$ terms can only be given by models. Furthermore, the 2γ exchange amplitude will also contribute to the constant and $\cos^2\theta$ terms, and hence to the determination of $|G_M|$ and $|G_E|$ obtained as a fit of the angular distributions using eq.(54).

Investigations of the 2γ exchange in the Time-Like region are still very scarce. In [201], the presence of possible odd-$\cos\theta$ terms in the angular distributions measured in the e⁺e⁻→ p̄p experiment has been searched for, with a negative result, within error bars.

To our knowledge, only the calculations of 2γ exchange in a QCD factorization approach [171] are as of now starting to be extended to the Time-Like region [202]. The preliminary prediction is a 2% contribution of odd-$\cos\theta$ terms in the $\bar{\text{p}}\text{p}\rightarrow\text{e}^+\text{e}^-$ angular distribution at an incident antiproton energy of 15 GeV, which is out of reach at $\bar{\text{P}}$ANDA.

3.5 Limitations of previous experiments

In Table 9 the kinematical and technical aspects of the existing TL FFs experiments are summarized. All previous results have been limited by statistics, which prevented from a precise determination of angular distributions.

Accelerator	FAIR	CERN-LEAR	SLAC-PEP II	FERMILAB	BEPC
Experiment	PANDA (Sim)	PS170	BABAR	E835	BES II
Reaction	$\bar{p}+p \rightarrow e^+ + e^-$	$\bar{p}+p \rightarrow e^+ + e^-$	$e^+ + e^- \rightarrow \bar{p}+p+\gamma$	$\bar{p}+p \rightarrow e^+ + e^-$	$e^+ + e^- \rightarrow \bar{p}+p$
q^2 [GeV/c]^2	5 - 27	3.52 - 4.18	3.5 - 20	8.84 - 18.4	4 -9.4
$\mathcal{L}$ [cm^{-2} s^{-1}]	$2 \cdot 10^{32}$	$3 \cdot 10^{30}$	$3 \cdot 10^{33}$	$2 \cdot 10^{31}$	$< 10^{31}$
I_{Beam}	10^{11} $\bar{p}/s$	$3 \cdot 10^6$ $\bar{p}/s$		$5 \cdot 10^{11}$ $\bar{p}/s$	
Target	pellets or jet	LH2	collider	gas jet	collider
$|\cos\theta|$	<0.8	< 0.8	< 1	< 0.62	<0.8
Efficiency	40-10%	~ 10 %	17 %	67%	$\sim 50\%$
B/S	< 1%	< 5%	< 5%	< 2%	$1.5\% - 7.8\%$

Table 9: Compared characteristics of TL FFs experiments.

- LEAR: In the case of the PS170 experiment at LEAR, the detector acceptance was limited, in particular due to the covering in azimuthal angle. In addition, due to the limited luminosity and to the limited beam periods used to perform the experiment very low statistics were available. The electrons were identified using tracking and Cherenkov signal and the $\bar{\text{p}}\text{p}\rightarrow\text{e}^+\text{e}^-$ reaction was selected using kinematical cuts. The main background in the experiment was the $\pi^+\pi^-$, which was estimated to be 5%.

- Fermilab: The large efficiency for E835 is due to the detection based on Cerenkov detector, which gives an average pion suppression on the order of $5\ 10^{-3}$. This allows to have good identification with relatively loose cuts. Efficiencies could be checked using the J/ψ and ψ' decays into e^+e^-. Due to the absence of tracking, the main sources of background were the $\bar{\text{p}}\text{p} \rightarrow \pi^0\pi^0$ and $\bar{\text{p}}\text{p} \rightarrow \pi^0\gamma$ reactions, with contaminations estimated to 3 % at maximum, which could be neglected with respect to the statistical errors and systematic error due to efficiency corrections.

- BABAR: The FFs measurement of BABAR is indirect, as it is based on initial state radiation. The angular factors of the electric and magnetic terms are derived from elaborated simulations including the hard photon emission probability. The thorough study of the systematic errors is described in Ref. [195]. The background reactions (with main contribution from $\pi^0\pi^0\gamma$) are very efficiently rejected and the main systematic error is due to the p and $\bar{\text{p}}$ identification. The final reconstruction efficiency is 17%.

- BES: Rather large systematic errors (of the order of 10%) were obtained in this experiment, due to background reactions (mainly,...) and efficiency uncertainties. The errors were however dominated by the statistics, as in all other experiments.

3.6 Nucleon models

The issue of the different models is to give a simultaneous description of the proton and neutron form factors, and when possible, both in the Time-Like and Space-Like regions.

- Perturbative QCD models

Perturbative QCD is expected to be valid at very high q^2 (see sec. 3.2.4). The corresponding counting rule prediction in the Space-Like region

$$G_M^{SL}(Q^2) \sim \frac{C}{Q^4 \ln^2(Q^2/\Lambda^2)} \qquad (66)$$

is indeed fulfilled, starting from $Q^2=8$ $(GeV/c)^2$ for $G_M(Q^2)$, but $G_E(Q^2)$ is decreasing more rapidly.

This observation triggered new perturbative QCD calculations taking into account higher order corrections involving quark orbital momentum. In [152], it is shown that these models influence the spin-flip current in such a way that a new asymptotic behaviour is derived for the ratio of Pauli and Dirac form factors :

$$F_2(Q^2)/F_1(Q^2) \sim \ln^2(Q^2/\Lambda^2)/Q^2 \qquad (67)$$

The experimental ratio $F_2(Q^2)/F_1(Q^2)$ measured by JLab in the Space-Like region is found to follow rather well this trend with $\Lambda=0.3$ GeV, over the whole range of available Q^2, between 1 and 5.6 $(GeV/c)^2$. This is however surprising, since perturbative QCD is not expected to work at so low Q^2. In [152], this behaviour is thought to be due to cancellations of higher order terms in the $F_2(Q^2)/F_1(Q^2)$ ratio. So, the region where perturbative QCD starts to be valid has still to be determined and in this respect, the comparison of Space-Like and Time-Like data can be very useful.

As discussed in sec. 3.4.2, the effective form-factors measured in the Time-Like region are well fitted for both proton and neutron [195, 203] by using eq.(66) and the assumption $G^{TL}(q^2)= G^{SL}(-q^2)$, i.e.

$$G_M^{TL}(q^2) \sim \frac{C}{q^4 \ln^2(Q^2/Lambda^2)}. \qquad (68)$$

In this formula, the phase of the Time-Like form-factor is zero and the asymptotic behaviour is fulfilled, by construction. However, the coefficient C coming out of the fit of the data in the Time-Like region is twice as large as for the magnetic form factor fit in the Space-Like region for $Q^2 >8$ GeV/c^2, in contradiction to the Phragmén-Lindelöf theorem (see 3.2.4).

A more relevant extension (also fitting the data) is obtained using eq.(66) also for negative $Q^2=-q^2$, hence

$$\left| G_M^{TL}(q^2) \right| \sim C/(\ln^2(q^2/\Lambda^2) + \pi^2)/q^4. \qquad (69)$$

This expression fulfills the Phragmèn-Lindelhöf theorem ($F_{TL}(q^2)= F_{SL}(-q^2)$) at very large q^2, where

$$\ln^2(q^2/\Lambda^2) + \pi^2 \sim \ln^2(q^2/\Lambda^2). \qquad (70)$$

More elaborated parametrizations have been developped (the so-called improved QCD-fits [204]), to better reproduce the Space-Like data at low Q^2.

Although these expressions seem to be able to fit the data, perturbative QCD is not expected to be valid at so small Q^2. Similar problems as the one stressed above affect the analytic continuation to Time-Like region.

- Vector Meson Dominance models

  An other serie of models is inspired by the Vector Dominance, which assumes that the electromagnetic interaction is mediated by a vector meson. This model is inspired by the prominent production of vector mesons ($\rho(770)$, $\omega(782)$ and $\phi(1020)$,....) in e$^+$e$^-$ collisions at the appropriate values of positive q^2. This dominance of vector mesons in the Time-Like region should then play a major role also in the Space-Like region. In the most simple approach, the form factor is written as a sum of vector meson pole contributions:

  $$F_{1,2}(Q^2) = \sum \frac{a_i}{Q^2 - m_i^2} \tag{71}$$

  with residues a$_i$ fitted to the data. The masses m$_i$ of the first vector mesons ($\rho(770), \omega(782)$ and $\phi(1020)$) are usually taken from the PDG values and the higher masses fitted to the data. The first of these fits was provided by Iachello [153], with only $\rho(770), \omega(782)$ and $\phi(1020)$ mesons and gave the early prediction of a linear decrease of the proton G_E/G_M ratio, in surprisingly good agreement with the present results from the polarization transfer experiments. This model consists of an intrinsic form-factor and a vector meson part, with five free parameters in the Space-Like region [140]. The analytical continuation of the vector meson part to the Time-Like region is driven by the description of the $\rho \to \pi^+\pi^-$ channel, while a phase is introduced for the intrinsic form-factor and is determined by a fit to the Time-Like proton data. However, the overall phase of the form-factor is not vanishing asymptotically, in contrast with the Phragmèn-Lindelöf theorem.

  More recently, an effort has been made to provide a unified description of different baryon electromagnetic form-factors in both Space-Like [86] and Time-Like region [87]. The analytic expression of the form factors has been derived from the baryon wave-functions and the baryonic electromagnetic transition operators assuming a two-component coupling, i.e. one direct coupling to the quarks and one coupling mediated by vector mesons. A similar agreement with elastic nucleon form factor data is achieved as with the previous version of the models, with only four free parameters for the elastic form-factors (plus one phase in the Time-Like region). This version of the model has been described in more details in PartI, since it was used for the analysis of the Δ Dalitz decay process in the HADES data, which are sensitive to the N-Δ transition form-factor.

  The extensions of vector meson models, known as GKex models, which include more mesons and take into account the pQCD scaling relations have also been developped [205]. They give a good description of the electric and magnetic form-factors of both proton and neutron, with 14 free parameters. An extension of this parametrization to Time-Like region is described in [206].

- Dispersion relations

  This approach has been used since a long time to analyse the form factor measurements [208]. It relates the Space-Like and Time-Like regions, but in a more mathematical way, using the general properties of analytical functions in the complex plane. The form-factor is therefore obtained using the following relation:

  $$F(q^2) = \frac{1}{\pi} \int\limits_{t_0}^{\infty} dq'^2 \frac{\Im m F(q'^2)}{(q'^2 - q^2)}, \tag{72}$$

  where the form-factors in the Time-Like region are parametrized and include both the vector meson poles and non-resonant contributions, as well as a term providing the p-
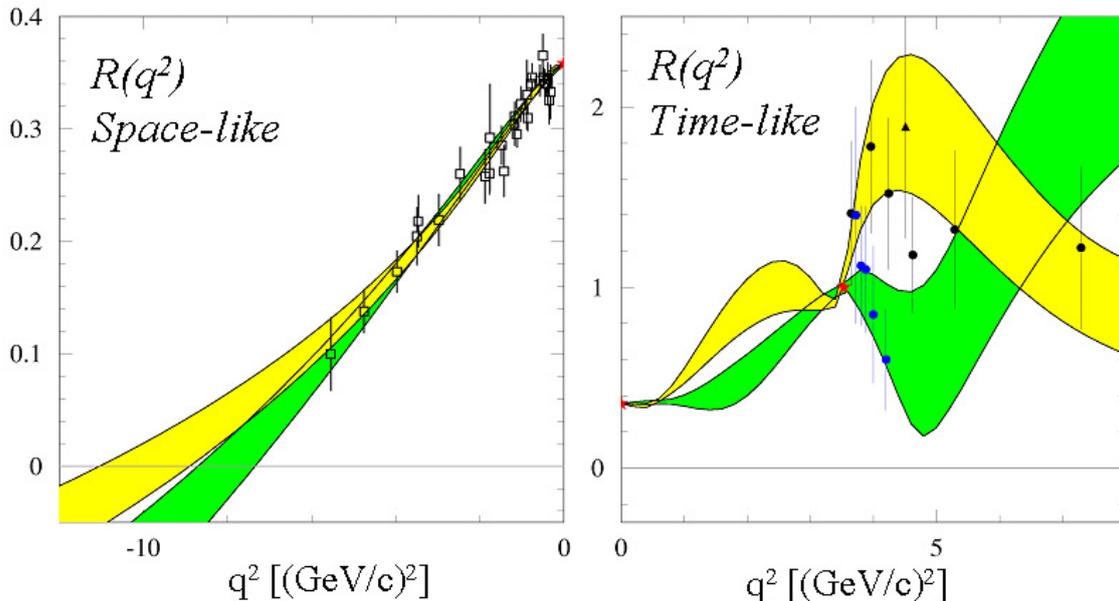
Figure 103: Figure from [207]. The yellow (respectively green) bands show dispersive relation fits of R(q^2)= $\mu_p G_E(q^2)/G_M(q^2)$ constrained by the Time-Like BABAR, DM2, FENICE and E835 data (see sec. 3.4.2) (respectively by the LEAR data) compared to the Space-Like data (left) and to the Time-Like data. Note that the definition of R(q^2) used here is different by a factor μ_p from eq.(55).

QCD limit as F$_2$/F$_1 \sim$1/Q^2. In the most recent version of the model, the parametrization includes in addition to the vector mesons, the non resonant 2π, $\rho\pi$ or K$\bar{\text{K}}$ contributions. In total, 15 parameters are fitted to the available data [209].

Recently, model independent dispersion relation analysis, based on Chebyshev polynomial fits of the experimental values of R=|G$_E$|/|G$_M$| were proposed [207]. They include the QCD asymptotic behaviour and the Phragmèn-Lindelöf theorem (see sec. 3.2.4). Since in the Time-Like region, the BABAR and LEAR data for the ratio R disagree, two different fits have been performed, which yield a zero crossing at somewhat different q^2 values in the Space-Like region, and asymptotic constant value of G$_E$/G$_M$=-1 in the case of the BABAR data and about -2.3 in the case of the LEAR data (fig. 3.6). It is interesting to see how the values of form factors in both kinematical regions are intimately connected and how additional data in some restricted kinematical region can constrain the overall behaviour of the form factors as a function of q^2.

- Nucleon shapes

  Despite the complexity introduced by the treatment of relativistic effects, the Fourier transform of the Space-Like form-factors in the Breit frame (see sec.3.2.3) are exploited to extract the rest frame charge and magnetization densities for neutron and proton [210].

  On the other hand, constituent quark proton wave function models constrained by the electromagnetic form factor data are used to study the transverse distributions of charge and magnetization [211].

  Such approaches are relevant for the interpretation of Space-Like data only.

- Chiral perturbation theory

106

At low four-momentum transfers, the nucleon electromagnetic form factors can also be studied within chiral perturbation theory expansions based on chiral lagrangians with pion and nucleon fields. The model of [212] extended to Time-Like region [199] gives a reasonable agreement for the proton form factors, but underpredicts the neutron form factors (see fig. 102). These approaches are however limited to very low q^2.

- Quark models

  Initiated by the early non-relativistic constituent quark models (CQM) by Isgur and Karl [213], a large serie of relativistic constituent quark models has been developped during the last years. The very recent calculation of [214] provides predictions in the Time-Like region, which are in reasonable agreement with the magnetic proton form-factor data, but fail to describe the neutron form-factor.

- Generalized Parton Distributions

  The GPD are probability densities of the partons as function of three kinematical variables. While the experimental extraction of these distributions is still challenging, the form factor measurements can be used to give constraints on the GPD models. The first moments of GPD's are indeed related to the elastic form-factors of the nucleon through model independent sum rules. A fairly good agreement with the experimental values of electric and magnetic proton and neutron form-factors is obtained with the "modified Regge model" [215]. The extension of such studies to Time-Like region is however not straightforward.

- Lattice QCD calculations

  There are high expectations from lattice QCD calculations, since they start from QCD first principles. Although tremendous progress have been achieved during the last years, the predictions are still limited by computing powers to pion masses of the order of 350 MeV/c^2. The extrapolation to physical pion mass is then provided by chiral perturbation theory, which is however reliable only for Q^2 lower than 0.5 (GeV/c)^2.

4 Measuring proton electromagnetic form factors with $\bar{\mathrm{P}}$ANDA

Following the motivations described in the last section, we investigated the feasibility of the measurement of proton electromagnetic form factors in the reaction $\bar{\mathrm{p}}\mathrm{p}{\rightarrow}\mathrm{e}^+\mathrm{e}^-$ with the $\bar{\mathrm{P}}$ANDA detector. Throughout this work was done in close collaboration with Thierry Hennino. The early studies which lead to the first presentation of the project at the IN2P3 scientific council (nov 2006) include Emilia Becheva's post-doctoral work, which I supervised, as well as dE/dx calculations by Jacques Van de Wiele and Ronald Kunne. For the tests of the GEANT4 hadronic models, the simulations were performed by Thomas Zerguerras (IPN "R&D detecteurs") and we benefitted from interactions with the GEANT4 hadronic model team (Dennis Wright). Interactions with the BABAR electron PID team (Helmut Marsiske) have been also helpful. Saro Ong, Dominique Marchand and Egle Tomasi-Gustaffson also contributed for the cross-section estimate and angular distribution fits. The full scale GEANT4 simulations (2008-2009) are due to the work of Malgorzata Sudol, under the supervision of Thierry Hennino. These results were described in the PANDA Physics Book [136] chapter on electromagnetic processes, presented at the IN2P3 and IPN Scientific Council (june 2009 and nov 2009 respectively) and included in the paper accepted for publication in EPJA [200]. I will

here summarize these results, refering to these publications for the details, as well as for some pictures and tables. I will also add some informations concerning kinematics, identification and error calculation.

4.1 Counting rates and angular distributions

The first steps of this feasibility study consisted in estimating the counting rates and investigating the possibility of measuring separately $|G_E|$ and $|G_M|$ by analyzing the angular distributions.

4.1.1 Cross-sections and form-factor inputs

q^2 ((GeV/c)^2)	p (GeV/c)	T_{inc} (GeV)	σ_{tot} (pb)	$|G_M|$ R=1	$|G_M|$ R=0	$|G_M|$ R=3	N
5.4	1.70	1.	538.	1.22 10^{-1}	1.405 10^{-1}	7.08 10^{-2}	10^6
7.27	2.78	2.	72.	5.90 10^{-2}	6.58 10^{-2}	3.69 10^{-2}	1.4 10^5
8.21	3.30	2.5	32.	4.34 10^{-2}	4.78 10^{-2}	2.79 10^{-2}	6.4 10^4
11.0	4.84	4.	4.5	2.02 10^{-2}	2.17 10^{-2}	1.39 10^{-2}	9.1 10^3
12.9	5.86	5.	1.6	1.34 10^{-2}	1.42 10^{-2}	9.54 10^{-3}	3.2 10^3
13.8	6.35	5.5	1.	1.11 10^{-2}	1.12 10^{-2}	7.99 10^{-3}	2 10^3
16.7	7.90	7	0.29	6.69 10^{-3}	7.04 10^{-3}	5.04 10^{-3}	580
22.3	10.9	10	0.04	2.96 10^{-3}	3.07 10^{-3}	2.35 10^{-3}	81
27.9	13.9	13	0.01	1.68 10^{-3}	1.73 10^{-3}	1.38 10^{-3}	18

Table 10: $|G_M|$ values and counting rates as a function of the q^2 values used for the simulations of the $\bar{p}p \rightarrow e^+e^-$ reaction. The corresponding incident antiproton momenta and kinetic energies are also indicated. The total cross-sections σ_{tot} are calculated from eq.(61), with $|G_{eff}|$ given by the parametrization (73). The $|G_M|$ value are deduced from $|G_{eff}|$ using eq.(60) for three different values of the ratio R=$|G_E|/|G_M|$. The number of counts N is calculated for a luminosity of 2 fb^{-1} (120 days at $2 \cdot 10^{32}$ cm^{-2}s^{-1}) assuming full acceptance and efficiency.

Different parametrizations can be used to fit the available data for the effective form factor in the Time-Like region. we used the expression given in [203] :

$$\left| G_{eff}(q^2) \right| = \frac{22.5 \; G_d(-q^2)}{(1 + q^2/3.6)^{-2}} \tag{73}$$

with q^2 given in (GeV/c)^2 and G$_d$(q^2) the dipole form factor defined as in eq. (47). The function (73) was fitted to experimental data of effective form factors existing in 2005. It is compared in fig. 99 with all the data known in 2009, and a good agreement is also observed with the more recent measurements by BABAR, although the precision does not allow for a strong constraint. Eq. (73) can therefore be taken as a useful parametrization of the data, although it has no theoretical background and its asymptotic behaviour is in q^{-6} instead of q^{-4} (see sec. 3.2.4). In addition, for larger q^2, where no measurement exists, it allows for conservative estimates. It has indeed been checked in [216] that other parametrisations, also fitting the existing data, yielded higher cross-sections.

For each q^2, the cross-section was then deduced from G$_{eff}$ using eq.(61). The cross section was then kept constant and the angular distributions were claculated using eq.(54), with three different hypotheses for the ratio R=$|G_E|/|G_M|$ (R=1,R=0 and R=3). The nine

q^2 values chosen for the simulations of the signal (see sect.4.12.1) are displayed in Table 10 together with the corresponding incident antiproton energies and momenta and the cross-sections derived as explained above. The values of $|G_M|$ are deduced from the cross sections using eq.(59) (or equivalently from G_{eff} using eq. (60)) for the three different hypotheses.

The counting rate estimates are based on an integrated luminosity $L_{eff} = 2$ fb^{-1}, corresponding to the maximum expected instantaneous luminosity 2 10^{32} cm$^{-2}s^{-1}$ during a period of 10^{7}s.

4.1.2 Center of mass angular distributions

We assumed in a first step full acceptance and efficiency of the detector. The corresponding integrated counting rates are given in the last column of Table 10. The angular distributions for the three different hypothesis with a $\cos\theta$ bin width of 0.1 are shown in fig. 104.
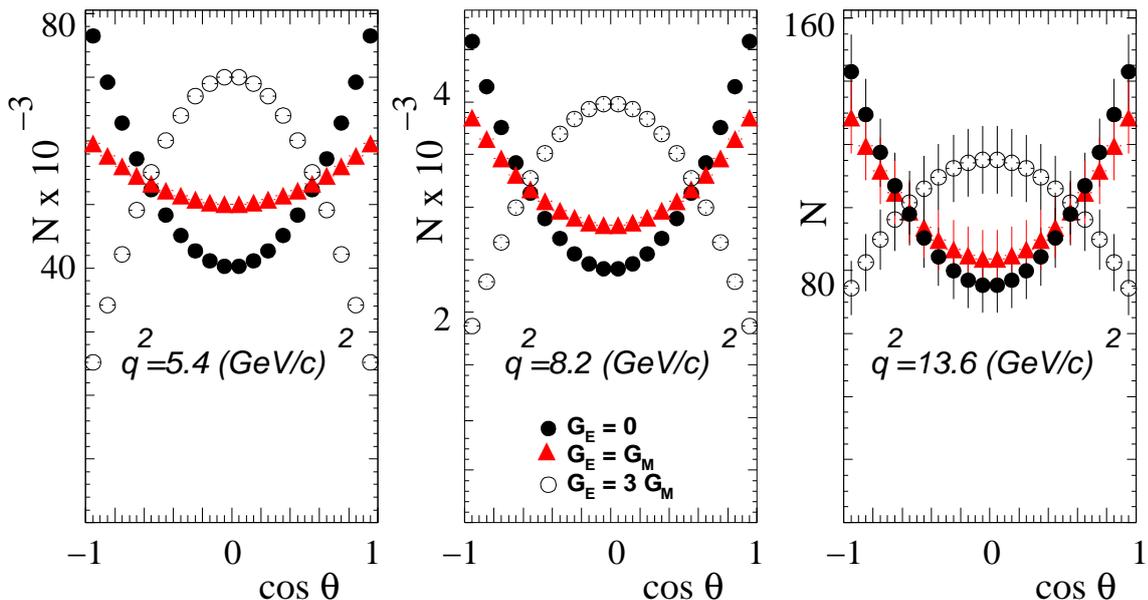
Figure 104: Distribution of count number for bins of width 0.1 in $\cos\theta$ estimated for R=0, R=1 and R=3 using a luminosity of 2 fb^{-1} and the cross sections of Table 10.

At low energy, the statitical errors are very small and the curves obtained for the different values of R are very well separated, but they come closer with increasing $\bar{p}$ energy, as a consequence of the decreasing sensitivity of the angular distribution to the $|G_E|^2$ term (see eq.(53)).

4.2 Kinematics and acceptance considerations

4.2.1 Kinematics of electrons in the laboratory

Fig. 105 displays some features of the two-body kinematics of the reaction $\bar{p}\rightarrow e^+e^-$. On the first row, the correlation between momentum and angle of one of the leptons shows the extension of the range of momenta with increasing incident energy. Independently of the incident energy, the electrons have a minimum energy varying slowly with incident momentum p_{inc}:

$$p_{min} = \frac{m_p}{2}\left(1 + \frac{m_p}{2p_{inc}} + o\left(\left(\frac{m_p}{p_{inc}}\right)^2\right)\right) \tag{74}$$
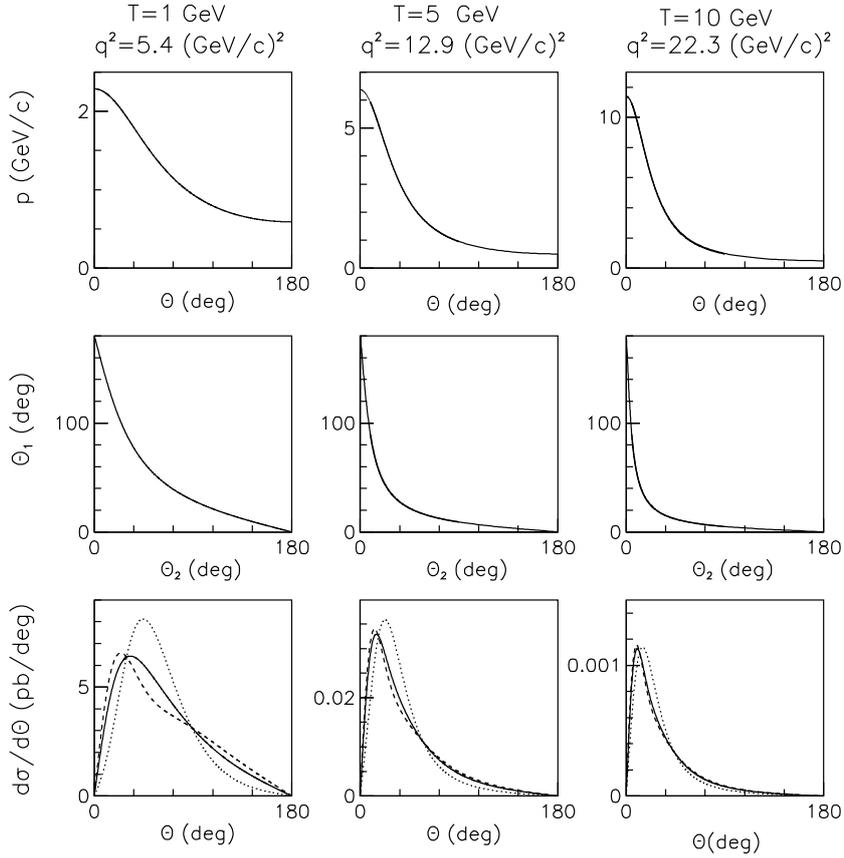
Figure 105: *For three different incident energies of the antiprotons, the correlations between the momentum and angle of one lepton and the angles of the two leptons are displayed in the first and second rows. The third row shows the laboratory angular distributions for R=0 (dashed line), R=1 (solid line) and R=3 (dotted line).*

and of the order of 500 MeV (i.e. close to $m_p/2$), which is reached at the most backward

T (GeV)	q^2(GeV/c)	θ_1 (deg)	p_1 (GeV/c)	θ_2 (deg)	p_2 (GeV/c)
1	5.4	19.	2.1	114.	0.76
2.5	8.2	14.	3.5	96.	0.9
5	12.9	10.8	5.8	80.	1.1
10	22.8	7.8	10.3	64.4	1.6

Table 11: Values of laboratory angles and momenta of the two leptons for $\cos\theta_{cm}=0.9$ at four different kinetic energies of the incident antiproton beam.

T (GeV)	q^2(GeV/c)	θ_1 (deg)	p_1 (GeV/c)	θ_2 (deg)	p_2 (GeV/c)
1	5.4	54.	1.44	54.	1.44
2.5	8.2	41.	2.2	41.	2.2
5	12.9	31.5	3.4	31.5	3.4
10	22.8	23.4	5.9	23.4	5.9

Table 12: Same as Table 11 for $\cos\theta_{cm}=0$.

angles. The maximum energy, reached at 0^0, is related to the incident momentum by:

$$p_{max} = p_{inc}(1 + \frac{m_p}{2p_{inc}} + o((\frac{m_p}{p_{inc}})^2)) \tag{75}$$

The correlation between the laboratory angles of the two leptons (second row) is the reflect of the back to back emission in the center of mass frame, whith the value of the angles of the leptons on the symmetry axis of the distribution corresponds to a center of mass angle of 90°.

The laboratory angular distributions are displayed in the third row. These distributions extend up to 180°, but the proportion of events at small angles increases with incident energy, due to the Lorentz boost.

In Tables 11 and 12, the laboratory momentum and angles are indicated for each incident energy for $\cos\theta_{cm}$=0.1 and $\cos\theta_{cm}$=0.9 respectively.

4.2.2   Angular coverage of the different subdetectors

Although $\bar{P}$ANDA has a very large acceptance, some losses due to the gaps between the detectors and to the beam pipes are unavoidable. In addition, the quality of the tracking and of the particle identification depends on the subdetectors encountered by the particle. Due to the almost perfect azimuthal symmetry of the $\bar{P}$ANDA detector, both effects depend to first order only on polar angle.

These subdetectors corresponding to the main angular ranges are listed in the table 13. The barrel part is playing the major role at low energies. The forward spectrometer is important at the highest energies for the most forward angles.

The hole due to the beam pipe, which sets the detection limit to 3^0 in the laboratory, corresponds to a cm angle such that $|cos\theta_{cm}| > 0.8$, even at the largest incident energies, so a very large fraction of the center of mass angular distribution will be measured, even for the highest q^2. However, the efficiencies and Particle IDentification (PID) capabilities of these detectors depend strongly on angle and momentum, which makes a study with full simulations mandatory (see sec. 4.12).

4.3   Different background reactions

Events coming from the reaction $\bar{p}p \rightarrow e^+e^-$ will be selected using the three following criteria: identification of an e^+e^- pair, kinematical constraints on their measured momenta and angles and absence of detection of an other particle. However, the cross-sections for this process (see table 10) is very small compared to the total annihilation cross-section which is of the order

angular range	electromagnetic shower	energy loss	Cerenkov light	tracking
0°-3°	no	no	no	no
3°-10°(hor.) 3°-5°(vert.)	Shashlik	MVD	dual radiator RICH	MVD + Forward spectrometer
5°-22°(hor.) 10°-22°(vert.)	EMC forward endcap	MVD + reduced STT	Forward DIRC	MVD+ reduced STT
22°-140°	barrel EMC	full STT	barrel DIRC	MVD+full STT
140°-185°	backward EMC endcap	reduced STT	no	reduced STT
185°-190°	no	no	no	no

Table 13: Different detector information available as a function of the polar angle.

of 70 mb for 9 $(\text{GeV/c})^2 \leq q^2 \leq 14$ $(\text{GeV/c})^2$, and is dominated by multi-pion production. Charged pions might be misidentified as electrons. In addition, a very intense production of dilepton pairs in $\bar{p}p$ reaction will come from photon conversion following π^0 decay into 2 gammas and π^0 Dalitz decay $(\pi^0 \to \gamma e^+ e^-)$. Three kinds of background were therefore investigated:

- two-body charged signals $(\bar{p}p \to \pi^+\pi^-, \bar{p}p \to K^+K^-,..)$, the two hadrons being misidentified as electrons: These channels have cross-sections of the order of 1-2 μb in the same energy range. Due to the lower pion mass, the e/π discrimination is the most difficult and the kinematics of the $\bar{p}p \to \pi^+\pi^-$ reaction is also the closest to the $\bar{p}p \to e^+e^-$ reaction. So, the background coming from $\bar{p}p \to \pi^+\pi^-$ has to be treated very carefully.

- Three or more body reactions like $\pi^+\pi^-\pi^0$, $\pi^+\pi^-\pi^0\pi^0$ ... with two misidentified hadrons as e$^+$e$^-$ pair and no other particle detected: These reactions have even higher cross-sections than two-body hadronic reactions. They are however easier to reject, since kinematic constraints will be more efficient than in the previous case.

- Backgrounds of the type e$^+$e$^-$X: (cross-sections?) Those might arise, either from direct production (like in the case of e$^+$e$^-\pi^0$) or, which is much more likely, from photon conversion, due to the very high cross-section for the production of π^0's. To reject these channels, the PID is of no help, but as the energy is shared among more particles, the hermeticity of the detector and the kinematical constraints should be very efficient.

Relying on these simple arguments, we investigated in more details the rejection power for the $\bar{p}p \to \pi^+\pi^-$ reaction.

4.4 Specific problem of the $\bar{p}p \to \pi^+\pi^-$ reaction

4.4.1 Event generator for $\pi^+\pi^-$ reaction

Global simulations are necessary to predict the residual background taking into account in a detailed way the expected performances of the different detectors and the pion angular distributions.

For this, a generator for the reaction $\bar{p}p \to \pi^+\pi^-$ was developed in order to take into account as well as possible the (rather scarce) existing data from CERN [217, 219, 218]. This is explained in detail in [220, 136, 200] and I will only show an example of description of the data in fig. 106. In addition, fig. 107 shows that the ratio

$$R_{\pi^+\pi^-} = \frac{\sigma(\bar{p}p \to \pi^+\pi^-)}{\sigma(\bar{p}p \to e^+e^-)} \tag{76}$$

of cross-sections for the reaction $\bar{p}p \to \pi^+\pi^-$ and $\bar{p}p \to e^+e^-$ provided by this generator varies for $q^2 = 8.21$ $(\text{GeV/c})^2$ from 10^5 at $\cos\theta_{cm} = 0$ to 3.10 [6] at $\cos\theta_{cm} = 0.8$. These numbers are obtained in the case of $G_M = G_E$, but within some factors 2-5, they give typical values for this ratio. The $\pi^+\pi^-$ channel angular distribution being much more forward peaked than the $\bar{p}p \to e^+e^-$ reaction, the rejection power will then have to be larger at forward/backward angles.

It has to be noted that the model used at high energies is not adapted for the forward/backward angles, but this has no consequence for our studies, since the detector efficiency is anyway very small for $|\cos\theta_{cm}| > 0.8$ (see section 4.12.1). This region has therefore been excluded from the simulations. The systematic errors due to the uncertainties of the $\pi^+\pi^-$ channel cross-sections and angular distributions will be discussed in sec. 4.12.4.
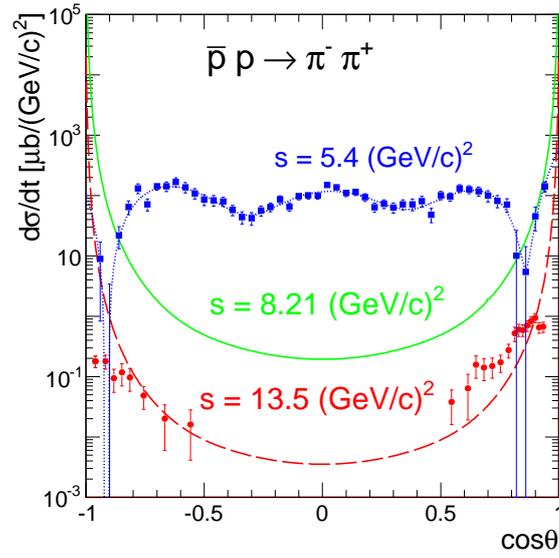
Figure 106: Center of mass angular distributions used to simulate the $\bar{p}p \to \pi^+\pi^-$ reaction at different energies compared to the data from [217] (squares) and [218] (circles).

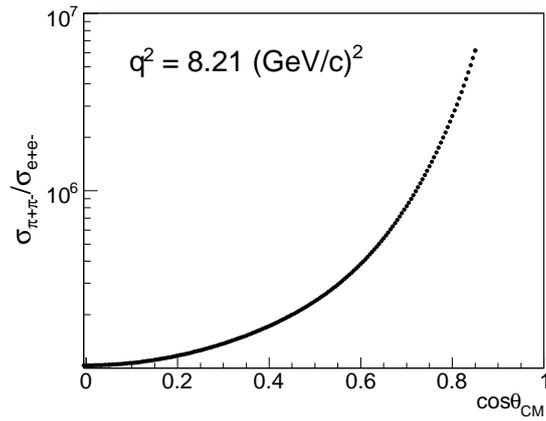Figure 107: Ratio of cross-sections of the $\bar{p}p \to \pi^+\pi^-$ to $\bar{p}p \to e^+e^-$ reactions as a function of center of mass angle for $q^2=8.21$ (GeV/c)^2.

4.4.2 Orders of magnitudes of needed rejection power

The reduction of the background $B_{\pi^+\pi^-}$ coming from the reaction $\bar{p}p \to \pi^+\pi^-$ to the level of $\sim 1\%$, requires, with the values of $R_{\pi^+\pi^-}$ quoted above a rejection factor

$$P_{rej} = R_{\pi^+\pi^-}/B_{\pi^+\pi^-} > 3\,10^8 \tag{77}$$

Just to give an idea of the challenging performances which are required, let us assume for a moment a constant pion MisIDentification (MID) probability $\mathcal{P}_{MID}$ for each pion, and disregard possible additional rejection factor related to the kinematic constraints. One would then need $\mathcal{P}_{MID} > 6.10^{-5}$.

Considering the geometry of the $\bar{P}$ANDA detector, the pion misidentification probability will in fact depend strongly on polar angles θ_1, θ_2 and momentum p_1, p_2, but more slightly on the azimuthal angles ϕ_1, ϕ_2, the condition (77) can then be written:

$$P_{rej}^{-1} = \mathcal{P}_{kin}(p_1, \theta_1, \phi_1, p_2, \theta_2, \phi_2) \text{ x } \mathcal{P}_{MID}(\theta_1, p_1) \text{ x } \mathcal{P}_{MID}(\theta_2, p_2) \; < \; 3\,10^{-9}, \tag{78}$$

where $\mathcal{P}_{kin}(p_1, \theta_1, \phi_1, p_2, \theta_2, \phi_2)$ is the probability of the $\pi^+\pi^-$ pair to fulfill the kinematical constraints.

Adding now that the different detectors provide independant informations related to e/π identification, one can further write:

$$\mathcal{P}_{MID}(\theta, p) \; = \; \mathcal{P}_{MID}^{(dE/dx)}(\theta, p) \text{ x } \mathcal{P}_{MID}^{(DIRC)}(\theta, p) \text{ x } \mathcal{P}_{MID}^{(EMC)}(\theta, p) \tag{79}$$

This illustrates that the complementarity of the different subdetectors in the different momentum and angle ranges is therefore crucial to achieve the required rejection factors. The individual capabilities of the detectors will be discussed in sec. 4.6, 4.7, 4.8 and will be used to estimate the rejection of the reaction $\bar{p}p \to \pi^+\pi^-$ either using the very simple relation (79) or using full-scale simulations.

4.5 Different simulation studies

The simulations consists in two steps. The first one, based on the GEANT4 code, is the propagation of the particles through the detector. The information on the hits and the energy losses in each detector has been digitized, adding models for electronic noise and detector responses. The second step is the reconstruction of the physical quantities, as described in detail in [136].

4.5.1 Recent global simulations

The results of our feasibility study are based on full scale simulations using the so-called BABAR software which has been used for the physics benchmark simulations presented in [136]. They will be presented in section 4.12 and are the subject of our paper accepted for publication to EPJA [200].

4.5.2 Older local and global simulations

The first steps of these studies started however at a time (2004-2006) where the full scale simulation and analysis software (version 2.2.6) was not fully reliable and the geometry of the detectors not fixed, in such a way that only qualitative results could be deduced. So, local simulations aimed at studying the response of each detector individually, were also developped and used in particular for the electromagnetic calorimeter and for the central tracker, as will be

shown in the following subsections. One of the interests was an easier study of the sensitivity to the parameters of the simulations. We tried also, whenever possible, to use available information on particle identification with existing detectors. We will not present a detailed report of these early studies, but we will throughout the following subsections discuss some key problems that were first studied at that time and point out the crucial points that should be controlled in the simulations.

4.6 e/π discrimination with energy loss in central tracker

In $\bar{P}$ANDA, two detectors will provide dE/dx measurements, the MVD and the central tracker. The MVD informations can not be useful for e/π discrimination due to the small total thickness ($\sim$100 μm of Si). As for the central tracker, we investigated in detail the STT option, since the TPC should display even better identification capabilities due to the higher number of measurements and better track length resolution.

4.6.1 Check of energy loss calculations in GEANT4

The basic mechanism of the ionization process is an inelastic collision of the incoming charged particle with the electrons of the material, ejecting an electron from the atom : e^- + atom $\rightarrow e^-$ + atom$^+$ + e^-. In each individual collision, the energy transferred to the electron is peaked at about 20 eV. The fluctuations of the energy loss in a given length of material are due to the fluctuations of the number of collisions, and are therefore all the more reduced than the length of material is larger. The standard calculation of energy loss in GEANT4 (G4eIonisation) is based on a very simple model of the particle-atom interaction. The atoms are assumed to have only two energy levels E1 and E2, and the particle-atom interaction can be either an excitation with energy loss E1 or E2 or an ionization with energy loss distribution g(E) $\sim 1/E^2$.

In order to check the validity of the model used in GEANT4, an independent code was developed by Jacques Van de Wiele to calculate the energy loss by using directly the atomic cross sections [221, 222]. These calculations are in good agreement with the Bichsel's method [223] which has been recently successfully applied to describe ionization energy losses of pions in the STAR TPC [223] and protons in the Alice test TPC [224]. The energy losses obtained with Jacques Van de Wiele's model have been compared to the standard G4Eionisation model for an incident electron at 500 MeV/c in Ar gaz and different widths (fig.108). In average, about 40 collisions occur per cm of Ar gas at 1 atm and, as expected, the tail of the distributions increases when the thickness of material decreases. The STT should be operated at 2 atm, so these numbers should be scaled by a factor 2.

For thickness larger than 5mm, the two calculations nicely agree, however for smaller widths, there is an increasing difference. This means that only the first moments of the energy loss distribution in one collision are correctly described by the G4eIonistaion model, which is not sufficient for small material thickness, due to the small number of collisions.

However, GEANT4 also provides a more sophisticated model for energy loss in small width of material: the PAI model (Photoionisation absorption model) [225], which uses the photoionisation cross section, exactly as Jacques Van de Wiele is doing himself . The comparison is shown for widths of 1 and 2 mm of gaz in fig.109. One can see that the agreement is very good, (although not perfect, maybe due to some approximations made in the model for the implementation in GEANT4). In oder to treat with the best precision the energy loss in the case of small path in the straw tubes, we therefore recommended the use of the PAI ionisation model in the PANDA GEANT4 simulations. The good accuracy of the
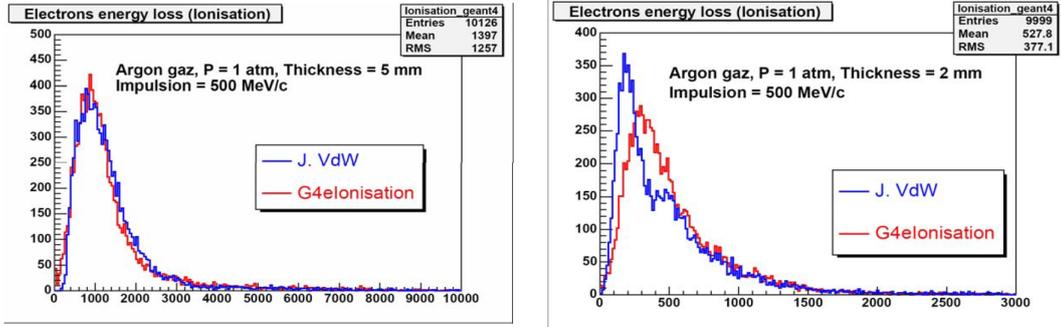
Figure 108: Electron energy loss by ionisation in (5 mm) (left) and 2 mm (right) of Ar gas at 1 atm calculated in Jacques Van de Wiele's calculation (J.VdW, blue) and using G4eionisation (red).
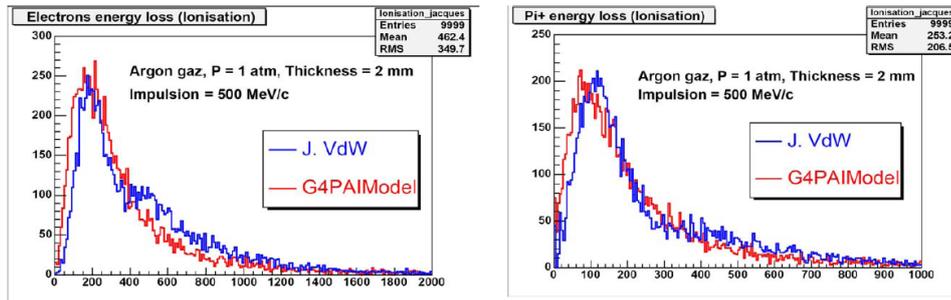
Figure 109: Electron energy loss by ionisation in 2 mm (left) and (1 mm) (right) of Ar gas at 1 atm calculated in Jacques Van de Wiele's calculation (J.VdW, blue) and using the PAI GEANT4 model (red)

description of ionization energy loss of high energy protons and electrons by the PAI model in GEANT4 has also been tested recently in [226] for straw tubes filled with Xe/CO_2.

It is however obvious, that the measurements for very small track length should be eliminated, since the fluctuations are in this case very large. An important parameter is also the precision in the determination of the track length, which is reduced in the case of particles passing at the extremities of the straw tubes. Investigations in this respect have been started [227], but still need to be pursued to determine a value for this minimum width or eventually to adapt the method to take into account the different track length.

At present, the standard truncated mean method is used, as will be explained now.

4.6.2 Truncated mean method

The first use of this now widely used method can be traced back to the particle identification in the JADE detector [228]. It is based on the fact that by rejecting the highest dE/dx measurements from the sample, the average of the remaining value has a much narrower and gaussian-like distribution than the full energy loss distribution. The proportion of dE/dx measurements to be kept is optimized [229] for each detector, since it depends on the number of samples and the length of the volume.

The truncated means of the energy losses of the simulated events in the STT are displayed on fig. 110 as a function of the reconstructed momentum. The track length is calculated from the intersection of the reconstructed track with the straw tube, taking into account a position measurement resolution σ=150 μm, in agreement with the tests of the STT prototypes.
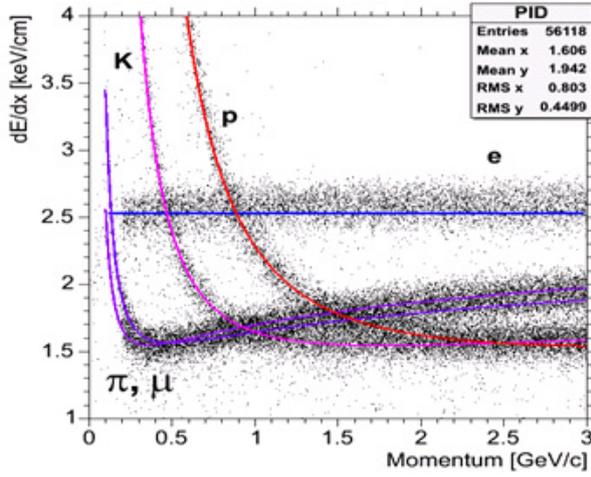
Figure 110: dE/dx of different particles as a function of momentum in the TPC.
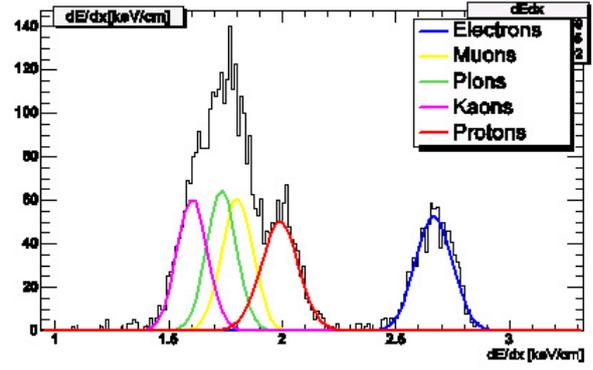
Figure 111: dE/dx in the STT for different particles at p=1.2 GeV/c.

The average and sigma values of gaussian fits of the truncated mean distributions are then parametrized for 50 bins in polar angle and momentum. The width of the gaussian decreases when the polar angle goes from $17°$ to $22°$, due to the increasing number of hit tubes. When the maximum number of 24 hit tubes is reached, the width of the gaussian gets larger as the angle increases due to the decrease of the thickness.

The truncation parameter, i.e. the proportion of energy loss measurements used for the calculation of the mean, has been fixed to 70%. The main criterium of this optimization is not the reduction of the gaussian width (which would lead to a truncation parameter of 80%, but the suppression of the non-gaussian tails which might lead to an overlap of the electron and pion dE/dx distribution. The resulting energy loss is found to be gaussian for each particle species to an extremely good precision, see fig. 111. The separation between electrons and pions is about 6-8 σ at 1 GeV/c and still 3-5 σ at 3 GeV/c, which ensures a significant e/π identification power up to large momenta.

4.6.3 PID likelihoods for dE/dx measurements

Distributions of PID likelihoods (fig. 112) have been calculated using uniform distributions of particles with momenta between 0.2 and 10 GeV/c and polar angles between $14°$ and $140°$. For a given triplet (p, θ, dE/dx$_{trunc}$), five likelihoods are calculated for the different particle species (e, μ, π, K and p) using gaussian distributions obtained as explained in the previous section. The peak at 0.2 is due to the fact that when the five likelihoods are below 1%, an equal probability of 0.2 is set to each particle identification.

4.6.4 dE/dx resolution obtained with other detectors

The dE/dx resolution of drift chambers follows the empirical formula [230]:

$$\sigma/(dE/dx)_{trunc} \sim 0.41 n^{-0.32}(tp)^{-0.43}, \tag{80}$$

where n is the number of measurements, t the thickness in cm, which goes as $1/sin\theta$ and p the pressure in bar. This trend has been experimentally measured in several detectors. As an example, we show the spectrum measured using the BABAR Cylindrical Drift Chambers (CDC), covering a total width of 54 cm in 40 layers [231], and using a mixture of He (80%) and isobutane (20%), which is fully gaussian for electrons with a width of 7.5 % (fig.113),
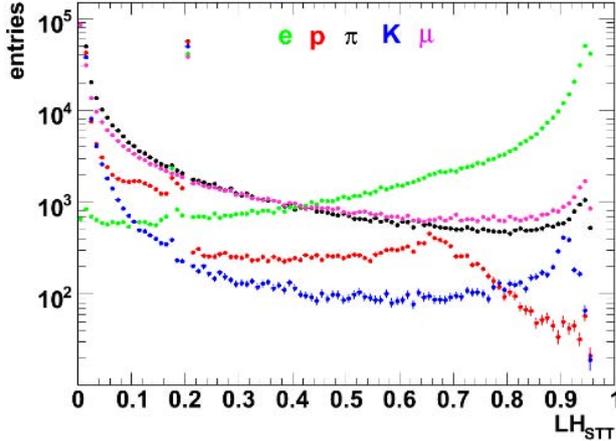
Figure 112: Distributions of PID likelihoods obtained for the STT detector for different particle species.
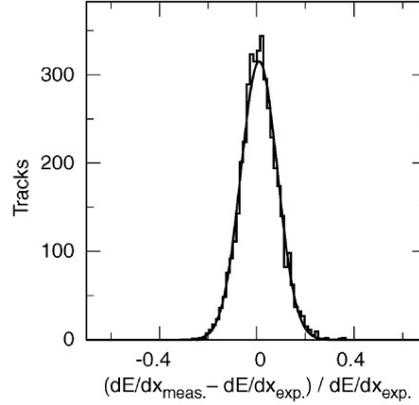
Figure 113: dE/dx resolution measured in the BABAR experiment using Babbha scattering events, defined as the relative difference between the measured truncated mean $(dE/dx)_{meas}$ and the expected one (dE/dx_{exp}).

close to the expectations. Similar results are also obtained for the BELLE Small Cell drift Chamber (CDC).

The angular dependence of the resolution obtained for the $\bar{P}$ANDA STT simulations is in good agreement with eq.(80), which gives confidence that the simulations are realistic.

Nevertheless, according to the experience from these detectors, precise calibrations of the dE/dx measurements, on a cell by cell basis, are necessary, to obtain such resolutions, due to fluctuations of temperature, gaz mixture, or electronics.

In cylindrical drift chambers or TPC's, the different energy loss measurements correspond to approximately the same track lengths. This is very different in the case of cylindrical straw tubes, and the determination of the track length for each straw tube is one source of error for the determination of $(dE/dx)_{trunc}$, as already discussed at the end of section 4.6.1. This is however in principle taken into account in the simulation using a position resolution of 150 μm which was checked in the STT protype.

4.7 e/π discrimination with the DIRC

p(GeV/c)		β	$\beta\gamma$=p/m	$\cos\theta$	θ (deg)
π^-	0.5	0.963	3.597	0.706	45.11
e^-	0.5	1.000	980.	0.680	47.16
π^-	0.8	0.985	5.755	0.690	46.36
e^-	0.8	1.000	1570.	0.680	47.16
π^-	1.	0.990	7.194	0.687	46.64
e^-	1.	1.000	1960.	0.680	47.16
π^-	1.5	0.996	10.791	0.683	46.93
e^-	1.5	1.000	2940.	0.680	47.16

Table 14: Cerenkov angles in the DIRC for electrons and pions of same momenta.

118

A charged particle with velocity β produces Cerenkov light in the quartz cristal emitted in a cone of angle θ with $\cos\theta = 1/n\beta$, where n=1.47 is the refraction index of the quartz. In Table 14, the Cerenkov angles for electron and pions are shown at different momenta. At a given momentum, the cone of light produced by an electron at any momentum has a fixed opening angle of 47.16°, while it is narrower for a pion, due to its lower velocity. However, the difference between these angles diminishes rapidly with increasing momentum (see fig. 114).
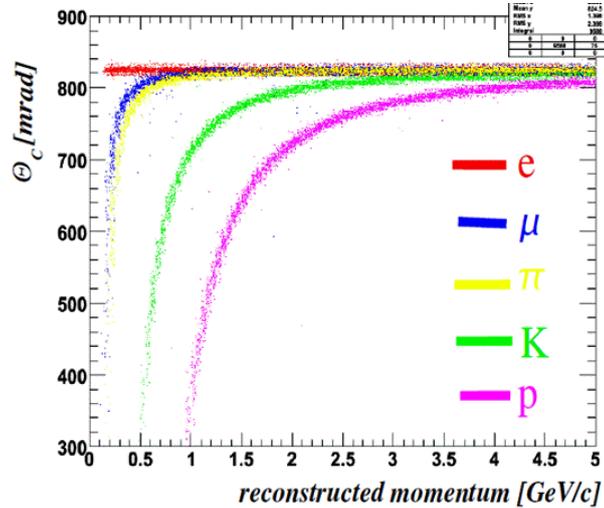
Figure 114: Reconstructed DIRC light cone angle as a function of the reconstructed momentum
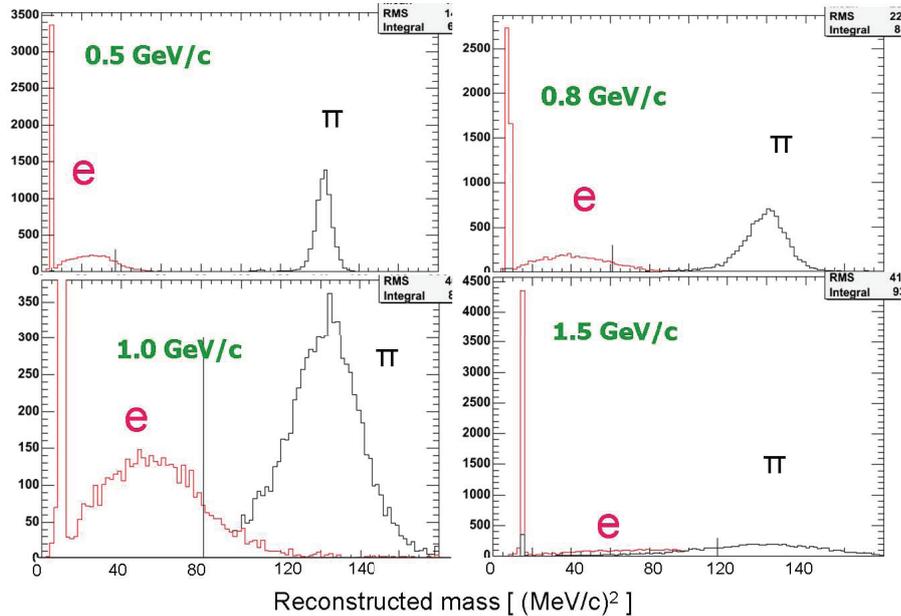
Figure 115: Reconstructed mass in the DIRC detector for electrons and pions at given momenta.

As the resolution expected for the measurement of the DIRC angle is ~ 2.3 mrad at 1 GeV/c, one can already conclude from Table 14 and fig. 114 that the discriminating power of the DIRC will be very good at 500 MeV/c and will almost vanish around 1.5 GeV/c. The parametrization of the resolution used in the simulation should be realistic since it was checked with real data in the case of the BABAR DIRC, which is, with the exception of the

imaging very similar to the BABAR DIRC [232, 233]. The simulation and reconstruction softwares are also to a great extent copies of the BABAR ones.

In the first version of the software, a mass was also calculated from the angle θ of the light cone measured in the DIRC and the momentum provided by the tracking using the equations

$$\beta = \frac{1}{n cos\theta} \tag{81}$$

$$m = \frac{p}{\beta\gamma} = \frac{p}{\sqrt{n^2 cos^2\theta - 1}} \tag{82}$$

The distribution of this "mass" is shown for electrons and pions at given momenta in fig. 115. Due to the resolution, the angle can be found to be larger than the physical limit given by $cos\theta = 1/n$. In this case, the mass assigned to the particle is set to a constant value depending on the momentum, which explains the peaks in the picture. The latter are of course mostly due to electrons which have Cerenkov angles close to the limit, but it can also happen for pions at the highest energies. The pictures show clearly that this "mass" variable has a rather large discriminating power up to 1 GeV/c. We will show in sec. 4.9.1 estimates based on this mass variable. In the BABAR software used for the main results of these studies, a PID probability for each particle species (e,π,μ,K,p) is calculated directly from the Cherenkov angle distribution as a function of the momentum and angle of the particle.

4.8   e/π discrimination in the ElectroMagnetic Calorimeter

4.8.1   Involved physical processes
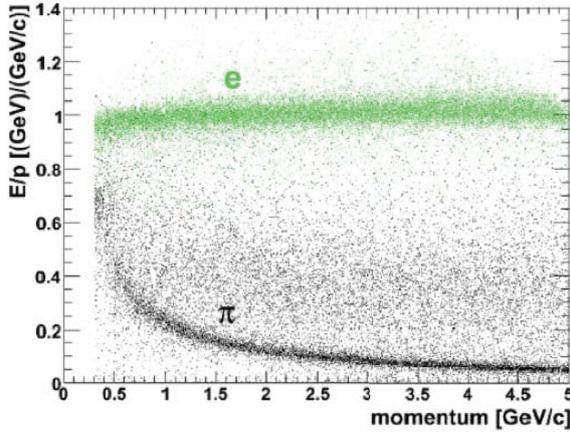
Figure 116: Ratio E/p of the energy deposit in the Electromagnetic Calorimeter to the particle momentum as a function of the particle momentum.
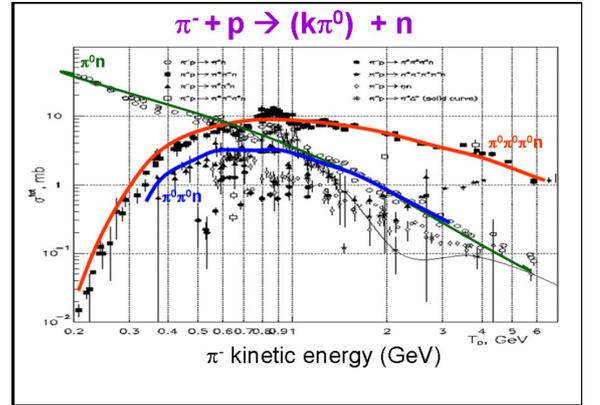
Figure 117: Cross sections for different π^0 production channels of the π^-p reaction.

The principle of pion/electron discrimination in the electromagnetic calorimeter is based on the different energy deposits of both particles at a given momentum:

The most important process for electrons with energies above 10 MeV is the production of an electromagnetic shower. Due to the large crystal length (l=22.5 X_0), almost all its energy will be converted into light. As for pions, only a fraction of the incident energy is deposited in the calorimeter, via ionization process. For minimum ionizing particles (i.e. pions of about 400 MeV/c), the average energy loss is 10.2 MeV/cm in PbWO4, which means that assuming normal incidence on the crystals, such pions will loose about 200 MeV. Over the whole energy

range from 500 MeV to 15 GeV, the energy loss ΔE_{ion} increases only by 40%, so the fraction of energy deposit due to the ionization $\Delta E_{ion}/$p decreases very rapidly, as shown in the fig. 116.

However, due to the rather small interaction length of PWO4 material ($\lambda_I = 20.2$ cm), the probability of a nuclear interaction of the pions in the crystals is of the order of 60%. Dealing with pion/electron identification, the most important number is the probability that the pion looses most or even all its energy in the calorimeter, making this pion behave like an electron.

Quasi elastic charge exchange processes : $\pi^+ + (Z, A) \to \pi^0 + (Z+1, A)^\star$ or $\pi^- + (Z, A) \to \pi^0 + (Z-1, A)^\star$ are the best candidates for such maximum energy deposits, since they provide the highest possible energy to one single π^0. This particle decays immediately into two γ which have a high probability to loose all their energy in the calorimeter. In addition, the small recoil and excitation energy of the nucleus can be converted into light. The total energy deposit will of course depend on the depth of the interaction point in the crystal and on the emitted particles energy, but it has some probability to be close to the total pion energy ($E_{dep} \sim E_\pi + m_\pi$). At higher energies, the production of several neutral pions has a higher cross-section than the charge-exchange cross-section (see fig. 117). As a consequence, it can also contribute to the high energy deposits. As these cross-sections decrease with energies, the e/pion discrimination with the EMC should be however easier at higher energies.

These first observations point to the fact that a precise description of these complex hadronic reactions is needed in order to provide realistic description of the energy deposit distributions of pions in the calorimeter and especially at the end point.

4.8.2 Physics models in Geant4

GEANT4 is a very broadly used software toolkit for the simulation of the passage of particles through matter [234, 222, 235]. The physical processes include electromagnetic and strong interactions over an energy range covering optical photons and thermal neutrons to the highest energies available at LHC or in cosmic rays experiments.

Although some refinement of the electromagnetic interaction physics lists, concerning e.g. multiple scattering or electromagnetic interactions at very low energies were performed recently [222, 235], the level of precision of the description of electromagnetic processes is considered as very high. An example of accuracy obtained for an application concerning electronic showers in an Electromagnetic Calorimeter is shown in fig.118 for the BABAR EMC [236]. The description of hadronic processes is a more difficult task. Geant4 includes cross-
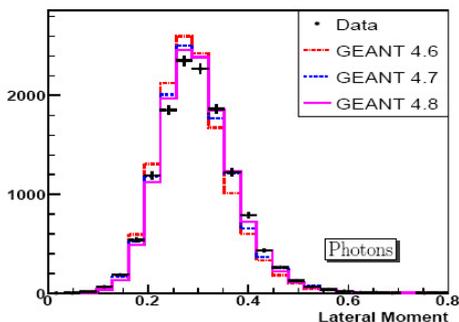

Figure 118: The lateral moment, which describes the lateral shower shape measured in the BABAR EMC (see eq.(83)) is compared to simulations with different versions of GEANT4.

sections and physical models for hadronic interactions from thermal energies (for neutrons) to hundreds of GeV, as shown on fig.119. In many cases, the user has to choose between several
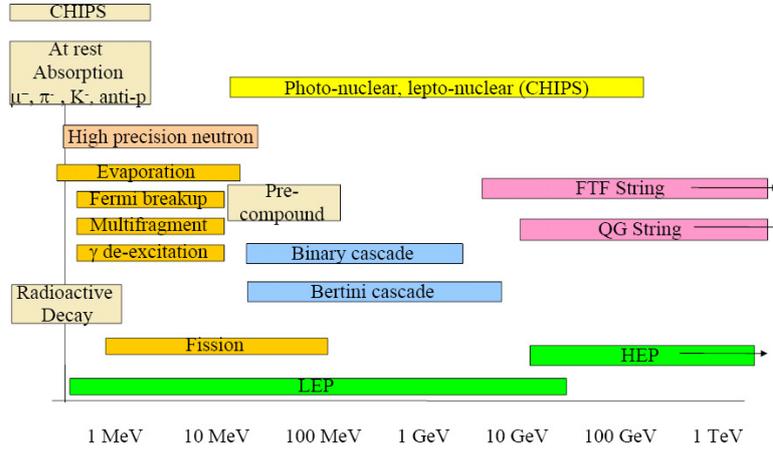
Figure 119: Hadronic models in GEANT4

models, depending whether the priority is set on the CPU reduction or on the precision. In the latter case, it has also to be considered that the level of precision of a given model also depends on the exit channels (neutron production, pion production,...). In addition, the domain of applications of the models have to be checked carefully for each version of the software.

The interaction is described in most of the cases by two different models: one describing the initial stage of the reaction, where fast particles are produced, and the other describing the deexcitation phase of the excited nucleus. We will focus on the initial stage. The Quark Gluon String (QGS) model and a Fritiof-like String model (FTF) can be used at high energies (E$\geq$ 20 GeV), and for energies below E$\sim$10 GeV, two cascade models are provided: the Bertini Cascade and the Binary cascade. The Bertini type cascade is suited for incident nucleons, pions, kaons and hyperons up to 10 GeV [237]. The Binary Cascade (BIC) [238] describes interactions of incident protons, neutrons, pions, or light ions and is based on two-body to two-body or two-body to one-body interactions within the target nucleus. In this model, inelastic nucleon-nucleon interactions or meson-nucleon interactions produce resonances which then interact with other nucleons or decay. The Binary Cascade is known to describe better the production of secondary particles produced in interactions of protons and neutrons with nuclei. However, it is at the moment restricted to lower energies than the BERTINI Cascade, especially for the pions. A fast alternative to these theory-driven models is provided by the LEP (Low Energy Parametrized) and HEP (High Energy Parametrized) models which use parametrizations of interaction models and cover all long-lived particles at all energies. They have their origin in the GHEISHA Fortran code which was used in Geant3 and are combined in the different Geant4 physics lists, like LHEP,LHEP_BERT,QGSP_BERT, QGSP_BIC, ...

We focused on energies below 5 GeV and investigated the choice between LEP or BERTINI and Binary cascade, having in mind that the crucial problem is the description of the highest pion energy deposits, related to the charged pion charge exchange process (see sect. 4.8.1)

4.8.3   Validation of low energy hadronic models

Since 2002, a big effort was made to validate the low energy hadronic models used in Geant4 on existing data. This "validation suite" was motivated by different types of experiments requiring both full scale simulations and high precision description of hadronic interactions. The need for precise simulation of hadronic showers in the hadronic calorimeter for LHC experiments played a major role. As these showers result from various physics processes occuring at very different energies, the simulations present a sensitivity to the low energy

hadronic models. It has in particular been shown that the effect of cascade models is to make these showers longer and wider, in better agreement with the test beam data [239].

There are also recent validation studies concerning electromagnetic calorimeter response to hadronic particles, more precisely from CMS electromagnetic calorimeter test beams performed in 2004 and 2006. This is of particular interest to us since the crystals consist of the same material and have a length only 10% larger than the PANDA's ones (ref sur CMS calorimeter).

The picture 120 shows the energy deposit of pions of 5 GeV energy in the CMS Electro-Magnetic Calorimeter compared to GEANT4 simulations using the physics list QGSP-BERT [240, 241]. The response displays two peaks, corresponding respectively to ionization and to nuclear interactions. The detailed comparison of the response of the crystals to pions at the
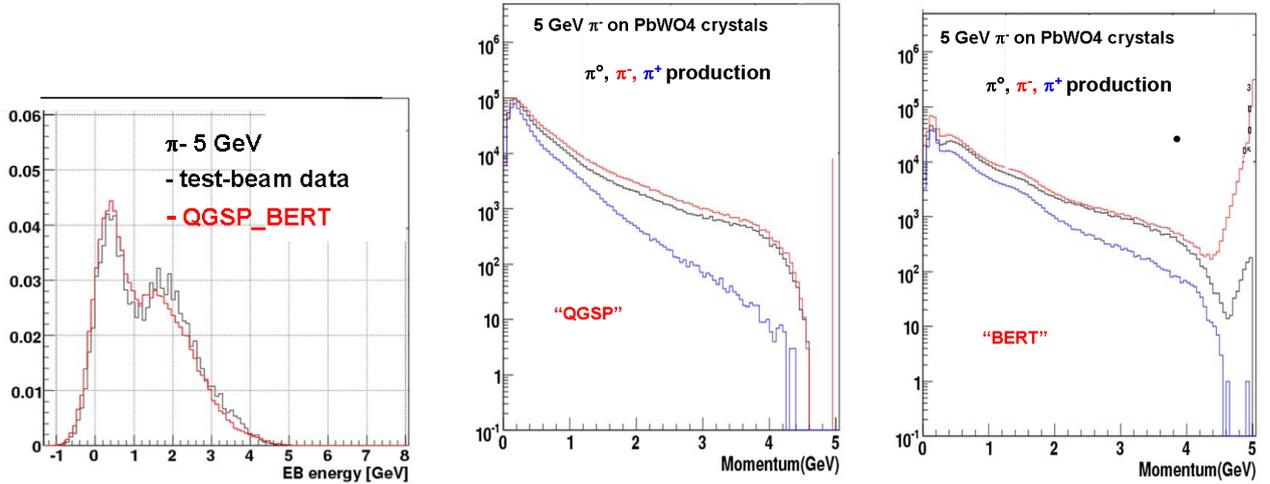
Figure 120: Left:Comparison of the energy deposit by 5 GeV π^- in the CMS EMC to GEANT4 simulations using the physics list QGSP-BERT [240]. Center and right: momentum distributions of π^+, π^- and π^0's produced in the interaction of 5 GeV π^- with Pb in the GEANT4 physics lists QGSP (left) and QGSP-BERT (right) [240].

lowest energies is also very interesting (fig.120). The energy deposit is quite well reproduced, and the simulations has even a tendancy to overestimate the yield at the highest values, which conforts the fact that simulations with the BERTINI cascade are not too much optimistic. Incidentally, these tests also give interesting information related to the light collection in PbWO4 crystals, which should be studied in more detail.

A simulation study of the particle production following interaction of protons, neutrons and negative pions with the PbWO4 crystals has also been made in [240, 241]. For example, fig.120 shows the pion production in pion interactions on PbWO4 crystals at 5 GeV in QGSP (which uses the LEP model at low energy) and QGSP_BERT, which uses the Bertini cascade. A higher yield of high energy π^0s produced in the quasi elastic charge exchange process is observed in the physics model including the cascade. As we expect these π^0s ptoduction to be just the limiting factor for e/π discrimination, this shows that it is safe to use the Bertini cascade, as the most "pessimistic" model in this respect.

4.8.4 "Local" simulations of pion energy deposits

In the course of our preliminary studies, we also studied the sensitivity of the pion energy deposit distribution to different physics models available in the GEANT4 library.
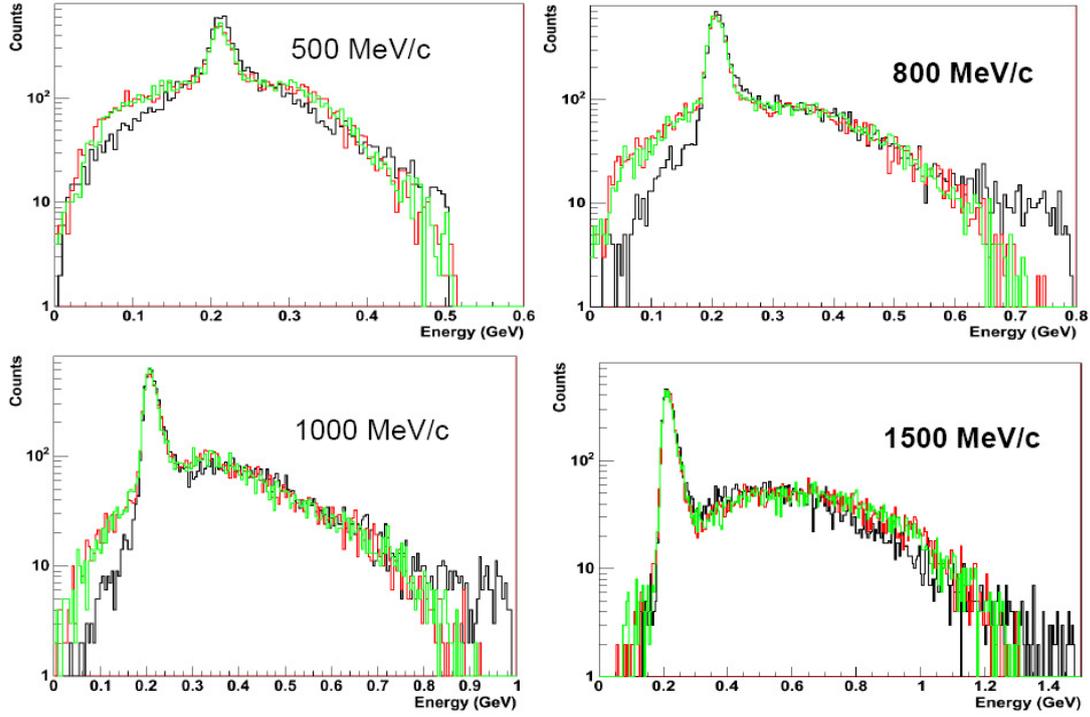
Figure 121: Energy deposit distribution in a 9x9 matrix of PbWO4 crystals for π^- at different incident momenta simulated with GEANT4, using different physics lists: LHEP (red), LHEP-BIC (green) , LHEP-BERT (black).
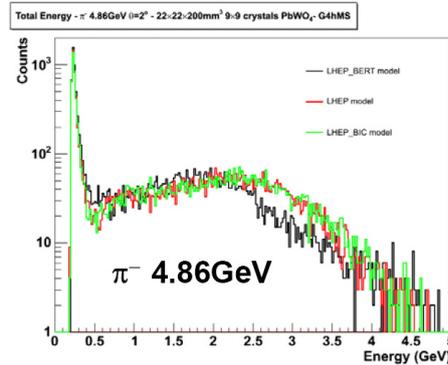
Figure 122: Same as fig. 121 for π^- at 4.86 GeV.

This was done using a "local" GEANT4 simulation using a 9*9 PbWO4 crystal matrix (2 cm x 2 cm x 20 cm) and studied the response of this "reduced-size" calorimeter to 10^6 positive and negative pions impinging on crystals at normal incidence and with momenta between 500 MeV/c and 5 GeV/c. We used 3 different hadronic models currently used in GEANT4 simulations: LHEP, LHEP_BERT, LHEP_BIC.

The first library includes the LEP and HEP parametrized models only, while the two others use the Bertini or Binary cascade, as described in sec.4.8.2.

The results of the simulation, shown on fig.121, on fig.122, clearly show the ionisation peak, centered at about 200 MeV and a much broader distribution, covering all energy loss values, up to the total incident pion energy. The broader structure is obviously due to hadronic processes and concerns at 500 MeV/c about 2/3 of the pions which undergo an interaction in the PBWO4 crystal, in agreement with the rough estimate from the nuclear
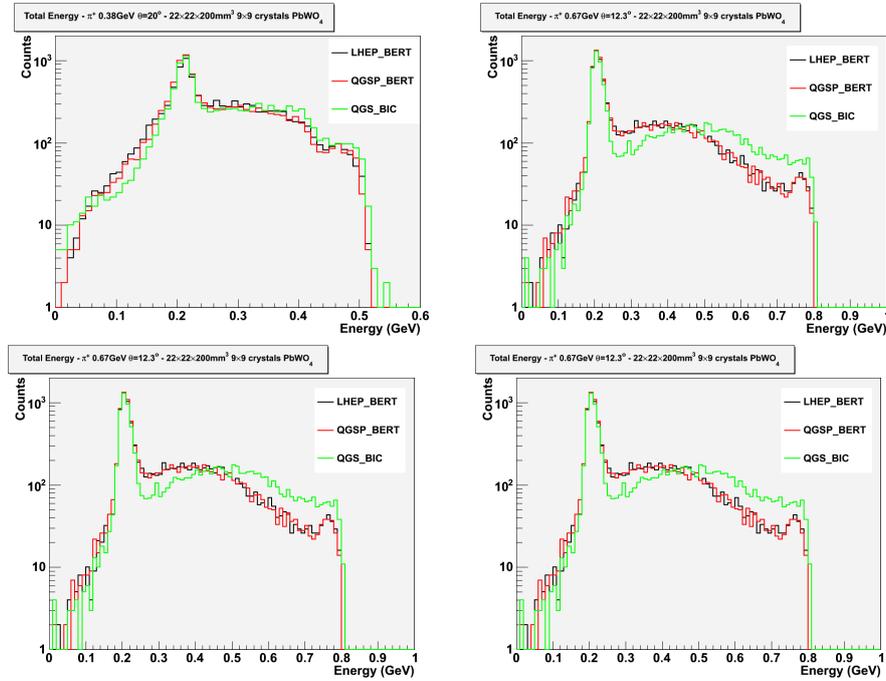
Figure 123: Same condition as fig.121, with comparison of π^+ fot LHEP (black), QGSP-BERT (red), QGSP-BIC (green) physics lists.

interaction length. In addition, the contributions at energy deposits close to the incident pion total energy, decrease with pion energy, as expected from our considerations about charge exchange cross sections.

In the version 8.0 which was used for this study, the Binary Cascade was implemented only for pions, which explains that the results are the same than for LHEP. The physics list LHEP_BERT, with the BERTINI Cascade for pions up to 10 GeV, gives somewhat different results. The difference at the lowest energy deposits is due to the different treatments of absorption and evaporation processes. Most interesting for our studies is the contribution at the highest energy deposits, which is, for both π^+ and π^-, higher in the model including the BERTINI cascade. The contribution at high energy deposits is higher for π^+ by about a factor 2, than for π^-, which can be qualitatively explained by the higher number of neutrons in the crystal nuclei, resulting in a higher probability of the charge exchange process.

Another physics list has been tested: QGS_BIC which uses the Binary cascade for pions of energies lower than 1.2 GeV and is available in GEANT4, for versions more recent than 9.0. The results obtained with QGSP_BERT and LHEP_BERT are very close, which is expected. since the models differ only for energies greater than 5 GeV. The QGS_BIC physics list, which includes the Binary Cascade for pions with energies up to 1.2 GeV produces a factor 2-3 more yield in the region of the highest energy deposits. This difference is smaller in the case of π^-.

4.8.5 Conclusion about hadronic models in GEANT4

The version of the PANDA software used for the TPR was using the library LHEP in a GEANT4 version 8.2. This model was fine for most of the PANDA applications, but not suited for describing π interactions in the Electromagnetic Calorimeter around 1 GeV. This is one of the reasons why the global simulations performed at that time could not be used for the estimates of pion rejection (see sec. 4.9.1).

The final results of our estimates used the BABAR software, where the hadronic model, taken from the CLHEP libraries built by the BABAR collaboration, is close to the LHEP_BERT

GEANT4 model, which gives good reproduction of the available data, as was shown before.

At the moment, the pion energy for the Binary cascade is limited to 1.2 GeV, and this model has therefore not been used in the PANDA simulations. With the Binary Cascade, the yields in the high energy deposit region are however higher than those obtained with the Bertini cascade by factors 2-3. Although the present results from EMC response to pions are in good agreement with physics lists including the BERTINI cascade, this shows the level of uncertainty that might arise from different models. Clearly, it will be necessary to continue to follow the validation studies of hadronic models in GEANT4 in the next years and update our simulations with the best physics lists. Besides, one can consider that the data from the P̄ANDA EMC will consitute good tests for these GEANT4 physics models.

4.8.6 Material budget and bremstrahlung effect on the electron response
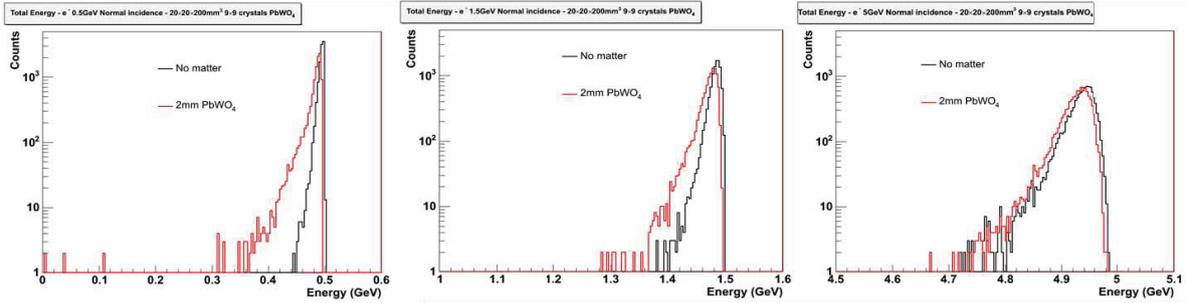
Figure 124: Effect of a 2 mm PbWO$_4$ slab (X/X$_0$=0.2) on the energy deposit of an electron at different momenta
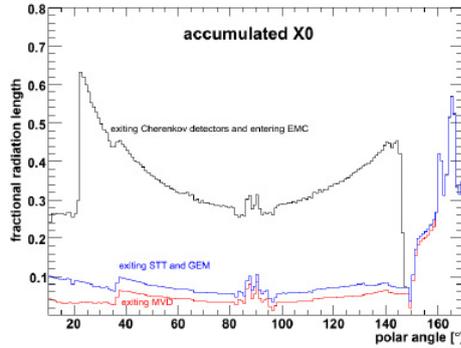
Figure 125: Distribution of material budget measured in radiation lengt units, as a function of polar angle.

For an electron at a given momentum, the energy deposit in the calorimeter appears at an energy slightly lower than the incident energy and with an asymmetric distribution. This is the effect, on the one hand of the energy loss by radiation and ionization of the electron, before entering the calorimeter and, on the other hand, of the photons or electrons produced in the electromagnetic shower and escaping from the crystal. The width of the energy deposit distribution becomes larger with increasing electron momentum, due to the larger longitudinal extension of the shower and the higher probability for secondary electrons and photons to escape. However, the relative ($\Delta E/E$) width decreases, as expected from the usual behaviour of EMC resolutions.

To investigate the effect of Bremsstrahlung, we calculated the photon emission probability for electrons with different energies traversing a length X/X0= 20% corresponding to the full material budget in front of the calorimeter. Of course, the probability to emit high energy photons increases with energy, but it remains very small for this material budget.

To quantify the effect of the radiation before the EMC to the energy deposit in the calorimeter, the response of the calorimeter to an electron in normal incidence on the crystal is calculated both in the case of no material in front of the calorimeter and in the case of a 2 cm PbWO4 slab, corresponding to 20% X_0 (fig.124). This is a simplified way of quantifying the effect of material budget. This material piece in front of the calorimeter induces a shift, which is independent of energy, due to the ionization energy loss and a broadening due to the energy loss by Bremsstrahlung. The latter is significant at 500 MeV/c, but it is hardly visible at 5 GeV/c. Indeed, although the probability of high energy losses by Bremsstrahlung increases with incident energy, this is hidden by the energy loss resolution in the calorimeter. So the material budget is mostly important for the lowest energy electrons.

The Bremstrahlung effect is calculated with great precision in Geant4. It depends on the distribution of matter seen by a particle which is shown as a function of the polar angle in radiation length units in fig.125.

4.8.7 Conclusions for PANDA EMC particle identification

From these general observations, we can conclude that the key parameters for elecron/pion discrimination in the calorimeter are:

- the probability of π charge exchange reactions in the material (which depends both on the atomic composition of the crystal and its atomic surfacic density).

- the bremsstrahlung probability which is linked to the number of radiation lengthes of material in front of the calorimeter.

- the energy resolution of the EMC

- the momentum resolution, since a correlation between the energy deposit and the momentum is needed to distinguish pions and electrons.

4.8.8 Transverse shower shape and neural network

As ilustrated in fig. 126, the shower of an electron is on average narrower than the one developed by a pion. The shower shape can be parametrized using the following quantities:

- E1/E9, which is the ratio for a given shower of the largest energy deposit in one crystal to the sum of the 9 largest energy deposits.

- E9/E25, which is the ratio for a given shower of the sum of the nine largest energy deposits in one crystal to the sum of the 25 largest energy deposits. This is the quantity used in the BELLE analysis.

- mom$_{LAT}$, which is the quantity used by BABAR and is defined as:

$$LAT = \sum_{i=3}^{n} E_i r_i^2 / \left(\sum_{i=3}^{n} E_i r_i^2 + E_1 r_0^2 + E_2 r_0^2 \right) \qquad (83)$$

 – n: number of modules associated to the shower
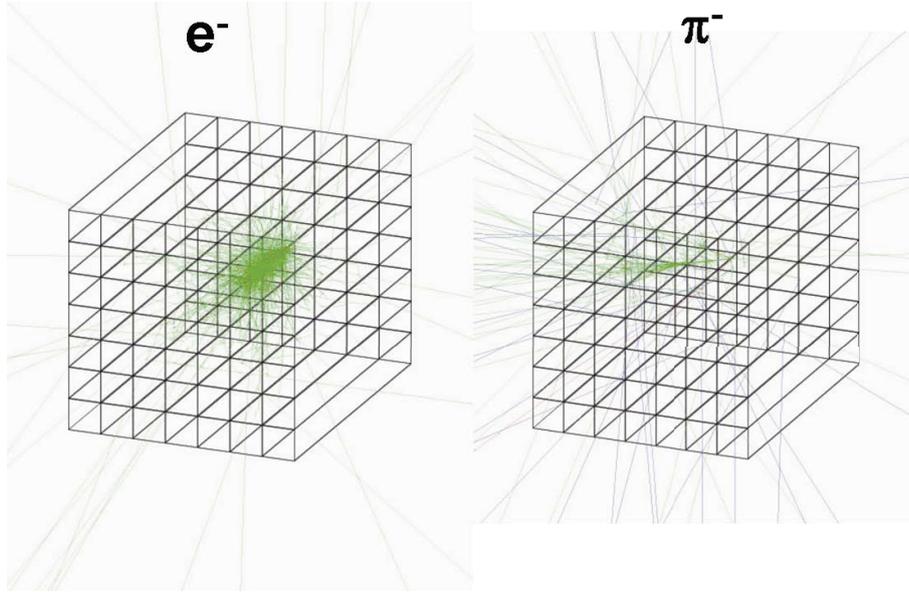
Figure 126: Examples of showers induced by an electron and a pion
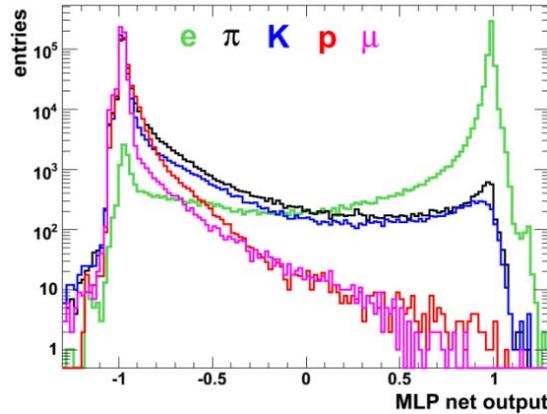
Figure 127: Distribution of neural network outputs for different particle species with uniform momentum and angle distribution between 300 MeV/c and 5 GeV/c.

- E_i: the energy deposited in the ith module with $E_1 \geq E_2 \geq .... \geq E_n$
- r_i: lateral distance between the central and the ith module
- r_0: the average distance between two modules

• 4 Zernike moments: 00, 31, 33 and 42 which describe the energy distribution within a cluster by radial and azimuthal polynomials.

To handle so many variables, instead of searching for optimal cuts in a multi-dimensional space, a neural network approach is adopted, based on the BABAR neural network PID code. The 7 quantities listed above, as well as E/p, p and the polar angle of the cluster are set as inputs of a neural network. In the learning phase, 850000 events for each species (e, μ, π, K, p) are used and the output is set to 1 for elecrons and -1 for the other particle species. The results for a test sample is shown on fig.127, which shows that this output has a very good identification power. A likelihood is then associated to the neural network output for the different particle species. In these conditions, the efficiency for electrons is above 98% for

E_{p_bar} (GeV)	Q^2 (GeV/c)²	θ_{CM}	θ_{lab}	p (GeV/c)	MP ECAL×DIRC×dE/dx	MP$_{tot}$
1.	5.4	20°	13°	2.2	$0.001 \times 0.5 \times 0.05 = 2.5\ 10^{-5}$	$0.1\ 10^{-9}$
		20°	132°	0.57	$0.033 \times 0.003 \times 0.03 = 3.0\ 10^{-6}$	
		90°	54°	1.43	$0.001 \times 0.3 \times 0.03 = 9.\ 10^{-6}$	$0.1\ 10^{-9}$
		90°	54°	1.43	$0.001 \times 0.3 \times 0.03 = 9.\ 10^{-6}$	
2.	8.2	20°	10°	3.7	$0.001 \times 1. \times 0.05 = 5.\ 10^{-5}$	$0.3\ 10^{-9}$
		20°	117°	0.7	$0.014 \times 0.014 \times 0.03 = 6.\ 10^{-6}$	
		90°	41°	2.2	$0.001 \times 1. \times 0.03 = 3.\ 10^{-5}$	$0.9\ 10^{-9}$
		90°	41°	2.2	$0.001 \times 1. \times 0.03 = 3.\ 10^{-5}$	
5.	12.9	20°	7.4°	6.1	$0.001 \times 1. \times 0.1 = 10^{-4}$	$0.6\ 10^{-9}$
		20°	102°	0.8	$0.014 \times 0.014 \times 0.03 = 6.\ 10^{-6}$	
		90°	32°	3.4	$0.001 \times 1. \times 0.05 = 5.\ 10^{-5}$	$2.5\ 10^{-9}$
		90°	32°	3.4	$0.001 \times 1. \times 0.05 = 5.\ 10^{-5}$	
10.	22.3	20°	5.4°	10.9	$0.001 \times 1. \times 0.3 = 3.\ 10^{-4}$	$5.4\ 10^{-9}$
		20°	85°	1.0	$0.005 \times 0.12 \times 0.03 = 1.8\ 10^{-5}$	
		90°	24°	5.95	$0.001 \times 1. \times 0.1 = 1.\ 10^{-4}$	$10.\ 10^{-9}$
		90°	24°	5.95	$0.001 \times 1. \times 0.1 = 1.\ 10^{-4}$	

Figure 128: E_{pbar} and Q^2 are the incident antiproton energy and corresponding four-momentum transfer squared, for two center of mass angles $\theta_{CM}=20°$ and $\theta_{CM}=90°$, the angles and momenta of each lepton of the e^+e^- pair are indicated in each line. The sixth column shows for each lepton the associated misidentification probability (MP) of a charged pion calculated as a product of the three individual misidentification probabilities in each detector type. MP$_{tot}$ is the product of the misidentification probability of a $\pi^+\pi^-$ pair emitted with a kinematics close to the e^+e^- pair.

momenta larger than 1 GeV, with π contaminations of a few 10^{-3}. At lower momenta, the efficiency drops, while the contamination increases, clearly showing the need for additionnal PID identification. More details about the neural network procedure and Zernike moments can be found in [136]. It is clear from these simulations, as well as from the results of BABAR [242] that taking into account the shower shape helps for the e/pi identification.

In $\bar{\text{P}}$ANDA, the size of the crystals being about twice as small as for BELLE/BABAR, a better precison on the shower shape can be expected. However, at the same time, the Moliére radius is smaller and the showers are expected to be narrower. In BABAR and BELLE's analysis, informations about the longitudinal shower shape could be extracted by a correlation between the hit crystal distribution and the extrapoled track. This could also be investigated in the $\bar{\text{P}}$ANDA EMC.

The most discriminating variable is however the total energy deposit divided by the momentum E/p.

4.9   Results for the rejection of the $\bar{\text{p}}\text{p} \to \pi^+\pi^-$ reaction

4.9.1   Rough estimates based on "hard cuts"

A rough global estimate of the pion misidentification probability was deduced in our preliminary studies by multiplying the three individual pion misidentification probabilities obtained for each detector (see eq.(79)). The latter were deduced in each case from the residual pion yield within "hard-cuts" applied on the most sensitive variables:

- For the DIRC, the global simulations with the version 2.2.6 of the $\bar{\text{P}}$ANDA software were used. A lower limit on the reconstructed mass (see sec. 4.7) was set in order to keep 90% of the electrons.

- As for the dE/dx, the estimates were based on gaussian truncated dE/dx distributions and keeping 90% of the electrons. To take into account possible non-gaussian tails, a minimum value of 3% was assumed for this misidentification probability.

- The lower limit on the ratio E/p was deduced from electron energy deposit spectra produced by the global simulations with the software 2.2.6 in order to have an efficiency of 80%. However, this simulation could not be used to estimate the pion misidentification probability, since the hadronic model used for GEANT4 was LHEP, which is too optimistic with respect to the yield at large energy deposits, as was shown in sec. 4.8.2. We used instead the local simulations with the $LHEP_{BERT}$ hadronic model (see sec.4.5.2).

The results of this procedure are displayed in the table shown in fig. 128. For each point of the angular distributions, the laboratory angle and momenta of both electrons have been calculated and the corresponding pion misidentification probabilities were estimated as described above. They give rough estimates for the pion misidentification probabilities for global electron efficiencies of 65%. The resulting numbers are higher than 10^8, which was our goal. These estimates do not take into account the kinematical correlation between both particles in the two body reaction, which are slightly different in $\bar{p}p \to e^+e^-$ and $\bar{p}p \to \pi^+\pi^-$. These numbers were therefore taken as a good indication for the feasibitility of the measurement. However, now that much more reliable numbers have been obtained from updated global simulations (see sec. 4.5.1), the interest is more limited. The variation of misidentification probabilities for the different detectors as a function of the momentum can be explicitly seen. It also demonstrates that for the most forward/background points of the angular distributions, the requested pion misidentification probability can be obtained as a product of a lower misidentification probability for the forward particle and a higher for the backward particle.

4.9.2 Effect of tracking resolution

As the PID is obtained as a correlation between DIRC angle, dE/dx and EMC informations and momentum, the momentum resolution might have an influence on the PID capabilities. However, the dependence of the dE/dx and Cerenkov angle with momentum is quite slow, so that a very small effect is expected. This is somewhat different for the EMC calorimeter, since the sensitive variable is E/p. With a 2% resolution on the EMC energy deposit, the momentum resolution will start to dominate the E/P resolution for momenta larger than 3-4 GeV depending on the angle. The tracks in the target spectrometer are fitted by the Kalman Filter algorithm (see [136] for details). The momentum resolution depends on multiple scattering, energy loss and bremsstrahlung, as well as position measurement resolution which are all taken into account in the full-scale simulations.

4.9.3 Final results based on full scale simulations

The final results of the $\bar{p}p \to \pi^+\pi^-$ are based on the full-scale GEANT4 simulations with the "BABAR software" (see sec. 4.5.1). In these simulations, the hadronic physics lists are taken from CLHEP libraries built by the BABAR collaboration, which should be very close to the $LHEP_{BERT}$ hadronic physics list of GEANT4 version 7.1. Concerning the ionization, the PAI model is used. Several batch farms have been used at GSI, IPN Orsay and CCIN2P3 during several weeks, to achieve these calculations.

Samples of 10^8 or $2\ 10^8$ events were generated at three different q^2, using the generators described shortly in 4.4.1 and in more details in [220], [136] and in [200]. Different levels of cuts on the electron identification probability (i.e. Loose:85%, Tight:99% or Very Tight:99.8%) have been tested. In complement to the number of $\pi^+\pi^-$ events surviving these cuts which

can be found in Table 2 of ref. [200], we show in Table 15 the rejection factors. The latter are defined as a ratio between the number of generated events to surviving events after each cut. With the Very Tight PID cuts, a reduction of a few 10^7 is achieved, corresponding to a physical background lower than 5%.

In addition to the PID cuts, the kinematical fit (four-momentum conservation) have been studied. By requiring two conditions fulfilled at the same time, namely: $CL_{e^+e^-} \geq 0.001$ and $CL_{e^+e^-} \geq 10\, CL_{\pi^+\pi^-}$, an additionnal reduction of a factor 50 to 100 can be achieved, with only slight dependence on the center of mass angle [136]. This provides a global reduction factor of a few 10^9, which is well above the requirements (see sec. 4.4.2).

q^2 [(GeV/c)^2]		8.2	12.9	16.7
	Loose	$2.3\ 10^5$	$2.3\ 10^4$	$6.7\ 10^4$
PID cuts	Tight	$3.2\ 10^6$	$1.4\ 10^6$	$1.7\ 10^6$
	Very Tight	$5\ 10^7$	$2\ 10^7$	$3.3\ 10^7$
kin. fit		125	100	80
kin. fit and PID Very Tight cuts		$6.3\ 10^9$	$2\ 10^9$	$2.6\ 10^9$

Table 15: Rejection factors of the reaction $\bar{p}p \to \pi^+\pi^-$ obtained on the one hand for different PID cuts corresponding to three different minimum values of the electron identification probability (Loose: 85%, Tight: 99% or Very Tight: 99.8%) and on the other hand for a minimum value of the confidence level of the kinematical fit of 10^{-3}. The last row shows the global rejection factor obtained as a product of factors obtained with Very Tight PID cuts and with the kinematical fit confidence level cuts.

4.9.4   Results obtained by BELLE and BABAR detectors

Useful informations about e/π discrimination can be found by studying performances of existing detectors, despite the fact that few experiments needed a discriminating power at the level of the one which is needed for our experiment. We have used in particular the results from the BELLE and BABAR experiments, which have some similarities with the $\bar{P}$ANDA set-up. The interesting point is that, in these experiments, the response of the detectors to samples of pions and electrons have beeen measured and that the pion misidentication probability and electron efficiency could be checked on real data[4].

In both detectors [231, 243], the identification is provided by a Cerenkov gas counter, an Electromagnetic Calorimeter and drift chambers and details about the electron identification performances can be found in [244, 245, 242, 246, 247]. The particle identification is based on probability distributions of sensitive variables for the different particle species, exactly as it is done in the $\bar{P}$ANDA simulations. The only difference is that, for the lateral shower shape, only one variable is used (see sec. 4.8.8) instead of 7 in the case of $\bar{P}$ANDA.

For both detectors, pure samples of electrons coming from the Bhabba events, with a pion contamination less than 10^{-3} and from pions coming from $K_s \to \pi^+\pi^-$, with an electron contamination below 10^{-4}. These events could be used to measure the pion rejection capability and electron efficiencies with real data and check the detector response. The results for electron efficiencies and pion misidentifications in comparison to simulations are shown for the BELLE detector on figs 129 and 130 and compared to the simulations [247]. The number of misidentified pions measured by BELLE is therefore 0.25% for pions with momenta between 1 GeV/c and 3 GeV/c for cuts adjusted in order to have an electron efficiency of 92%. The

---

[4]The results obtained with the CMS Electromagnetic Calorimeter (see section 4.8.2) have also been used to discuss the validity of the GEANT4 simulations.
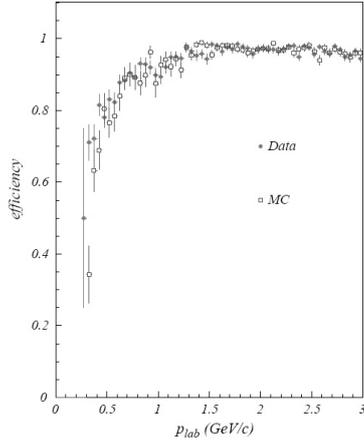
Figure 129: Electron efficiencies in real data (diamonds) and Monte-Carlo simulations (squares) for the BELLE detector. The figure is extracted from [247]
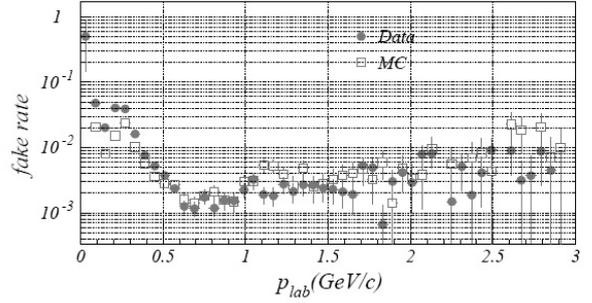
Figure 130: Pion misidentification probabilities in real data (full dots) and Monte-Carlo simulations (open squares) for the BELLE detector. The figure is extracted from [247]
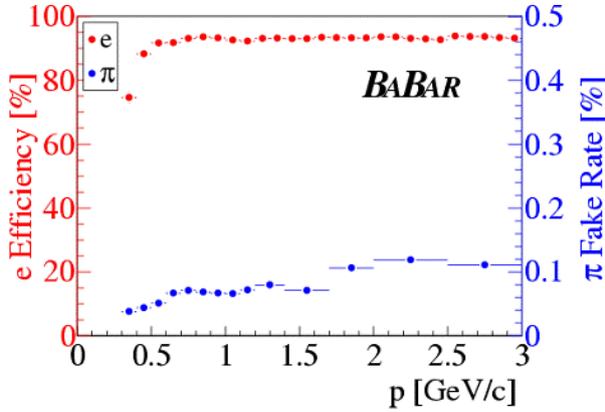
Figure 131: Electron efficiency and pion misidentification probabilities measured in the BABAR experiment [248].

precision of the data at momenta larger than 2 GeV/c is however rather poor. The pion misidentification probabilities measured by BABAR (fig. 131) are lower by factors 3 to 5, for similar efficiencies [5]. As the BELLE and BABAR detectors are quite similar, this difference is probably due to different optimization of the analysis (calibrations, corrections ,...), which has been taken into account in great details in BABAR [242]. The simulation, based in both cases on LHEP_BERT reproduces the BELLE values rather well, and underestimates the BABAR measurements by 30% for π^- and by a factor 2 for π^+ [249]. The efficiencies are also rather well reproduced, as shown in the case of BELLE on fig.129. These results confirm that predictions based on simulations are rather trustful. Nevertheless, the quality of the results at large momenta, which are the most interesting, is poor.

In these experiments, pion misdentification probabilities of about 10^{-3} could be obtained at 3 GeV, which was sufficient for the study of semi-leptonic decays of resonances produced in e^+e^- collisions. The rate of misidentified pions could be further decreased by increasing the minimum likelihood fraction as studied in [242], but the electron efficiency was still kept to values higher than 85%, with pion misidentification probabilities of a few 10^{-4} up to 2 GeV/c

---

[5]Note that this picture from a talk gives lower values of misidentication probabilities than [231], due probably to an improvement of the analysis procedure, and in agreement with the numbers quoted in [244, 245].

(no data above).

A direct extrapolation to P̄ANDA is impossible, due to the different material of the calorimeter. This study is however very interesting, since it shows the importance of pure pion and electron samples to measure the efficiencies and pion misidentification probabilities.

4.10 Rejection of $\bar{p}p \to \pi^0\pi^0$ reaction
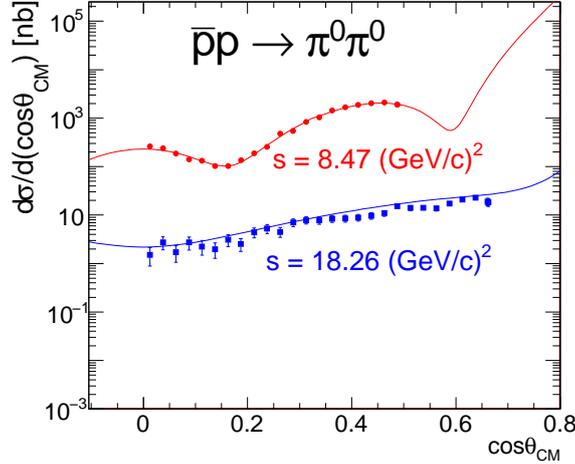
Figure 132: Angular distributions of pions produced in $\bar{p}p \to \pi^0\pi^0$ annihilation at two different energies. The curves are the results of the event generator and the data points are from [250]

In the same way as for the $\bar{p}p \to \pi^+\pi^-$ reaction, a generator has been written [220, 200, 136] to provide a good description of the available data from Fermilab [250], as shown on fig. 132. The cross-sections are slightly lower than for the $\bar{p}p \to \pi^+\pi^-$ reaction at a given energy. e^+e^- pairs are produced in the $\pi^0\pi^0$ channel after conversion of the photons from the main π^0 decay, in particular in the beam pipe before the tracking system. In addition, one (or both) π^0 may undergo Dalitz decay, $\pi^0 \to e^+e^-\gamma$, with probability 10^{-2} each. These channels have been generated and analysed in detail using the full-scale GEANT4 simulations [136]. The detected e^+e^- pairs do not fulfill the kinematical constraints required for the $\bar{p}p \to e^+e^-$ reaction (see sec.4.5.1), due to the energy of the other electrons or photons. As a consequence, rejection factors higher than 10^8 can be obtained, even without considering the possible detection of these other particles, which would exclude to take the event as originating from the $\bar{p}p \to e^+e^-$ reaction.

4.11 Rejection of other reactions

The rejection of other reactions, like $\bar{p}p \to \pi^+\pi^-\pi^0$ and $\bar{p}p \to J/\psi\pi^0$ was also estimated. In the first case, the cross-section is about a factor 10 higher than the 2π production cross-section, i.e. a factor 10^7 larger than the $\bar{p}p \to e^+e^-$ reaction. However, due to the additionnal emitted pion, the kinematical constraints are very efficient to distinguish the reaction from $\bar{p}p \to e^+e^-$. In the case of $\bar{p}p \to J/\psi\pi^0$, the cross-section is about 200 pb for q^2 around 8 GeV/c^2, but even taking very pessimistic assumptions on the momentum resolution, the background will be negligible.
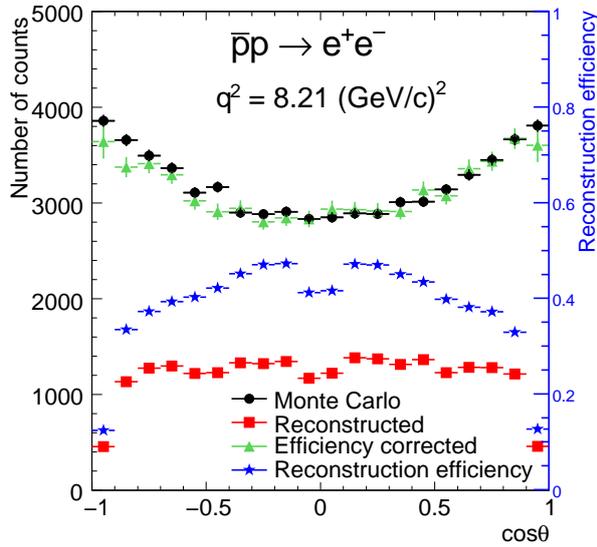
Figure 133: Center of mass electron angular distribution from $\bar{p}p{\rightarrow}e^+e^-$ reaction at q^2=8.21 $(GeV/c)^2$ generated events (black circles), reconstructed events (red squares) and acceptance and efficiency corrected events(green triangles). The acceptance and efficiency correction is also shown (blue stars, right scale)
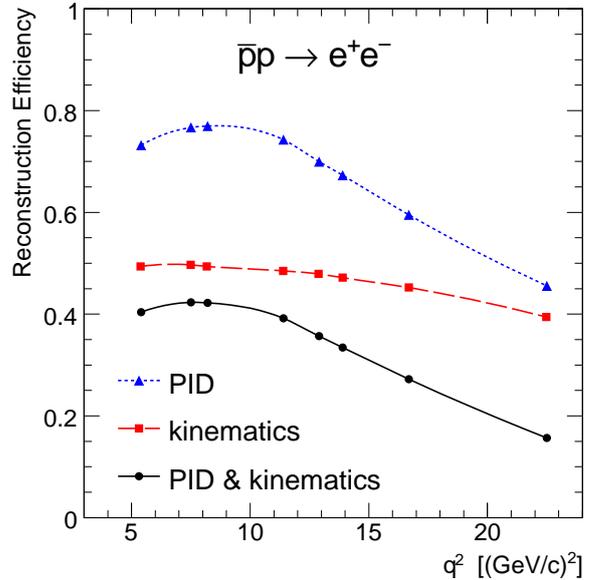
Figure 134: Average reconstruction efficiency as a function of q^2 (black solid line). The effect of applying kinematical constraints (red dashed line) and PID cuts (blue dotted line) are shown separately.

4.12 Precision of form-factor measurements

4.12.1 Efficiency for the $\bar{p}p{\rightarrow}e^+e^-$ reaction reconstruction

Sets of 10^6 events for each q^2 have been generated with the ingredients described in sec. 4.1.1 and reconstructed with the full scale simulation software. The Very Tight PID cuts were applied, as well as the kinematical fit condition, as explained in the previous subsection. In fig. 133, the angular distribution generated at q^2=8.2 $(GeV/c)^2$ for $|G_E|=|G_M|$ is compared to the angular distribution of the reconstructed events with e^+e^- final state. The statistics corresponds to an integrated luminosity of 2 fb^{-1}. The reconstruction efficiency displayed as triangles on the picture has been obtained with an independent set of events generated with an isotropic angular distribution and is defined as the ratio of reconstructed to generated events in a given $\cos\theta_{cm}$ bin. The distribution corrected using this efficiency overlaps with the generated one, which is a test of the self-consistency of this analysis. As expected from the poor dE/dx information at the lowest laboratory angles, the efficiency is dropping at the most forward/backward angles. It stays however above 40% for $|\cos\theta_{cm}| < 0.8$ and presents a structure around $\cos\theta_{cm}$=0 due to the target system. Fig. 134 displays the evolution of the signal efficiency, after integrating over $|\cos\theta_{cm}| < 0.8$. The triangles show the combined effect of acceptance, detector efficiency and PID cuts, the squares the effect of the kinematical fit cut and the full dots the total reduction factor. As a comparison, the precision of the BABAR experiment did not allow for an analysis of the angular distributions at the same q^2. The efficiency is decreasing with q^2, as a consequence mainly of the degrading PID capabilities, but remains reasonably high. For example, the efficiency quoted by the BABAR experiment is 0.17 in all their available q^2 range.

Only the statistical errors appear on the pictures. The precision of the form factor extraction relies however on the precision of the efficiency correction, which will be the main source of systematic error as will be discussed in sec. 4.12.4.

4.12.2 Final numbers for contamination

Taking into account the efficiency $\epsilon_{e^+e^-}$ for the $\bar{p}p \to e^+e^-$ reaction and the rejection factor P_{rej} for the $\bar{p}p \to \pi^+\pi^-$ reaction, we can deduce the average contamination in the signal measurement by:

$$P_{\pi^+\pi^-} = \frac{R_{\pi^+\pi^-}}{\epsilon_{e^+e^-} \cdot P_{rej}} , \tag{84}$$

where $R_{\pi^+\pi^-}$ is the ratio of cross-sections of $\bar{p}p \to \pi^+\pi^-$ to $\bar{p}p \to e^+e^-$ reactions (see eq.(76)).

The expected contamination (see Table 16) is therefore negligible. Although these numbers should be taken with safety margins, this gives confidence that the $\bar{p}p \to e^+e^-$ reaction can be selected in a very clean way. In addition, there is still some room for improvement, since neither the TOF, nor the Shashlik calorimeters have been taken into account for particle identification. At high energies, the two-body kinematics could also be used to calculate the momentum of the electron or positron from the measured angle. In this way, the momentum resolution, and hence the resolution on the E/p ratio could be improved, for a more efficient e/π discrimination.

q^2 [(GeV/c)^2]	8.2	12.9	16.7
e^+e^- efficiency	0.4	0.35	0.25
$\pi^+\pi^-$ rejection factor	6.3 10^9	2 10^9	2.6 10^9
$\pi^+\pi^-$ / e^+e^- cross-section ratio	6.3 10^5	4.4 10^5	3.4 10^5
$\pi^+\pi^-$ contamination (%)	0.025	0.06	0.05

Table 16: Final estimates for electron efficiencies, rejection factors and contamination of $\bar{p}p \to \pi^+\pi^-$ to $\bar{p}p \to e^+e^-$ reaction.

4.12.3 Errors on R, |G$_E$| and |G$_M$|

The final goal of the experiment consists in the extraction of the parameters σ_{tot} and R from the reconstructed and normalized angular distributions using fits to eq. (54). The expected normalisation error from the luminosity measurement will be 3%. Using R^2 as parameter is more appropriate when R is close to zero, to avoid unprecise errors. MINUIT fits using R, R^2 or A (see eq. 57) as fit parameters have been compared to the results of a Monte-Carlo method [216]. Differences between these methods appear when the errors are larger than 40%. This study will be of real interest at the level of the data analysis. The errors obtained in the case R=1 and shown as a yellow band in fig. 135, demonstrate that meaningful values of R can be obtained at least up to q^2=14 (GeV/c)^2, which will enhance very significantly the knowledge of form factors in the Time-Like region, both above 8 (GeV/c)^2, where no data exist and in the lower q^2 region, where the precision is expected at least one order of magnitude better than the one of the existing data.

It has to be also reminded that the increase of the errors on the R determination as q^2 increases are not only due to the decreasing statistics, but also to the decreasing sensitivity of the angular distribution to R (see sec. 4.1.2). this can be seen as an intrinsic limitation of these measurements.

We checked that the errors in σ_{tot} and R from the fits are independent, which is expected since σ_{tot} is related to the integral of the distribution and R to the shape. $|G_E|$ and $|G_M|$ can then derived from R and σ_{tot} using the relations:

$$|G_M|^2 = \frac{24m_p^2\tau\sqrt{\tau(\tau-1)}}{\pi(\alpha\hbar c)^2}\frac{\sigma_{tot}}{8\tau+4R^2},$$

(85)

$$|G_E| = R\,|G_M|$$

(86)

and the errors and correlations can be easily calculated.
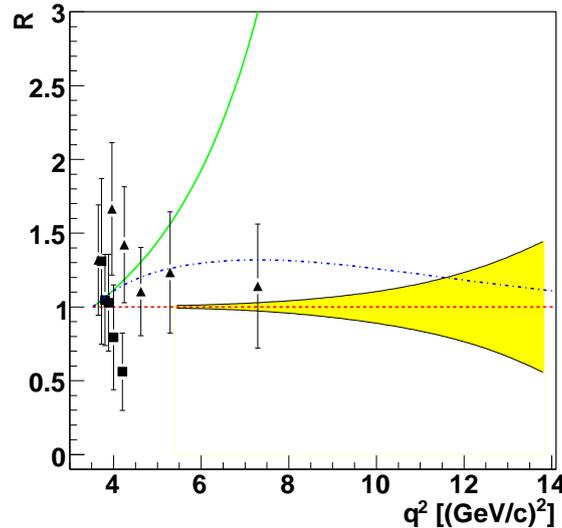
Figure 135: The yellow band shows the expected statistical precision on the determination of the ratio R, in the case R=1, as a function of q^2, compared with the existing data from Curves are theoretical predictions, as described in the text.

The precision on the total cross-section is much better than on R and the value of the effective form-factor G_{eff} can therefore be extracted , using eq.(61), up to $q^2 \sim 28$ $(GeV/c)^2$, as shown in fig. 136.

4.12.4 Systematic errors

It has to be stressed that no systematic error was taken into account in our estimates. Only arbitrary guess about these systematic errors can be made for the moment. Systematic errors can only be determined by comparing for known channels the measurements to expectations from the simulations. The philosophy is therefore to produce clean data samples which are used to check the reconstruction efficiencies provided by the simulations. Possible correction factors are then applied at the level of the inputs of the simulations (calibration, drift time error, light collection,...) or directly at the level of the efficiencies. The precision on the determination of these correction factors is then used to calculate the sytematic error.

We will here list the different sources of systematic errors for the measurements which have been cited in the course of the last sections and will propose some ways to control them:t

- cross-section of background reactions: We have seen that the most important source of background is the $\bar{p}p \to \pi^+\pi^-$ reaction and that there are quite large uncertainties on the cross-sections and angular distributions of this reaction. However, very precise
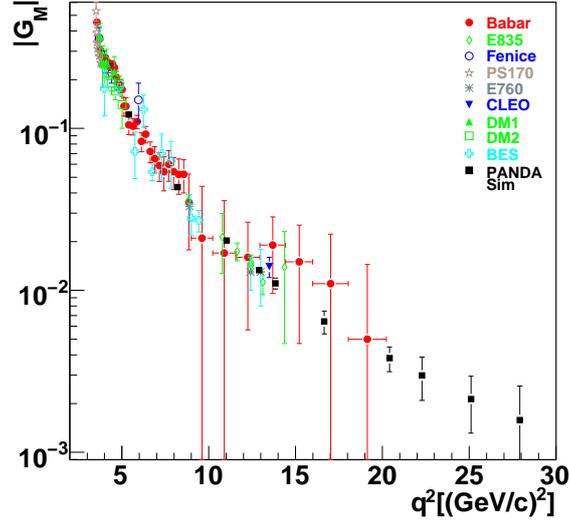
Figure 136: The existing measurements of the effective form-factor G_{eff} are shown together with estimates using the parametrization of the data following eq.(73). The error bars on these points show the precision of the expected measuremnts with $\bar{P}$ANDA.

measurements of these angular distributions in the same angular range as $\bar{p}p \rightarrow e^+e^-$ can be easily done with $\bar{P}$ANDA, and will be used to estimate very precisely the background. The reaction $\bar{p}p \rightarrow \pi^+\pi^-$ is anyway interesting in itself, in order to study pQCD mechanisms at large momentum transfers. Meanwhile, new generators based on Regge trajectories are being developped [251] to prepare these experiments, and could be used to update the background estimates for the $\bar{p}p \rightarrow e^+e^-$ reaction.

- Tracking efficiency and resolution: The matching of tracks and showers is important for the e/π discrimination in the calorimeter. It is also crucial to optimize the kinematical fit rejection of the $\bar{p}p \rightarrow \pi^+\pi^-$ reaction. This background reaction can in fact be used for these checks: the detection of one charged pion allows for the measurement of efficiency reconstruction or momenum resolution on the other pion. The high statistics which can be obtained in such a channel can be used to study these effects as a function of momentum and angle, in small zones of the detectors.

- EMC calibration: The electromagnetic calorimeter is a crucial ingredient for the electron/pion separation. Besides the calibration using cosmic rays, the check of energy reconstruction of the γ's in four γ events from the $\bar{p}p \rightarrow \pi^0\pi^0$ reaction, will allow for a calibration at the subpercent level over a very broad range of energies.

The excitation of the J/ψ and its decay to e^+e^-, with a branching ratio of 6% allows for specific checks of electron reconstruction efficiency. The production cross-section at threshold (q^2=9.6 $(GeV/c)^2$) is equal to 25nb [252], and the angular distribution is known. Within one week of beam time, the per-bin efficiency could therefore be determined with a relative precision of 1% in each bin ($\Delta \cos\theta_{cm}$ =0.1). Considering the results of our simulations, the $\bar{p}p \rightarrow \pi^+\pi^-$ reaction could be rejected rather easily since the ratio of cross-sections is in this case only about 13000.

At the ψ' threshold, which corresponds to q^2=13.59 $(GeV/c)^2$, e^+e^- pairs with higher energies are produced, but the $\pi^+\pi^-$ background suppression has to be studied.

Reconstruction checks implying even higher electron energies can be achieved for the

channel $\bar{p}p \to J/\psi \pi^0$ where the J/ψ is identified by its dilepton decay. The cross-section is about 200 pb and the background from $\pi^+\pi^-\pi^0$ is very large, but this channel has still known cross-section and angular distributions and could therefore be useful for reconstruction checks for the reaction $\bar{p}p \to e^+e^-\pi^0$.

- EMC response to pions: It is also of high importance to check that the response of the EMC to pions, including the high energy tails, is correctly described in the simulation. By using only kinematical fit or dE/dx, very clean samples of $\pi^+\pi^-$ pairs from the $\bar{p}p \to \pi^+\pi^-$ reaction should be obtained.

4.13 Model discrimination

Some model predictions are shown in fig. 135. A QCD prediction, based on scaling laws [141], gives R=1 (red dashed line). The green solid line is based on the VDM approach by [153] and the blue dash-dotted line is also based on VDM but includes asymptotic QCD behaviour (see sect. (3.2.4). Although these models reproduce reasonably well the space-like data, they give quite different predictions for the form factor ratio in the time-like region, which enhances the interest of the measurement. In the next future, the sensitivity to more models could be studied, for example, the recent quark-model which is available for the time-like region [214].

5 Other form-factor studies

5.1 The $\bar{p}p \to \mu^+\mu^-$ channel

Measuring the $\bar{p}p \to \mu^+\mu^-$ channel could bring very interesting and complementary information to the $\bar{p}p \to e^+e^-$ reaction. The expression of the angular distribution of $\bar{p}p \to \mu^+\mu^-$ to the electromagnetic form factors is exactly the same as in the case of the $\bar{p}p \to e^+e^-$ since the lepton mass difference has a negligible effect (eq.(53)). This channel presents the interest of lower radiative corrections than the $\bar{p}p \to e^+e^-$ channel, so it would help to clarify the contradictory predictions concerning the radiative corrections .

However, the situation is very different from $\bar{p}p \to e^+e^-$ from the experimental point of view. In this channel, due to the very close masses of muons and pions, the kinematics constraints do not help to reject the $\pi^+\pi^-$ background and the extraction of the signal relies only on the performance of the muon detector. The fine segmentation of the yoke which acts as a pion absorber, with interleaved tracking detectors, is exploited to identify the muons and recognize kinks from pion decays. Detailed simulations will be performed in a near future to investigate whether a sufficient rejection of the $\pi^+\pi^-$ background can be achieved, while keeping a reasonable signal efficiency. This will be performed within the collaboration we are setting up with the $\bar{P}$ANDA team in Torino (Marco Maggiora et al.), who already studied the efficiency of muon reconstruction for other physics channels.

5.2 Electromagnetic form factors in the unphysical region

Using the $\bar{p}p \to e^+e^-$ reaction, only q^2 higher than 4m$_p^2$, where m$_p$ is the proton mass can be reached. To access the "unphysical" region corresponding to q^2 lower than this threshold, the reaction $\bar{p}p \to e^+e^-\pi^0$ can be used (fig.137), as was first proposed in [127]. The q^2 at the $\bar{p}p$ vertex is indeed lowered in this case, due to the pion emission. The study of the feasibility of this measurement is the subject of Jérôme Boucher's PhD at IPN Orsay and simulations have been started using the new PANDA-ROOT software, with a generator based on the calculations of [253].
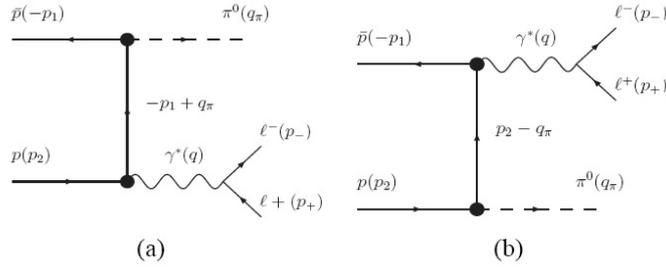
Figure 137: Graphs for the study of Time-Like form-factors below the $\bar{p}p$ threshold in $\bar{p}p{\rightarrow}e^+e^-\pi^0$ reactions.

The selection of this reaction is again a challenge, due to the huge cross section for hadronic background reactions. The most important is the $\pi^+\pi^-\pi^0$ channel, which has the closest kinematics. Taking into account the studies of optimization of the electron identification already performed for the $\bar{p}p{\rightarrow}e^+e^-$ case, the requirement of reconstruction of an (e^+, e^-) pair will provide a rejection factor of the $\bar{p}p{\rightarrow}\pi^+\pi^-\pi^0$ reaction of about a few 10^7. Kinematical constraints can be used (missing mass has to be close to π^0 mass). The background rejection is also enhanced due to the probability to reconstruct the π^0 using the two γ from its decay. Detailed simulations of $\bar{p}p{\rightarrow}e^+e^-\pi^0$and of the $\bar{p}p\pi^+\pi^-\pi^0$ are currently being performed by Jérôme Boucher for his PhD work.

Informations about proton form factors in the unphysical region is a very challenging goal, since in many models, the electromagnetic interaction at low q^2 is mediated by vector mesons (ρ, ω, ϕ), which produce poles located in the unphysical region [254]. The region just above threshold is also very interesting, since structures around the $\Lambda\bar{\Lambda}$ threshold are expected in some models and are supported by experimental indications found in the LEAR results, which however have to be confirmed by more precise data [255].

Another way to access the unphysical region is to study the reaction $\bar{p}+ A \rightarrow e^+e^-(A\text{-}1)$. In this case, the annihilation takes place on a bound proton, moving according to the Fermi momentum distribution. Lower q^2 than in the $\bar{p}p{\rightarrow}e^+e^-$ reaction could therefore be accessed. The simplest case is the deuterium nucleus and estimates have been started at the lowest available $\bar{p}$ momentum of 1.5 GeV/c [256] by Hélène Fonvieille at LPC Clermont-Ferrand in collaboration with V.A. Karmanov and O. Dalkarov from the Lebedev Physical Institute in Moscow. Detailed simulations of this reaction will however be necessary to investigate the feasibility of the measurement.

5.3 The interest of polarization

The possibility of FAIR to provide a polarized antiproton beam with reasonable intensity is currently investigated by physicists in GSI and Mainz. As explained in sec. 3.4.1, such a beam would allow for the first time to access the phase difference of the electric and magnetic form factors, which is of high interest to constrain the different models [144, 204, 203, 207]. A feasibility study could be started in case of a positive information about the availability of polarized beams.

5.4 The international competition on nucleon form factor measurements

5.4.1 Time-Like region

Let's examine the different experiments for the time like form factors measurements.

The BABAR experiment has now stopped data taking. The remaining data to be analysed will bring the total statistics to 500 fb^{-1}, which can improve the actual statistical errors by only 30%.

At DAϕNE, the DANAE (DAϕNE New Adjustable Energy) new facility could allow to expand the center of mass energy range from the actual value of $\sqrt{s}$ =1.019 GeV up to 2.5 GeV with a luminosity of 10^{33} cm^{-2}s^{-1} at the lowest energies to 10^{32}cm^{-2}s^{-1} at the highest energy. The measurement of electromagnetic form factors for both proton and neutron is proposed by the DANTE (DAnae Nucleon Time-like form factor Experiment) collaboration for q^2 values ranging from the threshold up to 5.7 (GeV/c)^2 with expected precisions of a few percent. In addition, the polarization of the outgoing proton could be measured, which would allow the determination of the relative phase of the electric and magnetic form factors with a 10% precision. It would cover the lowest energies closest to threshold, which can not be accessed by PANDA and would provide data for the neutron. The project is however currently not supported.

At VEPP-2000, the measurement of neutron electric and magnetic form factors will be done using NaI counters with flash-ADC for q^2 up to 4 (GeV/c)^2.

The BELLE experiment, running at the KEK e$^+$e$^-$ collider could in principle, like the BABAR experiment, look at the Initial State Return process (e$^+$e$^- \rightarrow$ p̄pγ reactions), to extract information about electromagnetic proton form factors. The increased e$^+$e$^-$ luminosity scheduled from 2011 at the SuperKEKB could give very high statistics. However, due to the very steep decrease of the cross section for photon emission in the initial state as q^2 decreases, the measurement could be competitive with PANDA only at q^2 larger than 25 (GeV/c)^2, where the separation between |G$_E$| and |G$_M$| is hardly possible due to the decrease of sensitivity of the cross section to |G$_E$|.

A more direct competition comes from the BESIII experiment starting at the e$^+$e$^-$ collider BEPCII at Beijing. However, to measure the nucleon electromagnetic form factors, center of mass energies corresponding to formation of resonances have to be excluded, which is in contradiction with the main focus of the BESIII experiment. Such experiments can therefore only be envisaged for a further future. A program of form factor measurement using the ISR technique has however started, and the expected counting rates are of the same order than the one previously obtained by BABAR. In this respect, PANDA presents a serious advantage, since the search of exotic states requires long periods of data taking at energies not corresponding to excitation of known states, which fits perfectly well with the requirements for form factor measurements.

Anyhow, even if other experiments produce in the next years new data concerning the proton form factors, the interest for such measurements is so high, and the region of q^2 to scan is so wide, that a dedicate measurement by PANDA, in the p̄p reaction would be highy justified.

5.4.2 Space-Like region

In a near future, the knowledge of the form factors in the space like region will also be improved.

First, cross sections of reactions induced by e$^+$ and e$^-$ beams will be compared with a

better precision than today. This should allow to quantify the role of two-photon exchange and the possible distortion of the different form factor measurements due to this process , in connection with the discrepancy between the measurements obtained in the Space-Like region using the Rosenbluth and polarization techniques respectively (see sec. 3.3.4). The importance of two photon exchange is also a crucial issue in the Time-Like region, since the determination of the form-factors in this region is also based on the dominance of the one photon exchange graph.

The measurement of electric and magnetic nucleon form factor has an important place in the program of the JLab12GeV facility.s Measurements of the ratio of electric to magnetic proton form factors using the polarization measurement of the recoil proton are proposed at JLab-12GeV, where Q^2 up to 15 $(GeV/c)^2$ can be reached (exp PR12-07-109/Hall A (Gep-V) [257], PR12-009-001/HallC (Gep-IV) [258]). It is also foreseen to achieve a precise measurement of the elastic ep scattering cross-section up to 17.5 $(GeV/c)^2$ (exp PR12-07-108/Hall A (high Q^2-x sec) [259]).

Several planned experiments aimed also at improving the knowledge of the neutron electromagnetic form factors.

As a conclusion, there will be in the next years a very intense experimental activity related to nucleon form factors. It can therefore be foreseen that these new data, together with the expected progress of theoretical models and of lattice QCD calculations will improve our knowledge of the nucleon stucture and constrain the models much more than today.

Part III
Conclusions and outlook

This report presents two different activities: on the one hand, data analysis in the HADES experiments at the present SIS-18 facility at GSI, Darmstadt, on the other hand, a prospective work and feasibility studies in view of the future FAIR facility at Darmstadt. Despite the obvious differences between the main objectives of both experimental programs, we focus on specific channels which present a common sensitivity to time-like electromagnetic structure of hadrons.

The HADES experiments are in an active phase of production of results. With the study of the C+C system, the long-standing "DLS puzzle" is now settled, and an intense theoretical activity was triggered. Although the description of the data improved a lot, the theoretical predictions still present significant dispersion. The role of the HADES measurements in elementary reactions is to bring the missing experimental constraints to reduce these uncertainties.

The pp system was measured at an incident energy of 1.25 GeV focusing on three channels, the inclusive dilepton production, the exclusive pion and eta production and the exclusive dilepton channels. The results can be explained in a coherent way within the resonance model, with the Δ resonance as dominant contribution.

The pp$\rightarrow$ppe^+e^- exclusive analysis allows to identify unambiguously the Δ Dalitz decay process, thus providing the first measurement of the branching ratio. The pp dilepton inclusive spectrum shows a sensitivity to the Time-Like N-Δ transition form-factor, using the model of Iachello and Wan. As this model aims at a unified description of all baryonic form factors in space-like and time-like region, it made an interesting link to our studies of elastic proton Time-Like form-factors with $\bar{P}$ANDA.

The nice description of the pp system is in contrast with the puzzling results obtained for the quasi-free n+p reaction. In the latter case, the decrease of the dilepton yield at large dilepton masses is much smoother than in the case of the pp system, a feature that no model is able to reproduce at the moment. As a consequence, no final conclusion on the pn bremsstrahlung contribution could be obtained. The ongoing analysis of the exclusive dilepton channel: quasi-free n+p $\rightarrow$ npe^+e^- should shed more light on this problem and on the possible contributions of off-shell ρ-meson production, or non quasi-free processes.

The recent p+p data at 3.5 GeV will provide a precise measurement of the inclusive ω and ρ production, one important source of uncertainties in the models.

The study of the C+C system paved the way for the investigation of dilepton production in nuclear matter. Other systems have been measured in the mean time, like Ar+KCl at 1.76 AGeV, and p+Nb system at 3.5 GeV, which were not discussed in this report. In these studies, the p+p and "n"+p inclusive spectrum allow to build a very useful reference to quantify the excess dilepton production from the dense phase. The various measurements provide a systematic study of these effects for different system sizes, in order to pin down in-medium changes of vector meson spectral functions. Following the lessons from previous experiments, a convergence of signals observed in different conditions of temperature and densities is indeed necessary for a clear identification of these effects. On the theory side, a consistent description of all the measured spectra is not yet achieved, especially concerning the quasi-free n+p dilepton spectra and the vector meson region in heavy-ion collisions.

A very important aspect of the HADES experiments, which was not discussed in this report, is the strangeness production measurements. HADES turns out to be an efficient detector for charged kaon identification, allowing the study of in-medium K^+ and K^- pro-

duction. Other strange hadrons can also be reconstructed by their decay: $K^0_S \rightarrow \pi^+ \pi^-$, $\phi \rightarrow K^+ K^-$, $\Lambda \rightarrow p\pi^-$, and $\Xi^- \rightarrow \Lambda\pi^-$. A complementary study of the hot and dense hadronic matter is provided by these strangeness production studies.

The HADES spectrometer has been recently upgraded with a high-granularity RPC time-of-flight wall, covering the low polar angles ($18° < \theta < 45°$), providing now, together with the TOF system, excellent particle identification. It offers new possibilities in a high multiplicity environment with state of the art time resolution. In addition, a completely new detector read-out and data-acquisition system has been implemented which will greatly improve our data taking rate.

HADES will now enter a new phase of its experimental program, with the study of heavier systems: Ag+Ag at 1.65 AGeV and Au+Au at 1.25 AGeV. The main aim of the program proposed here is to investigate properties of compressed baryonic matter by means of rare penetrating probes, namely dielectrons and strange hadrons, using the highest beam energies and largest system sizes available from the SIS18 accelerator. These studies can be continued with the HADES detector et the FAIR facility, with heavy-ion beams of energies up to 8 AGeV.

The pion beam at GSI offers another perspective for the HADES experimental program in the next years and the IPN group is willing to take an important part in this activity. The dilepton spectroscopy in π induced experiments on nuclei is proposed to study medium effects on ρ and ω mesons. We will more specifically focus our activity on experiments on nucleon targets, which will bring detailed information on dilepton production by baryonic resonances heavier than the Δ. Such experiments could be foreseen in 2012-2013.

In 2018, the FAIR facility will deliver antiproton beams, stored in the HESR, in the momentum range between 1.5 and 15 GeV/c, with a luminosity one order of magnitude higher than at previous facilities. The internal target universal $\bar{P}$ANDA detector is designed to cover almost the full solid angle and to detect photons, leptons and charged hadrons in a very wide energy range. The IPN Orsay detector R&D group is strongly involved in developments concerning the thermal insulation, the mechanics and the integration of the barrel electromagnetic calorimeter, operated at -25°C. An intense activity is devoted to the tests of prototypes, in order to assess the technical choices, as well as to quantify the response of the $PbWO_4$ crystals to cosmic rays or photon beams. This activity will continue with the participation to the construction of the full-size electromagnetic calorimeter.

A broad physics program is accessible with $\bar{P}$ANDA, addressing fundamental questions of strong interaction physics. In particular, the physics of strange and charm quarks and of gluonic excitations could be accessed with an unprecedented accuracy.

At IPN Orsay, we would like to address with the $\bar{P}$ANDA detector the Time-Like electromagnetic structure of the nucleon. A complete feasibility study of this measurement in the reaction $\bar{p}p \rightarrow e^+ e^-$ has been achieved. The main challenge of such an experiment is the rejection of the background coming from the $\bar{p}p \rightarrow \pi^+ \pi^-$ reaction. Combining particle identification information from the different detectors and kinematical fits, the background contribution to the $\bar{p}p \rightarrow e^+ e^-$ reaction can be reduced to the level of less than 1%, with efficiencies on the signal reconstruction decreasing from 40% at $q^2 = 10$ (GeV/c)^2 to 15% at $q^2 = 22$ (GeV/c)^2. This feasibility study relies on full scale GEANT4 simulations including all details of the detector geometry and of the digitalization of the physics signals. A preliminary study based on more simple and specific simulations and on performances of existing detectors allowed to check the reliability of these simulations by pointing to the remaining uncertainties in the description of the physics processes. It was shown that the description of hadronic models in GEANT4 plays a particularly important role.

The final conclusion is that the determination of $|G_E|$ and $|G_M|$ can be made up to 14

$(\mathrm{GeV}/c)^2$, with a precision at least one order of magnitude better than previous experiments.

For higher q^2, where the statistics is reduced and the sensitivity to $|G_E|$ is too small, the measurement of the cross sections, which is possible up to 28 (GeV/c^2), is still interesting, to determine the effective form factor $|G_{eff}|$ in a region which is very challenging to check perturbative QCD predictions. These measurements can be completed in the unphysical region using the reaction $\bar{\mathrm{p}}\mathrm{p}\rightarrow \mathrm{e}^+\mathrm{e}^-\ \pi^0$ or the reaction $\bar{\mathrm{p}}\mathrm{d} \rightarrow \mathrm{e}^+\mathrm{e}^-\mathrm{n}$, for which feasibility studies are in progress. Measurements with a polarized beam would bring additionnal, completely new, informations on the difference of phase between the electric and magnetic form-factors.

Other electromagnetic processes: $\bar{\mathrm{p}}\mathrm{p}\rightarrow \gamma\gamma$, $\bar{\mathrm{p}}\mathrm{p}\rightarrow \mathrm{e}^+\mathrm{e}^-\gamma$, $\bar{\mathrm{p}}\mathrm{p}\rightarrow \mathrm{e}^+\mathrm{e}^-\ \pi^0$, $\mathrm{e}^+\mathrm{e}^-\ \rho$ would allow to measure different observables related to the structure of the proton, for example, the Transition Distribution Amplitudes [260, 261] which are universal non perturbative objects describing the transitions between two different particles.

The measurement at large s and large center of mass angles of some hadronic processes, like $\bar{\mathrm{p}}\mathrm{p}\rightarrow \pi^+\pi^-$, $\mathrm{K}^+\mathrm{K}^-$, $\phi\phi$ or $\rho\rho$ is also proposed to study perturbative QCD mechanisms. The scale for the onset of the perturbative QCD regime can indeed only be deduced from experiments, and seems to depend on the processes, hence the interest of measuring different exit channels. In addition, such experiments allow to test the competition between different reaction mechanisms in the perturbative QCD regime. A precise measurement of the angular distributions in the reaction $\bar{\mathrm{p}}\mathrm{p}\rightarrow \pi^+\pi^-$ will anyway be necessary to control the main background of the reaction $\bar{\mathrm{p}}\mathrm{p}\rightarrow\mathrm{e}^+\mathrm{e}^-$.

The color transparency is the reduction of strong interactions that can occur in the case of a very hard scattering selecting very small transverse size components in the hadronic wave functions, for which a coherent cancellation of perturbative interactions occurs. The signature of this effect can be seen by comparing the differential cross section at 90^0 for the reaction on a proton and on the nucleus. These reactions have large cross sections, and could be quite easy to measure, although complete simulations are of course needed. Detailed simulations are necessary to prove the feasibility of these additional measurements. Thanks to a state of the art detector on an antiproton ring, $\bar{\mathrm{P}}$ANDA at FAIR will offer a bright future for the study of the strong interaction, ranging from perturbative QCD to the non perturbative regime.

References

[1] P. Braun-Munzinger, Nucl. Phys. **A681**, 119 (2001), *Chemical equilibration and the hadron-QGP phase transition.*

[2] P. Braun-Munzinger, K. Redlich, and J. Stachel, Particle production in heavy ion collisions, R. C. Hwa, X. N. Wang (editors), Quark-Gluon Plasma vol.3 (World Scientific) p491, 2004.

[3] M. Bleicher *et al.*, J. Phys. **G25**, 1859 (1999), *Relativistic hadron hadron collisions in the ultra- relativistic quantum molecular dynamics model.*

[4] J. J. Sakurai, Phys. Rev. Lett. **22**, 981 (1969), *Vector-Meson Dominance and High-Energy Electron-Proton Inelastic Scattering.*

[5] A. Faessler, C. Fuchs, M. I. Krivoruchenko, and B. V. Martemyanov, J. Phys. **G29**, 603 (2003), *Dilepton production in proton proton collisions at BEVALAC energies.*

[6] R. Rapp, J. Wambach, and H. van Hees, (2009), *The Chiral Restoration Transition of QCD and Low Mass Dileptons.*

[7] S. Leupold, V. Metag, and U. Mosel, (2009), *Hadrons in strongly interacting matter.*

[8] R. S. Hayano and T. Hatsuda, (2008), *Hadron properties in the nuclear medium.*

[9] U. Mosel, *Fields, Symetries and Quarks* (Springer, Berlin, 1999).

[10] T. Hatsuda and T. Kunihiro, Phys. Rev. Lett. **55**, 158 (1985), *Fluctuation Effects in Hot Quark Matter: Precursors of Chiral Transition at Finite Temperature.*

[11] H. Fukaya *et al.*, Phys. Rev. Lett. **104**, 122002 (2010), *Determination of the chiral condensate from 2+1-flavor lattice QCD.*

[12] Y. Aoki, G. Endrodi, Z. Fodor, S. D. Katz, and K. K. Szabo, Nature **443**, 675 (2006), *The order of the quantum chromodynamics transition predicted by the standard model of particle physics.*

[13] Y. Aoki, Z. Fodor, S. D. Katz, and K. K. Szabo, Phys. Lett. **B643**, 46 (2006), *The QCD transition temperature: Results with physical masses in the continuum limit.*

[14] S. Klimt, M. Lutz, and W. Weise, Phys. Lett. **B249**, 386 (1990), *Chiral phase transition in the SU(3) Nambu and Jona- Lasinio model.*

[15] T. Hatsuda and S. H. Lee, Phys. Rev. **C46**, 34 (1992), *QCD sum rules for vector mesons in nuclear medium.*

[16] G. E. Brown and M. Rho, Phys. Rev. Lett. **66**, 2720 (1991), *Scaling effective Lagrangians in a dense medium.*

[17] M. Harada and C. Sasaki, Phys. Rev. **D74**, 114006 (2006), *Thermal dilepton production from dropping rho based on the vector manifestation.*

[18] K. Saito, K. Tsushima, and A. W. Thomas, Phys. Rev. **C55**, 2637 (1997), *Variation of hadron masses in finite nuclei.*

[19] G. Chanfray, Acta Phys. Polon. **B27**, 3203 (1996), *Pions in the nuclear medium.*

[20] J. Delorme and P. A. M. Guichon, Phys. Lett. **B263**, 157 (1991), *evidence for the nuclear pionic mode in the (^{3}He,t) reaction.*

[21] D. Contardo *et al.*, Phys. Lett. **B168**, 331 (1986), *study of the Delta isobar excitation in nuclei with the (^{3}He,t) reaction.*

[22] M. Roy-Stephan *et al.*, , *Coherent pion production and Delta's in nuclei*, 28th International Workshop on Gross Properties of Nuclei and Nuclear Excitation: Hadrons in Dense Matter, Hirschegg, Austria, 16-22 Jan 2000.

[23] B. Ramstein *et al.*, Eur. Phys. J. A **16**, 583 (2003), *$^2H(^3He,t)2p$ reaction at 2 GeV.*

[24] J. L. Boyard *et al.*, Nucl. Phys. **A755**, 507 (2005), *Coherent pion production in heavy ion charge exchange reactions.*

[25] T. Udagawa, S. W. Hong, and F. Osterfeld, Phys. Lett. **B245**, 1 (1990), *Delta excitations in nuclei.*

[26] T. Hennino *et al.*, Phys. Lett. **B303**, 236 (1993), *Coherent pions in charge-exchange reactions.*

[27] B. Ramstein *et al.*, Acta Phys. Polon. **B27**, 3229 (1996), *Delta production and propagation in nuclei.*

[28] Tarlé-Rousteau S., Etude des voies de décroissance de la résonance Δ exci'ée dans l''^{4}He et autres noyaux par la réaction (^{3}He,t) á 2 GeV, PhD Thesis, Joseph Fourier university, Grenoble.

[29] M. Post and U. Mosel, Nucl. Phys. **A699**, 169 (2002), *Vector mesons and baryon resonances in nuclear matter.*

[30] M. Post, S. Leupold, and U. Mosel, Nucl. Phys. **A741**, 81 (2004), *Hadronic spectral functions in nuclear matter.*

[31] R. Rapp and J. Wambach, Eur. Phys. J. **A6**, 415 (1999), *Low mass dileptons at the CERN-SPS: Evidence for chiral restoration?*

[32] M. F. M. Lutz, G. Wolf, and B. Friman, Nucl. Phys. **A706**, 431 (2002), *Scattering of vector mesons off nucleons.*

[33] C. Amsler *et al.*, Phys. Lett. **B667**, 1 (2008), *Review of particle physics.*

[34] P. Muehlich, V. Shklyar, S. Leupold, U. Mosel, and M. Post, Nucl. Phys. **A780**, 187 (2006), *The spectral function of the omega meson in nuclear matter from a coupled-channel resonance model.*

[35] S. Leupold and U. Mosel, Phys. Rev. **C58**, 2939 (1998), *On QCD sum rules for vector mesons in nuclear medium.*

[36] R. J. Porter *et al.*, Phys. Rev. Lett. **79**, 1229 (1997), *Dielectron cross section measurements in nucleus nucleus reactions at 1.0-A-GeV.*

[37] M. Masera, Nucl. Phys. **A590**, 93c (1995), *Dimuon production below mass 3.1-GeV/c**2 in p W and S W interactions at 200-A/GeV/c.*

[38] G. Agakichiev *et al.*, Eur. Phys. J. **C41**, 475 (2005), *e+ e- pair production in Pb Au collisions at 158-GeV per nucleon.*

[39] D. Adamova *et al.*, Phys. Lett. **B666**, 425 (2008), *Modification of the rho meson detected by low-mass electron-positron pairs in central Pb-Au collisions at 158 A GeV/c.*

[40] R. Arnaldi *et al.*, Phys. Rev. Lett. **96**, 162302 (2006), *First measurement of the rho spectral function in high- energy nuclear collisions.*

[41] R. Rapp, G. Chanfray, and J. Wambach, Nucl. Phys. **A617**, 472 (1997), *Rho meson propagation and dilepton enhancement in hot hadronic matter.*

[42] R. Arnaldi *et al.*, Eur. Phys. J. **C64**, 1 (2009), *ϕ Production in In-In Collisions at 158 AGeV.*

[43] A. Toia, J. Phys. **G35**, 104037 (2008), *e+e- Pairs: a clock and a thermometer of heavy ion collisions.*

[44] G. J. Lolos *et al.*, Phys. Rev. Lett. **80**, 241 (1998), *Evidence for rho0 mass modification in the He- 3(gamma,rho0)p p n reaction.*

[45] G. M. Huber *et al.*, Phys. Rev. **C68**, 065202 (2003), *In-medium rho0 spectral function study via the H-2, He-3, C12(gamma,pi+ pi-) reaction.*

[46] R. Muto *et al.*, Phys. Rev. Lett. **98**, 042501 (2007), *Evidence for in-medium modification of the phi meson at normal nuclear density.*

[47] M. Naruki *et al.*, Phys. Rev. Lett. **96**, 092301 (2006), *Experimental signature of the medium modification for rho and omega mesons in 12-GeV p + A reactions.*

[48] D. Trnka *et al.*, Phys. Rev. Lett. **94**, 192303 (2005), *First observation of in-medium modifications of the omega meson.*

[49] M. Kotulla *et al.*, Phys. Rev. Lett. **100**, 192302 (2008), *Modification of the ω-Meson Lifetime in Nuclear Matter.*

[50] V. Metag, J. Phys. **G34**, S397 (2007), *Medium modifications of vector mesons in elementary reactions and heavy-ion collisions.*

[51] E. L. Bratkovskaya, W. Cassing, R. Rapp, and J. Wambach, Nucl. Phys. **A634**, 168 (1998), *Dilepton production and m(T)-scaling at BEVALAC/SIS energies.*

[52] W. Wilson, Phys. Rev. **C57**, 1865 (1998).

[53] C. Ernst, S. A. Bass, M. Belkacem, H. Stoecker, and W. Greiner, Phys. Rev. **C58**, 447 (1998), *Intermediate mass excess of dilepton production in heavy ion collisions at BEVALAC energies.*

[54] G. Agakichiev *et al.*, Eur. Phys. J. **A41**, 243 (2009), *The High-Acceptance Dielectron Spectrometer HADES.*

[55] I. Froehlich *et al.*, PoS **ACAT2007**, 076 (2007), *Pluto: A Monte Carlo Simulation Tool for Hadronic Physics.*

[56] I. Froehlich, A versatile method for simulating pp $\rightarrow$ ppe+e- and dp $\rightarrow$ pne+e-p$_{spec}$ reactions, arXiv:0909.5373[nucl-ex].

[57] A. Rustamov, Inclusive meson production in 3.5 GeV pp collisions studied with the HADES spectrometer, proceedings of the HADRON 2009 conference, Tallahasse, USA, 2010.

[58] S. Teis *et al.*, Z. Phys. **A356**, 421 (1997).

[59] V. Dmitriev, O. Sushkov, and C. Gaarde, Nucl. Phys. **A459**, 503 (1986), *Delta formation in the $^1H(^3He,t)Delta++$ reaction at intermediate energies.*

[60] K. Shekhter, C. Fuchs, A. Faessler, M. Krivoruchenko, and B. Martemyanov, Phys. Rev. **C68**, 014904 (2003), *Dilepton production in heavy ion collisions at intermediate energies.*

[61] F. Balestra *et al.*, Phys. Rev. **C69**, 064003 (2004), *Exclusive eta production in proton-proton reactions.*

[62] E. J. Moniz and A. Sevgen, Phys. Rev. **C24**, 224 (1981), *Pauli blocking in the nuclear medium piN transition matrix.*

[63] Morinière, E., Contribution à l'anlyse de résctions de production de dileptons en collisions proton-proton avec HADES, Ph.D. thesis, PARIS XI university, Orsay, France, 2008.

[64] D. V. Bugg *et al.*, Phys. Rev. **133**, B1017 (1964), *Proton-Proton Scattering at 970 MeV.*

[65] K. Gottfried and J. D. Jackson, Nuovo Cim. **33**, 309 (1964), *On the Connection between production mechanism and decay of resonances at high-energies.*

[66] A. B. Wicklund *et al.*, Phys. Rev. **D35**, 2670 (1987), *Study of the reaction (p polarized) p → p pi+ n with polarized beam from 1.18-GeV/c to 1.98-GeV/c.*

[67] A. B. Wicklund *et al.*, Phys. Rev. **D34**, 19 (1986), *Study of the reaction pp(polarized) → p pi+ n with polarized beam from 3 to 12 GeV/c.*

[68] T. C. Bacon *et al.*, Phys. Rev. **162**, 1320 (1967), *Comparison of Isobar Production in pp and pbar n Interactions at 2.8 GeV/c.*

[69] F. Shimizu *et al.*, Nucl. Phys. **A389**, 445 (1982), *study of pp intercations in the momentum range 0.9-GeV/c to 2.0-GeV/c.*

[70] D. L. Prout *et al.*, Phys. Rev. Lett. **76**, 4488 (1996), *Spin decomposition of the Delta resonance cross-section using the C-12(p(pol.),n(pol. reaction at E(p) = 795-MeV.*

[71] E. Oset, E. Shiino, and H. Toki, Phys. Lett. B **224**, 249 (1989), *The ($^3He,t$) reaction on nucleons and nuclei.*

[72] R. Dahl, Angular correlations in Δ decay, Master Thesis, Niels Bohr Institute, 1995.

[73] L. Ray, Phys. Rev. **C49**, 2109 (1994), *Phenomenological transition amplitudes for N N → N Delta at 800-MeV.*

[74] M. I. Krivoruchenko and A. Faessler, Phys. Rev. **D65**, 017502 (2002), *Comment on Delta radiative and Dalitz decays.*

[75] M. Zetenyi and G. Wolf, Phys. Rev. **C67**, 044002 (2003), *Baryonic contributions to the dilepton spectrum of nucleon nucleon collisions.*

[76] H. F. Jones and M. D. Scadron, Ann. Phys. **81**, 1 (1973), *Multipole gamma N Delta form-factors and resonant photoproduction and electroproduction.*

[77] M. I. Krivoruchenko, B. V. Martemyanov, A. Faessler, and C. Fuchs, Annals Phys. **296**, 299 (2002), *Electromagnetic transition form factors and dilepton decay rates of nucleon resonances.*

[78] I. G. Aznauryan *et al.*, Phys. Rev. **C80**, 055203 (2009), *Electroexcitation of nucleon resonances from CLAS data on single pion electroproduction.*

[79] R. Beck *et al.*, Phys. Rev. **C61**, 035204 (2000), *Determination of the E2/M1 Ratio in the $\gamma\, N \to \Delta(1232)$ Transition from a Simultaneous Measurement of $p(\vec{\gamma},p)\pi^0$ and $p(\vec{\gamma},\pi^+)n$.*

[80] E. Bratkovskaya and W. Cassing, Nucl. Phys. **A807**, 214 (2008), .

[81] G. Wolf *et al.*, Nucl. Phys. **A517**, 615 (1990), *Dilepton production in heavy ion collisions.*

[82] E. L. Bratkovskaya, W. Cassing, M. Effenberger, and U. Mosel, Nucl. Phys. **A653**, 301 (1999), *e+ e- production from p p reactions at BEVALAC energies.*

[83] M. Zetenyi and G. Wolf, Heavy Ion Phys. **17**, 27 (2003), *Dilepton decays of baryon resonances.*

[84] T. M. Aliev and M. Savci, Phys. Rev. **D60**, 114031 (1999), *The radiative Delta –¿ N gamma decay in light cone QCD.*

[85] L. Xiong, Z. G. Wu, C. M. Ko, and J. Q. Wu, Nucl. Phys. **A512**, 772 (1990), *Dielectron production from nucleus-nucleus collisions.*

[86] Q. Wan and F. Iachello, Int. J. Mod. Phys. **A20**, 1846 (2005), *A unified description of baryon electromagnetic form factors.*

[87] Q. Wan, Ph.D. Thesis, Yale University, New Haven, Connecticut, 2007.

[88] R. Bijker, F. Iachello, and A. Leviatan, Ann. Phys. **236**, 69 (1994), *Algebraic models of hadron structure. 1. Nonstrange baryons.*

[89] F. Iachello and Q. Wan, Phys. Rev. **C69**, 055204 (2004), *Structure of the nucleon from electromagnetic timelike form factors.*

[90] E. L. Bratkovskaya, O. V. Teryaev, and V. D. Toneev, Phys. Lett. **B348**, 283 (1995), *Anisotropy of dilepton emission from nuclear collisions.*

[91] B. Martemyanov, private communication, 2009.

[92] S. Huber and J. Aichelin, Nucl. Phys. **A573**, 587 (1994), *Production of Delta and N* resonances in the one boson exchange model.*

[93] B. Julia-Diaz, (2010), *The status of the Excited Baryon Analysis Center, talk given at the HADRON 2009 conference, Tallahasse, USA.*

[94] C. Gale and J. Kapusta, Phys. Rev. **C35**, 2107 (1987).

[95] R. Shyam and U. Mosel, Phys. Rev. **C67**, 065202 (2003), *Role of baryonic resonances in the dilepton emission in nucleon nucleon collisions.*

[96] L. P. Kaptari and B. Kämpfer, Nucl. Phys. **A764**, 338 (2006), *Di-electron bremsstrahlung in intermediate-energy p n and D p collisions.*

[97] R. Shyam and U. Mosel, Phys. Rev. **C79**, 035203 (2009), *Dilepton production in nucleon-nucleon collisions revisited.*

[98] T. Galatyuk, Ph.D. thesis, Frankfurt university, Germany, 2009.

[99] L. P. Kaptari and B. Kämpfer, (2009), *Di-Electrons from Resonances in Nucleon-Nucleon Collisions.*

[100] P. Moskal *et al.*, Phys. Rev. **C79**, 015208 (2009), *Near threshold production of the eta meson via the quasi- free pn –¿ pn eta reaction.*

[101] Markert, J., Untersuchung zum Ansprechverhalten der Vieldraht-Driftkammern niedriger Massenbelegung des HADES-Experiments, PhD Thesis Johann Wolgang Goethe-Universität Frankfurt, 2005.

[102] M. H. Wood *et al.*, Phys. Rev. **C78**, 015201 (2008), *Light Vector Mesons in the Nuclear Medium.*

[103] G. Agakichiev *et al.*, Phys. Rev. Lett. **98**, 052302 (2007), *Dielectron production in C-12 + C-12 collisions at 2-AGeV with HADES.*

[104] G. Agakichiev *et al.*, Phys. Lett. **B663**, 43 (2008), *Study of dielectron production in C+C collisions at 1 AGeV.*

[105] A. Kugler, Studying hadron properties in baryonic matter with HADES, proceedings of the HADRON 2009 conference, Tallahasse, USA, 2010.

[106] Y. Pachmayer, Dielektronenproduktion in 12C + 12C Kollisionen bei 1 GeV pro Nukleon.

[107] M. Thomere, C. Hartnack, G. Wolf, and J. Aichelin, Phys. Rev. **C75**, 064902 (2007), *Analysis of Dilepton Invariant Mass Spectrum in C+C at 2 and 1 AGeV.*

[108] H. W. Barz, B. Kampfer, G. Wolf, and M. Zetenyi, (2006), *Propagation of broad meson resonances in a BUU type transport model: Application to di-electron production.*

[109] G. Agakichiev et al. (the HADES Collaboration), Origin of the low-mass electron pair excess in light nucleus-nucleus collisions, arXiv:0910.5875[nucl-ex], accepted for publication in Phys. Lett. B.

[110] A. Rustamov, Exclusive η Meson Reconstruction in Proton-Proton Collisions at 2.2 GeV with the HADES Spectrometer and High Resolution Tracking.

[111] S. Spataro, Characterization of the HADES spectrometer in pp collisions at 2.2 GeV: elastic scattering and exclusive eta reconstruction.

[112] A. I. Titov, B. Kampfer, and B. L. Reznik, Eur. Phys. J. **A7**, 543 (2000), *Production of Phi mesons in near-threshold pi N and N N reactions.*

[113] G. Agakichiev *et al.*, Eur. Phys. J. **A40**, 45 (2009), *Measurement of charged pions in 12C + 12C collisions at 1A GeV and 2A GeV with HADES.*

[114] A. M. Eisner, E. L. Hart, R. I. Louttit, and T. W. Morris, Phys. Rev. **138**, B670 (1965), *Proton-Proton Scattering at 1.48 BeV.*

[115] W. J. Fickinger, E. Pickup, D. K. Robinson, and E. O. Salant, Phys. Rev. **125**, 2082 (1962), *p-p Interactions at 2 Bev. 1. Single-Pion Production.*

[116] S. A. El-Samad *et al.*, Eur. Phys. J. **A30**, 443 (2006), *Single-pion production in p p collisions at 0.95-GeV/c. I.*

[117] S. Abd El-Samad *et al.*, Eur. Phys. J. **A39**, 281 (2009), *Single-Pion Production in pp Collisions at 0.95 GeV/c (II).*

[118] V. V. Sarantsev *et al.*, Eur. Phys. J. **A21**, 303 (2004), *The study of the neutral pion production in proton proton collisions at beam momenta 1581-MeV/c and 1683-MeV/c.*

[119] E. Pickup, D. K. Robinson, and E. O. Salant, Phys. Rev. Lett. **8**, 329 (1962), *Three-Pion Mass Distributions and the η Meson.*

[120] K. Wisniewski *et al.*, Acta Physica Polonica **41**, 415 (2010), *Strangeness production of heavy-ion collisions at intermediate energies revisited with pions.*

[121] T. Weidmann, E. L. Bratkovskaya, W. Cassing, and U. Mosel, Phys. Rev. **C59**, 919 (1999), *e+ e- pairs from pi- A reactions.*

[122] W. Schn, H. Bokemeyer, W. Koenig, and V. Metag, Act. Phys. Pol. **B27**, 2959 .

[123] W. Cassing, E. S. Golubeva, A. S. Ilinov, and L. A. Kondratyuk, Phys. Lett. **B396**, 26 (1997), *Medium effects in the production and decay of omega- and rho-resonances in pion nucleus interactions.*

[124] Y. S. Golubeva, L. A. Kondratyuk, and W. Cassing, Nucl. Phys. **A625**, 832 (1997), *Medium effects in the production and decay of vector mesons in pion nucleus reactions.*

[125] A. I. Titov and B. Kämpfer, Eur. Phys. J. **A12**, 217 (2001), *Isoscalar-Isovector Interferences in $\pi N \to N e^+ e^-$ Reactions as a Probe of Baryon Resonance Dynamics.*

[126] D. A. Geffen, Phys. Rev. **125**, 1745 (1962), *Reaction, pi-+p $\to$ e++e-+n, as a Means of Measuring the Electromagnetic Form Factor of the Charged Pion.*

[127] M. P. Rekalo, E. Tomasi-Gustafsson, and D. Prout, Soviet. Jour. of Nucl. Phys. **1**, 760 (1965), *On a possibility of determining nucleon from factors for time-like measurements.*

[128] D. O. Riska and G. E. Brown, Nucl. Phys. **A679**, 577 (2001), *Nucleon resonance transition couplings to vector mesons.*

[129] C. Caso *et al.*, Eur. Phys. J. **C3**, 1 (1998), *Review of particle physics.*

[130] M. Lutz, B. Friman, and M. Soyeur, Nuclear Physics A **713**, 97 (2003).

[131] Lykasov, G., private communication, Orsay, 2009.

[132] S. Ong, J. Van de Wiele, and M. P. Rekalo, Eur. Phys. J. **A6**, 215 (1999), *Pion electroproduction in parity violating elastic e p scattering experiment.*

[133] J. Diaz *et al.*, Nucl. Instrum. Meth. **A478**, 511 (2002), *Design and commissioning of the GSI pion beam.*

[134] Conceptual Design Report: An International Accelerator Facility for Beams of Ions and Antiprotons, GSI, GSI, 2001.

[135] FAIR Baseline Technical Report, http://www.gsi.de/fair/reports/btr.html, 2006.

[136] The PANDA Collaboration, (2009), *Physics Performance Report for PANDA: Strong Interaction Studies with Antiprotons.*

[137] the PANDA collaboration, PANDA detectors Technical Design Reports, http://www-panda.gsi.de/auto/home.htm.

[138] J. Boucher, Test of a 60 crystal calorimeter for PANDA, internal report, 2008.

[139] R. G. Sachs, Phys. Rev. **126**, 2256 (1962), *High-Energy Behavior of Nucleon Electromagnetic Form Factors.*

[140] A. Zichichi, S. M. Berman, N. Cabbibo, and R. Gatto, Nuovo Cimento **24**, 170 (1962), *Proton-antiproton annihilation into electrons, muons and vector bosons .*

[141] S. J. Brodsky and G. R. Farrar, Phys. Rev. **D11**, 1309 (1975), *Scaling Laws for Large Momentum Transfer Processes.*

[142] E. Titchmarsh, *Theory of functions* (Oxford university Press, London, 1939), p. 179.

[143] A. I. Akhiezer and M. P. Rekalo, Sov. Phys. Dokl. **13**, 572 (1968), *Polarization phenomena in electron scattering by protons in the high energy region.*

[144] A. I. Akhiezer and M. P. Rekalo, Sov. J. Part. Nucl. **4**, 277 (1974), *Polarization effects in the scattering of leptons by hadrons.*

[145] R. Hofstadter and R. Herman, Phys. Rev. Lett. **6**, 293 (1961), *Electric and Magnetic Structure of the Proton and Neutron.*

[146] R. M. Littauer, H. F. Schopper, and R. R. Wilson, Phys. Rev. Lett. **7**, 141 (1961), *Scattering of Bev Electrons by Hydrogen and Deuterium.*

[147] C. F. Perdrisat, V. Punjabi, and M. Vanderhaeghen, Prog. Part. Nucl. Phys. **59**, 694 (2007), *Nucleon electromagnetic form factors.*

[148] J. Arrington, Phys. Rev. **C68**, 034325 (2003), *How well do we know the electromagnetic form factors of the proton?*

[149] M. K. Jones *et al.*, Phys. Rev. Lett. **84**, 1398 (2000), G_{E_p}/G_{M_p} *Ratio by Polarization Transfer in* $\vec{e}p \rightarrow e\vec{p}$.

[150] O. Gayou *et al.*, Phys. Rev. **C64**, 038202 (2001), *Measurements of the elastic electromagnetic form factor ratio* μ_p *GEp/GMp via polarization transfer.*

[151] V. Punjabi *et al.*, Phys. Rev. C **71**, 055202 (2005), *Proton elastic form factor ratios to* $Q^2 = 3.5 GeV^2$ *by polarization transfer.*

[152] A. V. Belitsky, X.-d. Ji, and F. Yuan, Phys. Rev. Lett. **91**, 092003 (2003), *A perturbative QCD analysis of the nucleon's Pauli form factor* $F_2(Q^2)$.

[153] F. Iachello, A. D. Jackson, and A. Lande, Phys. Lett. **B43**, 191 (1973), *Semiphenomenological fits to nucleon electromagnetic form- factors.*

[154] C. F. Perdrisat, Nucl. Phys. **A827**, 267c (2009), *New proton form factor ratio recoil polarization measurements in Hall C at JLab.*

[155] B. E., The GEp-III Experiment: Recent Results on the Proton Electromagnetic Form Factor Ratio, talk at the HADRON2009 conference, to appear in the proceedings, 2009.

[156] C. B. Crawford *et al.*, Phys. Rev. Lett. **98**, 052301 (2007), *Measurement of the proton electric to magnetic form factor ratio from $^1H(\vec{e}, e'p)$.*

[157] D. Higinbotham, Precision Measurements of the Proton Elastic Form Factor Ratio, talk at the HADRON2009 conference, to appear in the proceedings, 2009.

[158] L. W. Mo and Y.-S. Tsai, Rev. Mod. Phys. **41**, 205 (1969), *Radiative Corrections to Elastic and Inelastic e p and μ p scattering.*

[159] L. C. Maximon and J. A. Tjon, Phys. Rev. **C62**, 054320 (2000), *Radiative corrections to electron proton scattering.*

[160] Y. M. Bystritskiy, E. A. Kuraev, and E. Tomasi-Gustafsson, Phys. Rev. **C75**, 015207 (2007), *Structure function method applied to polarized and unpolarized electron-proton scattering: A solution of the GE_p/GMp discrepancy.*

[161] P. A. M. Guichon and M. Vanderhaeghen, Phys. Rev. Lett. **91**, 142303 (2003), *How to reconcile the Rosenbluth and the polarization transfer method in the measurement of the proton form factors.*

[162] P. G. Blunden, W. Melnitchouk, and J. A. Tjon, Phys. Rev. Lett. **91**, 142304 (2003), *Two-photon exchange and elastic electron proton scattering.*

[163] A. V. Afanasev, S. J. Brodsky, C. E. Carlson, Y.-C. Chen, and M. Vanderhaeghen, Phys. Rev. **D72**, 013008 (2005), *The two-photon exchange contribution to elastic electron nucleon scattering at large momentum transfer.*

[164] P. G. Blunden, W. Melnitchouk, and J. A. Tjon, Phys. Rev. **C72**, 034612 (2005), *Two-photon exchange in elastic electron nucleon scattering.*

[165] Y.-C. Chen, C.-W. Kao, and S.-N. Yang, Phys. Lett. **B652**, 269 (2007), *Is there model-independent evidence of the two-photon- exchange effect in the electron-proton elastic scattering cross section?*

[166] J. Arrington, W. Melnitchouk, and J. A. Tjon, Phys. Rev. **C76**, 035205 (2007), *Global analysis of proton elastic form factor data with two-photon exchange corrections.*

[167] M. P. Rekalo, E. Tomasi-Gustafsson, and D. Prout, Phys. Rev. **C60**, 042202 (1999), *Search for evidence of two photon exchange in new experimental high momentum transfer data on electron deuteron elastic scattering.*

[168] M. P. Rekalo and E. Tomasi-Gustafsson, Eur. Phys. J. **A22**, 331 (2004), *Model independent properties of two-photon exchange in elastic electron proton scattering.*

[169] E. Tomasi-Gustafsson and G. I. Gakh, Phys. Rev. **C72**, 015209 (2005), *Search for evidence of two photon contribution in elastic electron proton data.*

[170] W. M. Alberico, S. M. Bilenky, C. Giunti, and K. M. Graczyk, Phys. Rev. **C79**, 065204 (2009), *Electromagnetic form factors of the nucleon: new fit and analysis of uncertainties.*

[171] N. Kivel and M. Vanderhaeghen, Phys. Rev. Lett. **103**, 092004 (2009), *Two-photon exchange in elastic electron-proton scattering : QCD factorization approach.*

[172] J. Arrington *et al.*, Proposal E05-017 at Jlab, 2005.

[173] R. Gilman *et al.*, Jlab proposal E04-019, 2004.

[174] G. I. Gakh and E. Tomasi-Gustafsson, (2008), *General analysis of two photon exchange in elastic electron ^4He scattering and $e^+ + e^- \to \pi^+ + \pi^-$.*

[175] E. Tomasi-Gustafsson, M. Osipenko, E. A. Kuraev, Y. Bystritsky, and V. V. Bytev, (2009), *Compilation and analysis of charge asymmetry measurements from electron and positron scattering on nucleon and nuclei.*

[176] B. Raue, Measurement of Two-Photon Exchange (TPE) Effect with CLAS, talk at the HADRON2009 conference, to appear in the proceedings, 2009.

[177] W. Brooks *et al.*, Beyond the Born Approximation: A Precise Comparison of Positron-Proton and Electron-Proton Elastic Scattering in CLAS, Jlab proposal E07-005, 2007.

[178] J. Arrington, Phys. Rev. **C69**, 032201 (2004), *Evidence for two photon exchange contributions in electron proton and positron proton elastic scattering.*

[179] J. Lachniet *et al.*, Phys. Rev. Lett. **102**, 192001 (2009), *A Precise Measurement of the Neutron Magnetic Form Factor GMn in the Few-GeV2 Region.*

[180] S. Rock *et al.*, Phys. Rev. **D46**, 24 (1992), *Measurement of elastic electron - neutron scattering and inelastic electron - deuteron scattering cross-sections at high momentum transfer.*

[181] E. Geis *et al.*, Phys. Rev. Lett. **101**, 042501 (2008), *The Charge Form Factor of the Neutron at Low Momentum Transfer from the $^2\vec{H}(\vec{e}, e'n)p$ Reaction.*

[182] Van de Wiele, J., private communication on polarized cross-section.

[183] M. Castellano *et al.*, Nuovo Cim. **A14**, 1 (1973), *The reaction e+ e- $\to$ p anti-p at a total energy of 2.1 gev.*

[184] G. Bassompierre *et al.*, Phys. Lett. **B68**, 477 (1977), *First Determination of the Proton Electromagnetic Form- Factors at the Threshold of the Timelike Region.*

[185] B. Delcourt *et al.*, Phys. Lett. **B86**, 395 (1979), *STUDY OF THE REACTION e+ e- $\to$ p anti-p IN THE TOTAL ENERGY RANGE 1925-MeV - 2180-MeV.*

[186] D. Bisello *et al.*, Nucl. Phys. **B224**, 379 (1983), *a measurement of $e^+ e^- \to \bar{p} p$ FOR 1975 MeV $\leq \sqrt{s} \leq$ 2250 MeV.*

[187] D. Bisello *et al.*, Z. Phys. **C48**, 23 (1990), *Baryon pair production in e+ e- annihilation at $\sqrt{s}$ = 2.4 GeV.*

[188] G. Bardin *et al.*, Phys. Lett. **B255**, 149 (1991), *Measurement of the proton electromagnetic form-factor near threshold in the timelike region.*

[189] G. Bardin *et al.*, Nucl. Phys. **B411**, 3 (1994), *Determination of the electric and magnetic form-factors of the proton in the timelike region.*

[190] A. Antonelli *et al.*, Phys. Lett. **B334**, 431 (1994), *Measurement of the electromagnetic form-factor of the proton in the timelike region.*

[191] T. A. Armstrong *et al.*, Phys. Rev. Lett. **70**, 1212 (1993), *Measurement of the proton electromagnetic form-factors in the timelike region at 8.9 GeV^2 - 13GeV^2.*

[192] M. Ambrogiani *et al.*, Phys. Rev. **D60**, 032002 (1999), *Measurements of the magnetic form factor of the proton in the timelike region at large momentum transfer.*

[193] M. Andreotti *et al.*, Phys. Lett. **B559**, 20 (2003), *Measurements of the magnetic form-factor of the proton for timelike momentum transfers.*

[194] T. K. Pedlar *et al.*, Phys. Rev. Lett. **95**, 261803 (2005), *Precision measurements of the timelike electromagnetic form factors of pion, kaon, and proton.*

[195] B. Aubert *et al.*, Phys. Rev. **D73**, 012005 (2006), *A Study of $e^+e^- \to p\bar{p}$ using initial state radiation with BABAR.*

[196] M. Ablikim *et al.*, Phys. Lett. **B630**, 14 (2005), *Measurement of the cross section for $e^+ e^- \to p\bar{p}$ at center-of-mass energies from 2.0 GeV to 3.07 GeV.*

[197] R. Baldini, C. Bini, P. Gauzzi, M. Mirazita, N. Negrini, and S. Pacetti, , *A description of the ratio between electric and magnetic proton form factors by using space-like, time-like data and dispersion relations.*

[198] A. Antonelli *et al.*, Nucl. Phys. **B517**, 3 (1998), *The first measurement of the neutron electromagnetic form factors in the timelike region.*

[199] H.-W. Hammer, *Nucleon Form Factors in the Space- and Timelike Regions* , proceedings of e$^+$ e$^-$ Physics at Intermediate Energies, SLAC, Stanford, California, May 2001, p216.

[200] M. Sudol *et al.*, (2010), *Feasibility studies of the time-like proton electromagnetic form factor measurements with PANDA at FAIR.*

[201] E. Tomasi-Gustafsson, E. A. Kuraev, S. Bakmaev, and S. Pacetti, Phys. Lett. **B659**, 197 (2008), *Search for two photon exchange from $e^+ + e^- \to p + \bar{p} + \gamma$ data.*

[202] J. Guttmann *et al.*, Study of Two-Photon Corrections in the p$\bar{p}$ →e$^+$e$^-$ process, poster at the EINN09 conference, 2009.

[203] E. Tomasi-Gustafsson, Nuovo Cim. **C27**, 413 (2004), *Nucleon electromagnetic structure: Past, present, and future.*

[204] S. J. Brodsky, C. E. Carlson, J. R. Hiller, and D. S. Hwang, Phys. Rev. **D69**, 054022 (2004), *Single-spin polarization effects and the determination of timelike proton form factors.*

[205] E. L. Lomon, Phys. Rev. **C66**, 045501 (2002), *Effect of recent R(p) and R(n) measurements on extended Gari-Kruempelmann model fits to nucleon electromagnetic form factors.*

[206] E. Tomasi-Gustafsson, F. Lacroix, C. Duterte, and G. I. Gakh, Eur. Phys. J. **A24**, 419 (2005), *Nucleon electromagnetic form factors and polarization observables in space-like and time-like regions.*

[207] S. Pacetti, Eur. Phys. J. **A32**, 421 (2007), *Nucleon form factors and dispersion relations.*

[208] G. Hoehler *et al.*, Nucl. Phys. **B114**, 505 (1976), *Analysis of Electromagnetic Nucleon Form-Factors.*

[209] M. A. Belushkin, H. W. Hammer, and U. G. Meissner, Phys. Rev. **C75**, 035202 (2007), *Dispersion analysis of the nucleon form factors including meson continua.*

[210] J. J. Kelly, Phys. Rev. C **66**, 065203 (2002), *Nucleon charge and magnetization densities from Sachs form factors.*

[211] G. A. Miller, Phys. Rev. **C68**, 022201 (2003), *Shapes of the proton.*

[212] H. W. Hammer, U.-G. Meissner, and D. Drechsel, Phys. Lett. **B385**, 343 (1996), *Dispersion-theoretical analysis of the nucleon electromagnetic form factors: Inclusion of time-like data.*

[213] N. Isgur and G. Karl, Phys. Rev. **D20**, 1191 (1979), *Ground State Baryons in a Quark Model with Hyperfine Interactions.*

[214] J. de Melo, T. Frederico, E. Pace, S. Pisano, and G. Salme, Phys. Lett. **B671**, 153 (2009), *Time- and Spacelike Nucleon Electromagnetic Form Factors beyond Relativistic Constituent Quark Models.*

[215] M. Guidal, M. V. Polyakov, A. V. Radyushkin, and M. Vanderhaeghen, Phys. Rev. **D72**, 054013 (2005), *Nucleon form factors from generalized parton distributions.*

[216] D. Marchand *et al.*, Time-like observables: differential cross section and angular asymmetry, HAL : in2p3-00374971.

[217] E. Eisenhandler *et al.*, Nucl. Phys. **B96**, 109 (1975), *Measurement of Differential Cross-Sections for anti- Proton-Proton Annihilation Into Charged Pion and Kaon Pairs Between 0.79-GeV/c and 2.43-GeV/c.*

[218] T. Buran *et al.*, Nucl. Phys. **B116**, 51 (1976), *$\bar{p}p$ Annihilation Into $\pi^+\pi^-$ and $K^+ K^-$ at 6.2 GeV/c.*

[219] A. Berglund *et al.*, Nucl. Phys. **B137**, 276 (1978), *A Study of the Reaction anti-p p → pi- pi+ at 10- GeV/c.*

[220] S. Ong and V. de Wiele J., Event generators for two charged and neutral pions production in proton-antiproton annihilation, internal report IPNO-DR-08-01, HAL-IN2P3: in2p3-00222925., 2008.

[221] Van de Wiele, J., private communication.

[222] J. Allison *et al.*, IEEE Trans. Nucl. Sci. **53**, 270 (2006), *Geant4 developments and applications.*

[223] H. Bichsel, Nucl. Instrum. Meth. **A562**, 154 (2006), *A method to improve tracking and particle identification in TPCs and silicon detectors.*

[224] D. Antonczyk *et al.*, Nucl. Instrum. Meth. **A565**, 551 (2006), *Performance studies with an ALICE TPC prototype.*

[225] J. Apostolakis *et al.*, Nucl. Instrum. Meth. **A453**, 597 (2000), *An implementation of ionisation energy loss in very thin absorbers for the GEANT4 simulation package.*

[226] B. Beischer *et al.*, Nucl. Instrum. Meth. **A583**, 485 (2007), *Comparison of Geant4 transition radiation and ionization loss simulation to testbeam data.*

[227] R. Kunne, private communication.

[228] H. Drumm *et al.*, Nucl. Instr. Meth. **176**, 333 (1980), *experience with jet chamber of the JADE detector at PETRA.*

[229] M. Aderholz, P. Lazeyras, I. Lehraus, R. Matthewson, and W. Tejessy, Nucl. Instrum. Meth. **118**, 419 (1974), *High-resolution ionization measurements in the region of the relativistic rise.*

[230] W.-M. Yao et al., Journal of Physics G **33**, 1+ (2006), *Review of Particle Physics.*

[231] B. Aubert *et al.*, Nucl. Instrum. Meth. **A479**, 1 (2002), *The BaBar detector.*

[232] I. Adam *et al.*, Nucl. Instrum. Meth. **A433**, 121 (1999), *The DIRC detector at BaBar.*

[233] D. W. G. S. Leith, Nucl. Instrum. Meth. **A494**, 389 (2002), *DIRC: The particle identification system for BaBar.*

[234] S. Agostinelli *et al.*, Nucl. Instrum. Meth. **A506**, 250 (2003), *GEANT4: A simulation toolkit.*

[235] http://geant4.web.cern.ch/geant4/.

[236] S. Banerjee *et al.*, J. Phys. Conf. Ser. **119**, 032007 (2008), *Validating Geant4 versions 7.1 and 8.3 against 6.1 for BaBar.*

[237] H. W. Bertini and M. P. Guthrie, Nucl. Phys. **A169**, 670 (1971), *News item results from medium-energy intranuclear-cascade calculation.*

[238] G. Folger *et al.*, EPJA **21**, 407 (204), *The Binary Cascade.*

[239] J. Apostolakis *et al.*, Hadronic shower shape studies in Geant4, CERN-LCGAPP-2007-02, 2007.

[240] S. Kunori, G4 Physics discussion with G4 team, home.fnal.gov/ kunori/cms/meetings/...G4/080228-kunori-G4-physics.pdf, 2008.

[241] S. Banerjee, Calorimeter Simulation Task Force in CMS, http://www.tifr.res.in/ dhep/dhepseminars/08-04-2009.pdf.

[242] T. Brandt, Electron identification and measurement of the inclusive semileptonic branching fraction of B mesons at the BABAR experiment, Dresden Tech. University PhD thesis, 2001.

[243] A. Abashian *et al.*, Nucl. Instrum. Meth. **A479**, 117 (2002), *The Belle detector.*

[244] B. Aubert *et al.*, Phys. Rev. D **67**, 031101 (2003), *Measurement of the branching fraction for inclusive semileptonic B meson decays.*

[245] B. Aubert *et al.*, Phys. Rev. **D69**, 111104 (2004), *Measurement of the electron energy spectrum and its moments in inclusive $B \to Xe\nu$ decays.*

[246] K. Hanagaki, H. Kakuno, H. Ikeda, T. Iijima, and T. Tsukamoto, Nucl. Instrum. Meth. A **485**, 490 (2002), *Electron identification in Belle.*

[247] E. Nakano, Nucl. Instrum. Meth. **A494**, 402 (2002), *Belle PID.*

[248] T. Brandt, Charged particle identification at the BABAR-experiment, Talk given at the PANDA collaboration meeting, march 2005.

[249] H. Marsiske, PID with BABAR, private communication, 2007.

[250] T. A. Armstrong *et al.*, Phys. Rev. D **56**, 2509 (1997), *Two-body neutral final states produced in antiproton-proton annihilations at $2.911 \leq \sqrt{(s)} \leq 3.686$ GeV.*

[251] S. Ong and V. de Wiele J., to be submitted to EPJA, 2010.

[252] T. A. Armstrong *et al.*, Phys. Rev. Lett. **68**, 1468 (1992), *Precision measurements of charmonium states formed in $\bar{p}\,p$ annihilation.*

[253] C. Adamuscin, E. A. Kuraev, E. Tomasi-Gustafsson, and F. E. Maas, Phys. Rev. **C75**, 045205 (2007), *Testing axial and electromagnetic nucleon form factors in time-like regions in the processes $\bar{p} + n \to \pi^- + l^- + l^+$ and $\bar{p} + p \to \pi^0 + l^- + l^+$, $l = e$, μ.*

[254] O. D. Dalkarov, P. A. Khakhulin, and A. Y. Voronin, Nucl. Phys. **A833**, 104 (2010), *On the electromagnetic form factors of hadrons in the time-like region near threshold.*

[255] J. Carbonell, K. V. Protasov, and O. D. Dalkarov, Nucl. Phys. **A558**, 353c (1993), *A Possible quasinuclear state near the Lambda Anti-lambda threshold.*

[256] H. Fonvieille and V. A. Karmanov, Eur. Phys. J. **A42**, 287 (2009), *Antiproton-nucleus electromagnetic annihilation as a way to access the proton timelike form factors.*

[257] Pentchev, L. and Perdrisat, C.F. and Cisbani, E. and Punjabi V. and Wojtsekhowski, B., Large Acceptance Proton Form Factor Ratio Measurements at 13 and 15 GeV^2 using recoil polarization, Jlab proposal E12-07-109, 2007.

[258] E. Brash, M. J. Jones, C. F. Perdrisat, and V. Punjabi, "GEp/GMp with an 11 GeV electron beam in Hall C", Jlab proposal E12-009-001, 2009.

[259] J. Arrington., S. Gilad, B. Moffit, and B. Wojtsekhowski, Precision measurement of the proton elastic cross-section at large Q^2, Jlab proposal E12-07-108, 2007.

[260] B. Pire and L. Szymanowski, Phys. Lett. **B622**, 83 (2005), *QCD analysis of $\bar{p}\,N \to \gamma^\star \pi$ in the scaling limit.*

[261] J. P. Lansberg, B. Pire, and L. Szymanowski, Phys. Rev. **D76**, 111502 (2007), *Production of a pion in association with a high-Q2 dilepton pair in antiproton-proton annihilation at GSI- FAIR.*